INNER-OUTER INTERACTIONS IN A ROUGH-WALL TURBULENT BOUNDARY LAYER

BY

GOKUL PATHIKONDA

DISSERTATION

Submitted in partial fulfillment of the requirements
for the degree of Doctor of Philosophy in Theoretical and Applied Mechanics
in the Graduate College of the
University of Illinois at Urbana-Champaign, 2017

Urbana, Illinois

Doctoral Committee:

Professor Kenneth T. Christensen, Chair
Associate Professor Carlos A. Pantano-Rubino
Professor Surya Pratap Vanka
Professor James Best

ABSTRACT

The primary goal of the present effort is to enhance the current understanding of inner–outer interactions in rough-wall turbulent boundary layers. These interactions were recently established over smooth-wall turbulent boundary layers as modulating interactions, where the outer layer large scales amplitude and frequency modulate the near-wall small scales. Given that the outer layer dynamics responsible for these modulations are identical in most high-Reynolds-number (Re) rough-wall flows as well, similar modulation interactions are are explored to identify the similarities and differences of these interactions and establish a spatio–temporal description of the same. This is particularly important given the engineering significance of the flows over rough walls.

This work was performed as two parts. In the first part, high temporal-resolution boundary layer hot-wire measurements were made in a wind tunnel, that fully resolved all dynamical scales temporally at fixed points in the flow. Flows over smooth and rough walls were investigated, with the latter being a complex topography indicative of a realistic roughness commonly encountered in engineering applications. Single- and two-probe measurements provided a dual perspective on the large scales, and enabled analysis of analytical techniques commonly employed. With these measurements, it was found that the nature of amplitude and frequency modulation occur even over this complex topography, and that the structure is very similar to that observed in smooth-wall flow. Further, the simultaneous two-probe measurements enabled the investigation of predictive models, which interestingly suggested a possibly stronger modulation in rough-wall flow compared to the smooth-wall case. A 'quasi-steady, quasi-homogenous'

theory previously developed for smooth-wall flow showed promising predictions of the calibrations constants even in rough-wall flow, lending additional support to the mechanisms speculating that the small scales respond in a quasi-steady manner, *irrespective of the origin*, to the large scales.

With these inner–outer interactions established, the second part of the current work aimed to develop a spatio–temporal description of the modulating mechanisms using high frame-rate particle-image velocimetry (PIV). The experiments, performed in a refractive-index-matched flow facility, enabled the measurements very close to the surface without being impeded by the near-wall reflections that are common in smooth- and rough-wall PIV experiments. Following a preliminary demonstration of the relevant physics observed via point measurements, a representative large-scale structure was defined using conditional averaging. The associated changes to the small-scale turbulence close to the wall indicated similar modulation interactions, and provided a spatial tool to investigate the same. Further, the large-scale–small-scale interaction structure lended support to the speculations made on the same using hot-wire measurements in the current work and in the recent literature for smooth- and rough-wall flow.

These experiments identify and emphasize the significance of inner–outer interactions over rough-wall flows, and the necessity to accurately model them to enhance the fidelity of any high Re simulations over rough walls.

To my father, Narendra Rao, for a lifetime of inspiration

To my mother, Vasantha, for a lifetime of affection

ACKNOWLEDGMENTS

It is apt to start my acknowledgments by first thanking my father, whose firm encouragement gave me the confidence and set me on the path for this PhD.

This work would not have been possible without the enlightening and pleasurable guidance of my advisor, Prof. Kenneth Christensen, who taught me invaluable lessons in high quality research, turbulence and problem solving. Learning under his able guidance and working with him turned the various research challenges into pleasurable experiences. His understanding and accommodating nature went a long way in extracting the best work out of me even at turbulent times, and for this, I am thoroughly grateful.

I would like to thank Prof. Carlos Pantano and Prof. Will Anderson for the collaborative discussions about the work. I thank Wu Sicong for sharing his DNS results and for the discussions on analytical procedures. I would also like to thank my knowledgeable committee, Prof. Carlos Pantano, Prof. Jim Best and Prof. Surya Pratap Vanka, for accepting to serve on my committee, and providing critical and encouraging comments on my work.

I would like to thank the administrative staff at University of Illinois and University of Notre Dame for their help throughout, with particular mentions to Kathy Smith (UIUC), Greg Milner (UIUC), Rob Chlebek (ND), Melissa O'Neil (ND) and Tamara Mason (ND). I would like to acknowledge the financial support to this work provided by Air Force Office of Scientific Research (Grant No. FA9550-14-1-0101, Dr. Douglas Smith, Program Manager).

My stay at University of Illinois brought me a long list of friends for life, and while I cant list everyone, it definitely starts with Sohan Kale. The intangible

contributions to this work of his friendship, humble genius and the long conversations on science, game of squash and philosophy are more than is apparent here, and played a big factor in keeping me sane. I also had the pleasure of working with, and taking the help from many bright colleagues– Taehoon Kim, Gianluca Blois, Julio Barros, Nate Bristow, Farzan Kazemifar, Yaofa Li, Caitlyn Clark, to name a few. I have made liberal use throughout my PhD, with deep gratitude, of Taehoon's nature to help others, and of Gianluca's advices. The technology-related discussions I had with Julio and Nate were fun and necessary distractions from work. I must acknowledge the direct contributions to this work from Caitlyn Clark, who helped me a great deal in setting up the PIV experiments.

On the personal front, the trust and support of my family has been my real strength and motivation. Particularly significant has been the close presence of my beautiful wife, Shruthi, and my sister's family- Pavani and Praveen. Shruthi graciously let me immerse myself in science during our first year of marriage, and her trust in me gave me great strength and perseverance during the home-stretch of my PhD. Pavani and Praveen have been the friends, siblings and parents as the moment asked of them, and I cannot imagine doing this PhD without their help and support. My brother Jithu and Sapna were instrumental in taking many a hurdle off my way to this PhD from the other side of the ocean, and I'm deeply indebted to my joint Kothakota family. I express my sincere gratitude to Shankar family for trusting in my abilities, and backing me on my decisions.

TABLE OF CONTENTS

LIST OF TABLES

LIST OF FIGURES

LIST OF ABBREVIATIONS

AM	Amplitude Modulation
bFOV	big Field Of View
CTA	Constant Temperature Anemometry
CWT	Continuous Wavelet Transform
DNS	Direct Numerical Simulation
FM	Frequency Modulation
FOV	Field of View
HMP	High Momentum Pathway
IOIM	Inner-Outer Interaction Model
LES	Large Eddy Simulation
NaI	Sodium Iodide
NLT	Non-Linear Terms
PIV	Particle Image Velocimetry
PMES	Pre-Multiplied Energy Spectrum
POD	Proper Orthogonal Decomposition
QSQH	Quasi-Steady Quasi-Homogenous
RANS	Reynolds Averaged Navier Stokes
RI	Refractive Index
RIM	Refractive Index-Matching
RW	Rough Wall
sFOV	small Field Of View
sLSE	spectral Linear Stochastic Estimation

SW	Smooth Wall
TKE	Turbulent kinetic energy
VLSM	Very Large Scale Motion

LIST OF SYMBOLS

Latin Symbols

C	log-law constant
$\tilde{E}$	Wavelet power spectrum
$\hat{f}$	Wavelet center frequency
$\tilde{f}$	Instantaneous Frequency
f_c	Cut-off frequency
H_L	Transfer function in Fourier space
$\tilde{H_L}$	Smoothed and high-frequency-suppressed H_L
h_L	Transfer function kernel
k	Roughness height
k_s	Sand-grain equivalent height
k_x	Streamwise wavenumber
l^+	Inner-scaled hotwire length
$R_{x,y}$	Correlation function between x and y (See section 1.5.1)
Re_τ	Kármán number
$\overline{s}$	Specific gravity
t	Experiment time coordinate
t^*	Inner time scale
Δt	Sampling interval
Δt_s	Superposition time delay
U	Mean streamwise velocity

U_c	Convection velocity
U_∞	Free-stream velocity
ΔU	Roughness function
$\mathbb{U}$	Continuous wavelet transform of u
u	Streamwise velocity
$\tilde{u}$	Total velocity
$\hat{u}$	Modulated and superposed inner-velocity
u_τ	Skin-friction velocity
v	Wall-normal velocity
x	Streamwise coordinate
y	Wall-normal coordinate
y^*	Viscous length scale
y_c	Wall origin correction
y_o	Outer probe location

Greek Symbols

α	Superposition calibration constant
β	Amplitude modulation calibration constant (IOIM)
δ	Boundary layer thickness
$\tilde{\delta}$	'True' boundary layer thickness
Γ	Amplitude modulation calibration constant (mIOIM)
λ	Streamwise wavelength
λ_c	Cut-off wavelength
λ_x	*same as* λ
κ	von Kármán constant
ν	Kinematic viscosity

Π	Wake-parameter
ϕ_{uu}, ϕ_{vv}	Energy spectrum of streamwise and wall-normal turbulence
ρ	Density
σ	Small-scale wavelet energy
Θ	Argument of H_L
$\tilde{\tau}_L$	Large scale variation of τ_w
τ	Relative time coordinate (See section 1.5.1)
τ_w	Wall-shear stress
$\overline{\tau}_w$	Mean of wall-shear stress
τ'_w	Fluctuation of wall-shear stress

Superscripts

a	Amplitude modulation related
f	Frequency modulation related
$'$	Fluctuating
$*$	Inner-parameter
$+$	Inner-normalized

Subscripts

i	Inner
o	Outer
L	Large scale-
s	Small scale-
1P	1-probe
2P	2-probe

CHAPTER 1

INTRODUCTION

The prevalence of turbulence in the many natural and engineering scenarios, and the very ubiquity in various forms, sizes and descriptions, poses the first and most basic of the many questions studying it: *a precise mathematical definition of turbulence*. While turbulence can be observed everywhere, from faucets to rockets to stellar phenomena, common consensus is limited to identifying the same by its properties: that turbulence has a range of random fluctuations, a well-defined flow describable in a stochastic sense, be rich in vorticity and, importantly, is characterized by high 'mixing' of the fluid(s). While turbulence phenomena can be observed everyday, with its characteristics noted historically and studied extensively for over two centuries, it still remains an important bottleneck in many technological applications today.

Early experimental and quantitative studies were performed by Osbourne Reynolds, including the famous pipe flow experiment (Reynolds, 1883) where he observed that the ratio of inertial to viscous forces (Reynolds number, Re) can be used to reasonably predict the onset of 'turbulent motion' in a well controlled pipe flow. He formulated the Reynolds-averaged Navier-Stokes equations for turbulent flows, and pioneered the Reynolds decomposition of turbulent velocity fluctuations (Pope, 2001). In external flows over physical boundaries, Prandtl's formulation of the boundary layer concept came in 1905, where a 'boundary layer' region defined close to the wall was formulated in an asymptotic sense to embody all the viscous effects. This breakthrough idea has been so ubiquitous since, that it appears surprisingly obvious for such an idea to not have arrived sooner. While an analytical solution describing a laminar boundary layer was developed soon after, such a

solution seems too elusive for a turbulent boundary layer even with the great understanding achieved over the years in the mathematics of non-linear dynamics. Besides pipe- and boundary-layer flows, turbulence is commonly encountered in many scenarios ranging from simple flows such as grid flows, wakes, open and closed channels, etc., to complex multi-physical fluid flows such as compressible flows and gas dynamics, buoyancy driven convection in atmospheric flows, combustion, magneto-hydrodynamics etc. With the multifaceted nature of turbulent applications, the importance of turbulence research from a scientific and engineering standpoint cannot be overstated.

Highly non-linear nature and dynamic richness in flow scales pose two of the biggest challenges in turbulence research in many applications. The chief difficulty in computationally 'solving' for turbulence via direct numerical simulations (DNS) of Navier-Stokes equations arises in resolving ALL dynamical scales to completely describe the same– from the largest inertial scales to the smallest dissipative Kolmogorov scales. The computational requirement for the same becomes quickly prohibitive with increasing Re (as will be discussed in section 1.2), which limits the same to low-Re flows and small set of boundary conditions evaluated. Higher Re computations rely mostly on simplified computations (RANS and LES) that compute only the large dynamical scales and rely on models to describe small scale effects (*closure problem*). These models are formulated from experimental observations, scaling and theoretical arguments, and approximations based on low Re DNS observations. For this reason, it can be seen that statistically modeling turbulence phenomena and trying to enhance the fidelity of the computation tools is the goal of a large proportion of turbulent research.

Turbulent wall bounded flows have been observed to sustain coherent structures (with finite spatial and temporal coherence) which influence the behavior of the flow in a predictable way. For this reason, coherent structures in instantaneous turbulence snapshots have been of great interest in wall-bounded turbulence. A statistical representation of the associated physics can greatly ease and improve the fidelity of high Re turbulent simulations. The current work attempts such

an investigation on turbulent boundary layers over smooth- and rough-walls: *to better understand the inner-outer modulating influences imparted by the large- and very-large scale coherent motions (LSMs and VLSMs) on the near-wall turbulence.* This goal is discussed in more detail in the following sections.

The following sections provide a quick overview on high Re boundary layer structure, relevant dynamics, coherent structures, and inner-outer modulating interactions that were established recently on smooth-wall flows. Also discussed is a brief introduction to the effects of wall roughness on the boundary layer, and relevant preliminary arguments necessary for the current work.

1.1 The structure of turbulent boundary layers

An incompressible smooth-wall turbulent boundary layer at 'sufficiently' high Reynolds number (Re) can be, broadly speaking, divided into three regions: (1) an inner, near-wall, turbulence-generating region, (2) an outer, wake region, and (3) an inertial region in-between where both the outer and inner formulations are asymptotically and simultaneously valid. It can be argued that the near-wall dynamics are primarily dependent only on the near-wall conditions, and thus must be fully represented by the same, i.e., wall shear stress (τ_w) and kinematic viscosity (ν). Similarly, the outer layer dynamics must be defined primarily by velocity difference from the free-stream velocity (U_∞) and outer length scale (δ, the boundary-layer thickness), or equivalently Re. These two mechanisms must then be matched by a universal region in which both regions asymptotically approach and match. For many turbulent flow hypotheses, the 'sufficiency' of high Re is qualified by the existence and extent of such a universal region in the flow. This region, termed the '*inertial region*', can be viewed as the energy pathway between the demanding inner region and supplying outer region, operated by a cascade of energy-containing eddy scales. This inner-outer structure overlaid on the mean turbulence kinetic energy production in the different regions is indicated in figure 1.1 (Gad-el Hak & Bandyopadhyay, 1994). It must be remembered that

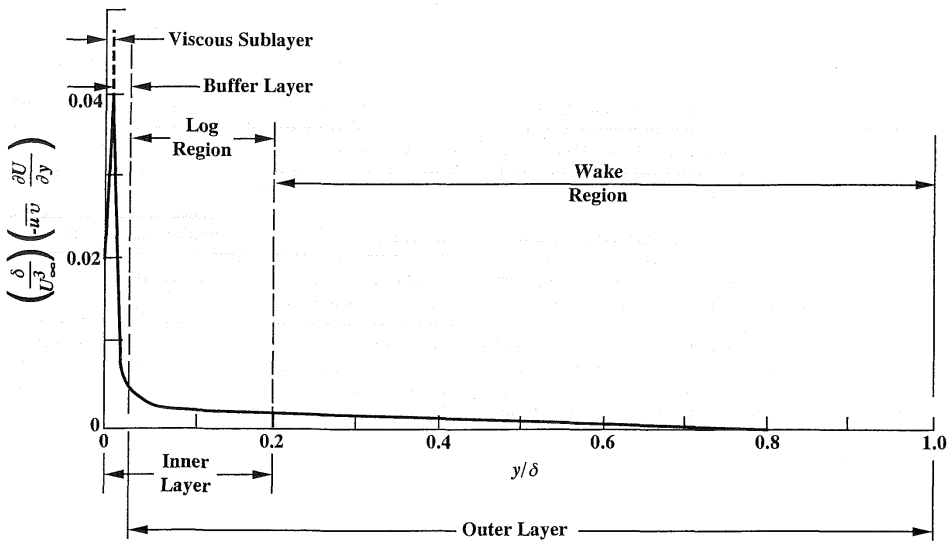

Figure 1.1: Different regions in a typical smooth-wall turbulent boundary layer marked over normalized turbulence energy production rate per unit volume (Kline *et al.*, 1967; Gad-el Hak & Bandyopadhyay, 1994).

this simplified description of a wall-bounded turbulent flow is valid in an average sense, and does not necessarily depict the instantaneous dynamics. An elaborated description and early experimental evidence for this perception of smooth-wall turbulent boundary layers can be found, for example, in Clauser (1956).

1.1.1 Coherent structures in wall-bounded flows

Besides the mean structure defined above, the turbulent flow at any instant is populated by scores of flow structures distributed throughout. A flow structure can be defined as any region of turbulent fluid that exhibits a finite spatial and temporal correlation in flow quantities such as velocity, pressure, vorticity etc. The size of the structure is defined by the extent of such a correlation. While any instantaneous view provides a distribution of structures of various sizes and shapes, only structures that occur repeatedly, that are dynamically significant,

and that characterize the general behavior of turbulent boundary layer are of primary interest in turbulent research. Additionally, a statistical representation of the same must be possible to be identified as a dynamical 'property' of a turbulent boundary layer. An overview of coherent structures and turbulence was summarized in number of studies (Robinson, 1991; Holmes *et al.*, 1998; Adrian, 2007, for example). Two particular types of coherent structures are relevant to the current study.

The turbulence-generating, near-wall region of smooth-wall flow has been observed to be populated by structures of quasi-streamwise-oriented vortices (Kline *et al.*, 1967). These structures were found to scale well with the inner scales of wall shear stress and viscosity, and have been proposed to form a self-sustaining, turbulence-generating mechanism (Jiménez & Pinelli, 1999; Panton, 2001). They had long been assumed to be dynamically independent of Re, as shown by simple scaling arguments and via the apparent invariance of the near-wall turbulent kinetic energy (TKE) peak in early hot-wire measurements and DNS simulations of such flows. Natural perturbations to these structures and subsequent flow instabilities lead to intermittent 'bursts' that result in 'ejections' of high turbulence (low momentum) fluid away from the wall and 'sweeps' of low turbulence (high momentum) fluid towards the wall. This mechanism sustains the near-wall turbulence cycle.

More recently, Kim & Adrian (1999) observed and provided a possible explanation for a significant TKE content ('outer peaks') in the inertial region of smooth-wall pipe flow at much larger streamwise scales ($\lambda > \delta$). In conjunction with DNS simulations, Zhou *et al.* (1999) proposed these large structures as a coherent packet of hairpin-like structures that were previously observed to be populating the inertial region (Head & Bandyopadhyay, 1981). This explained the earlier observations of inclined shear layers (Liu *et al.*, 1991) and uniform momentum regions in PIV fields (Meinhart, 1994; Meinhart & Adrian, 1995), with statistical evidence of such an organization (Christensen & Adrian, 2001) and spatial signatures of the same (Ganapathisubramani *et al.*, 2003; Hommema

& Adrian, 2003) investigated subsequently. These motions were categorized as 'large-' ($\lambda_x < 3\delta$) and 'very-large-scale motions' ($\lambda_x > 3\delta$) (Balakumar & Adrian, 2007) – LSMs and VLSMs, respectively. The VLSMs appeared in pre-multiplied spectral energy maps as a secondary TKE peak near the geometric center of the log region (Ng *et al.*, 2011), and at streamwise length scales $\sim O(10\delta)$ (Balakumar & Adrian, 2007), where δ is the outer length scale (the boundary-layer thickness, pipe radius or channel half-height). Similar observations of energetic motions at long streamwise scales have been made in turbulent channel flow (Balakumar & Adrian, 2007) and turbulent boundary layers (Hutchins & Marusic, 2007*a*), with the VLSMs also termed as 'superstructures'. Particle-image velocimetry (PIV) measurements established the structural characteristics of LSMs (Christensen & Adrian, 2001), and the dynamic significance of these superstructures as influential contributors to local Reynolds shear stress (Ganapathisubramani *et al.*, 2003) and momentum transport (Natrajan & Christensen, 2006). Sufficiently long hot-wire rake measurements were made to establish the spanwise and streamwise characteristics of superstructures by Hutchins & Marusic (2007*a*)–both statistically and instantaneously–as they far exceed the field of view of PIV measurements. A conditionally averaged signature of these 'super structures' using long hotwire time series via their footprint on wall skin friction (τ_w) was established recently by Hutchins *et al.* (2011).

It is thus evident that the near-wall and inertial region coherent structures play an important role in the dynamics of turbulence, and for this reason, has attracted much research attention.

1.2 High Reynolds number (Re) effects

As the Reynolds number increases, via an increase either in the boundary layer thickness or velocity scales, the range of dynamically significant scales increases. In other words, if the boundary layer thickness indicates the scale of the largest scales in the flow (say, the aforementioned LSM and VLSMs), the smallest dynam-

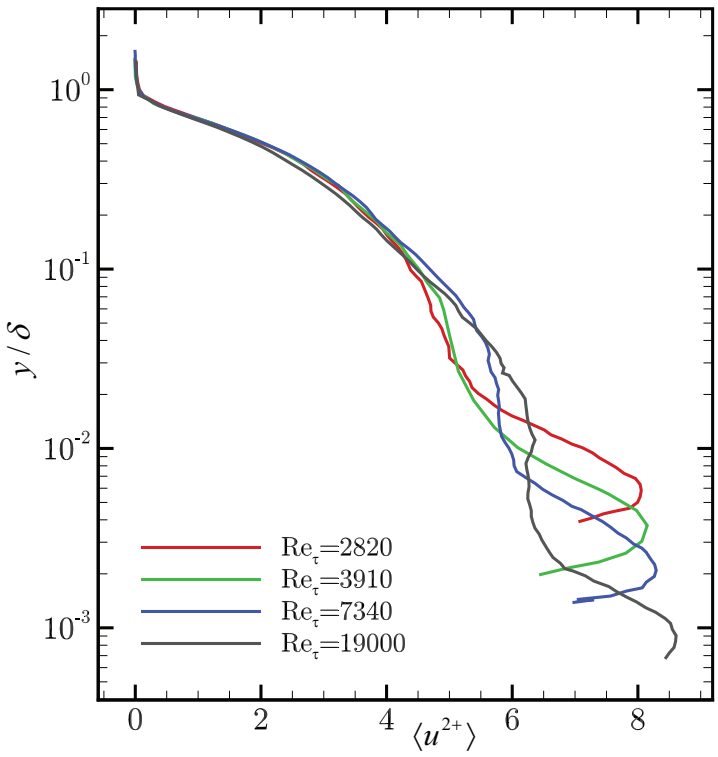

Figure 1.2: Variation streamwise turbulent kinetic energy in outer normalization at various Reynolds numbers (Data from Mathis *et al.* (2011*a*)).

ically significant scales decrease in relative size with increasing Reynolds number. For this reason, instead of conventional Reynolds numbers based on free stream velocity, turbulent boundary layers are commonly quoted by friction Reynolds number based on skin-friction velocity (or Kàrmàn number, $Re_\tau = \delta u_\tau/\nu = \delta/y^*$), which indicates the ratio of smallest scales $[O\,(y^* = \nu/u_\tau)]$ to the largest scales in the flow $[O(\delta)]$. Here, friction velocity ($u_{\tau_w} = \sqrt{\tau_w/\rho}$) is a measure of wall-friction, τ_w, and represents the velocity scale of the inner region dynamics (ρ is the density of the fluid).

Considering the three-region structure of the boundary layer discussed before, with increasing Re_τ, the inner region is reduced to a decreasing proportion of the boundary layer thickness, as the inertial region grows. This can seen in figure 1.2, where the outer-normalized boundary layer structure is shown with increasing Reynolds numbers (data from Mathis *et al.* (2011*a*)). Additionally, the inertial region structures grow increasingly stronger (as can also be seen in figure 1.2) with

cascades of energy scales that match the inner- and outer-region dynamics. The inner–outer interactions, elaborated in the section following, are a bye-product of these high Re effects.

The increasing range of dynamic scales at the high Re poses significant challenges in studying the boundary layers, both computationally and experimentally. DNS requires all dynamical scales to be resolved, and using dimensional analysis, it can be shown that the DNS computational effort required to resolve all the spatial and temporal scales in a flow increase as $Re^{9/4}$ (Pope, 2001). Thus, doubling the Reynolds number requires about 5 times the computational resources. Channel flow DNS at $Re_\tau \approx 5200$ (Lee & Moser, 2015) is one of the largest DNS simulations performed as of the current work. For a perspective, even a small aircraft has a Reynolds number, $Re_\tau \sim O(10^4 - 10^5)$ and the same routinely extends to $O(10^6)$ over large ship hulls, submarines and atmospheric boundary layers. Experimentally, the boundary layer thickness is typically limited by the physical scale of the experimental facility. In the current facility ($\sim 20\,m$ in length), the boundary layer thickness is typically $\sim 100\,mm$. An $Re_\tau \sim 5000$ implies a viscous scale (y^*) of $20\,\mu m$, which can be measured using miniature hotwire probes. Investigation of any higher Re_τ comes at the cost of severe spatial averaging of the sensor (typically $\sim 1\,mm$, Hutchins *et al.* (2009)). Other velocimetry techniques, such as laser doppler velocimetry (LDV) and PIV have comparable (at best) or larger (typically) measurement volumes. Thus, to make measurement using the current experimental techniques at a high Re_τ, either extremely large facilities (such as Nickels *et al.* (2007); Zagarola & Smits (1998); Vincenti *et al.* (2013); Örlü *et al.* (2017) etc.) or extremely small probes (such as Bailey *et al.* (2010)) need to be used. Further, Bailey *et al.* (2010) used pressurized air to reduce viscosity, in conjunction with MEMS probes to perform measurements at very large Re_τ. Even these flow facilities had to be facilitated by modern developments in instrumentation and computational post-processing capabilities. It can thus be said that much of high Re research has only been performed in the last two decades, and is an on going process. Smits *et al.* (2011) provides an excellent

review on this topic.

The experimental and DNS challenges reemphasize the necessity for scaling ideas for these physics and accurate models for LES simulations. Particularly in more engineering flows at high Re, LES becomes an indispensable tool to accommodate the complex geometries and wall-roughness effects. The fidelity of the same, however, is limited by the physicality of the sub-grid scale models that must come from either computations, experiments or theory, or a combination thereof. The current work aims to address this bottle neck via a better understanding of one of these high Re effects.

1.3 Inner-outer modulating interactions

As discussed in the previous section, with increasing Re, the near-wall region is reduced to an increasingly smaller proportion of the boundary layer, with the inertial region structures growing in size relative to the near-wall structures. It is then reasonable to expect that the inner region turbulent production cycle, while autonomous, could still be subjected to influence of the outer large scale structures that blanket them (Hutchins & Marusic, 2007*b*; Morrison, 2007, among others). Early observations by Rao *et al.* (1971) have observed evidence of this, with bursting frequency of the near-wall structures scaling with the outer scales. Bandyopadhyay & Hussain (1984) have also found variations in the small scale variance correlated with the large scales. More recently, Mathis *et al.* (2009*a*), with experiments at high Re, have established a strong correlation between the large scale signatures of the boundary layer, and the slow variations of the amplitude of the small scales ('small scale envelope' using Hilbert transforms)– thus establishing a definitive interaction and linkage between the outer and inner regions of smooth-wall flow through amplitude modulation of the latter scales by the former. It was found that a positive large scale fluctuation is typically associated with an increase in the amplitude of near-wall fluctuations and vice versa. Further, Mathis *et al.* (2011*a*) and Marusic *et al.* (2010) proposed a predictive

model, where a large scale signal sampled in outer region can be used to successfully 'predict' the near-wall small scale variation which accurately embodies the higher order moments and the spectral energy distributions of the 'true' small scales. The excellent agreement of the predictions with the measured values renewed the interest in the phenomenon of modulation interactions in high Re flows.

Additionally, Mathis *et al.* (2009*b*) have shown and compared the amplitude modulation interactions between the boundary layer, channel and pipe flows. Guala *et al.* (2011) showed changes in conditional average of energy spectra at small scales between the high- and low-speed large-scale events in atmospheric boundary layer. Mathis *et al.* (2011*b*) deconstructed the contributions of various terms in velocity skewness, and their relation with the amplitude modulation correlation coefficient. This distinguished the modulation coefficient from the velocity skewness, and formally showed the relation between the same. Duvvuri & McKeon (2015) and Duvvuri & McKeon (2016) imparted synthetic modes corresponding to large scales on the flow using perturbations on the wall, and examined the evolution of the small scales originating from a triadic interactions of the same. Bernardini & Pirozzoli (2011) showed amplitude modulation interactions in DNS simulations via multi-point correlations, and identified a strong correlation between the outer large scales and the inner small scales– a feature that was absent in synthetic signals.

In the logarithmic region of a smooth-wall turbulent boundary layer, Chung & McKeon (2010) and Hutchins *et al.* (2011) used conditional averaging to investigate small-scale activity around large-scale events using LES and experiments, respectively. The strong correlation between the streamwise gradient of large-scale velocity and the small-scale amplitude variations has been hypothesized to be from spanwise-meandering of the aforementioned superstructures. A similar correlation analysis in spectral space via the co-spectral densities was performed by Jacobi & McKeon (2013). In addition to the modulation of the streamwise velocity scales, the spanwise and wall-normal velocity components have also been shown to exhibit similar modulation phenomena (Talluru *et al.*, 2014). The wall

shear stress has also been observed by Mathis *et al.* (2013*a*) to be experiencing such influences, and a predictive model (along the lines of Mathis *et al.* (2011*a*)) was proposed to predict the same. Interestingly, such large- and small-scale interactions are not limited to wall-bounded flows, as similar interactions were reported recently in jet flows (Fiscaletti *et al.*, 2015). In addition to the canonical flows discussed so far, the wall-bounded flow with different boundary conditions were also investigated, such as effect of pressure gradient (Harun *et al.*, 2013; Dróżdż *et al.*, 2015), wall perturbations by sparse 2D roughness (Nadeem *et al.*, 2015) and cubes (Blackman & Perret, 2016).

Improvements in predictive models and theoretical formulations of these physics have also been proposed by many studies. Baars *et al.* (2016) have recently proposed an improvement on the earlier predictive model (Mathis *et al.*, 2011*a*) by using spectral stochastic estimation to better decouple the effect of linear superposition from that of modulation. LES simulations of such predictive models was performed by Inoue *et al.* (2012). From the theoretical standpoint, McKeon (2017) has employed resolvent mode analysis to describe the mechanisms of boundary layer leading to, among others, similar scale interactions. Keylock *et al.* (2016) have employed Hölder exponent framework for the same. Particularly relevant to the current study is the quasi-steady, quasi-homogenous (QSQH) hypothesis of inner-outer interactions, which was discussed in Hutchins *et al.* (2011), Hutchins (2014), Mathis *et al.* (2013*a*), etc., and was formulated in Chernyshenko *et al.* (2012) and Zhang & Chernyshenko (2016). QSQH hypothesis assumes that the small scales evolve in a quasi-steady sense to the relatively slow variations by the large scales. Predictions using the QSQH hypothesis have shown good agreement with those from Mathis *et al.* (2011*a*). Further, in addition to the presence of amplitude modulation as indicated by various studies, the assumptions of QSQH hypothesis also indicates the presence frequency and scale modulations. Baars *et al.* (2015) and Ganapathisubramani *et al.* (2012) have reported the presence of frequency modulation in wall bounded flows using different metrics, tending additional support the the theory. The recent work of Baars *et al.* (2017) nicely

summarizes the structure of inner-outer interactions observed so far over the smooth-wall flows.

It can thus be concluded that sufficient evidence is available to show the inner-outer interactions over the smooth-wall boundary layers at high Reynolds numbers. These phenomena show as amplitude and frequency modulation of the small scales by the large coherent scales that grow increasingly stronger with larger Re, with various formulations being proposed for the same.

1.4 Rough-wall turbulent boundary layers

While the study of smooth-wall boundary layer is very important to understand the basic mechanisms of the wall bounded turbulence, a large proportion of engineering applications involving boundary layers are naturally rough. Examples of high Re rough wall boundary layers include atmospheric boundary layers, flows over barnacle-ridden ship hulls, flows over canopies and urban terrian, damaged turbine blades (Bons, 2010) etc. The presence of roughness alters the canonical nature of the turbulent boundary layer, and correlating the roughness geometry to its skin friction performance in a turbulent boundary layer has been a historically important (and rather frustrating) question. While a lot of high quality scientific pursuit has been expended on the rough-wall flows, the reader is referred to the extensive reviews by Raupach *et al.* (1991) and Jiménez (2004) for the details on the same. Only the details of the current state of knowledge on rough-wall turbulent boundary layers relevant to the current flows are discussed here.

Similar to the smooth-wall flows, a boundary layer flow over wall roughness (of height k) that has developed 'sufficiently' long will reach a self-similar state. While numerous studies observed that the full turbulent structure of such a self-similar rough-wall boundary layer is dynamically different compared to the smooth wall counterparts (Krogstad *et al.*, 1992; L. *et al.*, 2002, etc.), a common consensus is that, in a turbulent boundary layer that is 'sufficiently' thick compared the wall roughness scales (i.e. $\delta/k \gg 1$), the two flows are identical in their

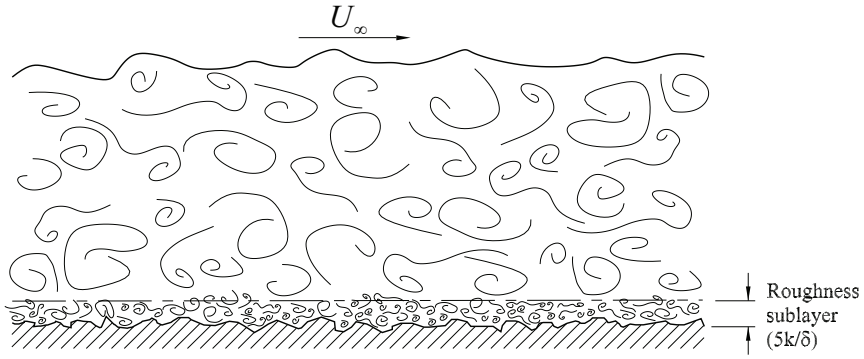

Figure 1.3: A schematic of rough-wall turbulent boundary layer indicating the roughness sub-layer and outer structures (Mejia Alvarez, 2011).

outer region (Flack *et al.*, 2005). Supported with sufficient experimental evidence (Schultz & Flack, 2005; Wu & Christensen, 2007, among others), this confines to the 'outer layer similarity' hypothesis, as developed by Townsend (1976), which states that the outer flow is independent of surface conditions. Jiménez (2004) stated that $\delta/k > 40$ is a good metric for this sufficiency to observe outer layer similarity, though Flack *et al.* (2005) found that $\delta/k_s > 40$ is a more accurate metric, where k_s is the 'equivalent sand-grain roughness' height. In the immediate vicinity of the wall roughness, however, the inner- turbulent production cycle is now replaced/influenced by a 'roughness sub-layer', where the effects of roughness are felt and deviations from smooth-wall turbulent boundary layer can be expected. In a high Re flow satisfying the above outer-layer similarity criterion, this roughness sublayer typically extends $3 - 5\,k$ away from the rough wall, as shown schematically in figure 1.3.

Under the self-similar conditions with outer-layer similarity, the velocity defect form of velocity profile [y/δ vs $(U_\infty - U)/u_\tau$] should thus be identical to the smooth-wall flow throughout the boundary layer except within the roughness sub-layer. In other words, given that the logarithmic region of the smooth-wall can be represented in inner units as a 'log-law' given by

$$U^+ = \frac{1}{\kappa}\ln(y^+) + C, \tag{1.1}$$

the rough-wall counterpart can be written with an additive constant, $-\Delta U^+$, representing the additional momentum loss due to roughness relative to the smooth-wall. Here the superscript '+' indicates normalization with inner units (u_τ and $y^* = \nu/u_\tau$) Thus, the rough-wall formulation would then be

$$U^+ = \frac{1}{\kappa}\ln(y^+) + C - \Delta U^+, \tag{1.2}$$

where ΔU^+ is commonly known as 'roughness function', and represents a measure of skin friction coefficient. The additive constant merely shifts the outer region mean flow relative to the smooth-wall when viewed with inner-nomalization figure 1.4. Nikuradse (1950) performed exhaustive experiments on pipe flows roughened by sand-grain sizes, and observed that the skin friction from many physical roughness (later categorized as *k-type* roughness, Perry *et al.* (1969)) can be reduced to an equivalent sand-grain roughness (k_s). His conclusions, in conjunction with Eqn. (1.2), can be reduced to the form,

$$\Delta U^+ = \frac{1}{\kappa}\ln(k_s^+) + C - 8.5. \tag{1.3}$$

This has led to the use of *equivalent sand-grain roughness* to indicate the skin-friction properties of a rough-wall turbulent boundary layers. Note that $k_s^+ = fn(k, Re)$, and that $k_s^+ = k_s/y^*$ is a measure of roughness effects to those of the viscous dynamics. Nikuradse (1950) further categorized such roughness effects into three regimes: a *hydrodynamically smooth* flow is where the wall roughness elements are submerged within the viscous-sublayer of the boundary layer (i.e., $k_s^+ < 5$), and that the flow is effectively equivalent to smooth-wall flow. A *transitionally rough* regime occurs for $5 \lesssim k_s \lesssim 70$ where the combined effects of the roughness elements and the viscous mechanisms are dominant in the roughness sub-layer. Finally, for $k_s^+ > 70$, the structures shed by the roughness elements fully dominate the near-wall dynamics, and the skin-friction is predominantly profile drag on the roughness elements. Also note that the qualification for outer-layer

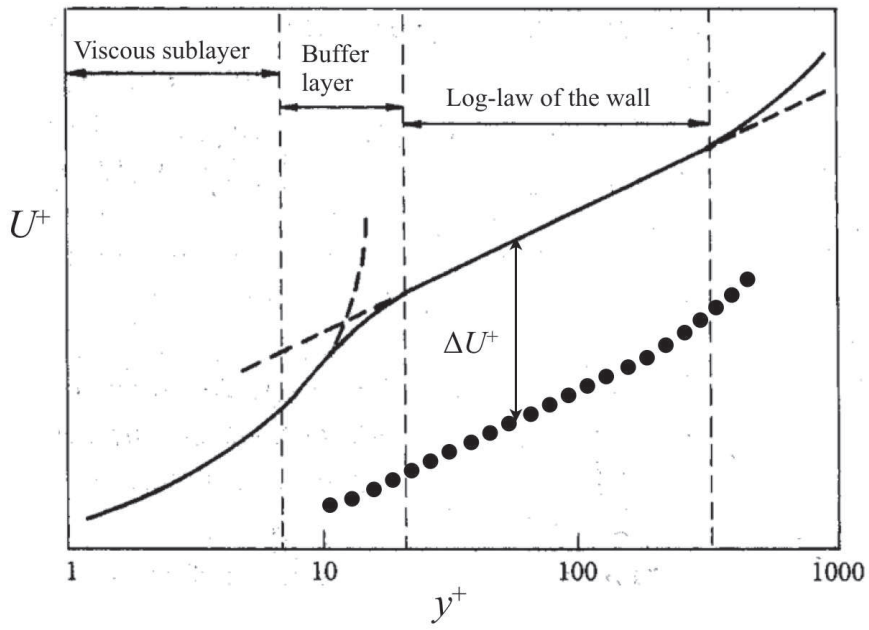

Figure 1.4: Example smooth- and rough-wall boundary layers plotted in inner units with the roughness function marked (Davidson, 2004).

similarity is based on δ/k_s, and that it can exist in either of the three types of roughness flows mentioned above.

1.4.1 High Re effects of rough-wall flows

With the current understanding of the rough-wall boundary layers presented so far, it is evident that the outer dynamics of the high Re flows that are identical under Townsend's hypothesis are going to play a significant role in the rough-wall boundary layers as well. Further, a physical roughness operating as a hydrodynaically smooth boundary layer at a given Re could transition to a transitionally or fully rough boundary layer with increasing Re (and k_s^+ due to an associated decrease in y^*). For this reason, it is very important to understand the high Re physical phenomena in the context of wall roughness.

With respect to the inner-outer modulating interactions that are of primary interest in the current work, recent studies have tried to investigate the same. In addition to the aforementioned sparse roughness experiments (Blackman &

Perret, 2016; Nadeem *et al.*, 2015), recent studies such as Squire *et al.* (2016) and Pathikonda & Christensen (2017) have experimentally investigated the same using experiments. LES simulations by Anderson (2016) have also observed the amplitude modulation phenomenon in rough-wall flows. Further, Squire *et al.* (2016) attempted to evaluate the predictive model of Baars *et al.* (2016), and observed that the model could not successfully estimate the small scale effects at a Re different to that of the calibration experiment. They, however, noted a higher value of calibration constant quantifying the strength of modulation interactions. Pathikonda & Christensen (2017) have observed frequency modulation in the rough-wall flow investigated, the results of which will be discussed in the current work too.

It can be said that given the importance of the inner-outer interactions over the smooth-wall and the ability of predictive models capturing the same, there is a need to investigate the same over the rough-wall flows given the engineering significance of the latter. Further, rough-wall flows are extremely hard to tackle extensively via DNS simulations, leaving only LES and experiments as viable tools. While limited DNS simulations on a prescribed wall roughness can still be performed to obtain a full flow description, the difficulties in scaling the observations to higher Re, or extending the same to a different roughness, limit the utility of DNS on rough-wall flows. While LES simulations can achieve high Re and can be repeated inexpensively on any surface of interest, the physicality of such simulations is limited by the sub-grid scale models involved. The current work is an attempt to bridge this gap in understanding of these phenomena via experimental methods.

1.5 Current Research

With this understanding, the current work experimentally examines the strength and robustness of inner–outer interactions in a rough-wall turbulent boundary layer using both AM and FM analyses. The research was performed on two parts.

The first part of the research (Chapters 2 and 3) examines these modulation interactions over a complex roughness topography reflective of the irregularity often encountered in pratice. We aim to identify if and how superstructures in the log region of this rough-wall flow (previously identified in Mejia-Alvarez *et al.* (2014)) interact with the near-wall velocity perturbations imparted within the roughness sublayer by a multi-scale roughness topography– whose flow behavior has been previously reported (Wu & Christensen, 2007; Mejia-Alvarez & Christensen, 2010; Wu & Christensen, 2010; Mejia-Alvarez & Christensen, 2013; Mejia-Alvarez *et al.*, 2014). The complex roughness used in the current study embodies a broad range of topographical scales and its heterogeneity in the spanwise direction was shown to induce spanwise-alternating, localized, δ-scale high- and low-momentum pathways (HMPs and LMPs, respectively) reflective of roughness-induced turbulent secondary flows (Barros & Christensen, 2014; Willingham *et al.*, 2014; Anderson *et al.*, 2015). Thus, the modulating influences of inner–outer interactions are studied at these localized spanwise conditions induced by the underlying roughness-induced secondary flows. The similarities and differences in the structure of amplitude and frequency modulations between the smooth- and rough-wall boundary layers are investigated. Besides amplitude and frequency modulations, the predictive models previously developed by Mathis *et al.* (2011*a*) and Baars *et al.* (2016) are evaluated for current roughness. The suitability of QSQH hypothesis in accurately predicting the super-position and amplitude modulation constants is investigated.

The second part of the research (Chapters 4 and 5) aims to provide a spatio-temporal description of these inner-outer interactions using high-frame-rate PIV in a refractive index-matched (RIM) facility. The ability of the refractive index matching in removing the near-wall reflections and enabling measurements close to the wall can be leveraged to investigate these interactions using high-frame rate PIV at moderate Re_τ. Various conditionally averaged statistical metrics were developed and their ability to capture the spatial structure of the modulation interactions was evaluated. The presence of scale modulation as predicted by

QSQH theory is also briefly investigated. The goal of these experiments is to ultimately provide a two-dimensional, two-component spatio-temporal model that can be extended to future LES simulations, the prospects of which are discussed with the current results.

1.5.1 Notations

Through the rest of the text, u is used to represent streamwise fluctuating velocity, while $\tilde{u}$ is used for total velocity. Vector quantities are denoted by a bold case (such as velocity, $\mathbf{u}$). Subscripts i and o are used to represent *inner* and *outer* measures, while subscript-suffixes L and s are used to refer to *large* and *small* scale variations in temporal or spatial sense of turbulent quantities. While t normally indicates the experiment time variable, τ is used to indicate a time delay (for example, correlation time delay, delay with respect to conditional event etc.), and is distinguished from the wall shear stress, τ_w.

Commonly used in the analysis, variable $R_{x,y}$ represents correlation function between respective sub-scripted quantities, and super-scripts a and f are used to indicate a quantity corresponding to amplitude modulation and frequency modulation, respectively. For example, u_{iL} represents *inner, large-scale, streamwise velocity time series*, and $R_{oL,iL}$ is given by

$$R_{oL,iL}(\tau) = \frac{\langle u^+_{oL}(t) * u^+_{iL}(t-\tau)\rangle}{\sqrt{\langle {u^+_{oL}}^2\rangle \langle {u^+_{iL}}^2\rangle}}, \tag{1.4}$$

where, according to convention given by Eqn. (1.4), τ indicates a *lead* (if $\tau > 0$) or a *lag* (if $\tau < 0$) of the latter quantity (u_{iL} here) with respect to the former (u_{oL} here) on the time axis.

CHAPTER 2

PART-I: HOTWIRE MEASUREMENTS OF TURBULENCE OVERLYING COMPLEX ROUGHNESS

Chapters 2 and 3 represent the first part of the current study on rough-wall boundary layers. This chapter details the experimental facility, instrumentation and measurement techniques employed, along with the flow characteristics and wall roughness used in the current flow. The following chapter addresses the analysis and results garnered from these hot-wire measurements.

2.1 Experimental facility

All hot-wire experiments were performed in an open-circuit, Eiffel-type, boundary-layer wind tunnel shown schematically in figure 2.1. The inlet section is rectangular, 3.4 m wide and 2.4 m tall, and is followed downstream by a series of honeycombs and meshes to breakdown any incoming turbulence or mean-flow abnormalities. The flow then passes through a laminarizing contraction section with an inlet–outlet area-ratio of 10:1, which dissipates small eddies broken down by the honeycomb screens to create a clean free-stream with minimal turbulence. After the 6.1 m long test section, the flow enters a slow and long diffusing section that decouples the flow in the test section from the effects of the suction fan and the motor at the downstream end of the test section.

The test section has a rectangular cross-section that is 0.91 m wide and 0.46 m tall above a boundary-layer plate floating 100 mm above the bottom wall of the test section. The boundary-layer plate is composed of an elliptical leading edge to prevent any leading-edge separation, and has a 5 mm boundary-layer trip mounted on the wall about 20 cm from the leading edge to stabilize the turbulence transition

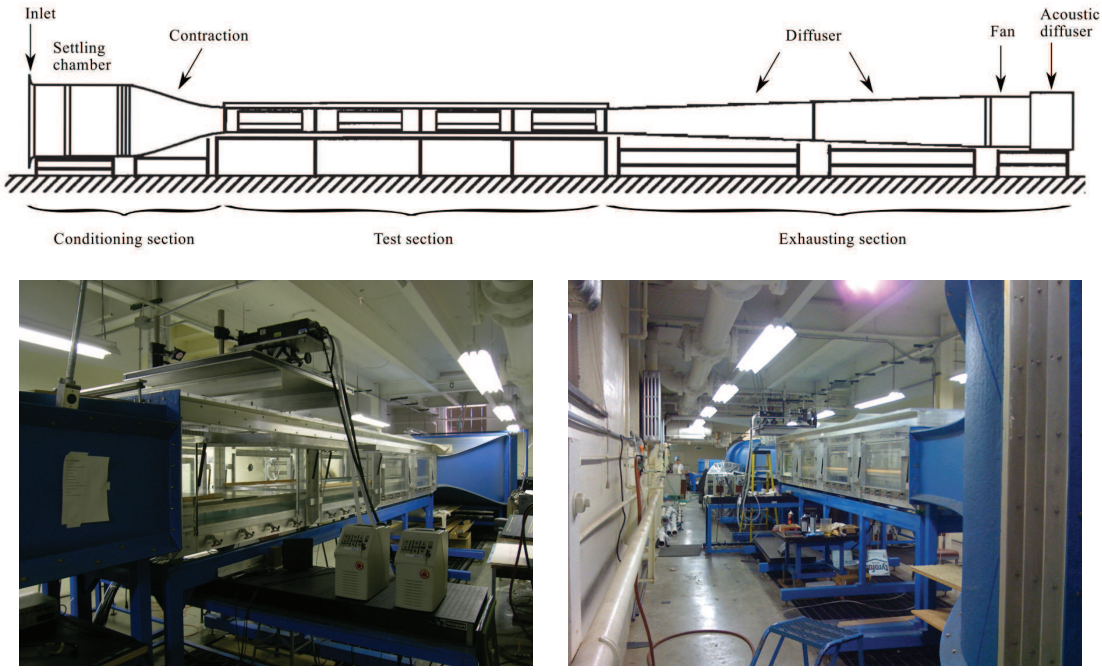

Figure 2.1: Wind tunnel schematic and images (Images from Meinhart (1994) and Barros (2014)).

location. The boundary-layer plate has a rigid aluminum frame near the side walls, within which a 1 in float-glass floor is mounted through much of the spanwise mid-extent. Further, the boundary-layer plate itself is formed in two streamwise halves (each $3\,m$ in length), which can be raised or lowered independently with respect to each other using adjustable screw mounts. This facilitates formation of a forward or backward facing step at the streamwise mid-section of the test-section ($3\,m$ from the leading edge). This capability was used to level the upstream half of the bottom plate flush with the downstream wall roughness, discussed later in section 2.3. Finally, four plexiglass windows on either side of the test section provide optical and physical access to the test-section interior. Wooden corner fillets with 1 in radius run the entire streamwise length of the boundary-layer plate–side-wall corners to prevent any corner-effects from corrupting the boundary layer two-dimensionality along the spanwise center of the test section.

The ceiling of the test section can also be contoured via screws to adjust the streamwise pressure gradient within. This capability, in conjunction with

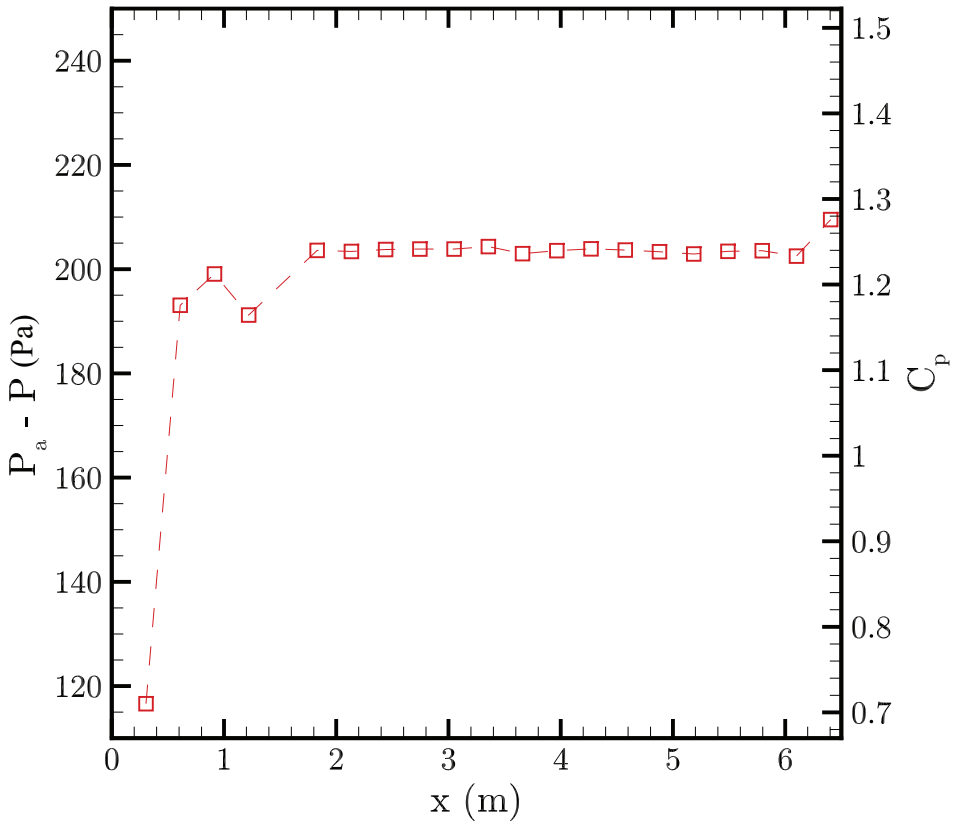

Figure 2.2: The streamwise static pressure distribution (below atmosphere, P_a) and pressure coefficient from the static ports for smooth-wall flow conditions. x is streamwise distance measured from the leading edge of the flat plate.

20 equidistant static pressure ports available along the streamwise extent of the plate, enabled monitoring and controlling of the streamwise pressure variations. The static pressure at these ports was measured using a Scanivalve W2 fluid switch wafer, a Validyne DP103-18 differential pressure transducer and Validyne CD-15 Carrier Demodulator. The streamwise pressure distribution, set before the current experiments, is presented in figure 2.2 and shows pressure variations limited to within 1% of the free-stream dynamic head.

The free-stream turbulence intensity of the flow was calculated from the hot-wire measurements made in the current work. Following Balasubramaniam (2005) and Meinhart (1994), free-stream turbulence intensity was calculated directly from

the bride voltage, without the need for calibration, using the relationship

$$\frac{u'}{U} = \frac{4e_1' E_1}{E_1^2 - E_{1_0}^2}, \tag{2.1}$$

where E_1 and e_1' are the mean and root-mean-sqaure of bridge voltage, respectively, and E_{1_0} is the bridge voltage at zero velocity. Using this approach, the free-stream turbulence intensity of the flow, at speeds relevant to this study, was measured to be less than 0.16%. This percentage is consistent with Balasubramaniam (2005) and Meinhart (1994), who also reported values for the same physical facility.

2.2 Hotwire anemometry

Hardware

Dantec StreameLine 90C10 constant temperature anemometry (CTA) modules were used for all hot-wire measurements reported in this work. Two modules were mounted on a Dantec 90N10 frame and operated simultaneously. Dantec 55P05 gold-plated boundary layer probes were used at an operating temperature of 224° C and an overheat ratio of 0.8. The sensing element consisted of $5\,\mu m$ tungsten wire and had a working length of 1.25 mm. A 16-channel National Instruments 6220 data acquisition system, capable of 250,000 Hz sampling rates per channel, was used to acquire the analog bridge voltage signals. In parallel, a T-type Omega thermocouple was used, along with National Instruments USB-9211 DAQ system, to capture the temperature of the flow at $6\,Hz$. This temperature signal was used to correct the bridge voltage to the reference temperature using the relation (Bruun, 1995)

$$E_{ref} = E_m \left(\frac{T_w - T_{a,ref}}{T_w - T_a} \right), \tag{2.2}$$

where E_{ref} is the bridge voltage at the reference temperature, E_m is the measured bridge voltage, T_w and T_a are the wire temperature (constant for CTA, 224° C here) and air temperature measured, respectively, and $T_{a,ref}$ is the reference air temperature. While all boundary-layer velocity measurements were done using the Dantec StreamLine software, velocity measurements for hot-wire calibration were acquired using Matlab. A signal conditional offset and gain were applied to maximize the dynamic range of the A/D system. A low-pass filter was applied ($1500\,Hz$ for calibration data, and $30,000\,Hz$ for boundary layer measurements) to avoid aliasing of any high-frequency noise on to the flow measurements.

Up to two probes could be mounted onto carriages that move independently over a thin rail that was mounted from the ceiling to not perturb the boundary layer that developed on the boundary-layer plate. Further, they extended in front of carriages by 250 mm and at an angle (as shown in the figure 2.3) to mitigate the aerodynamic effect of the fixtures on the boundary-layer flow. No significant probe fluctuations were found with this setup. A pitot-static probe was also mounted from the ceiling to aid with free-stream velocity measurements in the 2-probe measurements (discussed in section 2.4), and with the calibration of the hot-wire measurements. The dynamic head from the pitot-static pressure was measured using the same Validyne pressure transducer setup discussed in section 2.1.

Of the two probes that could be mounted, one of the probes could be translated on the guide rail vertically by a MA40 series Velmex Unislide translation stage (with a rated accuracy of $1.5\,\mu m$) mounted above the wind tunnel which was connected to the carriage by a push-rod. By this approach, a single probe could be moved from the wall up to 130 mm away from the wall. If two probes were mounted, the single probe could be translated from the wall to the outer probe location.

Figure 2.3: Images of one- and two-probe configurations in the wind tunnel.

Calibration

For each experiment discussed in section 2.4, two calibrations were performed – one before the start of the measurement, and one another after measurements in the boundary layer. The average of the two calibrations was used to convert the bridge voltage of each experiment to the corresponding velocities. Calibration was performed *in situ* by moving the probe(s) into the free-stream, and measuring the bridge voltage in tandem with the dynamic pressure from the pitot-static probe and temperature from the temperature probe. The velocities from the pitot-static probe were then used to calibrate the corrected bridge voltage to the velocity. A 4^{th} order polynomial fit was made for each calibration to convert the measured bridge voltage in section 2.4 to the corresponding velocities (Bruun, 1995). The calibration curves, with corrected bridge voltage and measured velocities are shown in figure 2.4, indicating the stability of the hot-wire system. The specific experimental details will be discussed in section 2.4.

2.3 Complex roughness characteristics

The rough surface used for the rough-wall turbulent boundary layer experiments was the same as that originally fabricated and studied by Wu & Christensen (2007, 2010); Mejia Alvarez (2011); Mejia-Alvarez & Christensen (2010); Barros (2014), and shown in figure 2.5. The topography was replicated from a topographical scan of an in-use turbine blade damaged by deposition of materials (Bons *et al.*, 2001), indicating the presence of a wide range of topographical scales irregularly arranged, and with a roughly Gaussian distribution of length scales. This rough surface has a mean peak-to-valley height of 4.25 mm and a root-mean-square (RMS) roughness height of 1.0 mm, while the skewness and kurtosis are 0.16 and 2.7 respectively. The tiles were manufactured by first creating a template with the prescribed scale distribution, and mirroring the template to extend it in the two wall-parallel directions. Over sixty individual tiles were fabricated using rapid

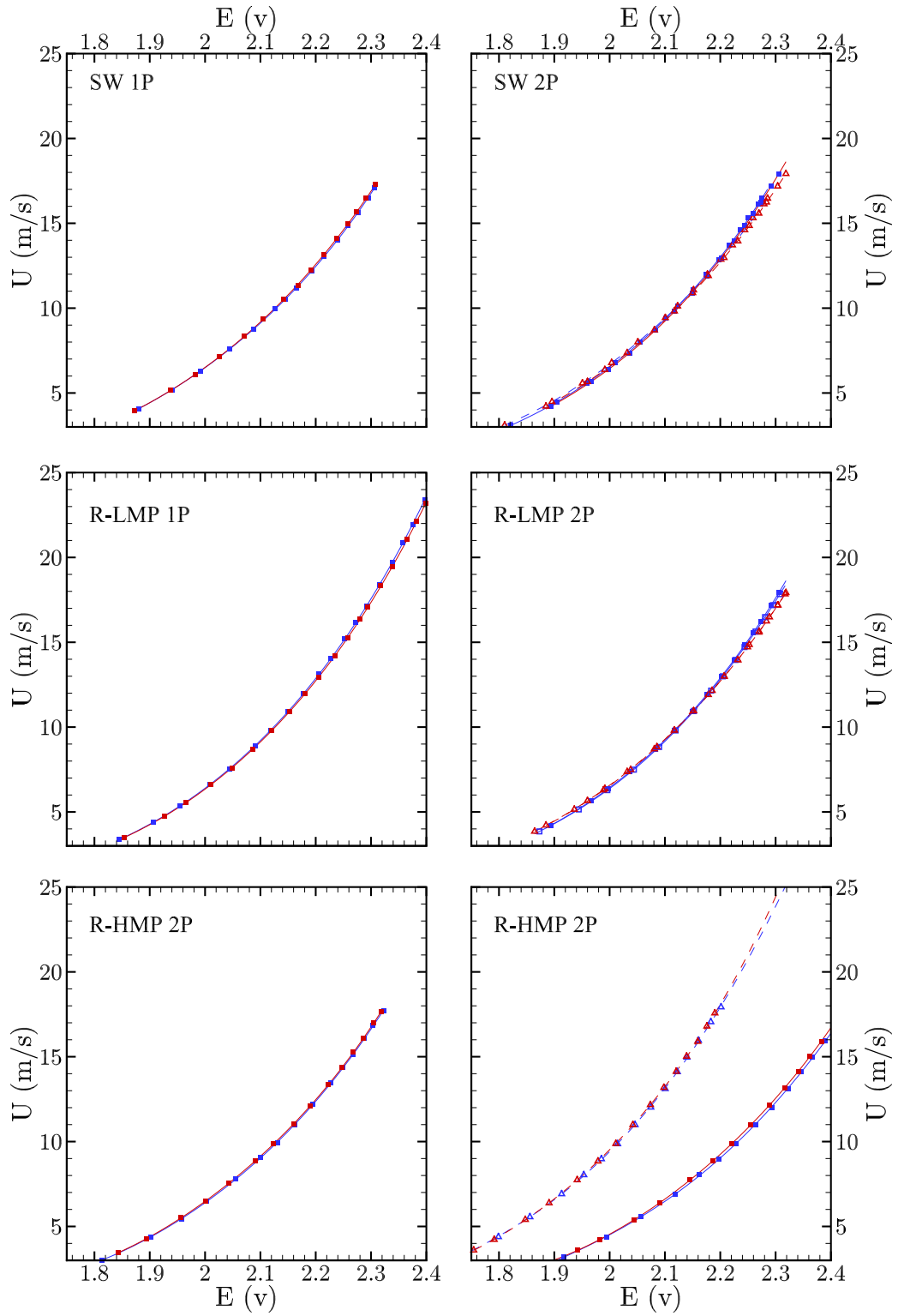

Figure 2.4: Pre- and post- experiment calibrations (*blue* and *red*, respectively) for various datasets. Note that for Rough HMP 2-probe experiment, the outer physical probe used was different. *Open* symbols are for the outer probe.

prototyping, arranged over multiple cast aluminum plates that span the spanwise extent of the test section. The roughness tiles on the aluminum base plates were placed along the downstream half of the test section floor (i.e., from 3 m to 6.1 m). As mentioned in section 2.1, the upstream half of the boundary-layer plate was elevated using the mount screws to be coincident with the mean roughness height of the downstream roughness (i.e., without any forward or backward facing steps). Thus the boundary layer, in this case, initially developed for 3 m over smooth-wall conditions and then developed over the roughness for another 3 m to the measurement location. This arrangement is consistent with past studies of this specific roughness topography that have observed flow features and characteristics relevant to the current study (Wu & Christensen, 2007; Barros & Christensen, 2014), the details of which are elaborated in the following sections. Further details of the manufacture, dynamic significance of the complexity, and the large-scale topographical features are found in the earlier works (Wu & Christensen, 2007, 2010; Mejia Alvarez, 2011; Mejia-Alvarez & Christensen, 2010; Barros, 2014).

2.3.1 Large-scale spanwise heterogeneities

Previous studies have made two important flow observations that are relevant to the current study. First, this particular roughness topography was found to impart large-scale, mean-flow heterogeneities in the form of spanwise alternating high- and low-momentum pathways (HMPs and LMPs), sandwiched between alternating weak roll cells (Barros, 2014; Barros & Christensen, 2014). These features have been attributed to the formation of roughness-induced turbulent secondary flows (Anderson *et al.*, 2015) and can be seen in the mean velocity field in the spanwise–wall-normal plane from stereo PIV measurements for flow over this roughness by Barros & Christensen (2014) and shown in figure 2.6. Here, LMPs coincide with spanwise "valleys" in the roughness while HMPs coincide with spanwise "peaks" in the roughness. Apart from this specific roughness topography, these roughness-induced secondary flows seem to be a common feature

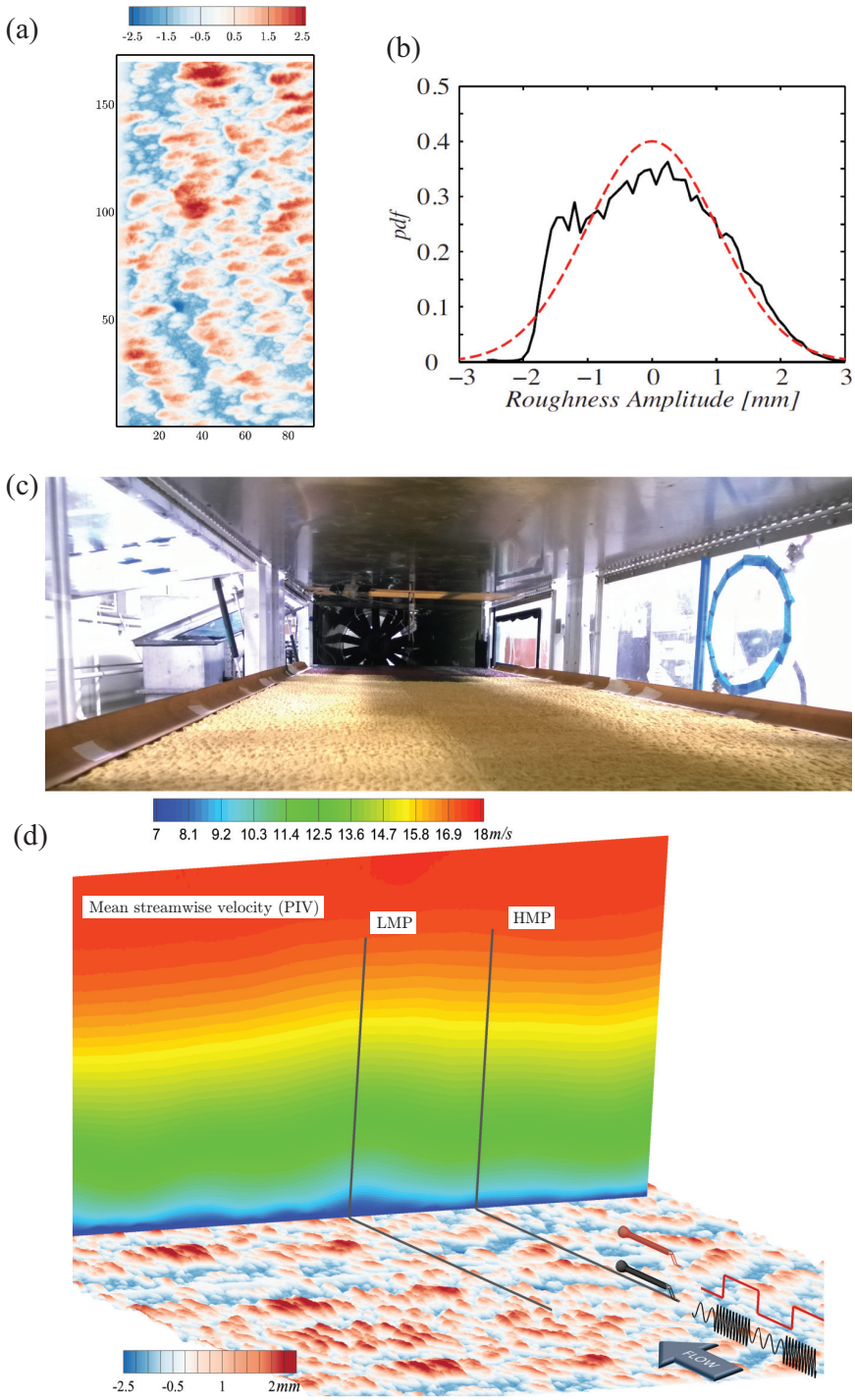

Figure 2.5: (a) Complex topography tile (in mm) that was used to replicate the roughness pattern used in current and previous studies (Wu & Christensen, 2007; Mejia Alvarez, 2011; Barros, 2014) (b) Near-Gaussian distribution of length scales (Barros, 2014, etc.) (c) Tiles of roughness laid on the downstream half of the test section (d) Schematic of current measurements at LMP and HMP locations marked relative to the PIV measurements previously performed (Barros, 2014).

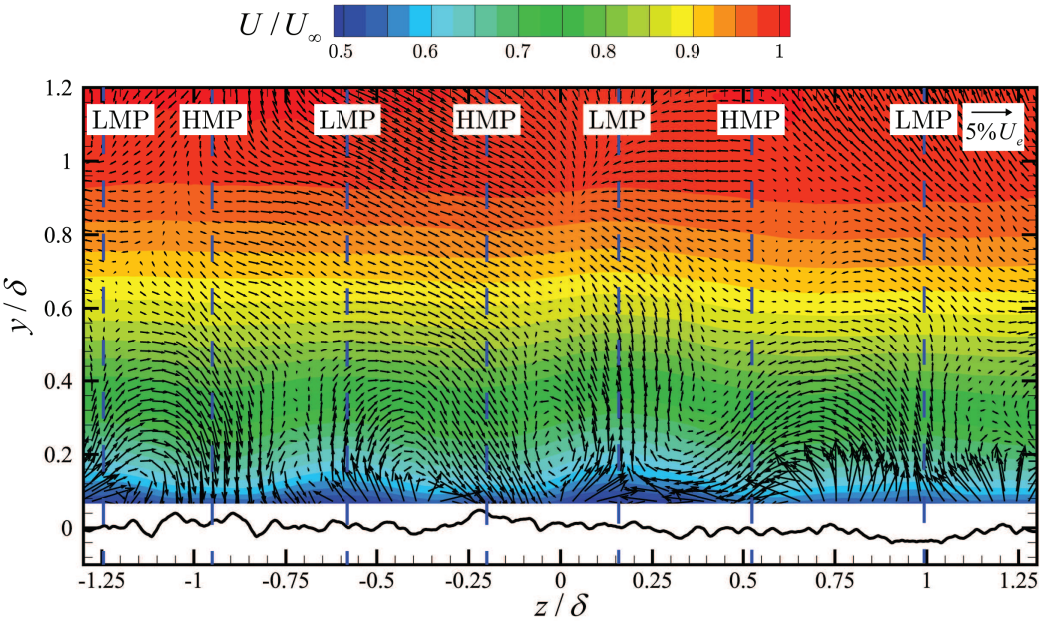

Figure 2.6: sPIV measurements by Barros (2014) on the current physical roughness indicating the spanwise alternating high- and low- momentum pathways (HMPs and LMPs). Sandwiched between the regions are spanwise alternating and counter rotating weak roll cells.

of wall-bounded flows whenever large-scale spanwise variations in the topography are present (Nugroho *et al.*, 2013; Willingham *et al.*, 2014; Kevin *et al.*, 2017). These mean-flow features are distinct from previously-reported low- and high-momentum regions (LMRs and HMRs) in canonical smooth-wall flows in instantaneous observations. While the latter are hypothesized to be related to the hairpin vortex packet paradigm in an instantaneous sense, the HMPs and LMPs are observable as mean-flow phenomena over roughness with large-scale spanwise heterogeneities. More details about these effects can be found in the corresponding works, but are introduced here to motivate the specific spanwise positions for the hot-wire measurements discussed herein.

2.3.2 Outer-layer similarity

A very relevant observation from the previous studies on the current roughness to the current investigation of inner–outer interactions is the occurrence of 'outer-

layer similarity' in flow over this roughness. In this context, the outer layer of a rough-wall flow would have a similar character to that of a smooth-wall flow except that it would adapt in a universal manner to the boundary-layer thickness and wall shear stress set by the roughness. In this regard, the roughness would only indirectly affect the outer layer through these two quantities. This similarity was quantified in previous studies (Wu & Christensen, 2007, 2010; Mejia Alvarez, 2011; Mejia-Alvarez & Christensen, 2010; Barros, 2014) and was not only observed in the statistical character of the outer layer but also in the structural aspects of the large-scale motions that occupy the outer layer. As was highlighted in section 1.4, given a similar outer-layer structure between smooth- and rough-wall flow, one can speculate the presence of modulation interactions in rough-wall flows may be similar to that of smooth-wall flow. Thus, we start with the assumption that the smooth- and rough-wall experiments in the current study are similar as far as the outer layer large- and very large-scale features are concerned. The same outer-layer similarity is also found with the current observations, as will be seen in various inner–outer interaction metrics discussed later in chapter 3.

2.4 Current experiments

Hotwire measurements were made in both smooth- and rough-wall turbulent boundary layers as a part of the current work. All measurements were first performed for smooth-wall flow as a means of comparing and confirming the modulation effects with previous literature, as well as a baseline against which the subsequent rough-wall data are compared. Two separate sets of measurements were performed for each case described in the current study: (a) with a single, wall-normal-traversing probe (termed *1-probe measurements* henceforth) and (b) with two probes at identical streamwise and spanwise positions making simultaneous measurements, with one probe fixed in the log region ($y_\circ$) and the other traversing from the wall towards the fixed outer probe (termed *2-probe measurements*). The 2-probe setup is similar to that reported in Mathis *et al.* (2011*a*), and is aimed

at directly measuring the large scales in the logarithmic region in sync with the small-scale velocities in the near-wall region. More discussion on this will be presented later in section 3.1. Additionally, two spanwise locations were chosen in the rough-wall boundary layer corresponding to previously-established LMP and HMP locations so that the characteristics of the inner–outer interactions could be quantified relative to these roughness-induced secondary flow features. The LMP measurement location was at a 6 mm offset from the test-section spanwise centerline, and the HMP measurement location was 61 mm offset in the same direction. The two measurement regions formed an adjacent LMP–HMP pair, with a weak roll cell sandwiched between them.

Thus, three different flow conditions are measured in the wind tunnel experiments – smooth-wall flow, rough-LMP flow and rough-HMP flow. For each measurement condition, first, the 1-probe measurements traversed the entire boundary layer, allowing all relevant parameters of the flow to be determined (u_τ, ΔU, δ, U_∞, etc.). Here, the boundary-layer thickness, δ, was taken as the wall-normal location where the mean streamwise velocity was 99% of U_∞. The two-probe measurements were then conducted at identical spanwise positions and flow conditions. All measurements were made at a sampling frequency of 70 kHz and a record length of 120 s per wall-normal position, giving a Nyquist frequency, $\Delta t^+ = 0.62$ (*superscript* '+' represents inner scaling), and a record length of $21,000\,\delta/U_\infty$. The inner-scaled length (l^+) of the hot-wire sensing element was ~ 45.

2.4.1 Hotwire time-series qualification

Since investigation of the modulation interactions required hot-wire measurements extremely close to the wall, a few additional sources of error were considered before the validity of the near-wall time series was accepted. For example, in smooth-wall flows over boundaries made of metallic material, increased heat loss via convection and radiation to the wall from the hot-wire can result in biased velocity measure-

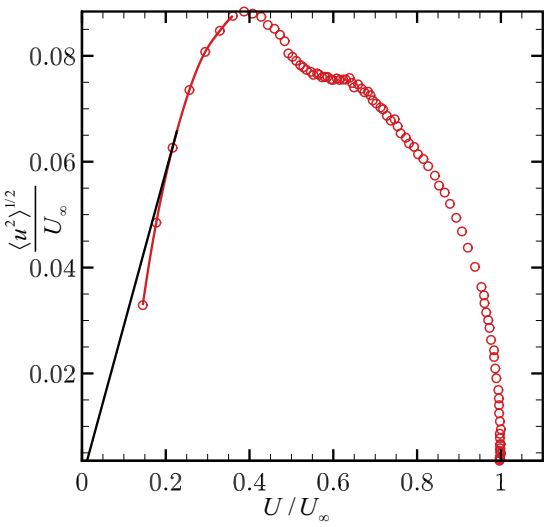

Figure 2.7: Diagnostic plot to identify near-wall effects in hotwire measurements. Also shown are cubic spline fit to near-wall data points and tangent from origin. (Alfredsson & Örlü, 2010).

ments. Further, the presence of a physical probe in close proximity to the wall can distort the flow by having a nozzle-effect between the probe and the wall. This would result in higher velocities being detected due to the probe intrusion. To validate the near-wall measurements, a diagnostic plot was used as described by Alfredsson & Örlü (2010), and near-wall points that failed the criterion were excluded for subsequent analysis. This validation is based on the expectation that flow near the viscous sublayer ($y^+ \sim 10$) is self-similar, and

$$\frac{\tau_w'}{\overline{\tau}_w} = \lim_{y\to 0} \frac{\langle u^2\rangle^{1/2}}{U} = \text{const.} \tag{2.3}$$

Thus, by plotting $\langle u^2\rangle^{1/2}/U_\infty$ vs U/U_∞, and drawing a tangent from $(0,0)$ to the curve, one can identify the near-wall measurement points that taper off below the tangent and thus do not comply with Eqn. (2.3). Figure 2.7 demonstrates the same on the current smooth-wall data, and more details can be found in Alfredsson & Örlü (2010).

For the rough-wall measurements at the HMP location, where roughness crests protruded farther into the flow than at the LMP location (coincident with a rough-

Table 2.1: Best-fit values of parameters extracted from various formulations on smooth-wall data.

Method	y_c	u_τ	$\tilde{\delta}$	Π
Clauser chart method (log law)	$230\,\mu$ m	0.578 m/s	–	–
Chauhan *et al.* (2007) (full)	$0\,\mu$ m	0.579 m/s	120.4 mm	0.496
Musker (1979) (inner-only)	$120\,\mu$ m	0.580 m/s	–	–
Chauhan *et al.* (2007) (wake-only)	$520\,\mu$ m	0.594 m/s	120.6 mm	0.4802

ness valley), some y-locations close to wall were discarded, whose corresponding time-series values fail a minimum-velocity criterion. This exclusion was done to avoid dubious hot-wire measurements in close vicinity of roughness elements where flow separation may be present, and to ensure the measured flow was always unidirectional.

2.4.2 Boundary-layer parameters

The inner and outer flow parameters were extracted via parameter optimization by non-linear regression fit of the 1-Probe data to theoretical forms. For the smooth-wall data, the composite profile formulated in Chauhan *et al.* (2007) was used as a reference. The composite profile is given as the sum of the Musker profile (Musker, 1979) and a wake formulation. Boundary layer parameters to be determined from this fit include a correction to the wall, y_c, the friction velocity, u_τ, the 'actual' boundary layer thickness where the velocity is identically equal to the free-stream velocity, $\tilde{\delta}$, and the boundary-layer wake parameter, Π. A Kármán constant, $\kappa = 0.384$, and an additive constant of $C = 4.17$ were used in the formulation (Chauhan *et al.*, 2009). Multiple initial guesses were used to verify robustness of convergence of the regression algorithm, and that the converged values were identical. These results were also compared to other indirect methods commonly employed, such as the Clauser chart method, Musker profile fit (Musker, 1979), etc., and they all gave identical results to within the uncertainties of the various approaches.

The flow parameters for the rough-wall casees were extracted in a similar fash-

Table 2.2: Boundary layer parameters.

Flow	Re_τ	U_∞ (m/s)	δ (mm)	u_τ (m/s)	y_* (μm)	ΔU^+	$y_\circ^+$
Smooth	3560	16.61	94.7	0.58	26.6	-	197 ($0.055\delta^+$)
R-LMP	5650	16.94	98.2	0.85	17.6	10.3	726 ($0.14\delta^+$)
R-HMP	4850	17.29	96.6	0.78	20.4	6.9	612 ($0.13\delta^+$)

ion, but with small distinctions. First, the origin of the uncorrected wall-normal positions was arbitrary due to the irregular nature of the roughness. Thus the wall correction by the regression fit was crucial to identify the virtual origin. Since the rough-wall cases do not have a theoretical inner mean velocity profile similar to smooth-wall flow (like the aforementioned Musker profile), only the wake fit was performed, with the roughness function, ΔU, as an additional parameter of the fit. However, this five-parameter regression fit was very 'flexible' and under-defined, and thus resulted in non-unique parametric sets with equally low goodness of fit. To render this approach more robust, the wake parameter, Π, was assumed to be equal to that of the smooth-wall boundary layer (given the existence of outer-layer similarity in this rough-wall flow), thus reducing it to a more rigid four-parameter fit. The values obtained were also compared to the modified Clauser chart method (Perry & Li, 1990), and were found to be very similar. Finally, a few near-wall points were excluded for parameter fitting to the theoretical values, as they were believed to be within the roughness sublayer, and thus would deviate from the logarithmic variation of the velocity.

Table 2.1 summarizes the converged parameters for the smooth-wall boundary layer based on the different methods commonly used. The wake parameter (Π) obtained by the parameter fit is very sensitive to pressure-gradient effects. That it converges to within the range cited by Chauhan *et al.* (2009), i.e., $\Pi \in 0.45 \pm 0.05$ reiterates the canonical nature of the current boundary-layer conditions. Further, the wake-only fit, without the use of any inner-region information, converged at relatively similar values of friction velocity as obtained by the other formulations.

Table 2.2 summarizes the parameters of the smooth- and rough-wall experi-

ments conducted. It should be noted that the Re of the smooth- and rough-wall flows are slightly different. Mathis *et al.* (2009*a*) addressed this issue for smooth-wall flow, and found that the near-wall plateau in the amplitude modulation correlation coefficient varies with Re_τ as

$$R^a = 0.304 \log_{10}(Re_\tau) - 0.997, \tag{2.4}$$

indicating that modulation effects increase with increasing Re_τ. For comparisons between the current experiments, an Re_τ effect, to the leading order, of $\Delta R^a \sim O(0.05)$ in the correlation coefficient can be estimated from the above equation. Thus, small differences in the strength of the inner–outer interactions between smooth- and rough-wall flow are possible due to Re differences, though any larger differences can then be ascribed to roughness effects. We do not include any corrections for this effect, as it doesn't significantly change the conclusions drawn in the current work.

2.5 Mean flow characteristics

The single-component streamwise velocity measurements garnered from the 1-Probe measurements can be used to assess the mean turbulent characteristics of the boundary layers. Figure 2.8a shows the mean velocity profiles for the smooth- and rough-wall cases in inner variables, with the logarithmic profiles and the roughness functions marked. Also shown in figure 2.8b are the mean velocity profiles in defect form, which indicate the consistency of the wake function between the smooth- and the rough-wall cases. Further, the collapse of the smooth- and rough-wall cases in defect form speaks to the outer-layer similarity of these flows in a mean sense.

Figure 2.8c shows the streamwise velocity contributions to the turbulent kinetic energy, $\langle u^2 \rangle$, as a function of wall-normal position for the three cases. The expected inner peak in the smooth-wall flow occurs close to the wall at $y^+ \approx 15$,

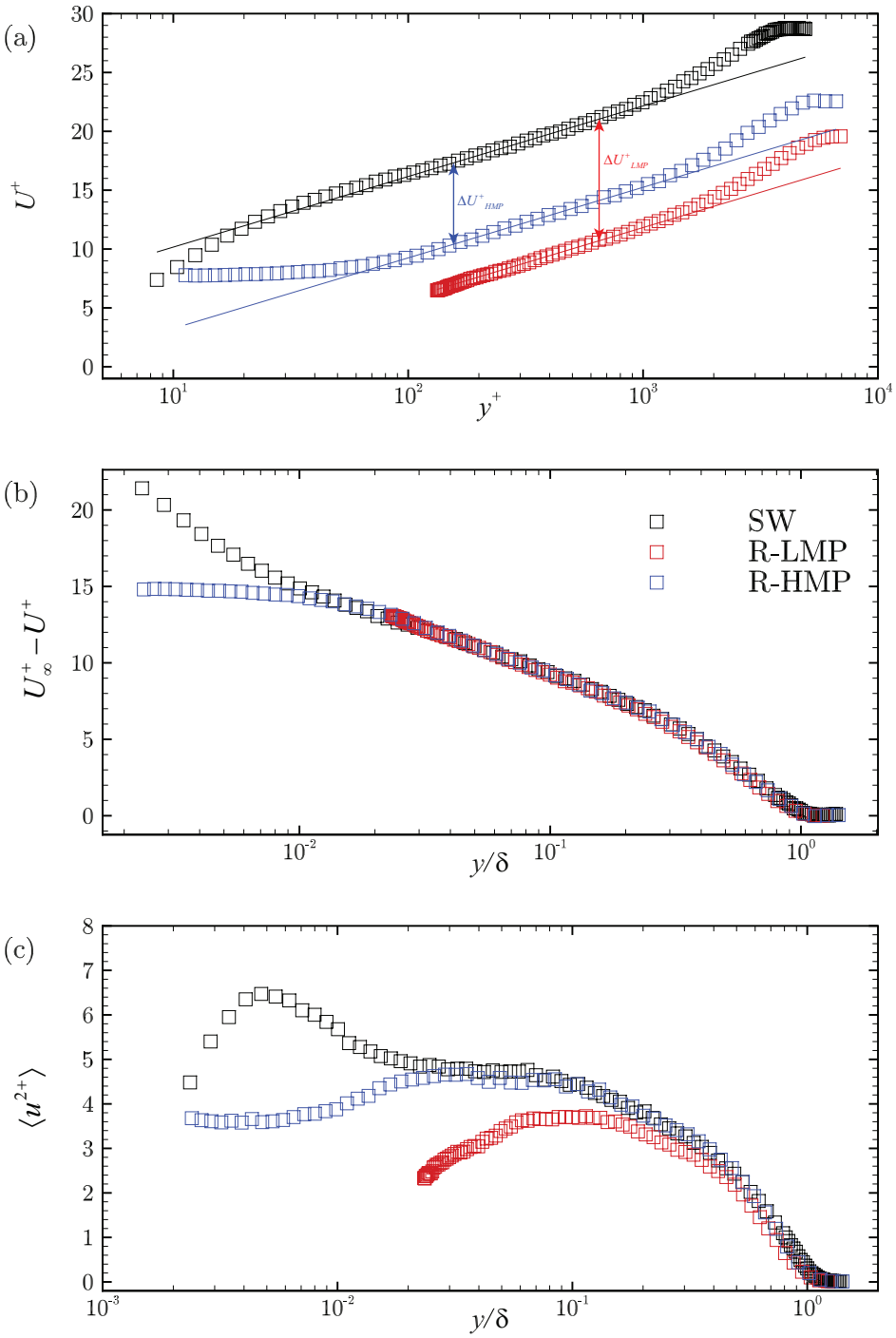

Figure 2.8: Mean profiles of (a) mean velocity in inner-scaling, with the roughness functions and log-profiles marked, (b) velocity in outer scaling and (c) streamwise turbulence for the three flows.

representing the near-wall turbulent cycle. The two rough-wall cases show significant reduction in $\langle u^2 \rangle$ owing to roughness, though the rough-wall cases converge to the smooth-wall result in the outer layer. This outer-layer collapse is again indicative of similarity between the smooth- and rough-wall flows as has been previously reported (Wu & Christensen, 2007) .

The streamwise velocity contributions to the turbulent kinetic energy, $\langle u^2 \rangle$, can be further decomposed at various scales into a pre-multiplied energy spectrum (PMES, $k_x^+ \phi_{uu}$) using the single-sided power-spectral density (ϕ_{uu}) of the velocity fluctuation time series. The PMES indicates the energy content of the velocity fluctuations at various logarithmically-spaced scales and the integral sum of energies at all logarithmic scales will recover the variance as

$$\langle u^2 \rangle = \int_0^\infty k_x^+ \phi_{uu} \, \mathrm{d}(\log k_x^+). \tag{2.5}$$

However, to convert the fluctuations in temporal scales measured into spatial (length) scales, Taylor's frozen field hypothesis was assumed. For all energy spectra reported in these hot-wire experiments, the local mean velocity at a given y-location was used as the convection velocity (U_c) to transpose temporal measurements into 'convecting spatial scales frozen in time'. That is,

$$\tilde{u}(x) = \tilde{u}(-U_c t), \tag{2.6}$$

Figure 2.9 shows the PMES for each flow, as computed from the single-probe measurements. These spectra are smoothed by averaging $6 floor(\log(k_x \delta))$ points (Balasubramaniam, 2005; Bendat & Piersol, 2011). From the smooth-wall flow (figure 2.9a), the near-wall turbulent kinetic energy peak is evident at $\lambda \approx 2000$ and $y^+ \approx 15$. Further, a secondary energy peak within the logarithmic region was found at $\lambda/\delta \approx 5$ and $y^+ \approx 200 \approx \sqrt{15 Re_\tau}$, consistent with earlier literature (Mathis *et al.*, 2009*a*, for example). This secondary peak indicates the energy embodied in the large- and very-large scale motions, and increases in strength

with increasing Re_τ.

Similar observations can be made with the rough-wall energy scales. Firstly, the scale organization of near-wall turbulence energy is completely replaced by a roughness sub-layer, evident in the different near-wall energy distribution between the two rough-wall conditions, compared to the smooth-wall case. The outer energy at large scales seems to be unaffected, though their exact magnitudes are expected to scale with local Re_τ conditions. Both the rough-wall LMP and HMP measurements indicate substantial energy at larger streamwise wavelengths, inferentially indicating the presence of energetic large and very large scale motions that could modulate the smaller-scales closer to the wall.

It can thus be seen that the experimental setup, experimental data and the flow conditions described in the current chapter are appropriate to investigate the modulating interactions. The high time-resolution and long time series would capture the small and large scale velocity evolution at fixed points. The rough wall boundary layers were further found embody the large scales in the outer region, and a completely different near-wall scale energies. With this information and measured data, the inner-outer interactions over smooth-wall and rough-wall can be discussed in the following chapter, and the similarities and differences in the same can be identified.

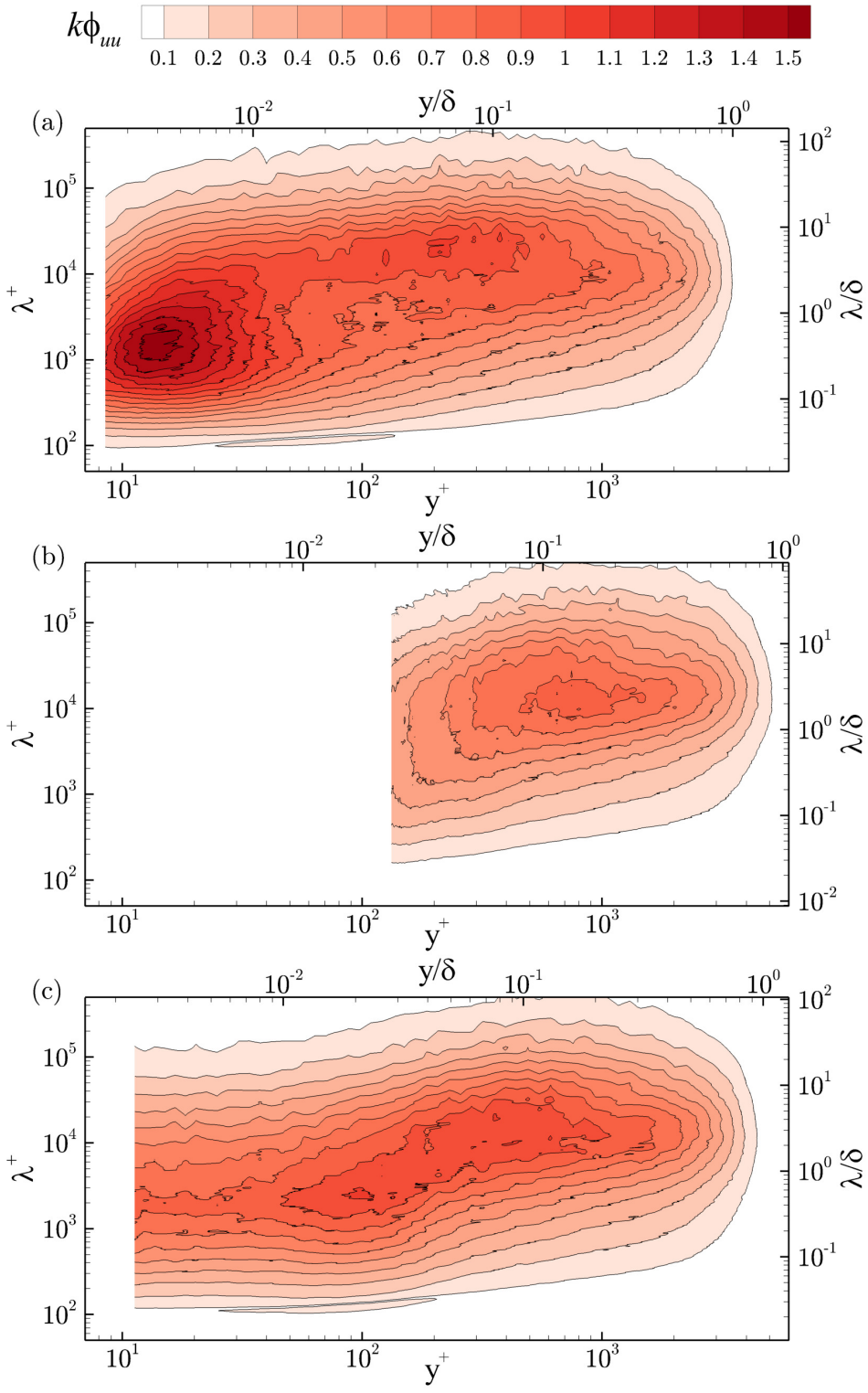

Figure 2.9: Mean pre-multiplied energy spectra of (a) smooth-, (b) rough-LMP and (c) rough-HMP boundary layers.

CHAPTER 3

PART-I: INNER-OUTER INTERACTIONS OVER COMPLEX ROUGHNESS

With the flow structure established in the previous chapter, the current chapter discusses the modulation interaction aspects of the boundary layer flow. Preliminaries of the interactions, brief conclusions from the past studies and methodologies of current analysis are described. The results from the current data set and their broader implications are discussed following the same.

3.1 Inner-outer interactions: one-probe vs two-probe measurements

The inner–outer interactions in a smooth-wall turbulent boundary layer are, in principle, the interactions between (a) the large-scale structures (LSMs and VLSMs) in the logarithmic region and (b) the small-scale structures near the wall produced by the 'autonomous' turbulence production cycle. Most experimental studies that have explored these interactions captured streamwise velocities corresponding to these two flow features acquired by single-component hot-wire anemometry. Various correlations (described later in section 3.2) between these two measured velocity signatures then quantify the degree of amplitude and frequency modulation present in the flow. Thus, to truly capture these two velocity signatures that reside in distinct regions of the flow, one must make simultaneous measurements at two different wall-normal positions to capture the signatures and quantify the modulating effect of the large-scale motions away from the wall with the small-scale motions near the wall. This is thus the objective of the 2-probe measurements presented herein: to unambiguously capture the velocity signatures

of the near-wall and outer-layer structures and quantify their degree of interaction.

However, it should be noted that recent studies in smooth-wall flow (Mathis *et al.*, 2009*a*) reveal that the large-scale streamwise velocity measured close to wall (u_{iL}) serves as an excellent proxy for the true large-scale signature in the logarithmic region (u_{oL}). This observation indicates that the large-scale motions away from the wall linearly superpose upon the wall-parallel smaller scales close to the wall. This notion is physically consistent with Townsend's attached eddy hypothesis (Townsend, 1976), and was later also shown by Metzger & Klewicki (2001) and Hutchins & Marusic (2007*b*). A similar consistency between u_{iL} and u_{oL} was noted in the current smooth-wall, 2-probe measurements which revealed a correlation between the inner and outer large-scale signals [$R_{oL,iL}$, Eqn. (1.4)] of at least 70%. Thus, the assumption of the 1-probe measurements and associated analysis presented herein, consistent with previous work utilizing 1-probe measurements, assumes that the large-scale velocity signal near the wall is a direct superposition of that which exists in the logarithmic layer (i.e., $u_{iL} \sim u_{oL}$).

This assumption that the large scales in the log region are linearly superposed on the near-wall velocity signal may not be valid for rough-wall flow. In rough-wall flow, the near-wall, viscous turbulence production cycle of smooth-wall flow is replaced by the roughness sublayer whose physics is driven directly by interactions between the flow and the roughness topography. At high Re, this is an inertia-dominated process owing to vortex shedding from the roughness features and so the population of near-wall smaller-scales could be dramatically different in character and in subsequent interaction with the larger-scale motions that reside far from the roughness. While previous studies have shown the presence of outer-layer similarity of the structures in rough-wall flows to those of smooth-wall flow where the roughness is small compared to the outer length scale of the flow (i.e., $\delta/k \gg 1$), it cannot be assumed *a priori* that these larger-scale motions will linearly superpose their signatures on the velocity signal within the roughness sublayer as has been shown in smooth-wall flow. Thus, to appropriately quantify the degree of true interaction between the larger-scale motions in the

outer region with the smaller-scale motions in the roughness sublayer, these two velocity signatures must be independently captured in rough-wall flow and a true 2-point analysis of this correlation is required. In this regard, the current 2-point measurements allowed quantification of the degree of similarity between u_{iL} and u_{oL} for the rough-wall flow, and while still relatively high, it was found to be less significant than in smooth-wall flow ($R_{oL,iL}|_{RW} \approx 50\%$). Finally, it should be noted that the superposition of the large scales on the near-wall region is not instantaneous, i.e., there is a time lag between the occurrence of an 'event' in the log region, and its imprint near the wall. This effect highlights subtle differences in correlations observed in 1-probe and 2-probe analyses, particularly via a time shift, τ. This effect will be elaborated on in later sections, when results from the two methods are compared.

3.2 Amplitude modulation

Amplitude modulation between the small- and large-scale velocity fluctuations in turbulent boundary layers has been investigated using various methods in earlier studies. All of these methods involve, as a first step, decomposing time series velocity data into small- and large-scale components (u_s and u_L, respectively) using an appropriate cut-off frequency (f_c). This decomposition is followed by identifying a representative measure to quantify the amplitude of the small scales. Observing the correlation between the large scales and such quantified 'amplitude' changes hence reveal any AM effects of the former on the small scales.

Bandyopadhyay & Hussain (1984) and Guala *et al.* (2011) have investigated the amplitude modulation as the correlation between the large scales (u_L) and the large-scale component of the small-scale velocity magnitude ($[|u_s|]_L$)– the latter obtained via the aforementioned cut-off frequency, f_c. A similar analysis can be performed using the large-scale variance of the small scales ($[u_s^2]_L$) (Ganapathisubramani *et al.*, 2012). Ganapathisubramani *et al.* (2012) have also reported changes in small-scale variance with the magnitude of the large scales using condi-

tional averaging instead of correlations. A more common approach introduced by Mathis *et al.* (2009*a*, 2011*a*) utilizes a Hilbert transform to investigate AM effects. Recent work of Baars *et al.* (2015) used continuous wavelet transforms (CWT) to obtain time–frequency spectrograms of the time-series data, and integrating the energy at scales below f_c gave a measure of small-scale energy. Correlations can then be examined to observe AM interactions. This metric is also briefly used to corroborate the findings in section 3.3. All of these approaches have shown qualitatively similar results in earlier studies corresponding to AM effects in smooth-wall turbulent boundary layers.

The current work uses the Hilbert Transform method, first employed by Mathis *et al.* (2009*a*). The 1-probe and 2-probe correlation coefficients ($R^a_{u_{iL},E_L[u_{is}]}, \equiv R^a_{1P}$ and $R^a_{u_{oL},E_L[u_{is}]}, \equiv R^a_{2P}$, respectively) between the large scales and the large-scale envelope of small scales are presented to investigate the amplitude modulation effects. Further, following Mathis *et al.* (2011*a*), a fixed cut-off wavelength of $\lambda_c^+ = 7000$ at all wall-normal locations is used to separate small and large scales (The wavelength (λ_c) is transposed into frequency domain (f_c) by using the local mean velocity and Taylor's frozen field hypothesis). Previous studies (Mathis *et al.*, 2009*a*) report the qualitative features of the correlation coefficients to be insensitive to the exact value of the cut-off frequency (f_c) chosen, so long as it 'adequately' separates the near-wall small scales from the large scales in the outer layer. This insensitivity to cut-off wavelength was confirmed in the current work. Since the interest herein lies in a phenomenological nature of the inner–outer interactions in rough-wall flow, and not on the scaling aspects of the same, a similar cut-off wavelength was found justified as it adequately separates the small scales from the very large scales based on the energy spectra (shown later in figure. 3.2). For the current rough-wall flow, since the energy of the roughness-generated flow scales resides at small wavelengths since $k \ll \delta$, a cut-off wavelength based on any of the roughness scales is not appropriate for this purpose.

The *1-probe* data processing for AM can be summarized as follows:

1. At each wall-normal location, y^+, the time series is decomposed into small- and large-scale time series (u_{is}^+ and u_{iL}^+, respectively) using a spectral filter. The current effort follows Mathis *et al.* (2011*a*) in using a fixed cut-off wavelength of $\lambda_c^+ = 7000$ at all wall-normal locations. Previous studies have shown the qualitative features of the correlations to be insensitive to the exact value of the cut-off frequency (f_c) chosen (Mathis *et al.*, 2009*a*), as long as it adequately separates the near-wall small scales from the large scales away from the wall (The wavelength (λ_c) is transposed into frequency domain (f_c) by using the local mean velocity and Taylor's frozen field hypothesis). The requirement for the cut-off filter frequency (f_c) is that it must adequately separate the near-wall production cycle (at $\lambda_x^+ \sim 1000$) (and the small scales involved therein) from the larger outer scales corresponding to LSMs and VLSMs. Previous studies have shown the qualitative features of the correlations to be insensitive to the exact value of the cut-off frequency (f_c) chosen (Mathis *et al.*, 2009*a*). Thus, the current effort follows Mathis *et al.* (2011*a*) in using a fixed cut-off wavelength of $\lambda_c^+ = 7000$ at all wall-normal locations.

2. The magnitude of the Hilbert transform of the small-scale signal is then computed, to obtain an envelope ($E[u_{is}^+]$) of the same. The large-scale component of this envelope, $E_L[u_{is}^+]$, is obtained using the same ideal filter used in step (1), and gives the large-scale envelope of the small scales.

3. Having obtained u_{iL}^+ and $E_L[u_{is}^+]$ for each wall-normal location, the correlation coefficient ($R^a_{u_{iL},E_L[u_{is}]}(y^+,\tau)$) between them can be computed using Eqn. (3.1). This correlation quantifies the AM of the small scales by the large scales at the same wall-normal location from a 1-probe measurement.

$$R^a_{u_{iL},E_L[u_{is}]}(y^+,\tau) = \frac{\langle u_{iL}^+(t) * E_L[u_{is}^+](t-\tau)\rangle}{\sqrt{\langle {u_{iL}^+}^2\rangle \langle E_L[u_{is}^+]^2\rangle}} \qquad (\equiv R^a_{1P}). \tag{3.1}$$

A similar procedure is utilized for AM analysis using the 2-probe measurements,

save for one key difference: the large-scale signal in the 1-probe analysis, i.e. u_{iL}, is replaced with the large scales measured using the fixed outer probe in the log region, i.e. u_{oL}. In short, using the 2-probe data, one can compute both R^a_{1P} and $R^a_{u_{oL},E_L[u_{is}]}(\equiv R^a_{2P})$, with the latter representing a 'direct' measure of inner–outer interactions as the large scales in the outer region are unambiguously sampled relative to the near-wall small scales (as explained earlier in section 3.1). A final minor difference in the 2-probe analysis is that the Taylor's hypothesis transformation of the time series between frequency–wave-number domains uses a common convective velocity– the outer probe mean velocity, for all wall-normal positions of the inner probe. This approach is consistent with previous studies (Mathis *et al.*, 2011*a*; Baars *et al.*, 2015).

In the coming discussion, pre-multiplied spectrograms of the streamwise TKE ($k\phi_{uu}$) are also presented to show the energy distribution among different scales as a function of wall-normal position. A frequency integral of this spectrum for a given wall-normal location recovers the corresponding variance of the streamwise velocity fluctuation signal.

3.2.1 1-Probe: AM effects in smooth-wall flow

From the data acquired from the 1-probe experiments, the pre-multiplied spectrogram ($k_x\phi_{uu}$) and the associated AM correlation map (R^a_{1P}) for smooth-wall data are shown in figure 3.1. These spectra and correlation characteristics are consistent with that previously reported for smooth-wall flow in various earlier studies (Hutchins, 2014; Baars *et al.*, 2015; Guala *et al.*, 2011; Chung & McKeon, 2010; Mathis *et al.*, 2009*a*, to name a few), and the important observations have been consolidated here for the sake of completeness and contextual relevance to the rough-wall results.

Both of these results highlight a few important features of the smooth-wall turbulent boundary layer. First, the pre-multiplied spectrogram (figure 3.1a) clearly shows the inner peak in TKE production at $y^+ \sim 15$ and $\lambda_x^+ \sim 1500$.

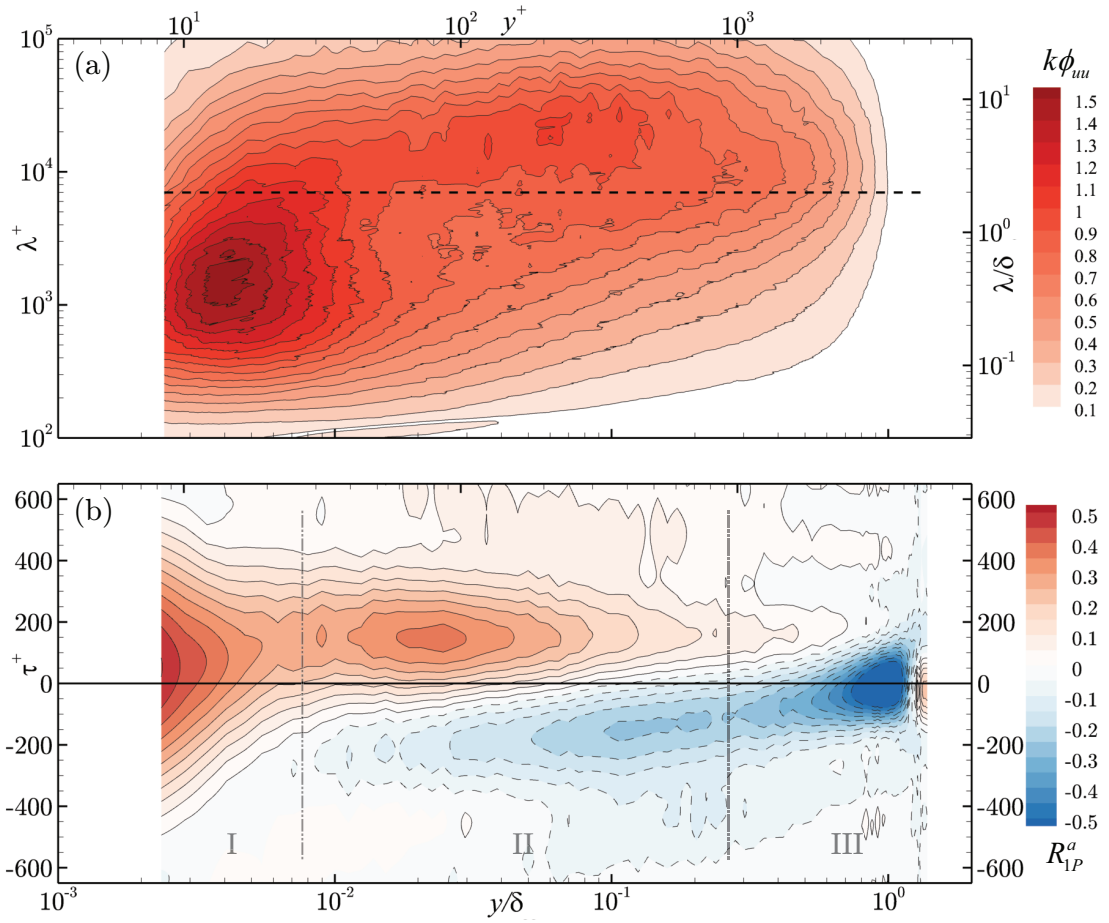

Figure 3.1: (a) Pre-multiplied streamwise TKE spectrogram seen earlier in figure 2.9, with $\lambda_x^+ = 7000$– the cut-off wavelength (*dashed line*) and (b) single-point AM correlation coefficient, R^a_{1P} (regions I, II and III marked in the correlation map) for smooth-wall flow.

However, in addition to this peak, an additional peak in TKE is noted in the outer layer, corresponding to the energetic VLSMs at $y^+ \sim 200\,(\equiv 3.9\sqrt{\delta^+})$ and $\lambda \sim 9\delta$, as seen in Ng *et al.* (2011). This secondary energy peak reflects the energy embodied in the very-large-scale motions that reside in the outer layer of this flow that are thought to modulate the near-wall, smaller scales.

Figure 3.1b presents the 1-probe AM correlation map, R^a_{1P}, for smooth-wall flow. Three distinct regions can be observed in this correlation result. The wake region ($\lambda > 0.7\delta$, region III in figure 3.1b) has a prominent anti-correlation peak near ($y = \delta$, $\tau^+ = 0$), implying that every time a positive large-scale velocity is measured, a simultaneous ($\tau^+ = 0$) reduction in small-scale energy is ob-

served, and vice versa. This behavior can be attributed to the intermittency in the wake region of the flow associated with large-scale entrainment, wherein a higher velocity comes from a free stream packet (of low turbulence) being entrained, and lower velocity comes from the turbulent fluid ejected from the near-wall region (Hutchins, 2014). As one would expect, this feature is absent in internal flows (pipes and channels, (Mathis *et al.*, 2009*b*)) where this free-stream intermittency is absent under fully-developed flow conditions. Apart from this outer peak in the wake region, a symmetric correlation–anti-correlation peak (region II in figure 3.1b), centered about the y-location of the aforementioned VLSM peak [$y^+ \sim 200\,(\equiv 3.9\sqrt{\delta^+})$], is observed in the inertial region. This feature can be interpreted as a symmetric arrangement of small scales around the inclined larger-scale structures (LSMs and VLSMs), as seen, for example, in Hutchins *et al.* (2011) and Chung & McKeon (2010). Duvvuri & McKeon (2015, 2016) have further analyzed this structural organization and receptivity to external forcing and is attributed to arrangement of the small scales relative to the large scales. Finally, the near-wall region ($y^+ < 25$, region I in figure 3.1b) contains a single dominant peak, indicating a small-scale energy that is correlated with the corresponding large scale measured, and so with a positive time delay (τ^a). As discussed in previous studies, we consider only this correlation peak to be an indication of true inner–outer interactions, distinct from the scale arrangement and intermittency effects in the inertial and wake regions of the flow, respectively. In other words, the correlation coefficient used to evaluate inner-outer interactions, i.e., R^a_{1P}, can additionally capture other phenomena, such as preferential arrangement of small scales and intermittency. This observation is further discussed in the corresponding frequency modulation correlation maps presented in section 3.3.

3.2.2 1-Probe: AM effects in rough-wall flow

Figure 3.2 shows the pre-multiplied spectrograms and 1-probe AM correlation maps for the rough-wall boundary layer at spanwise locations corresponding to a

low momentum pathway (LMP, *left*) and high-momentum pathway (HMP, *right*) [See figure 2.5]. The spectrograms for the LMP and HMP positions (figures 3.2a and 3.2b, respectively) show that the near-wall turbulence production peak is destroyed by the presence of roughness and is replaced with a different energy distribution in the roughness sublayer. In contrast, the outer regions of both spectrograms are qualitatively similar to one-another (LMP and HMP) and to smooth-wall flow (figure 3.1a). This consistency is in accordance with the notion of outer-layer similarity wherein the outer flow adapts in a universal manner and the roughness simply sets the wall shear and the outer length scale (when $\delta \gg k$). In this regard, the energy magnitudes at various scales are expected to scale according to the local conditions, such as δ and Re as reported in Table 2.2. These large scale spanwise heterogeneities in TKE are reported in more detail in Barros (2014). More relevantly, an outer peak at wavelengths and wall-normal locations corresponding to VLSM peak in smooth-wall flow is observable in both the spanwise locations, albeit with different magnitudes of energy. Thus, the outer region of the rough-wall flow embodies larger-scale motions that, at least in a statistical sense, embody energy similar to that of the smooth-wall flow.

In the AM correlation maps for the LMP and HMP positions (figures 3.2c and 3.2d, respectively), outer-layer similarity is also evident in the current rough-wall flow. In particular, the anti-correlation peak corresponding to wake-region-intermittency appears in both rough-wall results with characteristics consistent with that of smooth-wall flow. In addition, the bi-modal feature of the correlations in the inertial region (region II in smooth-wall flow in figure 3.1b) is also noted in the inertial region of the rough-wall cases. Of noted difference compared to the smooth-wall correlation, there exists a significant overlap between the inner-region modulation and the inertial-region scale arrangement in the rough-wall flow. This overlap makes it more difficult to clearly demarcate the aforementioned regions I and II, as was done in smooth-wall flow (figure 3.1b). This overlap is particularly severe in the LMP region compared to the HMP result. Nevertheless, the magnitude of the correlation coefficient close to the wall does indicate the

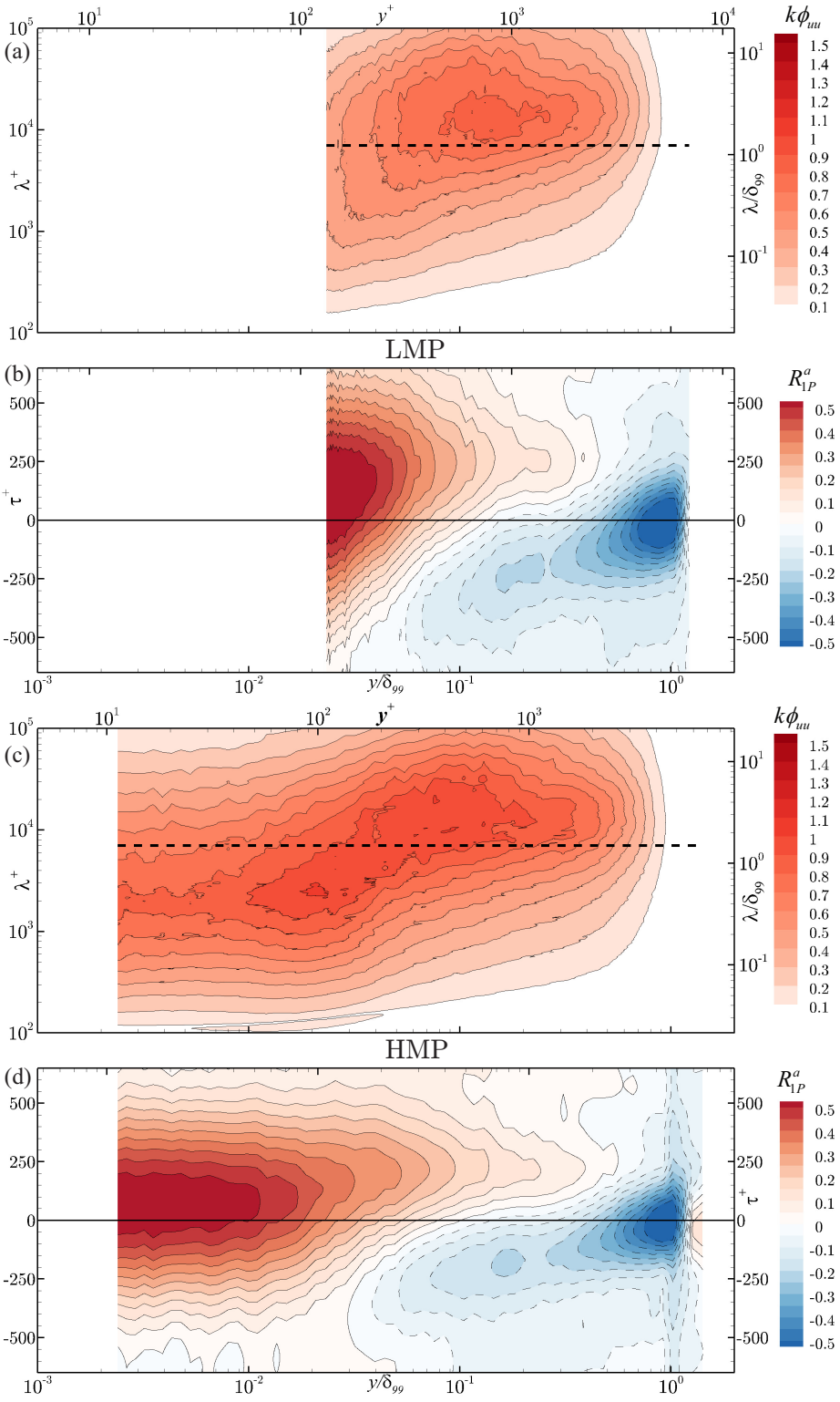

Figure 3.2: (a, c) Pre-multiplied streamwise TKE spectrograms (dashed horizontal line corresponds to $\lambda_x^+ = 7000$– the cut-off wavelength) and (b, d) single-point AM correlation coefficients, R^a_{1P}, for rough-wall flow at an LMP and a HMP, respectively.

presence of AM influences similar to that of smooth-wall flow, though the wall-normal extent of this AM region is ambiguous owing to the above mentioned overlap.

The degree of AM is more clearly seen in zero-time-delay correlation coefficients ($R^a_{1P}|_{\tau=0}$) that are more commonly reported in the literature (Mathis *et al.*, 2009*a*). Figure 3.3 presents wall-normal profiles of $R^a_{1P}|_{\tau=0}$ for the two rough-wall cases along with the smooth-wall result for comparison. The high degree of AM of the small scales within the roughness sublayer by the large scales is clearly evident and, in fact, *exceeds* that of smooth-wall flow until $y \approx 0.15 - 0.2\delta$. Beyond this wall-normal position, the two rough-wall correlation coefficients (LMP and HMP) collapse with the smooth-wall result, further supporting outer-layer similarity in the current rough-wall flow with smooth-wall behavior far from the roughness as previously reported by Wu & Christensen (2007) based on single- and two-point turbulence statistics. The fact that this AM diagnostic is higher in rough-wall flow than its smooth-wall counterpart is interesting given that roughness disrupts the near-wall turbulence production cycle that correlates well with the outer larger scales in smooth-wall flow. However, this increased AM correlation level is observed from the 1-probe measurements, which correlate large scales and small scales locally. Thus, local large scales could be a collective influence of outer-layer superposition and of the scales imparted by the roughness itself. The presence of enhanced AM in this context thus speaks to the strength of these phenomena, and its importance in rough-wall flows.

3.2.3 2-Probe: AM effects

As introduced earlier, the 2-probe measurements unambiguously capture the large scales that reside in the outer region and small scales in the near-wall region, thus allowing direct evaluation of inner–outer interactions. This is particularly important in the rough-wall flow as the large scales near the wall had reduced correlation to those in the outer region compared to smooth-wall flow. The 2-probe

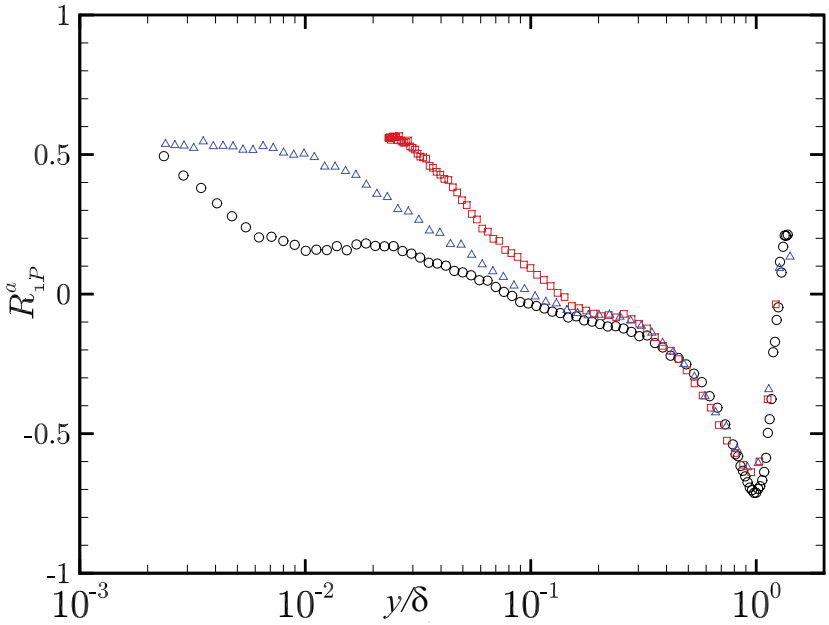

Figure 3.3: The zero-time-delay AM correlation coefficient, $R^a_{1P}|_{\tau=0}$, as defined by Mathis *et al.* (2009*a*), as a function of the wall-normal position. ◯: smooth; □: Rough (LMP); △: Rough (HMP).

analysis also provides a crucial confirmation that the enhanced AM effects noted in the 1-probe analysis of the rough-wall flow is due to true inner–outer interactions. Further, this 2-probe analysis allows confirmation that the 1-probe AM effects noted in both flows are not merely a manifestation of velocity skewness in the near-wall region (Schlatter & Örlü, 2010*b*; Bernardini & Pirozzoli, 2011), but represent actual interaction. Figures 3.4a–3.4c show the pre-multiplied spectrograms and correlation maps for the three cases: smooth-wall flow and the rough-wall flow at LMP and HMP locations, respectively. These pre-multiplied spectrograms are computed from the inner-probe data, and should be identical to their 1-probe counterparts. The cut-off filter indicated by the dashed curve in figure 3.4 appears distorted due to the difference in convection velocities used for converting to the two measures of streamwise wavelength: λ^+ (vertical axis in figure 3.4a–3.4c) and λ_c^{2P} (*dashed* line in figure 3.4a–3.4c). While the former utilizes the local mean velocity (for consistency with reported spectra in the literature and figure 3.1), the latter uses the constant mean velocity measured by the outer probe. Thus,

the cut-off line plotted is given by

$$\lambda_c^{2P} = \lambda_c^{1P} \frac{U_i}{U_o} = 7000 \frac{U_i}{U_o}. \tag{3.2}$$

where U represents the corresponding mean velocity.

The AM correlation maps from the 2-probe measurements presented in figures 3.4d–3.4f confirm the presence of AM effects in the two rough-wall cases as the correlation coefficient is of significant magnitude within the roughness sublayer. Though these 2-probe results show overall similarities with their 1-probe counterparts, a few subtle differences are also noted. In particular, the time delay for maximum correlation that occurs near the wall is quite different between the 1-probe and 2-probe analyses. As discussed earlier in section 3.2 and will be seen in more details in section 3.6, the superposition of the inertial region large scales on the near-wall region occurs with a scale-dependent time delay, Δt_s (Hutchins *et al.*, 2011), i.e., a large scale event detected in the logarithmic region occurs near the wall after a time Δt_s. In an attached eddy framework, this phenomenon can be viewed as measuring *a large scale that is inclined towards the downstream direction, and is convecting past the measurement point.* So, for a fixed streamwise location (as is the case for the probes in the current study), the large scale would be detected by the outer probe earlier (by time Δt_s) than the lower probe. Thus, a difference in the time delay for this correlation maximum between the 1-probe and 2-probe results is expected for this reason.

From the time delay (τ^+) for maximum near-wall correlation in the 1-probe analysis (for e.g., figure 3.1), the inner–outer AM interaction seems to occur ahead of the superposition of the large scales close to the wall (i.e., $\Delta t_s > 0$). However, the delay for maximum near-wall correlation from 2-probe analysis is found to be less than that observed in the 1-probe analysis. Figure 3.5 presents this difference in the time lags clearly, as determined for 1-probe and 2-probe analyses. For smooth-wall flow, the near-wall AM appears at roughly the same time as the outer large scale is detected in the 2-probe result, but a time τ^a earlier than the

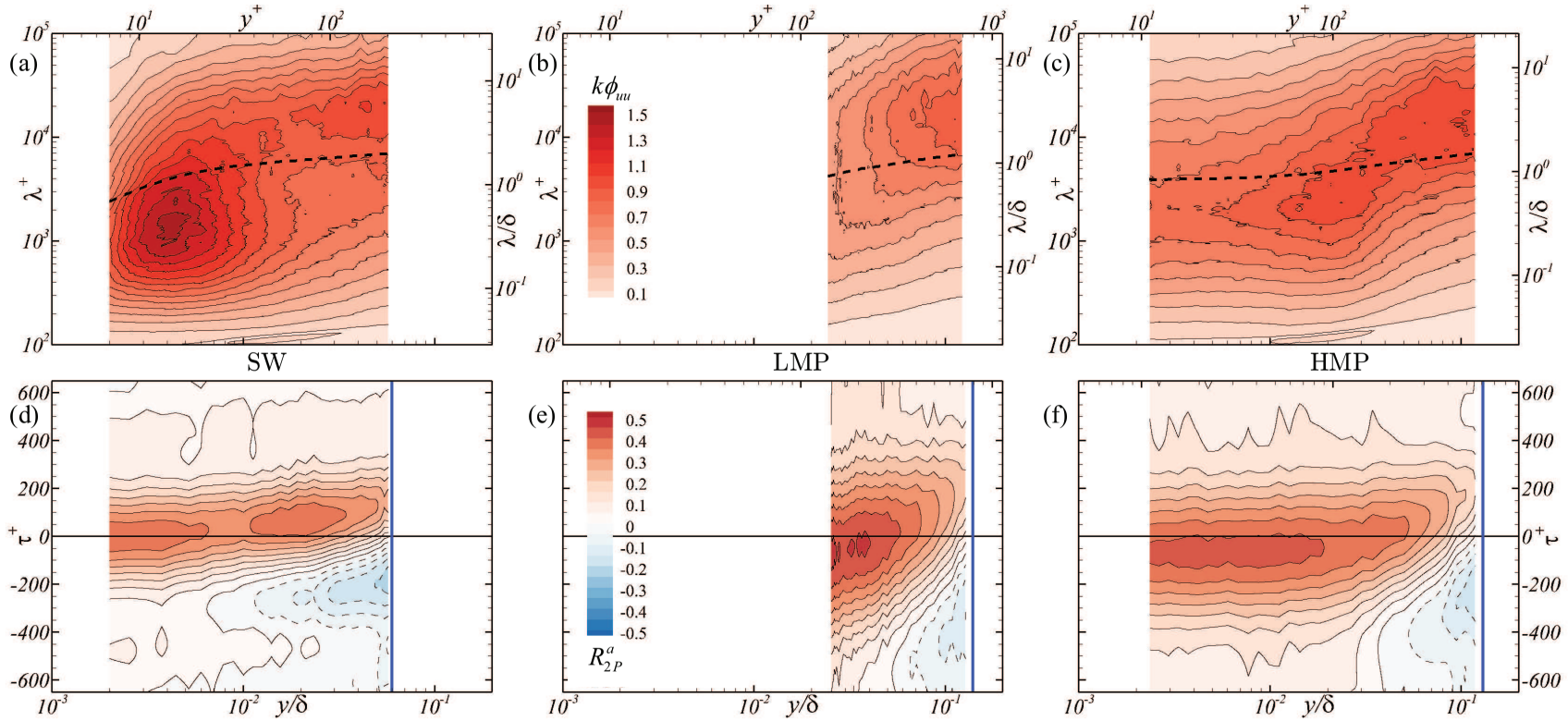

Figure 3.4: (a–c) Pre-multiplied streamwise TKE spectrograms (dashed horizontal line corresponds to $\lambda_x^+ = 7000$– the cut-off wavelength) and (d–f) two-point AM correlation coefficients, R^a_{2P}, for smooth- and rough-wall flow at an LMP and a HMP, respectively. The *blue* lines in (d–f) indicate the location of the outer probe for each case.

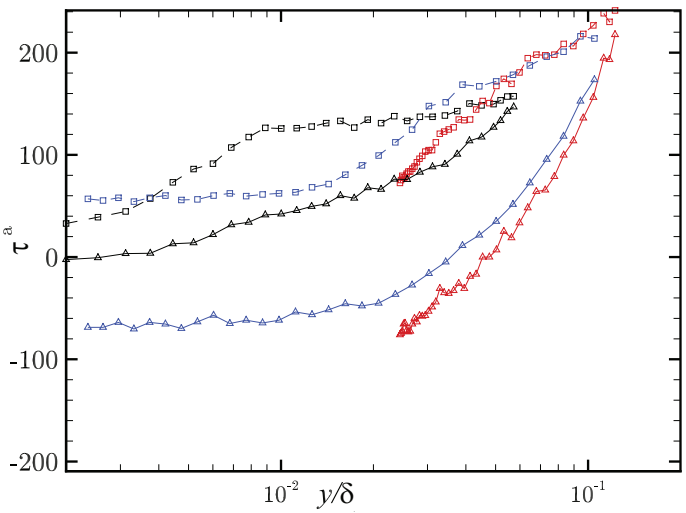

Figure 3.5: Time delay for maximum AM correlation coefficient. □: 1-probe; △: 2-probe. Smooth; Rough (LMP); Rough (HMP).

detection of the near-wall large scale in the 1-probe analysis. Further, in the rough-wall cases, the sign of τ^a is reversed, implying that the outer probe detects the large scale ahead of the corresponding AM in the near-wall region. This reversing was not due to the difference in convection velocities used for cut-off wavelength in 1- and 2-probe analysis. Rather, we suspect this delay to depend on the wall-normal location of the outer probe and the structure inclination angle in the inertial region (as is discussed later in section 3.4).

3.3 Frequency modulation

Frequency modulation (FM) in smooth-wall turbulent boundary layers has been investigated in earlier studies by Ganapathisubramani *et al.* (2012) and Baars *et al.* (2015). Both of these studies attempted to relate the change in small-scale 'instantaneous frequency' with the large-scale fluctuations in the boundary layer. Ganapathisubramani *et al.* (2012) accomplished this analysis by binning short segments of equal duration of large- and small-scale signals. The average 'frequency' of the small scales was then computed by counting the number of local maxima and minima occurring per segment, and was conditionally averaged on

the magnitude of the corresponding large scales. It was shown that the 'average frequency' of the small scales was higher when a positive large-scale fluctuation occurred locally. Alternatively, Baars *et al.* (2015) used continuous wavelet transforms (CWT) to perform a time-correlation method for quantifying FM effects, akin to the AM analysis performed in the previous section. The latter CWT method is used herein to investigate FM effects. While a comprehensive description of this method is given in the original work (Baars *et al.*, 2015), relevant details of the analyses performed in the current study are summarized herein.

The continuous wavelet transform (CWT, $\mathbb{U}(t', s)$) of a time series ($u(t)$) involves convoluting the signal with a 'mother wavelet' function, $\psi(t/s)$, as

$$\mathbb{U}(t', s) = \frac{1}{\sqrt{s}} \int_{-\infty}^{\infty} u(\tau)\psi\left(\frac{\tau - t'}{s}\right) d\tau. \tag{3.3}$$

The independent variables of the CWT are the translation, t', and the dilation scale, s. Note that a defined property for mother wavelets is a scale dependent center frequency, $\hat{f}(s)$. In a sense, the wavelet transform operation can be viewed as determining a coefficient that quantifies a resonance of the wavelet of scale s (and $\hat{f}$) with a segment of signal, $u(t)$, centered around time t'. A CWT decomposes a signal $u(t)$ into a time–frequency space, $\mathbb{U}(t', f)$, thus identifying various frequency components in the signal at various times. (akin to a short-time Fourier transform, STFT). The reader is referred to the signal processing literature (such as Alfred (1999) and Torrence & Compo (1998)) for a more detailed description of wavelet transforms and their applications. For simplicity in the current analysis, we treat the translation to be identical to the time variable, i.e., $t' \equiv t$. It must be noted that the wavelet transform suffers from an uncertainty principle, where large scales (and small f) are poorly resolved in time, but well resolved in frequency, and vice versa.

Following Baars *et al.* (2015), figure 3.6 shows the pre-multiplied wavelet power spectrum $[f\tilde{E}(t, f)]$ of an illustrative velocity time series segment, that can be

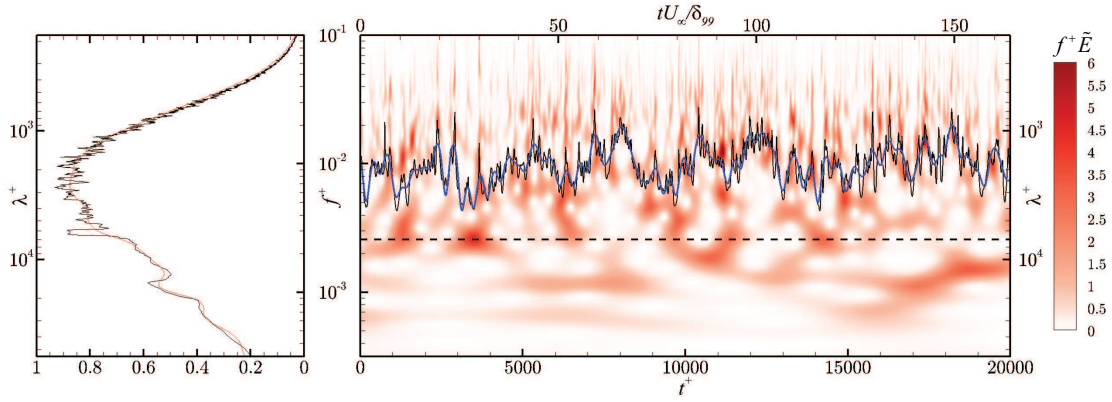

Figure 3.6: Pre-multiplied wavelet power spectrum ($f\tilde{E}$, *right*) of a velocity time series measured over smooth-wall flow at $y^+ = 9$. The time series on the plot mark the corresponding instantaneous frequencies, f_s and f_{sL}, and the cut-off frequency, f_c (*dashed*). The time average of the WPS ($f\langle\tilde{E}\rangle_t$) is compared with corresponding smoothed pre-multiplied power spectrum ($k\phi_{uu}$) on the *left*–both of which are measures of average distribution of energy among various scales.

computed from the CWT as

$$\tilde{E}(t, f) = |\mathbb{U}(t, f)|^2. \tag{3.4}$$

The wavelet power spectrum (WPS) at a given time t is thus analogous to an *instantaneous* power spectral density.

For the current work, analytic Morlet wavelet was used as the mother wavelet, and 128 logarithmically spaced scales were resolved, with the smallest scale corresponding to the Nyquist frequency (f_N) and the largest scale corresponding to $\lambda_x = 30\delta$. Also demarcated on the WPS in figure 3.6 are the large scales ($< f_c$) and the small scales ($> f_c$), using the cut-off wavelength (λ_c). The integral of the WPS at frequencies greater than f_c for each time, t, gives a small-scale energy time series [$\sigma_s(t)$, Eqn. (3.5)], which can also be used in lieu Hilbert transformed envelope signal for AM, as mentioned in section 3.2 and shown originally by Baars *et al.* (2015). A representative small-scale-frequency signal (or instantaneous frequency signal) can now be defined from the WPS. Following Baars *et al.* (2015), the first moment of the small-scale energy distribution at each time is used herein

as the instantaneous frequency, $f_s(t)$, that can be computed as

$$f_s(t) = 10^{F(t)}, \tag{3.5}$$

$$F(t) = \frac{1}{(\sigma_s(t))^2} \int_{f_c}^{f_N} \log_{10}(f) \left(f\,\tilde{E}\right) d\log_{10}(f), \tag{3.6}$$

$$\sigma_s(t) = \left[\int_{f_c}^{f_N} f\,\tilde{E}\, d\log_{10}(f)\right]^{\frac{1}{2}}. \tag{3.7}$$

The instantaneous frequency signal (f_s) and the filtered (at f_c) large-scale component (f_{sL}) are also shown in in figure 3.6. The fluctuating part (f'_s) of f_s gives a measure of small-scale frequency changes with time.

Using Eqn. (3.3), cross-correlation coefficients can be computed between the inner large scales (u_{iL}) and the large-scale frequency fluctuations of small scales (f'_{sL}) for quantifying FM effects from 1-probe data. Similar correlation coefficients between the large scales in the outer region (u_{oL}) and the inner frequency fluctuations (f'_{sL}) allows quantification of FM effects from 2-probe data, similar to the 2-probe AM analysis summarized earlier. The correlation functions we shall be investigating will be $R^f_{u_{iL},f'_{sL}} (\equiv R^f_{1P})$ for 1-probe, and $R^f_{u_{oL},f'_{sL}} (\equiv R^f_{2P})$ for 2-probe measurements given by

$$R^f_{u_{iL},f'_{sL}}(y^+,\tau) = \frac{\langle u^+_{iL}(t) * f'_{sL}(t-\tau)\rangle}{\sqrt{\langle {u^+_{iL}}^2\rangle \langle {f'_{sL}}^2\rangle}} \qquad (\equiv R^f_{1P}). \tag{3.8}$$

3.3.1 FM correlation coefficients

Figure 3.7 presents the 1-probe FM correlation maps for smooth- and the two rough-wall cases (LMP and HMP). The smooth-wall results agree well with the findings of Baars *et al.* (2015) which confirms the fidelity of the analysis procedure utilized herein. Further, by contrasting the smooth-wall FM (figure 3.7a) and AM (figure 3.1b) correlation maps, there exist some important similarities and

differences. First, the anti-correlation structure observed in the AM result at $y \sim \delta$ owing to wake region intermittency is also present in FM correlation map. However, the correlation–anti-correlation structure that marked the inertial region in the AM result, owing to small-scale arrangement around inertial region large scales (Region II in figure 3.1b), is absent in the FM correlation map for smooth-wall flow (figure 3.7a). Finally, a near-wall peak appears close to the wall in the smooth-wall FM result (figure 3.7a), representing the FM of the near-wall scales by the large scales measured at the same wall-normal location (as this result is from 1-probe analysis). Thus, this result supports the occurrence of modulation in the near-wall region of smooth-wall flow and that this modulation is restricted to the near-wall region.

The FM in both the smooth- and rough-wall cases is readily apparent in figure 3.8, which presents the FM correlation coefficient for zero time delay ($R^f_{1P}|_{\tau=0}$) plotted in figure 3.7–the counterparts to the AM correlation profiles in figure 3.3. The two rough-wall FM correlations collapse well for all wall-normal locations until very close to the surface ($y \lesssim 0.04\delta$), where they seem to plateau (~ 0.3) to a lesser value than that of smooth-wall (~ 0.4). Below this location, the FM correlation at the LMP increases sharply while the FM correlation at the HMP increases slowly, with both well-exceeding the smooth-wall result in the near-wall region until the HMP result crosses below the smooth-wall one at $y \approx 0.01\delta$. While the smooth-wall result becomes zero for $y > 0.05\delta$ until the wake region, where the correlation becomes negative owing to wake intermittency, the two rough-wall cases show non-zero correlation much further into the outer region and remain so until $y \approx 0.4\delta$ where they both collapse with the smooth-wall correlation profile through the wake region. This latter behavior could be a consequence of the roughness sublayer occupying a larger portion of the boundary layer (usually taken as $\sim 3-5k$, which would be $y \lesssim 0.13-0.22\delta$) compared to the buffer layer of the smooth-wall flow ($y \lesssim 0.02\delta$), and thus perhaps a larger inner region being modulated by outer-layer effects. However, these results must be interpreted with caution as, similar to the 1-probe AM correlation coefficients, these results show

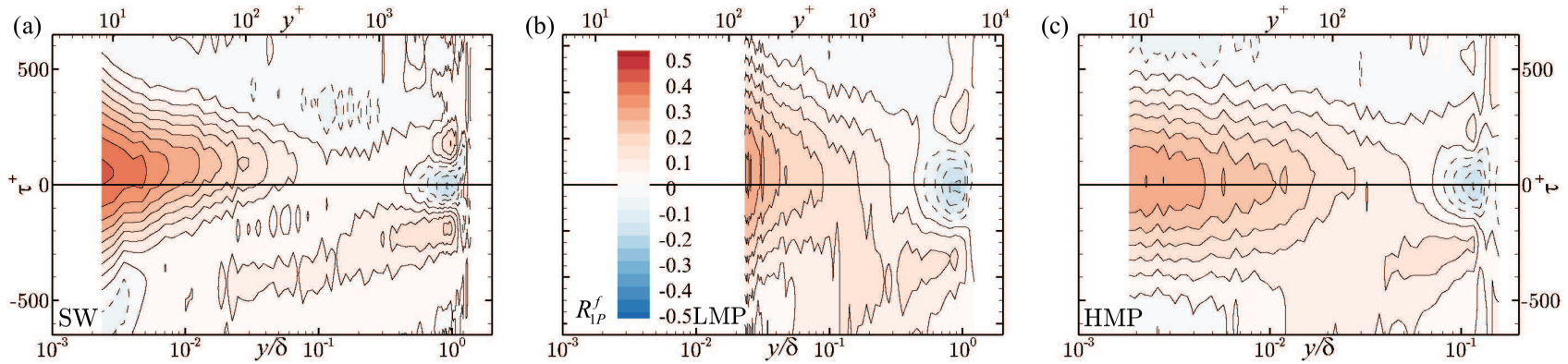

Figure 3.7: 1-probe FM correlation maps, R^f_{1P}, for (a) smooth and (b, c) rough-wall flow at an LMP and a HMP, respectively.

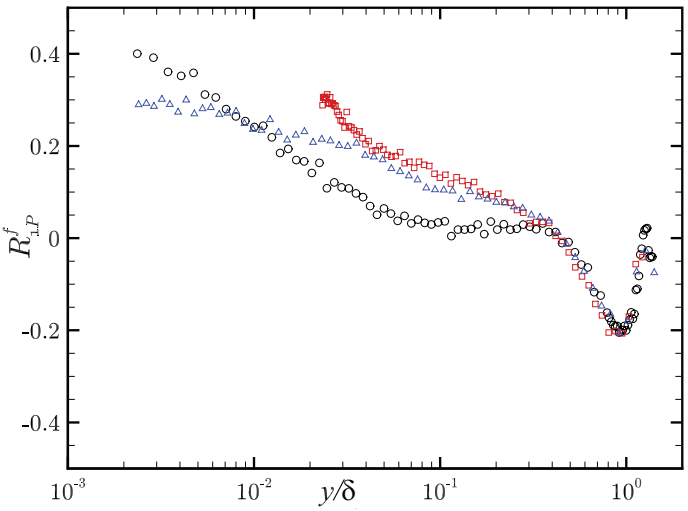

Figure 3.8: The zero-time-delay FM correlation coefficient, $R^f_{1P}|_{\tau=0}$, as a function of the wall-normal position. ◯: smooth; □: Rough (LMP); △: Rough (HMP).

the interaction between the small scales in the near-wall region with the large-scale signature at the same wall-normal location. Thus, particularly in the rough-wall cases, these local large-scale signatures may not be only from the outer layer but could also include near-wall larger scales that are attributable to roughness.

The 2-probe FM correlation maps, correlating the outer region large scales, u_{oL}, with the sublayer instantaneous frequency, f'_{sL}, are shown in figure 3.9. As noted from the 1-probe and 2-probe AM correlation maps, the 2-probe FM correlation coefficients shows qualitatively similar results to their 1-probe counterparts (figure 3.7) with subtle structural differences. Apart from clear strong FM correlation in the near-wall regions of the smooth- and rough-wall cases (with similar magnitude correlation in the two rough-wall cases but less than the smooth-wall case), these correlation maps reiterate the negative time delay for the maximum correlation ($\tau^f < 0$) between f'_{sL} and u_{oL}. It is interesting to note that two independent measures of inner–outer interaction, both AM and FM, indicate such a time delay, with this negative time delay exclusively observed in the two rough-wall cases. As was mentioned in section 3.2, this phenomenon likely relates to the inclination of the large-scale outer structure, which will be further discussed in section 3.4. But apart from these subtle differences, the 1-probe and 2-probe FM results agree

well, and establish the occurrence of FM inner–outer interactions in the presence of the roughness considered herein.

3.3.2 Amplitude modulation using wavelet power spectrum (WPS)

As a part of the frequency modulation analysis in the previous section, the small-scale energy time series $\sigma_s(t)$ was also computed (Baars *et al.*, 2015), which is a measure of small-scale energy evolution with this modulation. The large-scale evolution of this can also be used to compute the effect of large scales on the small-scale energy. Doing so serves as an alternative measure of the amplitude modulation correlation coefficient, R_{AM}, discussed in section 3.2. Thus, the correlation coefficient can be written as

$$R^a_{u_{iL},\sigma'_{sL}}(y^+,\tau) = \frac{\langle u^+_{iL}(t) * \sigma'_{sL}(t-\tau)\rangle}{\sqrt{\langle {u^+_{iL}}^2\rangle\langle {\sigma'_{sL}}^2\rangle}} \qquad (\equiv R^a_{1P,\sigma}), \tag{3.9}$$

where σ_{sL} is the large-scale component of σ_s from Eqn. (3.7) using the cut-off wavelength λ_c. The two-probe version can be similarly obtained ($R^a_{2P,\sigma}$).

Figure 3.11 shows this one-probe correlation coefficient, $R^a_{1P,\sigma}$, along with the Hilbert transform-based coefficient, $R^a_{1P,Env}$, for the smooth-wall and the two rough-wall measurements. Figure 3.12 shows the correlation maps of the one-probe measurements of the three flow measurements, with the time delay, τ. The observations are similar to those found earlier in section 3.2 (figures 3.1 and 3.2). The two small scale representations are equivalent to each other, and the amplitude modulation conclusions are re-emphasized by very different metrics.

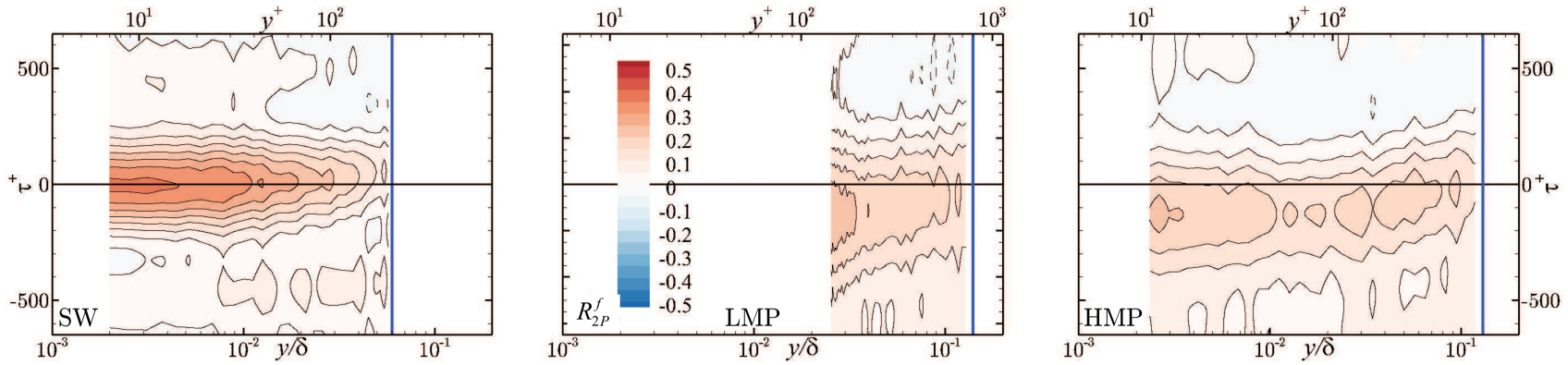

Figure 3.9: 2-probe FM correlation maps, R^f_{2P}, for (a) smooth and (b, c) rough-wall flow at an LMP and a HMP, respectively. The *blue* lines indicate the location of the outer probe for each case.

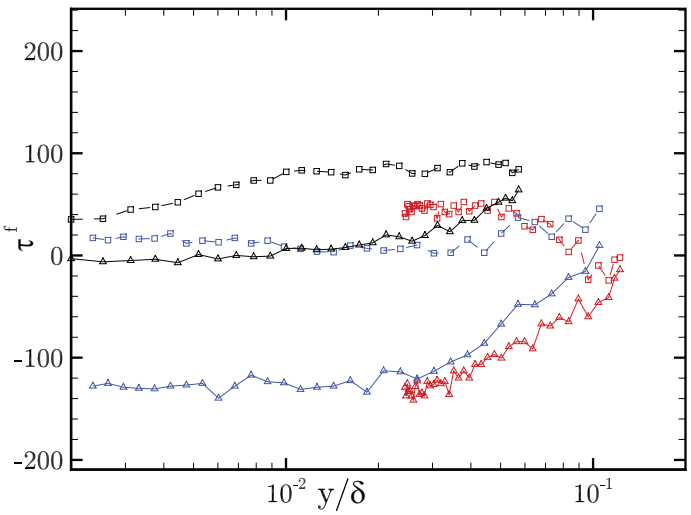

Figure 3.10: Time delay for maximum FM correlation coefficient. □: 1-probe; △: 2-probe. Smooth; Rough (LMP); Rough (HMP).

3.4 Time delays between the large-scale and modulation phenomena

With the understanding of inner–outer interactions so far, we seek to address the apparent differences between the smooth- and rough-wall results presented herein. Though rough-wall AM and FM correlation coefficients show similar magnitudes and wall-normal trends to that of smooth-wall flow, the time delay between the large scales and the near-wall modulation effects show differences. Since these influences are correlated with respect to the large scales (at $\tau = 0$), let the time delay for maximum AM at any wall-normal position be $\tau^a(y^+)$ and its FM counterpart be $\tau^f(y^+)$. In other words, τ^a and τ^f indicate times by which the modulation influences *lead* or *lag* the large scales (if > 0 or < 0, respectively), as given by the time delay associated with the peak in the respective correlation coefficient.

In this context, consider the schematic in figure 3.13, reproduced from Baars *et al.* (2015) but adjusted for the current rough-wall scenario. For smooth-wall flow (in figure 3.1 and Baars *et al.* (2015)), it was seen that $\tau^a_{1P} > 0$ and $\tau^f_{1P} > 0$, implying that the modulation influences lead the local large scales. By virtue of the inclination of the large scales towards the downstream, the detection of a large

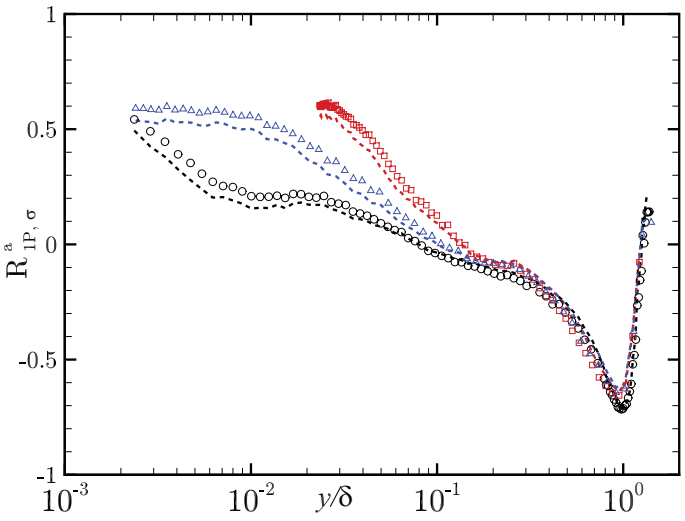

Figure 3.11: The zero-time-delay AM correlation coefficient via small-scale wavelet energy, $R^f_{1P,\sigma}|_{\tau=0}$, as a function of wall-normal position. ◯: smooth; □: Rough (LMP); △: Rough (HMP). Also shown as *dashed lines* are corresponding values of $R^a_{1P}|_{\tau=0}$ shown earlier in figure 3.8 using Hilbert transform methods.

scale at a higher y^+ location (say y^+_o) occurs at an earlier time relative to the local large scales (since $y^+ < y^+_o$). Hence, one would expect the time delay associated with maximum modulation to be smaller, i.e., $\tau^a_{2P} < \tau^a_{1P}$ and $\tau^f_{2P} < \tau^f_{1P}$. The smooth-wall correlation results clearly reflect this notion (figures 3.5 and 3.9). In contrast, the negative values of τ^a_{2P} and τ^f_{2P} for the rough-wall cases possibly stem from the outer probe residing farther away from the wall compared to the smooth-wall case. The inclined nature of the large-scale motions results in an even earlier detection by the outer probe relative to the modulation influences near the wall, and hence a lead relative to the latter. The uncertainties in the exact values of these correlation peaks, corrupted in part by the filter roll-off characteristics, limit precise quantification of these delays as a relative motion. However, the trends, and the possible physical explanation for the same, are unambiguous.

Further, if this schematic were true, the time delay between the AM and FM maxima measured by both the 1-probe and 2-probe measurements, should be identical. In other words, $\Delta\tau^{af}_{1P} = \Delta\tau^{af}_{2P}$, where $\Delta\tau^{af} = \tau^a - \tau^f$. Figure 3.14 establishes this trend via the measured values of $\Delta\tau^{af}_{1P}$ and $\Delta\tau^{af}_{2P}$ for smooth-wall (*black*), supporting the hypothesized interaction structure. For smooth-wall

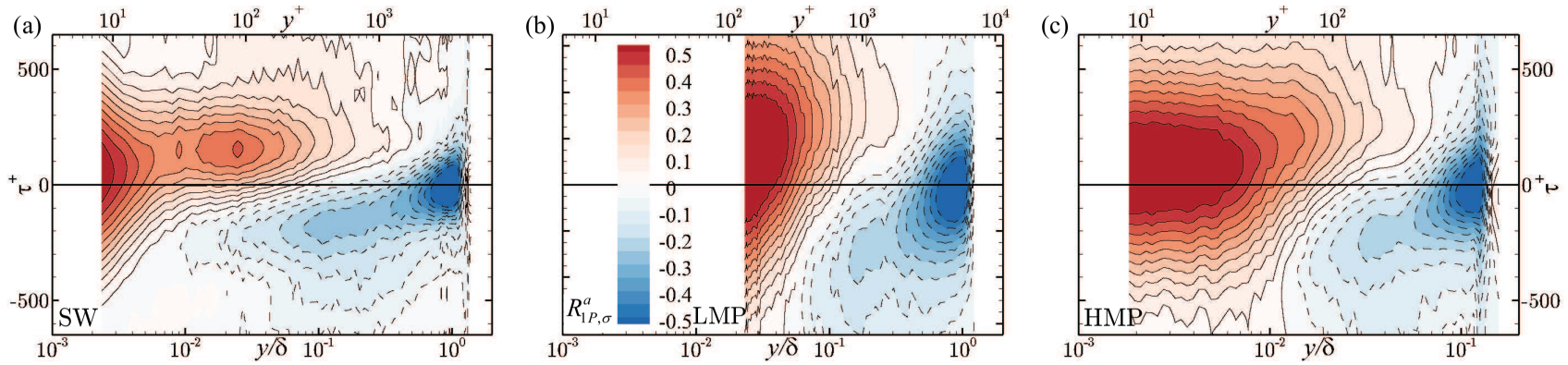

Figure 3.12: 1-probe AM correlation maps from small-scale wavelet energy, R^f_{1P}, for (a) smooth and (b, c) rough-wall flow at an LMP and a HMP, respectively.

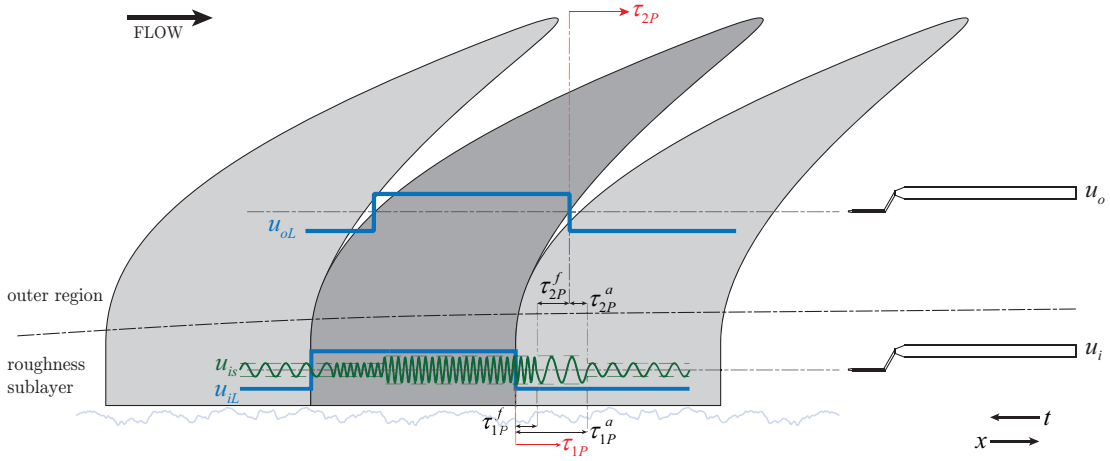

Figure 3.13: A schematic representation of inner–outer interactions that was originally presented by Baars *et al.* (2015), but modified to represent the current experiments and observations.

flows, this simply follows from figure 3.13 and is, in a sense, trivial. This, however, represents a sanity check for the measurements, analysis and conclusions we make from them.

The 'triviality' in smooth-wall flow comes from the fact that the large scales being measured by 1-probe and 2-probe are, in a way, 'identical'. This isn't necessarily true for the rough-wall flows, where they represent two different measures, depending on the strength of superposition of the large scales in the near-wall region. However, we can use the above measure as a 1$^{\text{st}}$ order check to ascertain whether figure 3.13 holds in rough-wall flows as well. Figure 3.14 shows the time-delay variations for rough-wall LMP and HMP regions. It can be seen that, in the near-wall region where the modulation effects are dominant, the two rough-wall measurements yield very similar $\Delta\tau^{af}$ (if not identical) even for the rough-wall flows at the LMP and HMP locations. This consistency suggests that a similar structure of interactions shown by schematic in figure 3.13 possibly operates even in the rough-wall flows. It must be remembered that the broad correlation peaks reduce the significance in precise locations of the correlation maxima (τ^a and τ^f). These are further marred by the sharp spectral filter characteristics that reflect in correlations.

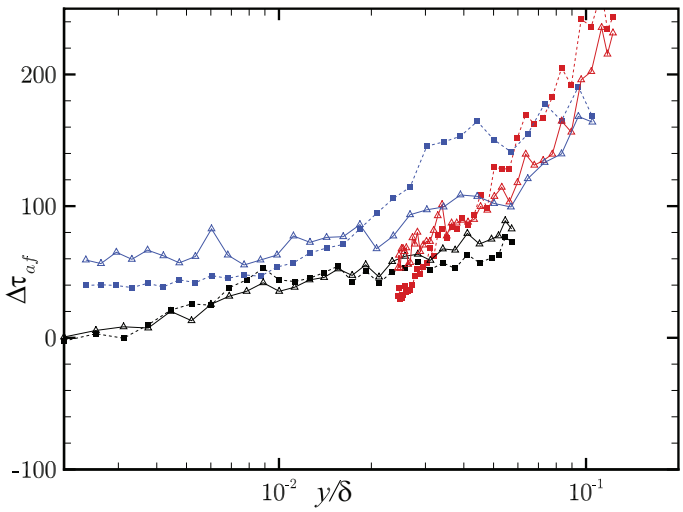

Figure 3.14: Time delay ($\Delta\tau_{af}$) between the amplitude and frequency modulation measured by 1-probe and 2-probes. *dashed, squares*:- 1-probe; *solid, triangles*:- 2-probe. *black*:- smooth-wall; *red*:- rough LMP; *blue*:- rough RMP.

Of particular interest are the negative values of τ^a_{2P} and τ^f_{2P} from figures 3.4 and 3.9, implying that the AM and FM influences occur at the near-wall probe ahead of the large scales in the logarithmic region. This observation can now be explained by assuming the above structure in figure 3.13. The negative values of τ^a_{2P} and τ^f_{2P} could occur from two potential scenarios. First, the inclination angle of the outer-layer structure in the rough-wall flow could be larger than that of the smooth-wall flow. Second, the position of the outer probe in the current experiments, relative to the modulating structures, could be lower in the rough-wall case than that of the smooth-wall flow. However, further experimentation is required to resolve this explanation completely. We can, however, conclude that the inner–outer interaction structure in the current rough-wall flow is similar in character to that of the smooth-wall phenomena.

3.5 Amplitude vs frequency modulation: A note on the differences

The correlation structure between the amplitude and frequency modulations can be investigated to observe an important distinction between them. Figure 3.15 shows the the correlation maps for smooth- and rough-wall HMP flow, presented earlier in section 3.2 and 3.3. The near-wall region (region I) and the inertial region (region II) have been marked between the two flows on the correlation maps.

It can immediately be seen, particularly from the smooth-wall flow that, while the amplitude modulation correlation maps capture the signature of both regions, the frequency modulation only captures the near-wall modulation, and not the scale arrangement in the latter. This distinction is particularly important in the rough-wall cases, as shown, where the thicker inner region and relatively identical outer regions implies that the near-wall modulation effects and scale arrangement are not discerned as clearly as in the smooth-wall flow. The ability of the FM correlation coefficient to only capture the near-wall modulation signature is particularly useful when trying to isolate the modulation effects. For this reason, we consider frequency modulation to be a better metric of inner–outer interactions than amplitude modulation, particularly when the scale separation between the near-wall region and the outer region is not large enough to warrant a clear demarcation between the two in the correlation maps. Flows over roughness and wall-bounded flows at relatively low Re are two common examples where this is true, and FM can be exploited.

3.6 Predictive models of inner–outer interactions in rough-wall boundary layers

As mentioned in section 1.3, much of the interest in investigating inner–outer interactions is the ability to extend such an understanding to greatly improve

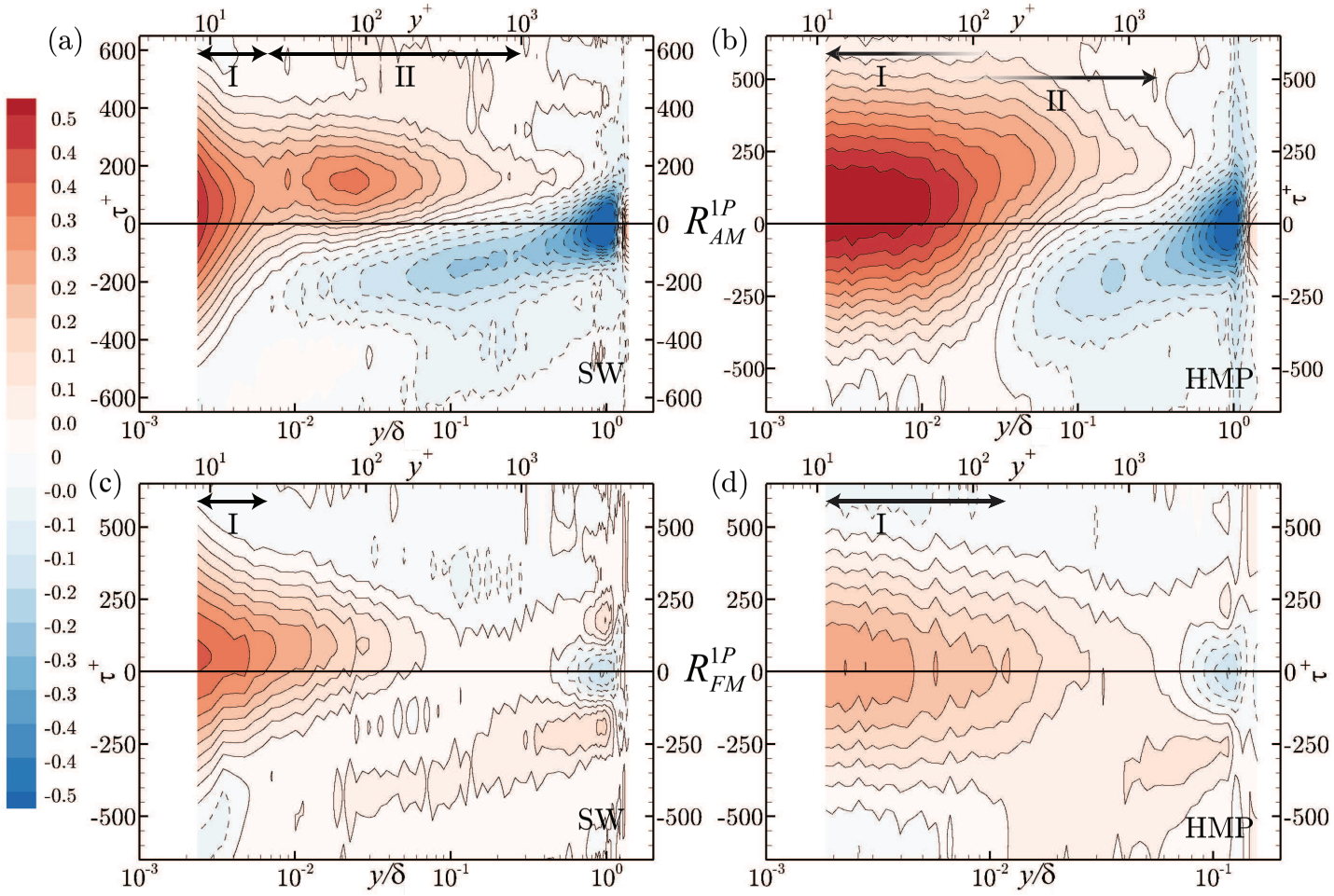

Figure 3.15: 1-probe (a,b) Amplitude and (c,d) Frequency modulation correlation maps of (a,c) smooth- and (b, d) rough-HMP measurements. Visually marked are regions I and II, as defined in section 3.2.1.

the fidelity of high-Reynolds number simulations. This is particularly relevant to the current case, as LES remains the most viable computational tool that can practically be applied for realistic high-Re flows, such as flows over complex roughness. Mathis *et al.* (2011*a*) proposed such a model for smooth-wall flow, where a Re-independent small-scale signal near the wall was extracted via a calibration procedure on multi-hot-wire measurements. The effectiveness and need for modeling the amplitude modulation effects to extract the Re dependence of higher-order statistics was demonstrated in the work. This approach was also extended to wall shear stress by Mathis *et al.* (2013*b*). The model was then further modified by Baars *et al.* (2016) by implementing a linear spectral stochastic estimation of the large-scale superposition on the near-wall flow to more effectively model a scale-dependent superposition of the large scales on the near-wall dynamics. McKeon (2017) used resolvent-mode dynamics to account for the inner–outer interactions, while Sidebottom *et al.* (2014) applied these predictive models in LES simulations of a smooth-wall boundary layer.

More recently, Squire *et al.* (2016) applied the modified model presented in Baars *et al.* (2016) on sand-paper roughness to quantify the amplitude modulation phenomenon on rough walls, and demonstrated the difficulty of extending the models to Reynolds numbers beyond that of the calibration experiment. In the current section, the applicability of these various predictive models on the current boundary layers under study is considered. The models not only quantify the interaction effects, but also shed additional light on the differences between the smooth- and rough-wall dynamics through comparisons of derived quantities (such as transfer functions, structure angles, etc.). For reference, all of the predictive models discussed in current work are limited to modeling only the amplitude modulation phenomenon, and assume the absence of other effects such as frequency and scale modulation.

3.6.1 Inner–outer interaction model (IOIM) using simple superposition

The current two-probe measurements enables us to investigate the applicability of the simple inner–outer interaction model (IOIM, Mathis *et al.* (2011*a*)) for flow over the complex roughness. This model requires information about the inertial-region large scales and the near-wall small scales that are captured simultaneously. The following briefs the method originally developed by Mathis *et al.* (2011*a*), and the reader is referred to that work for more details about the same.

By assuming the existence of a universal inner signal, $u^*(y)$, that complies with autonomous (Re-independent) turbulent production mechanisms, we can write a near-wall, small-scale signal, $\widehat{u}_i(y^+)$, that is only subjected to amplitude modulation and superposition of the outer large scales as

$$\widehat{u}_i(y^+,t^+) = u^*(y^+,t^+)\left[1+\beta(y^+)u_L(y_o,t-\Delta t_s(y^+))\right]+\alpha(y^+)u_L(y_o,t-\Delta t_s(y^+)). \tag{3.10}$$

Here, $u_L(y_o)$ is the large-scale streamwise velocity measured at a location in the logarithmic region while $\Delta t_s(y^+)$ indicates the delay between the detection of the large scales away from the wall and its associated superposition. This delay originates from the fact that the large scales convecting with the flow are inclined relative to the wall in the streamwise direction, and thus their footprint is measured away from the wall (at y_o) by a time Δt_s ahead of its corresponding superposition at $y^+(< y_o)$. This phenomenon can be seen in correlation maps in figure 3.16, and in conditionally-averaged large scales later in section 5.3. Here, $\alpha(y^+)$ indicates the strength of the superposition and $\beta(y^+)$ indicates 'strength[1]' of amplitude modulation, and are considered calibration constants extracted from the 2-probe measurements.

By simultaneously measuring the time series at the 'inner (y^+)' and 'outer (y_o)'

[1]More precisely in current modeling context (as can be seen in step 4 below), β represents the amount by which the measured signal should be de-modulated to 'undo' the modulation observed.

locations, unknown quantities in Eqn. (3.10) can be extracted/estimated with a 'calibration procedure,' where u^*, α and β are extracted to compute the 'inner' time series at any Re_τ of the boundary layer.

1. The inner- and outer-probe measurements of the two-probe experiments performed in the current work can be used to extract the time-series quantities, as $\widehat{u}_i(y^+) \equiv u_i^+(y^+)$ and $u_L(y_o) \equiv u_{oL}^+$ measured by the outer probe, and filtered as in section 3.2, step 1.

2. The superposition coefficient, α, is determined to be the maximum correlation coefficient between the inner large scales, u_{iL}, and the outer large scales, u_{oL}, and thus can be written as

$$\alpha(y^+) = max(R_{iL,oL}(y^+)), \tag{3.11}$$

   where $R_{iL,oL}$ is given by Eqn. (1.4). Further, $\Delta t_s(y^+)$ will be the time delay at which the above maximum in $R_{iL,oL}$ occurs. The $R_{iL,oL}$, maxima α and corresponding Δt_s are shown in figure 3.16 from the two-probe measurements for the smooth-wall case.

3. Using the above steps, the outer signal can then be 'de-trended' to remove the superposition of the outer, large scales on the inner, measured signal, to extract only the universal signal that is amplitude modulated. Thus, the de-trended signal can be written as

$$u_d(t) = u_i(t) - \alpha u_{oL}(t - \Delta t_s). \tag{3.12}$$

4. We define that the 'universal' signal is not amplitude modulated by the outer signal, and that no correlation exists between the large scale amplitude of this universal signal and the large scales themselves. Thus, the universal

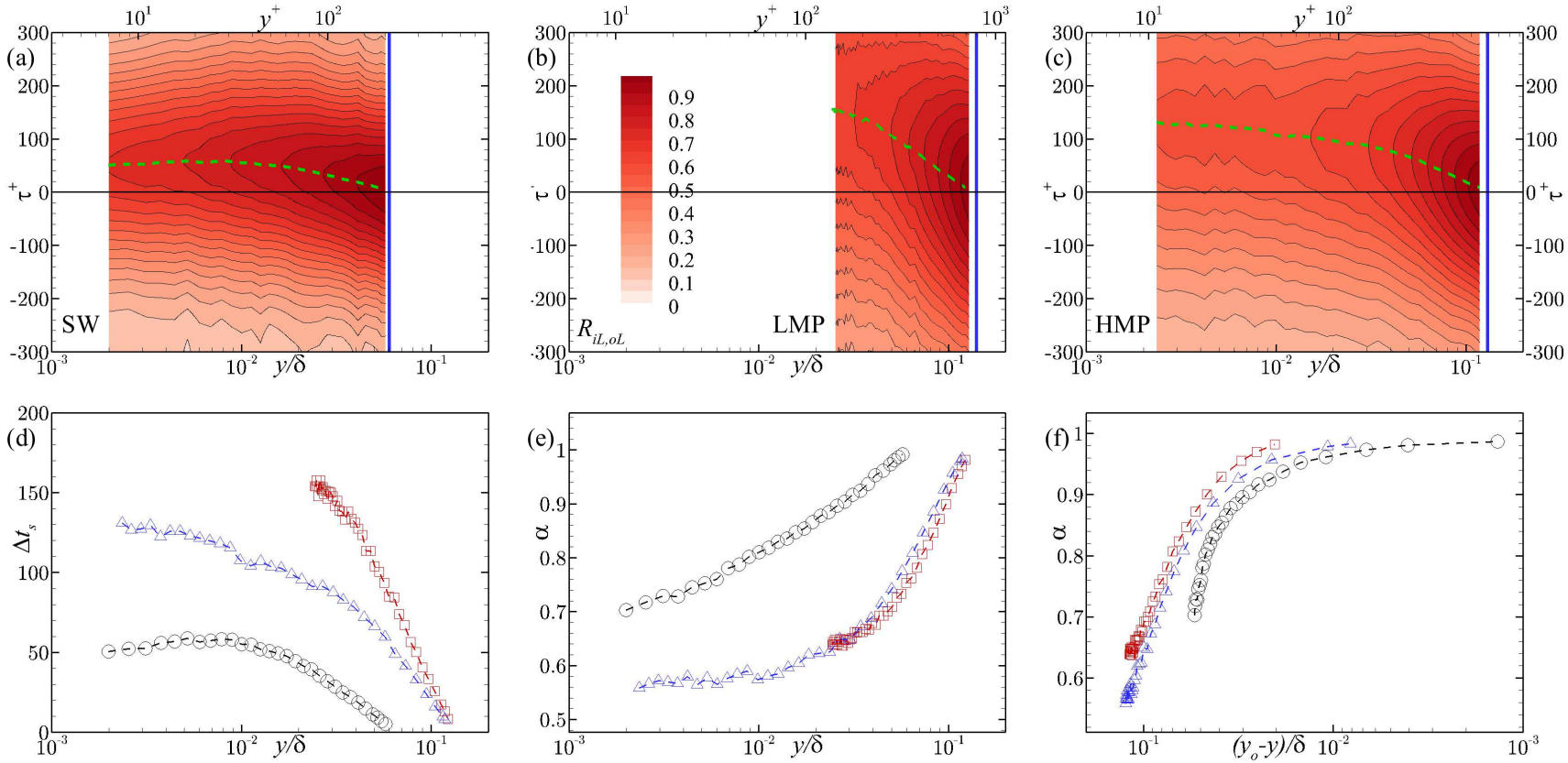

Figure 3.16: (a-c) Contours of $R_{iL,oL}$ for smooth-, rough-LMP and rough-HMP flows. The *dashed* line indicates the superposition delay $\Delta t_s(y^+)$, and *blue* line indicates the location of outer probe. (d) superposition delay, Δt_s. Also shown are superposition constant (α) variation with (e) distance from the wall and (f) relative distance from the outer probe for the three flows. ◯: smooth; □: Rough (LMP); △: Rough (HMP).

signal can be written as

$$u^*(y^+, t^+) = \frac{u_d(y^+, t^+)}{1 + \beta(y^+)u_{oL}(t - \Delta t_s)}, \tag{3.13}$$

where $\beta(y^+)$ is the calibration constant such that

$$R_{E_L[u^*],u_{oL}} = 0. \tag{3.14}$$

This value of β can be obtained by simple iteration procedures.

With a two-probe 'calibration experiment' and above analysis, u^*, α and β can be extended to any Re_τ to *estimate* a 'near-wall time-series' that correctly incorporates the superposition and amplitude modulation effects of outer, large scales measured in the outer region at any Re_τ. Mathis *et al.* (2011*a*) showed that such an estimated time series correctly represents the small-scale energy distribution and statistical properties, such as higher-order moments at least up to 6^{th} order. In fact, accommodating the amplitude modulation and superposition was essential to accurately estimate the statistics from small scales simulated using universal (Re_τ) mechanisms, particularly for the odd-order moments. Importantly, the calibration experiment and the constants thus obtained are only valid to predict the amplitude modulation of large scales sampled at the **same** outer location as that of the calibration experiment. The reader is directed to Mathis *et al.* (2011*a*) for a more detailed explanation of this calibration procedure and its application for smooth-wall flow.

The above methodology was applied to the results of the current experiments to extract the calibration constants for the current flow. Figure 3.16e shows the variation of superposition coefficient α with wall normal distance for the, smooth, rough-HMP and rough-LMP experiments performed. For all wall-normal positions, the superposition is stronger in smooth-wall flow (higher α) compared to the rough-wall cases. The two rough-wall cases show identical variation of α away from the probe. Note that α approaches unity as the two probes approach each

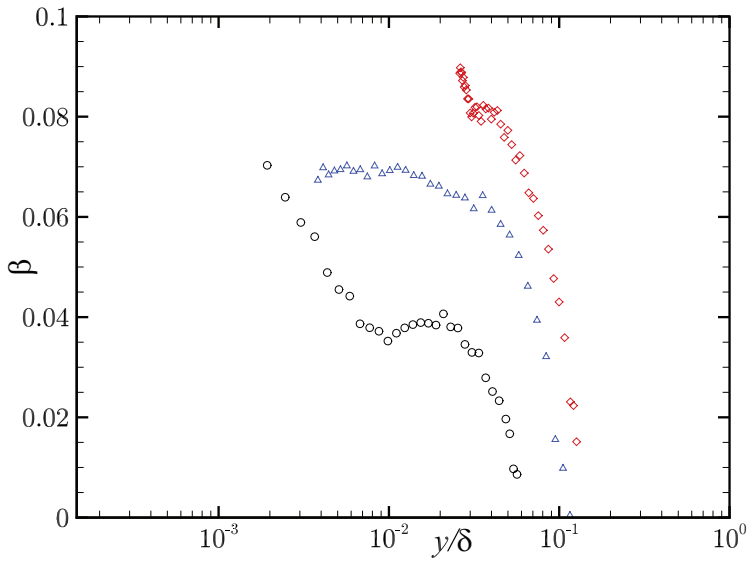

Figure 3.17: Amplitude modulation calibration constant, β, from IOIM (Mathis *et al.*, 2011*a*). ◯: smooth; □: Rough (LMP); △: Rough (HMP).

other, and thus measure identical signals. The difference between the smooth- and rough-wall flows is expected, since, the presence of roughness disrupts the correlations owing to the ability to impart large-scale structures from the roughness organization itself. Figure 3.16f also shows the variation of α with distance from the outer probe. In the neighborhood of the probe, the smooth-wall flow seems to decay slightly faster than the rough-wall cases. This, again, can be explained by the location of the outer probe in smooth-wall flow being physically closer to the wall than in the rough-wall cases.

Figure 3.17 presents the β variation with wall-normal position for the three cases. Surprisingly, the strength of the amplitude modulation as measured by β appears to be stronger for rough-wall flow than the smooth-wall case. Further, the LMP region appears to show higher β values generally than the HMP region. This observation is consistent with the observations in Squire *et al.* (2016). This, though counter-intuitive, was explained in Squire *et al.* (2016) through the QSQH framework, where the modulation phenomena can be viewed as the local change in Re_τ due to large scales (more on QSQH in section 3.7.2). The small-scale modulation in smooth-wall flow occurs through large-scale skin-friction changes,

and can be argued to change as $O(\sqrt{Re_\tau})$. The small scales in rough-wall flow, however, are shed by the roughness, and can respond to large scales as $O(Re_\tau)$, which accounts for a possible stronger amplitude modulation in the latter flow. However, caution must be exercised in drawing conclusions from β, as it effectively represents a calibration constant. In other words, no physical explanation has gone into the deduction of the β values, except the imposition that the demodulated signal must be uncorrelated with the outer, large scales.

3.6.2 Modified inner–outer interaction model (mIOIM) using linear stochastic estimation

It was seen in the previous section that the larger scales must be modeled as a simple linear superposition, with a delay, before the amplitude modulation can be modeled. Baars *et al.* (2016) modified the inner–outer interaction model using spectral linear stochastic estimation (sLSE) for scale-dependent linear superposition of large scales, and referred to as the 'modified inner–outer interaction model (mIOIM)'. We apply the modified inner–outer interaction model to gain clearer insight into these interactions for rough-wall flow.

The simple IOIM discussed in the previous section assumes that all energy components of the large scales (i.e., all structures $\lambda > \lambda_c$) superimpose identically on the inner region, with a specified delay Δt_s and super position constant α. Given the evidence that the large scales linearly superpose, one can consider this as a single-input, single-output operation and develop a scale-dependent transfer function between the various components of the large scales that superimpose (Bendat & Piersol, 2011). Thus, the outer scales (u_o) and the inner scales (u_i) can be written as

$$u_i = h_L * u_o + NLT, \tag{3.15}$$

where h_L is the transfer function of all linear physics, '$*$' is the convolution operator in time, and the NLT is the cumulative effect of all non-linear terms and estimation errors. "Linear stochastic spectral estimation" is the process of esti-

mating the optimal transfer function to minimize the NLT-term in Eqn. (3.15). Baars *et al.* (2016) implemented this idea for the IOIM and more details of the spectra stochastic estimation can be found in Bendat & Piersol (2011). The current work follows Baars *et al.* (2016) in implementing the same.

A few advantages of the sLSE over IOIM discussed before are immediately evident from Eqn. (3.15). First, the complex-valued transfer function, h_L, accounts for both the coefficient and phase of superposition. Thus, the calibration constants α and Δt_s in the previous section can be reduced to a single complex function, h_L. Here, h_L embodies far more information about the linear superposition than just the constants Δt_s and α, and captures the same for all linearly superposing scales individually (scale dependent superposition constants). Most importantly, the magnitude of h_L automatically accommodates the cut-off filter to isolate the superimposing scales without a need for assumptions in λ_c (i.e., u_i and u_o time series can be used instead of u_{iL} and u_{oL}).

Using Eqn. (3.15), the expressions for linearly superposing scales and the amplitude modulation relation in Eqn. (3.10) can be rewritten as

$$u_S(y^+) = h_L(t^+; y^+) * u_o, \tag{3.16}$$

$$\widehat{u}_i(y^+, t^+) = u^*(y^+, t^+)\left[1 + \Gamma(y^+)u_S(t^+)\right] + u_S(t^+), \tag{3.17}$$

where u_S represents the superposed scales, and Γ and h_L are the new calibration constants. For two measured signals, u_o and u_i, the transfer function h_L can be obtained in Fourier space as a normalized cross-spectrum of the two signals, given as

$$H_L(f^+) = \frac{\hat{U}_i(f^+)\overline{\hat{U}_o(f^+)}}{\hat{U}_o(f^+)\overline{\hat{U}_o(f^+)}}, \tag{3.18}$$

where $H_L(f^+)$, $\hat{U}_o(f^+)$ and $\hat{U}_i(f^+)$ are the Fourier space representations of $h_L(t^+)$, $u_o(t^+)$ and $u_i(t^+)$ respectively, and overbar (only in the above equation) implies complex conjugate of that term. The magnitude, $|H_L(f^+)|$, and phase, $\Theta(f^+)$, of the transfer function indicate the coefficient (or 'gain') of superposition and

'delay' in superposition of the component corresponding to f^+.

Figure 3.18 shows the magnitude and phase of the transfer function for the smooth-wall case between the outer probe and the inner probe at one wall-normal position. The transfer function of the large scales ($\lambda_x > 10^4$) indicates the coherence with a well-converged coefficient. The incoherence of the small scales can be seen with smaller gain and with the neighboring scales being vastly uncorrelated as seen by the unconverged values of gain and phase. A 'smooth' version of the filter ($\tilde{H}_L$) can then be designed from this result to represent the effect of linear superposition as shown, following the original work of Baars *et al.* (2016). To do this, the scale location where the gain rolls below a value of 0.05 was chosen, and an exponential decay to the gain was enforced for all scales smaller than the located scale. Doing so ensures that uncorrelated noise at the small scales does not transfer between the two signals, and that only coherent large scales are compensated for in Eqn. (3.17). The corresponding phase is not changed since the components are premultiplied with diminishing the gain. The smoothed filter $\tilde{H}_L$ is also shown in figure 3.18. The sharp cut-off filter $\lambda_c = 7000$ used in the previous section has also been marked.

The justification and the crudeness of the IOIM in section 3.6, and the advantages of mIOIM, can clearly be seen. The scale-dependent gain captures the superposition much more efficiently than the sharp cut-off filter, with the latter under-compensating for the large-scale fluctuations and over-compensating for the small-scale fluctuations. Further, coherent motions at $\lambda^+ < \lambda_c^+$ indicated in figure 3.18 are considered small scales in the simple IOIM model. More details of how this translates on the time series and the effects are presented in the original work of Baars *et al.* (2016). Using this stochastic filter, the detrended signal and the new amplitude modulation coefficient, Γ, can be computed using the same techniques as in section 3.6.1. Finally, by comparing Eqns. (3.10) and (3.17), the equivalency of Γ and ratio β/α is evident.

This modified inner–outer interaction model has been applied to the current smooth- and rough-wall cases. Figure 3.19 shows the variation of the amplitude

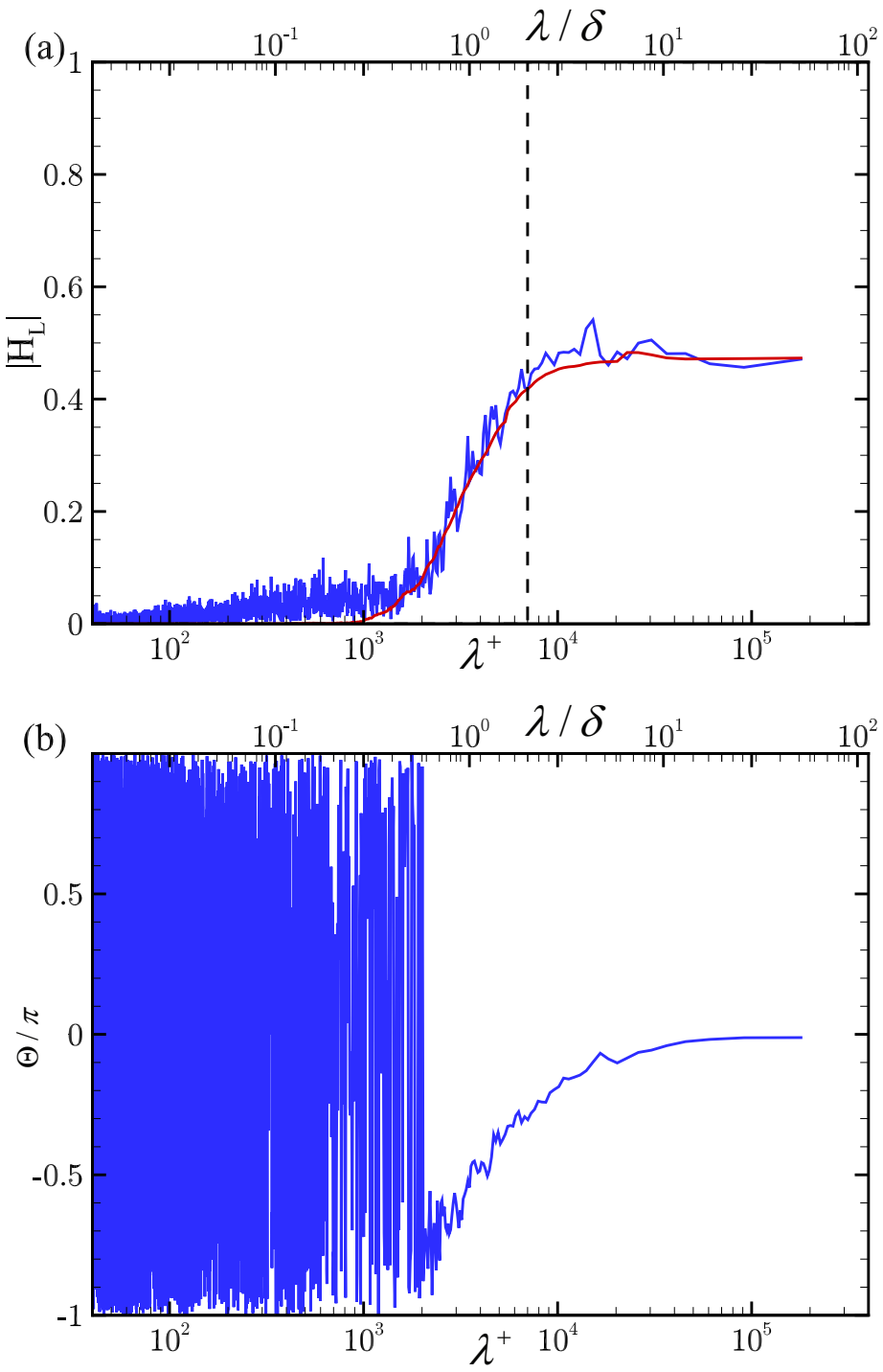

Figure 3.18: (a) Magnitude of raw transfer function ($|H_L|$, *blue*) and filtered transfer function ($\tilde{H}_L$, *red*). (b) Argument of transfer function (Θ). Signals were sampled for smooth-wall flow at $y^+ = 7$ and *dashed* line indicates $\lambda_c^+ = 7000$.

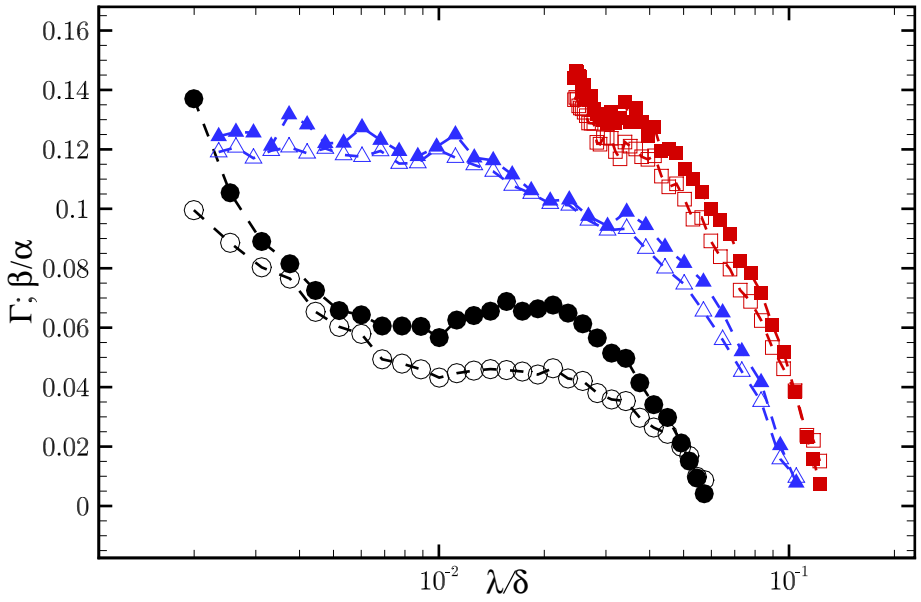

Figure 3.19: Modulation constants Γ (*filled*) estimated from mIOIM and β/α (*open*) estimated in section 3.6.1. ◯: smooth; □: Rough (LMP); △: Rough (HMP).

modulation coefficient, Γ, compared with β/α. It can be seen that correcting the superposition using sLSE enhances the value of β very close to the wall and in the inertial region. For the rough-wall flows, while the sLSE yields a higher value for Γ in LMP region, the difference is smaller with HMP region.

Further, figure 3.20 show the contours of H_L, indicating the structure of linear superposition in the smooth- and rough-wall cases at various wall-normal locations. The effect of roughness on disrupting the superposition is evident, where the gain ($|H_L|$) decreases close to the wall in the rough-wall cases. Further, superposition in smooth-wall flow extends to smaller scales than in the rough-wall cases and tapers off gradually, where only the largest of the scales are coherent in the latter. The contours of $|H_L|$ also show that cut-off filter chosen for IOIM ($\lambda_c = 7000$) is more appropriate for HMP region than it is for LMP or smooth-wall flow. This partly explains on how the β/α and Γ in figure 3.19 values are more identical in HMP region, than LMP region or in smooth-wall flow.

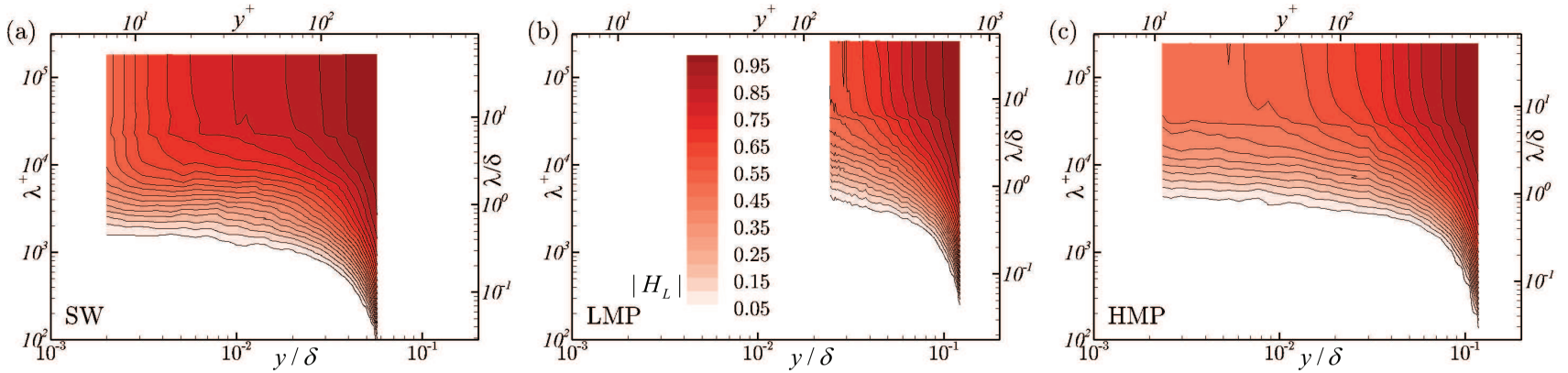

Figure 3.20: Contours of large scale superposition gain ($|H_L|$) at various wall-normal locations and wavelengths for (a) smooth- (b) rough-LMP and (c) rough-HMP regions.

Concluding, the IOIM and mIOIM indicate the strengths of superposition and amplitude modulation in smooth- and rough-walls. Both methods indicate an increased strength of amplitude modulation in rough-walls and more so in LMP compared to HMP. mIOIM further elucidated the superposition at various scales, and as expected in the rough-wall cases, only the larger scales superposed on the near-wall region while the smaller scale superposition was disrupted by the roughness. These observations reemphasize the importance of these phenomena in rough-wall boundary layers.

3.7 On the applicability of QSQH theory to the rough-walls

With the amplitude and frequency modulation of the small scales in high-Re flows established in both the smooth- and rough-wall cases, physical interpretations of the same can be attempted. Hutchins (2014) presented an explanation that the 'fast' small scales can be viewed to be operating in a quasi-steady environment under the influence of the relatively 'slow' large scales. This idea is referred to as *Quasi-steady, quasi homogenous (QSQH)* hypothesis. This is possible because the small scales evolve with the inner temporal and spatial scales of the order $\sim O(t^*)$ and $\sim O(y^*)$, while the outer scales evolve as $O(\delta/U_\infty)$ and δ, respectively. With a sufficiently large scale separation (i.e., high Re), the latter evolve on much larger scales and much slower than the near-wall, small scales. Thus, the small scales perceive the large scales as a *slowly varying local Reynolds number*, and quickly $[O(t^*)]$ adapt to the same, resulting in the modulation interactions. This behavior can be seen in the work of Hutchins *et al.* (2011), who found that the the boundary layer averaged with large-scale shear stress fluctuations supports such a picture. Agostini & Leschziner (2016) also investigated this notion using conditional averages based on DNS data. McKeon (2017) provided an explanation for these physics using resolvent mode analysis, while Keylock *et al.* (2016) evaluated the same using a Hölder exponent framework.

Zhang & Chernyshenko (2016) and Chernyshenko *et al.* (2012) provided a mathematical framework for this notion of 'quasi-steady, quasi homogenous' theory of inner–outer interactions. The universal nature of the near-wall physics is assumed, but a slowly varying Re is formulated as a slowly varying skin-friction coefficient that then dictates the near-wall turbulence scales. The first- and second-order perturbations in subsequent physics under these assumptions were then derived. More details about this idea can be found in the original works of Zhang & Chernyshenko (2016) and Chernyshenko *et al.* (2012).

The current study explores the application of this theory to the rough-wall cases in the current work. The premise of this analysis is that the QSQH theory, as formulated in previous research, does not assume a nature of the near-wall dynamics. Instead, it merely assumes the presence of an otherwise universal small-scale structure, and one that is subjected to lower-order influences imparted by the presence of the large scales. Thus, the evolution of the small scales, irrespective of their origin, could still be described by the theory. This premise is tested in the current section. The ideas behind this theory are briefly described below, though the full details can be found in Zhang & Chernyshenko (2016).

3.7.1 QSQH theory - an overview

An overview of the QSQH theory originally developed in Zhang & Chernyshenko (2016) and Chernyshenko *et al.* (2012) is presented here. The QSQH theory formulates the Re effects of the large scales as large-scale variation of the local skin friction. The classical theory of near-wall universality assumes that the wall skin friction (along with other near-wall quantities) can be written as

$$\tau_w = \overline{\tau}_w \tau_w^+(t^+, x^+, z^+), \tag{3.19}$$

where the superscript + indicates normalization with the mean skin friction coefficient ($\overline{\tau}_w$), kinematic viscosity (ν) and density (ρ). This universal formulation

assumes that τ_w^+ is Re-independent, with a unit mean. This 'universality' is modified in the QSQH theory to a quasi-steady universality, where the same holds in a quasi-steady sense for an imposed large scale variation in $\overline{\tau}_w$ as $\tilde{\tau}_L$ by the outer dynamics. Thus, Eqn. (3.19) can then be rewritten under quasi-steady assumption as

$$\tau_w = \tilde{\tau}_L(t)\tau_w^+ \left(t^+ \frac{\tilde{\tau}_L(t)}{\overline{\tau}_w}, x^+ \sqrt{\frac{\tilde{\tau}_L(t)}{\overline{\tau}_w}}, z^+ \sqrt{\frac{\tilde{\tau}_L(t)}{\overline{\tau}_w}} \right). \tag{3.20}$$

The quasi-steady formulation thus assumes the presence of a universal, Re-independent function τ_w^+, which now describes the actual wall friction, τ_w, with slowly-varying dependent variables and the amplitude. Further, the theory also implies that normalization of near-wall velocity fluctuations using the slowly-varying skin friction $\tilde{\tau}_L$ instead of $\overline{\tau}_w$ results in a universal formulation. Thus, the velocity counterparts of classical universality and quasi-steady universality can be written similarly as

$$u = \sqrt{\frac{\overline{\tau}_w}{\rho}} u^+(t^+, x^+, z^+), \qquad \text{[Classical universality]} \tag{3.21}$$

$$u = \sqrt{\frac{\tilde{\tau}_L(t)}{\rho}} u^+ \left(t^+ \frac{\tilde{\tau}_L(t)}{\overline{\tau}_w}, x^+ \sqrt{\frac{\tilde{\tau}_L(t)}{\overline{\tau}_w}}, y^+ \sqrt{\frac{\tilde{\tau}_L(t)}{\overline{\tau}_w}}, z^+ \sqrt{\frac{\tilde{\tau}_L(t)}{\overline{\tau}_w}} \right).$$

[Quasi steady universality] (3.22)

Note that τ_w and $\tilde{\tau}_L$ are total quantities and not fluctuating quantities. Also note the presence in Eqn. (3.22) of not only amplitude modulation of velocity components, but also scale and frequency modulation in the three spatial coordinates. By decomposing the large-scale skin friction variation ($\tilde{\tau}_L$) into mean ($= \overline{\tau}_w$) and fluctuations (τ_L'), Eqn. (3.20) can be rewritten as

$$\frac{\tau_w'}{\overline{\tau}_w} = \left(1 + \frac{\tau_L'}{\overline{\tau}_w} \right) \tau_w'^+ + \frac{\tau_L'}{\overline{\tau}_w}, \tag{3.23}$$

where $\tau_w'^+$ represents fluctuations of the universal function τ_w^+. This equation describes the amplitude modulation and superposition of the wall skin-friction

coefficient, and is similar to the formulation of the same by outer large-scale velocity fluctuations by Mathis *et al.* (2013*b*) given as

$$\frac{\tau_w'}{\overline{\tau}_w} = \left(1 + \beta_\tau u_{oL}^+\right) \tau_w'^+ + \alpha_\tau u_{oL}^+. \tag{3.24}$$

Thus, this implies that, for the above formulation to hold,

$$\alpha_\tau = \beta_\tau, \tag{3.25}$$

$$\frac{\tau_L'}{\overline{\tau}_w} = \alpha_\tau u_{oL}'^+. \tag{3.26}$$

The first condition was found to be valid experimentally, with Mathis *et al.* (2013*b*) reporting $\alpha_\tau = 0.0898$ and $\beta_\tau = 0.0867$. The second relation provides a method to actually apply the current theories by measuring the outer, large-scale velocity signature, and without directly measuring the large-scale variations in the skin friction. In fact, α_τ is the coefficient that relates the large-scale velocity footprint in the outer region to its corresponding skin friction footprint at the wall. Thus, it is a function of the outer location (y_o^+) where the large scales are measured, and not universal.

Extending the above analysis to the velocity components in Eqn. (3.22), and by expanding as a Taylor series for small perturbations, Chernyshenko *et al.* (2012) reduced the relation in the form of the superposition–amplitude modulation formulation presented earlier as Eqn. (3.10). This, relation, after truncating to first-order terms in large-scale velocity fluctuations, gives

$$\alpha(y^+) = \frac{1}{2}\left(U^+(y^+) + y^+ \frac{\mathrm{d}U^+(y^+)}{\mathrm{d}y^+}\right) \alpha_\tau, \tag{3.27}$$

$$\beta(y^+) = \frac{1}{2}\left(1 + \frac{z^+}{u_{rms}(y^+)} \frac{\mathrm{d}u_{rms}(y^+)}{\mathrm{d}y^+}\right) \alpha_\tau. \tag{3.28}$$

Chernyshenko *et al.* (2012) made one further simplification by filtering the relation for u-modulation and, for an outer velocity time series that is measured within

the log region, obtained

$$\alpha_\tau = \frac{2}{\left(U^+(y^+) + y^+ \frac{\mathrm{d}U^+(y^+)}{\mathrm{d}y^+}\right)_{y^+=y_o^+}}. \tag{3.29}$$

Further, if the outer probe is in log region, the logarithmic velocity profile can be used to reduce the above expression further to

$$\alpha_\tau = \frac{2}{\left(\frac{1}{\kappa}\ln y_o^+ + C + \frac{1}{\kappa}\right)_{y^+=y_o^+}}. \tag{3.30}$$

Using, Eqns. (3.27),(3.28) and (3.29), the superposition and modulation constants can be estimated.

3.7.2 Current experiments and QSQH predictions

The two-probe measurements from the smooth-wall flow are first used to compute the theoretical values of the superposition and amplitude modulation constants, α and β. The same can be compared to the values obtained in section 3.6.1 via the calibration procedure. Figure 3.21 shows the modulation constant, α_τ, of the smooth-wall flow from Eqn. (3.29), along with the theoretical variation as described by Eqn. (3.30). The agreement between the two in the log region is unsurprising, as both are measures of the velocity profiles in this region. This agreement is a manifestation of the profiles seen earlier in section 2.8. However, as can be seen in Eqn. (3.29), the α_τ value heavily depends on the gradient of the velocity, and thus is susceptible to noise in the same. The velocity gradients, when the two measuring probes are close to each other, are particularly susceptible to errors in the relative position of the probes, as can be seen in the value of α_τ. Thus, for the current analysis α_τ is chosen as the theoretical value at the location of the outer probe for the smooth-wall case, instead of the local gradient-based metric. The trends shown in figure 3.21 justify the same. Figure 3.22 further shows the variation of α and β values from the current theory to that from the

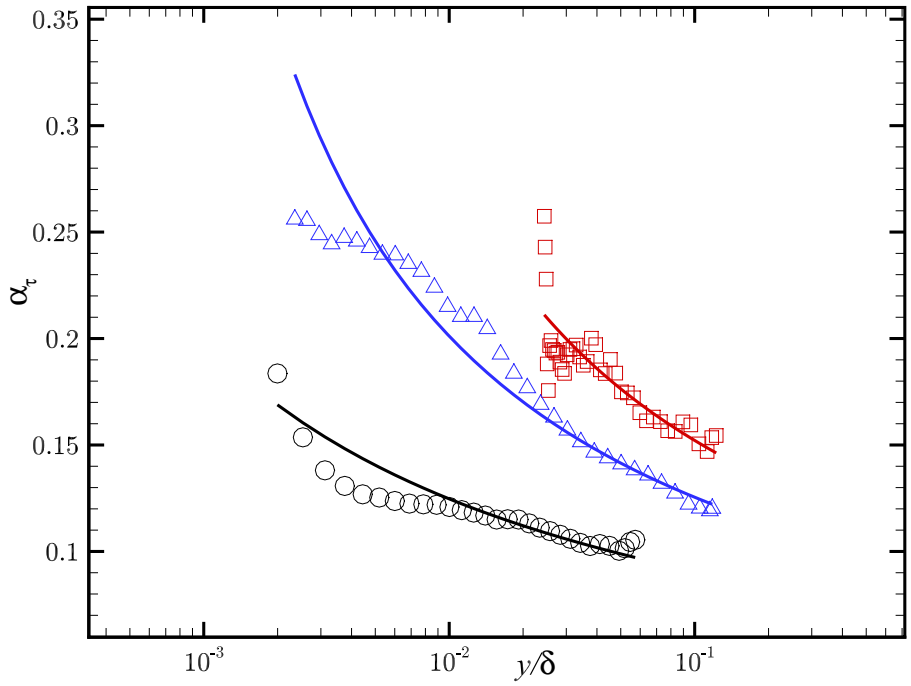

Figure 3.21: Comparison of α_τ for smooth- and rough-wall cases between the theoretical Eqn. (3.29) and from mean profiles Eqn. (3.30). ◯: smooth; □: Rough (LMP); △: Rough (HMP).

inner–outer interaction model. Also shown are comparisons of the coefficients Γ from the modified model in section 3.6.2, with the theoretically predicted β/α. It can be seen that the QSQH model predicts the values of superposition and modulation constants very well for the smooth-wall flow. The predictions of α very close to the wall are under predicted. It must, however, be recognized that the gradients in mean velocity and streamwise turbulence required to compute α and β are susceptible to larger errors in accurately measuring the wall position.

For the rough-wall cases, figure 3.21 also indicates the α_τ variation for LMP and HMP regions. The theoretical form of the equation for the skin friction modulation constant, α_τ was adjusted for the net momentum loss (roughness function, ΔU^+) due to roughness, by adjusting Eqn. (3.30) as

$$\alpha_\tau^{RW} = \frac{2}{\left(\frac{1}{\kappa}\ln y_o^+ + C - \Delta U^+ + \frac{1}{\kappa}\right)_{y^+=y_o^+}}. \tag{3.31}$$

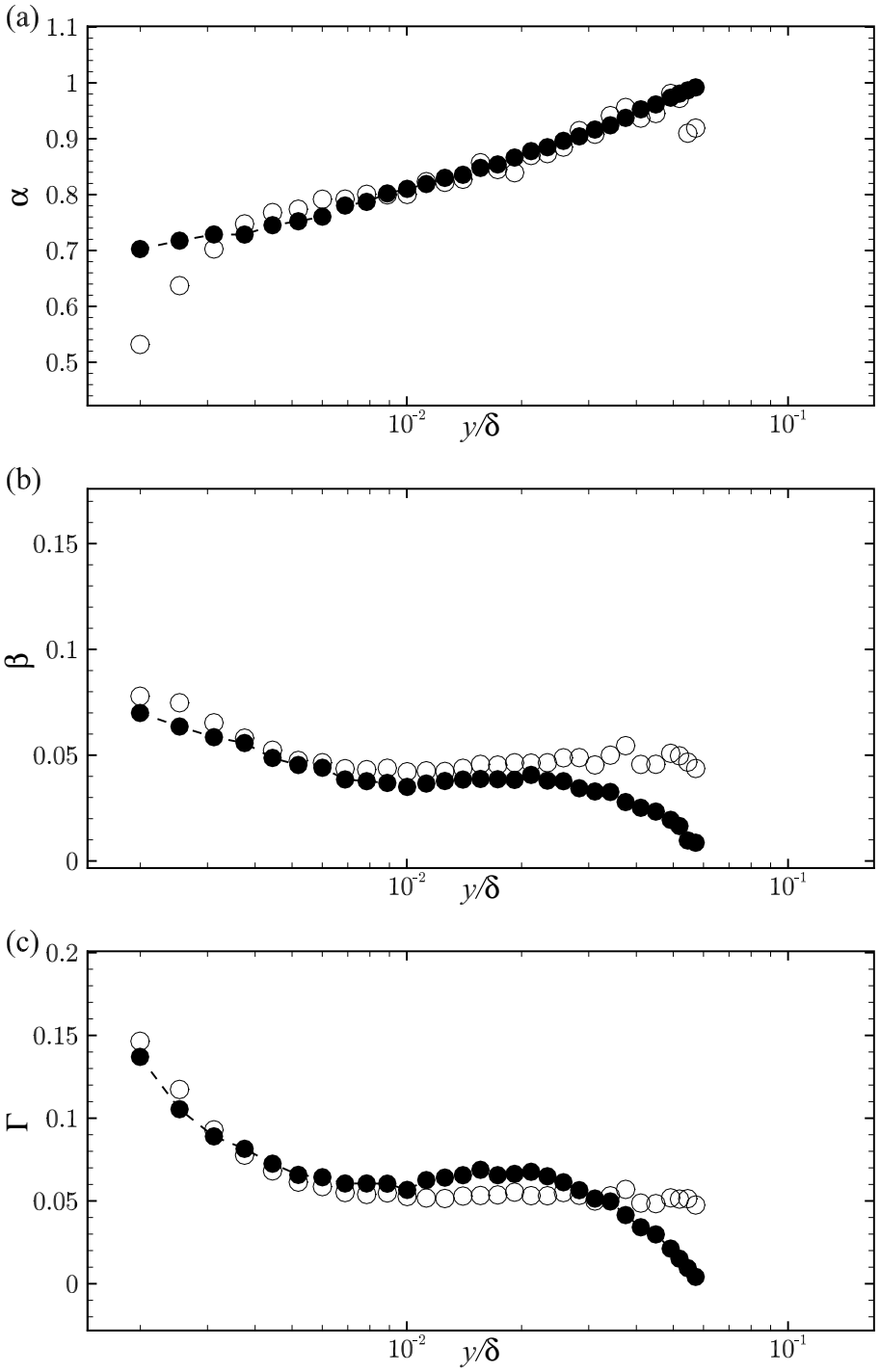

Figure 3.22: Calibration constants for smooth-wall flow (a) α, (b) β and (c) Γ estimated from current QSQH theory (*open*), IOIM (*closed*, α and β) and mIOIM (*closed*, Γ).

Figure 3.23 shows the predicted values of α, β, Γ and those of the estimated values using the predictive model in the rough-LMP region. The estimation of the superposition constant seems to be overestimated by the QSQH theory compared to the estimate from the correlations. However, the prediction of β and Γ seem to be very close to those predicted from the model, adding credibility to the hypothesis even in rough-wall flows. The estimates are noisy for this case close to the roughness due to associated fluctuations in gradients of velocity and streamwise turbulence. Figure 3.24 shows the various constants for the rough-HMP region. Similar to the Rough-LMP location, the model appears to better predict β, rather than α. Excellent agreement, however, seems to be present between the ratio β/α and Γ.

Before drawing conclusions from the above observations, a few important aspects must be considered. First, the estimation of constants α and β from the QSQH hypothesis involves calculations involving gradients of mean velocities and velocity rms. Thus, any errors in the same or in the wall-normal position propogate into the measures. These errors in spatial gradients are particularly severe in point-wise measurements such as with hot-wires, where each measurement is independent to the one at a neighboring location. Further, the estimation of gradients from the rms velocity is also affected from the small-scale averaging due to the size of the hot-wire sensor ($l^+ = 37$ in the current experiments). This averaging is particularly severe in smooth-wall measurements very close to the wall ($y^+ < 20$), where the near-wall gradients in rms velocities are greatly affected. This should, however, be less severe in the rough-wall cases, as the energy spectra do not indicate significant energy at the smaller scales (figure 3.2). Finally, note that opposite errors in estimation of α and β could cancel out, giving a better estimate of Γ. While the merit of the QSQH theory should be evaluated by comparing α and β individually, Γ has the advantage of canceling the effects of α_τ, and thus the assumption that the large scale velocity–skin friction interactions are identical between the smooth- and rough-wall cases. In other words, in rough-wall flows, there is no proof *a priori* that the large scales superpose and modulate the

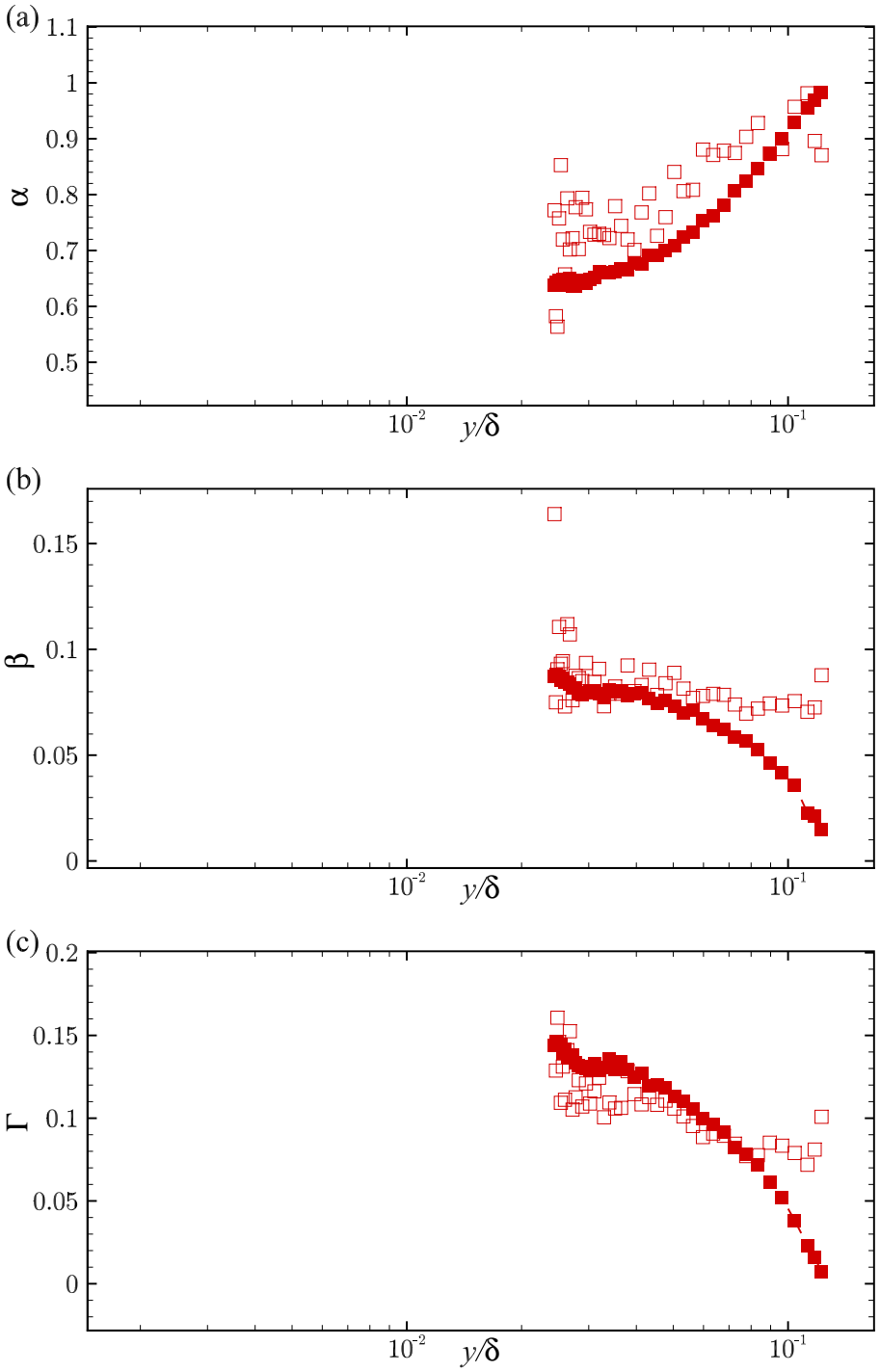

Figure 3.23: Calibration constants for rough-LMP flow (a) α, (b) β and (c) Γ estimated from current QSQH theory (*open*), IOIM (*closed*, α and β) and mIOIM (*closed*, Γ).

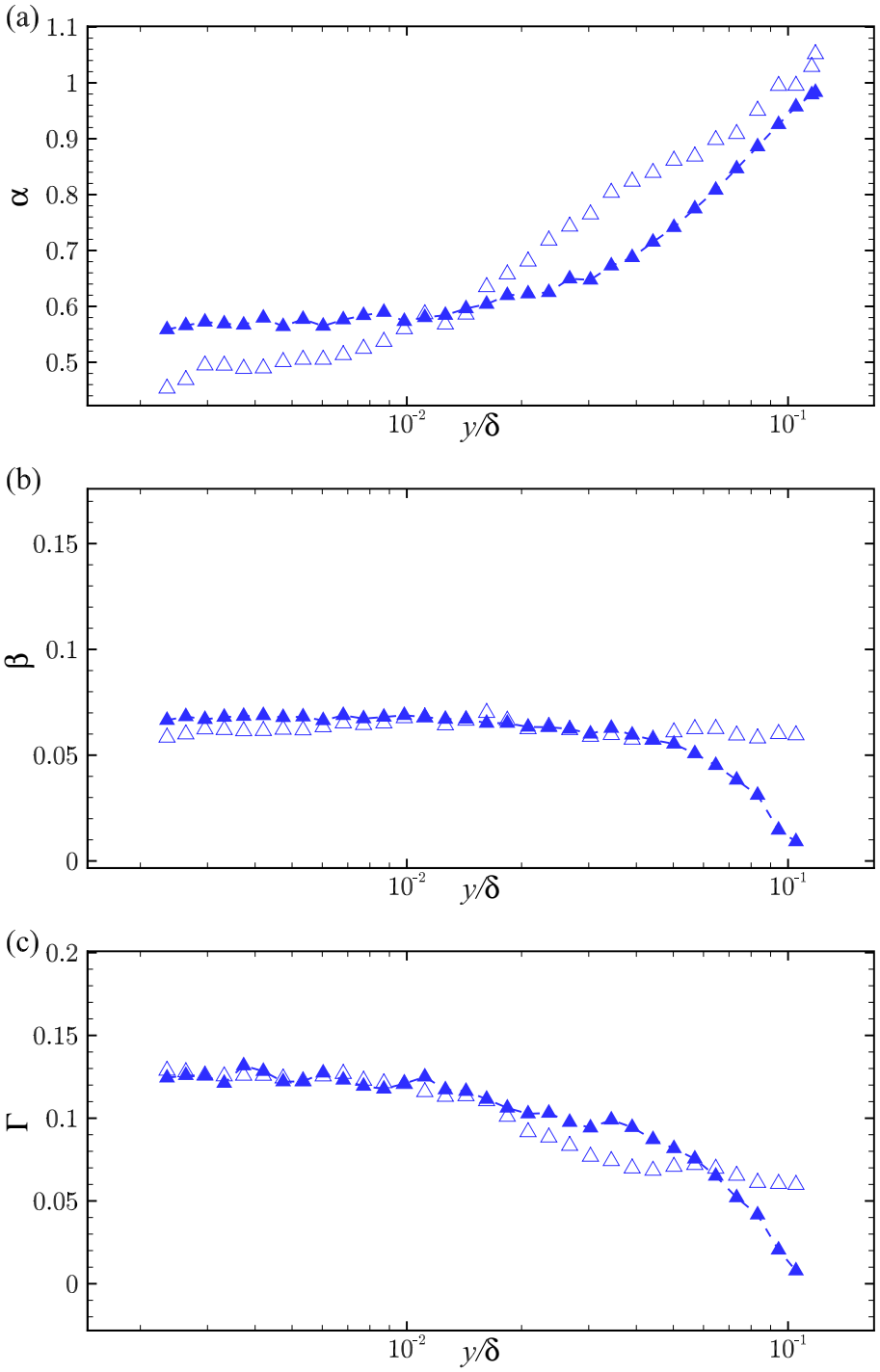

Figure 3.24: Calibration constants for rough-HMP flow (a) α, (b) β and (c) Γ estimated from current QSQH theory (*open*), IOIM (*closed*, α and β) and mIOIM (*closed*, Γ).

skin friction as given by Eqn. (3.23), thus justifying a constant α_τ. Comparisons of β/α and Γ would bypass this assumption, and might be more appropriate for the rough-wall cases.

The QSQH theory does not make any assumptions as to the mechanisms of the inner region. The only requirement is that the inner region small scales respond in a quasi-steady framework as described by the Eqn. (3.22), and that a linear filter exists that satisfactorily separates the two scales. More importantly, for the theory to be applicable to rough-wall flow, along with the assumptions that form the theory for smooth-wall flows, an additional assumption must be made in order to apply the theory as is–namely, that the 'skin friction' modulation mechanism [Eqns. (3.23) and (3.24)] by the outer large scales over the roughness is identical to that of the smooth-wall flow. This additional criterion is not obvious in most rough-wall cases, and depends on the dynamics of the roughness sublayer. This would require development of a roughness-dependent Eqn. (3.29). In fact, in fully-rough boundary layers, viscous effects are clearly not the dominant mechanism of the near-wall region, and a hybrid normalization based on the roughness scales would be necessary that can diminish or enhance the effect of skin friction. For this reason, the lack of better agreement between the predicted and measured α for rough-wall flow is unsurprising.

The reasonable agreement in the metrics of α, β and Γ indicates that similar mechanisms of modulation exist between the smooth- and rough-wall flows, at least in the roughness studied herein. Compensating for the hot-wire spatial resolution issues, including the higher-order terms in the QSQH-estimation (Zhang & Chernyshenko, 2016), and development of superior filters to separate the small and large scales could all potentially improve the predictions of QSQH theory. It can be said from the current observations that this theory provides a potential explanation that could also satisfactorily explain the inner–outer interactions in a rough-wall flow.

Summarizing the findings from Part-I of the current research, it can thus be said that the inner–outer interactions are a dynamically important phenomena in flows over rough-walls, even more so than the smooth-walls. As AM and FM correlations were investigated, not only is their presence evident, but the similarities in structure of interactions between the smooth- and rough-walls is also striking. Further investigation of the models deduced calibration constants that indicate a stronger amplitude modulation in rough-walls compared to the smooth-wall turbulent boundary layers. Finally, the QSQH hypothesis made predictions of the calibration constants that agreed well with those estimated from the measurements. This tended additional support to the identical action of the outer-layer structures between the two wall conditions. With this understanding the following Part-II of current research aims to corroborate the present findings using a spatio-temporal analysis using high frame-rate PIV.

CHAPTER 4

PART-II: EXPERIMENTS IN REFRACTIVE INDEX-MATCHED FACILITY

The Part-II of the current research aims at investigating the modulation interactions discussed thus far using high-frame-rate PIV. Independent experiments are designed and performed to best capture the dynamics of the interactions, based on the understanding from Part-I experiments. Particularly, we use the technique of refractive index-matching (RIM) to conduct these experiments. In most PIV experiments in wall-normal measurement planes over wall-bounded flows ($x-y$ or $y-z$ planes), strong reflections close to the boundary corrupt near-wall flow measurements. The presence of wall-roughness exacerbates this issue, due to the stronger reflections associated with a more complex topography. This issue is particularly crippling to investigate inner–outer interactions in conventional wind- and water-tunnel facilities with PIV, since much of the modulation interactions occur very close to the wall, meaning measuring velocities very close to the wall is crucial. We thus use the Refractive index-matched (RIM) flow facility at the University of Notre Dame to mitigate these issues, and successfully capture the modulation effects in both smooth- and rough-wall turbulent boundary layers with PIV for the first time.

Matching the optical refractive index between a flow model and the working fluid is a common technique used when the presence of solid boundaries in the model or boundaries impedes laboratory flow measurements. Such difficulties could be due to lack of optical access, or, when internal flows are considered, due to refraction of fields of view by the interface. Various working fluids can be used for matching the refractive index of models, such as mineral oils (Stoots *et al.*, 2001), glycerol (Shida *et al.*, 2011), sodium iodide (Chen, 1991; Hong *et al.*,

2011, etc.), etc., and their mixtures. Budwig (1994) provides a comprehensive review of the RIM technique. Similar to the current study, Hong *et al.* (2011) used refractive index-matching using sodium iodide to investigate the near-wall structure of a rough-wall flow. The current study applies similar techniques to better understand the effects of roughness on the near-wall turbulent production cycle in smooth- and rough-wall turbulent boundary layers.

The following sections in this chapter provide the details of the experimental facility and basic flow characteristics, while the chapter following explores the physics of these interactions.

4.1 Challenges in studying inner-outer interaction using PIV

As discussed earlier in section 1.2, the dynamic range in spatial and temporal scales of high-Re turbulence poses significant challenges in both computational and experimental research. Consider the smooth-wall turbulent boundary layer developed in a wind tunnel and analyzed using hot-wire anemometry in chapter 3. The smallest scales were of the order $\sim 25\,\mu m$ and the largest scales were of the order $\sim 1\,m$, while the smallest and largest time scales are of the orders $\sim 50\,\mu s$ and $\sim 100\,ms$, respectively. To have a complete spatio–temporal measure of such a boundary layer using planar PIV, one requires cameras with resolutions of order $\sim 100,000 \times 100,000\,\mathrm{px}^2$ that can acquire images at $\sim 10\,kHz$. These requirements are prohibitively impractical, not only in terms of technology required, but also the data processing and post-processing capabilities that such a data management would demand. These limitations further highlight the abilities of hot-wire anemometry in studying high-Re boundary layers via a high dynamic range, albeit point-wise, measurements. It is thus evident that replicating high-frame-rate PIV as an equivalent array of hot-wire sensors is highly impractical.

The investigation of inner–outer interactions via PIV poses further challenges. As seen in earlier experiments, and in Part-I of the current work, much of the

turbulent modulation occurs close to the wall ($y^+ \sim 20 - 50$) where small scales are rich and can respond to the larger scales in a quasi-steady, quasi-homogenous sense. With increasing Re, for a given physical experimental facility, this inner region occupies an increasingly smaller physical extent in the boundary layer. For example, in a boundary layer that is $\sim 100\,mm$ thick, at $Re_\tau \approx 2000$, the near-wall peak in $\langle u^{2+} \rangle$ is physically located around $\sim 750\,\mu m$. The same dynamics in $Re_\tau \approx 4000$ in the wind-tunnel facility, the turbulent peak moves to $\sim 370\,\mu m$. While this can be measured easily with a typical hot-wire sensor given the extremely small sensor sizes ($\sim 2 - 5\,\mu m$) relative to the boundary-layer structures, it is extremely difficult to resolve the same with a typical PIV interrogation window of $\sim 200\,\mu m$. Further, PIV involves volumetric averaging over a much larger volume [typically $O(100\,\mu m) \times O(100\,\mu m) \times O(1\,mm$ in sheet thickness)], which causes significant attenuation of small-scale energy compared to hot-wire sensors [typically $O(5\,\mu m) \times O(5\,\mu m) \times O(1\,mm$ in wire length)]. For this reason, PIV performs best in resolving small-scale energy in streamwise–wall-normal configuration (where bulk-averaging, $O(1\,mm)$, occurs in spanwise direction), compared to streamwise–spanwise or spanwise–wall-normal planes (where bulk averaging, $O(1\,mm)$, occurs in spanwise or streamwise directions respectively). Decreasing the Re_τ does not necessarily alleviate this issue, as the associated inner–outer interactions also become increasingly weaker at lower Re (Mathis *et al.*, 2009*a*, 2011*b*). Beyond issues of spatial resolution, PIV suffers from other challenges when one tries to measure too close to the wall, such as low seeding density and correlation biases due to high shear in the flow as well as finite wall-normal extent of the PIV interrogation spot size. One potential solution to these challenges is to increase the scale of the experiments, such as the High Reynolds Number Boundary Layer Wind Tunnel (HRNBLWT, Nickels *et al.* (2007)), the Princeton 'Superpipe' (Zagarola & Smits, 1998), the Flow Physics Facility at New Hampshire (Vincenti *et al.*, 2013), CICLoPE (Örlü *et al.*, 2017), or to perform experiments on the atmospheric boundary layer, such as Metzger (2002). But to the confines of a given experimental facility, it is thus an optimization problem

of decreasing the Re_τ to be able to capture the near-wall physics using PIV, and having significant enough modulation interactions to be captured.

Fortunately, significant physical understanding can be gained by making a few justifiable assumptions, even within the limitations of PIV technology and experimental facilities. Taylor's Hypothesis can still be used to estimate the large- and very-large-scale motions (that are much longer than typical PIV fields of view) from a sufficiently long PIV time series (Dennis & Nickels, 2008, 2011). The validity of this hypothesis will also be shown later in the current work (section 5.3). Great care needs to be taken during the experiments to minimize near-wall reflections, maximize the vector quality close to the wall, and satisfactorily deal with spurious vectors. The use of refractive index-matching greatly improves the near-wall quality, particularly in rough-wall flows, by greatly reducing the near-wall reflections. The following sections describe the experiments performed, the flow characteristics, and various tools used to investigate the inner–outer interactions.

4.2 Experimental facility

All the experiments were performed in the small RIM flow facility at the University of Notre Dame – a closed loop liquid facility, operated by a 7.5 HP centrifugal pump. Figure 4.1 shows a scaled outline of the actual facility. From the pump, the flow passes through a honeycomb, a series of screens and a converging section, before entering the test section. An in-line heat-exchanger in the flow loop, controlled by a thermostat, is operated by cold tap water to maintain the temperature of the solution at 20°C. The test section is 2.5 m long from entry to exit, has a square cross-section of side 112 mm, and is made of clear acrylic (Refractive index, RI = 1.49). The ceiling of the test section can be removed to provide physical access for setting up the experiment, and can be clamped back to hermetically seal the entire facility. Doing so enables a blanket of nitrogen to be sustained over the working solution, which is necessary to avoid oxidation and discoloration of the working solution (Uzol *et al.*, 2002). Ports are present upstream and downstream

to regularly inject seeding particles, and to displace the air inside with nitrogen. The entire facility has a functioning volume of 250 liters of the solution.

The working solution for the facility is a saturated solution of Sodium Iodide (NaI). By changing the solubility and controlling the temperature of the NaI solution, the RI can easily be controlled within a wide range between 1.33 - 1.51 (Bai & Katz, 2014). The current experiments were performed at 20°C and a solubility of 63% by weight, giving a refractive index (RI) of = 1.491, which is identical to that of the acrylic test section and the floor. Further, at these operating conditions, the specific gravity ($\bar{s}$) and kinematic viscosity (ν) of the working solution are 1.78 and $1.21 \times 10^{-6}\, m^2/s$, respectively. The entire solution is stored in a processor tank outside the facility, with a blanket of nitrogen under slight positive gauge pressure. At the beginning of each set of experiments, the solution is filled into the facility using an external pump before running the flow facility. During this process, the solution can optionally be bye-passed through a $0.25\,\mu m$ absolute rated particle filter to filter out the seeding particles if and when necessary. Similarly, at the end of each set of experiments, the solution is vacuumed back into the processor tank, stirred with nitrogen, and stored. Simultaneously, the flow facility is filled with nitrogen to prevent oxidation of residual solution that cannot be drained.

4.3 High-frame-rate PIV

4.3.1 Hardware

The high-frame-rate PIV measurements were made using a two-camera, two field of view (FOV) setup as shown in figure 4.1. Two high-speed Phantom V641 cameras are used and operated in a synchronized mode at full resolution, and different magnifications. The cameras are equipped with full-frame, CMOS sensors with a maximum resolution of $2560 \times 1600\,\mathrm{px}^2$ (4 MP), and a 6 Gpx/sec throughput at 12 bit resolution. These specifications give a maximum frame rate

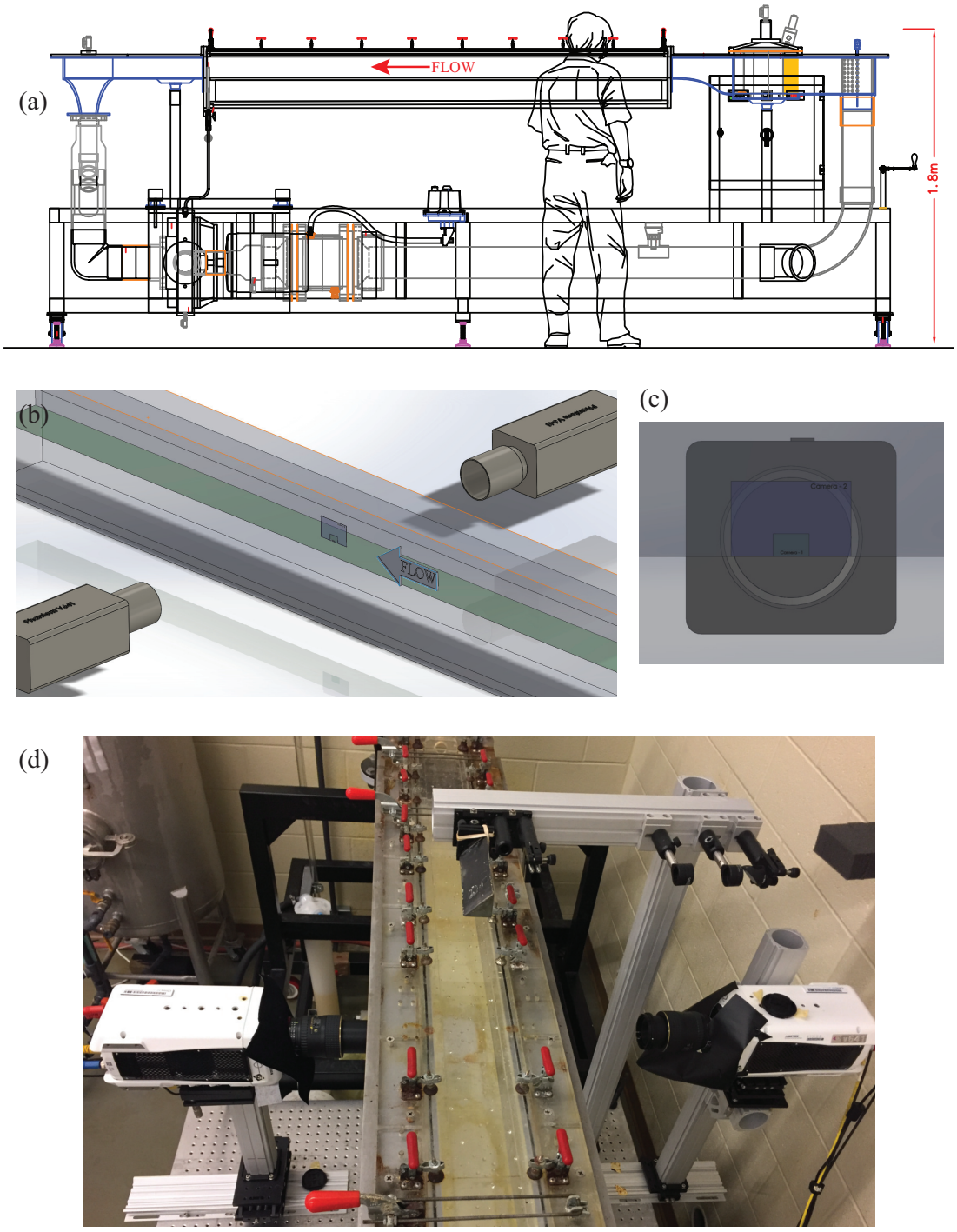

Figure 4.1: (a) Scaled schematic of the small-RIM facility in which current experiments were performed. (b) Schematic of the camera setup (floor is indicated in *green*) and (c) the FOVs. (d) Image of the camera and optical setups of the actual RIM facility.

of 1450 frames/sec, or 725 vector-fields/sec when operated at full resolution PIV-mode. Though higher frame-rates are possible at the cost of reduced image resolution, the high spatial resolution required herein to resolve all the small scales in the flow required that the cameras be operated at full resolution for all the results discussed in herein. The 32 GB on-board memory limited the duration of each continuous PIV time-series to 2734 vector-fields/sec/camera (5468 images, $\sim 3.9\,s$ at full frame rate), after which the images were saved to external storage via 10 GBit Ethernet interface before a new continuous PIV time series can be captured. Multiple time-series of this length were taken to ensure as large an ensemble of data as possible to compute the necessary statistics. More details of these parameters (in flow units) are discussed in Section 4.5. Each camera was fit with a Tamaron $105\,mm$ lens with a maximum aperture ($f^{\#}$) of 2.8.

A Northrop Grumman 'Patara' PA-050 laser was used to generate the light sheet for the high-frame-rate PIV measurements. It is a high-speed, dual cavity, Nd:YLF laser, and is capable of emitting $528\,nm$ *green* light, with an energy up to $54\,mJ$/pulse/cavity at pulse rates from 20 Hz to 1 kHz (i.e. beam power up to 108 kW). The laser power can be controlled by varying the diode-pumping current (the laser operates from 13 A to 30 A), and was operated at 26 A for all PIV measurements discussed here. Two beam-directing high-energy mirrors, a pair of plano-convex lenses, a cylindrical lens and a prism were aligned to generate a sheet of $1\,mm$ thickness at the bottom wall of the test section where the measurements were made.

A LaVision high-speed timing controller was used to control the image acquisition, synchronization and laser emission. The camera image exposure was controlled and synchronized using simultaneous `F-Sync` signals, and a `trigger` signal was applied to the cameras to indicate the end of acquisition. Two timed triggers were sent to each laser cavity as well, with the latter controlling the emission of each laser pulse. All devices had a rated response time of less than $20\,ns$ with respect to all `TTL` inputs.

A calibration target to map the camera coordinates to the world coordinates

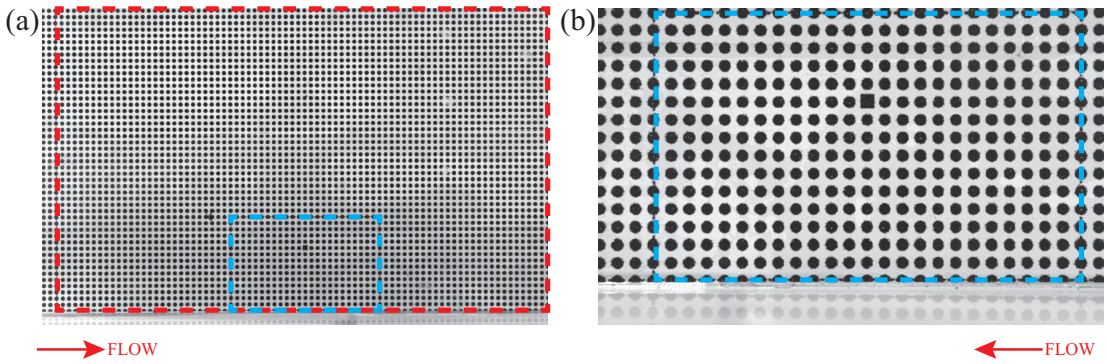

Figure 4.2: Calibration images from the (a) bFOV camera and (b) sFOV camera. The guide lines printed on the target that were used to setup the cameras to required magnification are highlighted in red and blue for bFOV and sFOV respectively. Also note that the flow direction in each camera is different.

was made by printing a regular grid of points (spaced at $1\,mm$) on a transparent sheet. A hand-held microscope with a $5\,\mu m$ reticle was used to verify the fidelity of the calibration target printed. A single square fiducial mark is also printed at a known location on the grid to be used to register the cameras with respect to each other. This target was carefully pasted on a $1/4\,$in acrylic plate that enabled viewing the target from both sides as required by the current camera arrangement. After aligning the calibration target carefully with the laser sheet, the FOVs of the cameras was adjusted using a thin outline also printed beforehand on the target. Doing so was essential to place the two fields of view precisely with respect to each other, and to obtain the appropriate magnifications desired. The cameras were aligned and focused on the target at maximum aperture ($f^{\#}\,2.8$) to best place the focal planes. Since the refractive index of the calibration plate matches that of the working fluid, the error due to refraction of the calibration grid through the $1/4\,$in plate (as viewed by one of the cameras) was found to be negligible. This was ensured by confirming that flipping the calibration target did not induce significant differences in the result between the two cameras. Figure 4.2 shows the calibration images for both cameras, the outline of the designed FOVs and the fiducial mark.

Table 4.1: Imaging parameters of sFOV and bFOV PIV systems.

Parameter	sFOV	bFOV
Dimensions	$40 \times 24\,mm^2$	$80 \times 50\,mm^2$
Aperture $f^{\#}$	22	16
Magnification	1.29	0.42
Image Resolution	$11.1\,\mu m/px$	$31.8\,\mu m/px$
Diffraction-limited spot size	$65\,\mu m$	$30\,\mu m$
Depth of field	$3.2\,mm$	$6.1\,mm$

Silver-coated solid glass spheres with a nominal diameter $2\,\mu m$ (specific gravity 3.5) were used as PIV tracer particles. While $15\,\mu m$ hollow glass spheres (specific gravity 1.9) were also tested, it was found that the former gave a much improved seeding density, particularly close to the wall which aided in achieving a high vector yield from the PIV images very close to the wall.

As shown earlier in figure 4.1, the two cameras have FOV dimensions of approximately $80 \times 50\,mm^2$ and $40 \times 24\,mm^2$ in the streamwise–wall-normal plane, and are henceforth referred to as, respectively, bFOV and sFOV images, vector fields etc. The sFOV was designed to capture and resolve small scales effectively in the near-wall region, while the bFOV was designed to capture a greater streamwise extent of the large scales in the outer layer as well as the bulk boundary-layer parameters. The two cameras viewed the measurement plane from the opposite sides of the laser sheet in a normal (perpendicular) arrangement. All PIV images were acquired at a $f^{\#}$ of 22 for sFOV camera, and a $f^{\#}$ of 16 for the bFOV camera. The absence of peak locking effects (Christensen, 2004) was also verified via histograms of $1\,mod(u)$ and $1\,mod(v)$, which gives the fractional portion of pixel displacements in the vector fields. A pixel-locked data would have higher counts of vectors towards 0 and 1 px, and a severe minima at 0.5 px. This was verified to not be the case in the current measurements, which had a flat distribution. Table 4.1 summarizes the experimental and optical parameters of the current experiments.

4.3.2 PIV processing

All PIV processing was performed using Davis 8.1.3 from LaVision. The calibration images were used to generate a polynomial calibration fit from the image coordinates to the world coordinates. To process the particle images, sliding background filter and particle intensity normalization adjustments were done to each image to enhance the weak particles and thus improve the signal-to-noise ratio. Using CPU processing, up to 4 prominent correlation peaks were stored for each interrogation spot and the best peak chosen based on various post-processing criteria (allowable vector range, universal median filter, peak-ratio etc). The bFOV images were processed using a multi-pass, successively decreasing window size PIV processing to a final square window of $16\times16\,\mathrm{px}^2$, with a 50% overlap between adjacent interrogation spots. The sFOV images were processed similarly, except using a $2x : 1y$ *elliptical Gaussian weighing of a bigger interrogation window* to achieve an effective interrogation spot of $16\times16\,\mathrm{px}^2$ (and with a 50% overlap). In the latter case, this tool uses an initial window twice the size, and Gaussian-weighs the center pixels to achieve an *effective* desired spot size of the final window. Thus, it is important to note that the smallest resolved structures, in this case, are *at least* $16\times16\,\mathrm{px}^2$ in physical size, and *at most* $32\times32\,\mathrm{px}^2$, depending on the seeding within the interrogation spot. A more thorough investigation of this nuance was not done, as it does not significantly affect the current results and conclusions.

In addition to the above vector post-processing to eliminate spurious vectors, additional outlier detection was required on the vector fields to maximize the quality of near-wall flow information. This additional post-processing was required because, to study inner–outer interactions, it is particularly crucial to optimize the flow information extracted at the nearest wall locations (where PIV is most prone to errors) and to eliminate outliers. Eliminating too many vectors close to the wall would demand too much interpolation/approximation for later analysis leading to 'artificial physics'. Alternatively, under-eliminating spurious vectors significantly affects the higher-order moments–an effect particularly detrimental

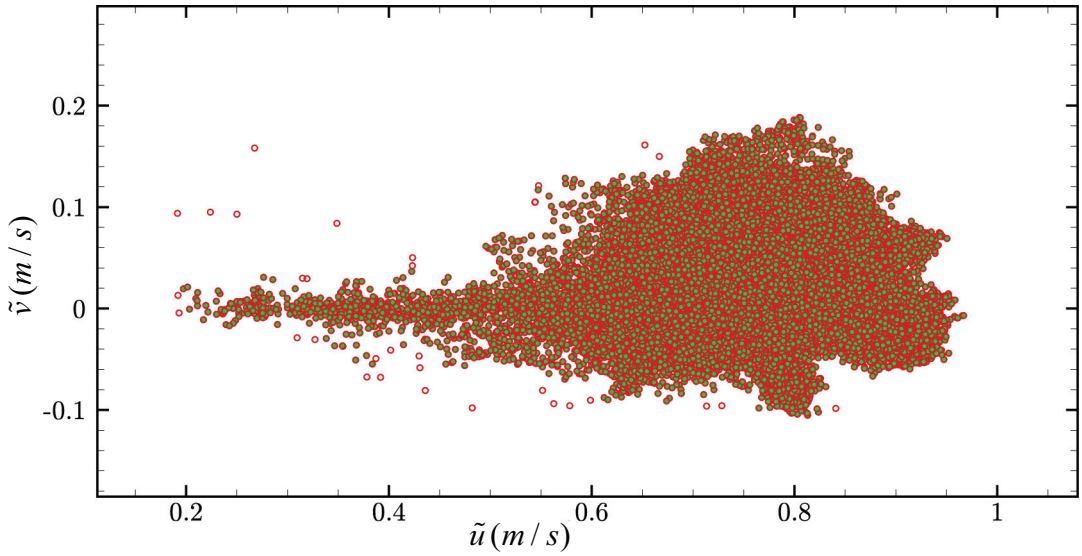

Figure 4.3: The $u - v$ scatter plot of a sample velocity field without (all circles) and with (filled circles) outlier removal using connectedness criteria.

for studying amplitude modulation ($\equiv \langle u_L u_s^2 \rangle$).

A scatter plot of $u - v$ vectors was used to identify the notable outliers, particularly small groups of spurious vectors which escape the earlier filters, and that occur when and where the particle seeding density is locally very low. These outliers were removed by applying a 'connectedness criteria'. The algorithm eliminates vectors by thresholding the number of vectors in a prescribed $\delta u - \delta v$ neighborhood of each vector. The result of such an outlier detection can be seen in figure 4.3, which successfully identifies these outliers and removes them from further analyses. With this additional conditioning, it was possible to calculate up to third-order moments, as will be shown in section 4.6.

Shown in figure 4.4 are sample vector fields from both the cameras at the same time instant, illustrating the accuracy of the calibration and processing procedure as well as the excellent agreement of the measurements between the two cameras. This agreement is particularly crucial given the high refractive index of the working solution which would exacerbate any misalignment in the parallelism of the FOV with either cameras' imaging plane. The higher resolution of the sFOV vector field is also evident. The inset in the figure shows the difference in

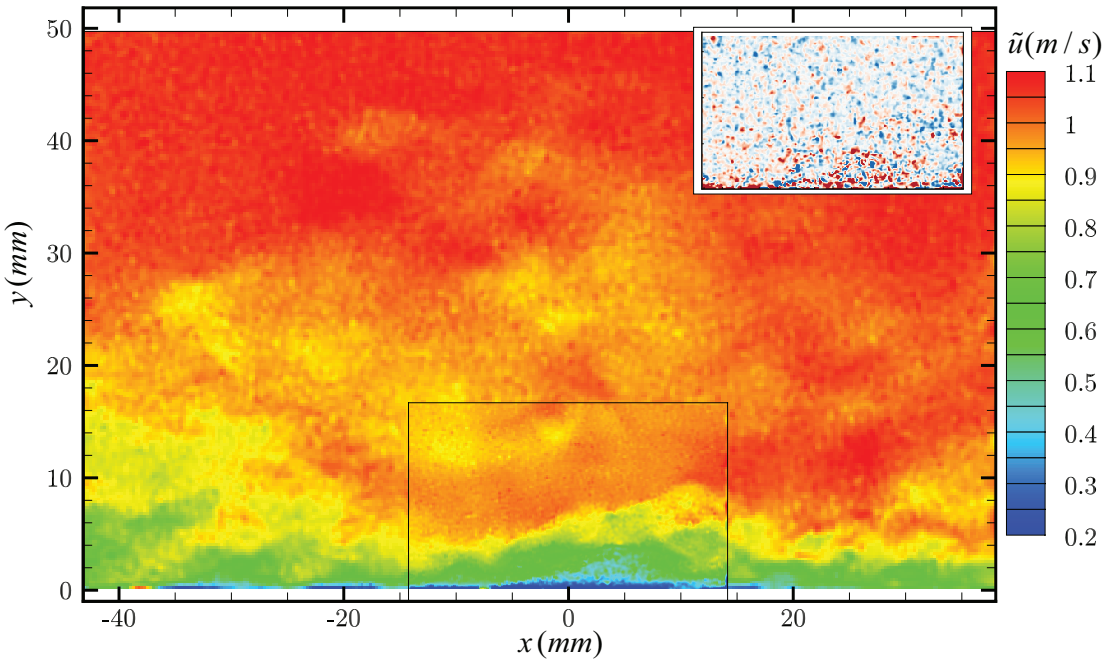

Figure 4.4: An example instantaneous snapshot of streamwise velocity contours from the two cameras. The small camera (sFOV) is embedded inside the big camera (bFOV) near the wall. Also shown in inset is the velocity difference between the two cameras within the sFOV (contours ranging from -0.04 m/s to 0.04 m/s).

the overlap region between the two measurements, and is found to be always less than 0.08 m/s (out of a 1.07 m/s free stream velocity). The largest discrepancies occur close to the wall, where the sFOV PIV system has a higher fidelity in capturing the flow structures compared to the bFOV.

4.4 Roughness characteristics

For these high-frame-rate PIV measurements in the small RIM flow facility, an idealized, hexagonally-packed hemispherical roughness pattern was used. A tile of this repeating roughness pattern was first designed on SolidWorks, and 3D printed using a ObJet30 Prime printer using VeroClear RGD720 material. The 3D printer has a maximum resolution of 16 μm. The tile was designed such that multiple tiles could be seamlessly concatenated in the streamwise direction along

the bottom wall of the test section.

Figure 4.5 shows the 3D model and the actual printed tile. The hemispheres are $2\,mm$ in diameter and hexagonally packed, while the tiles were $110\,mm \times 250\,mm$ in the spanwise and streamwise directions, respectively, with a base $4\,mm$ thick supporting the hemispheres. Thus, each tile spanned the entire test section ($112\,mm$), and multiple tiles were seamlessly concatenated to cover the entire streamwise extent of the bottom wall of the test section ($2.5\,m$). As the refractive index of the clear 3D printed plastic does not match that of the solution, one tile was cast in polyurethane and was used at the PIV measurement location ($\approx 2\,m$ from entrance section). The casting process involved first generating a negative mold using a 3D-printed tile as a template. Smooth-on Mold Star silicone mold was used to make this mold and Smooth-on Crystal Clear (RI= 1.49) was used to cast the transparent roughness tile. The process involved (sequentially) pre-mixing the ingredients, vacuum degassing to remove air bubbles at $-20\,mm\,Hg.$, injecting it into the mold, curing in a pressure pot at $15\,psi$ for 3 hrs, and curing in an oven at 65°C for 24 hrs. The tile was then de-molded and left on a flat surface for 3 days so that it achieves the specified properties. The $4\,mm$ base supporting the hemispherical roughness ensured negligible warping of the roughness tile while curing so that it laid flush with the bottom wall of the test section and connected to the 3D-printed tiles upstream and downstream of it. The vacuum degassing and more importantly, the pressure curing, prevented formation of micro-bubbles that could scatter light from PIV light sheet and degrade near-wall PIV measurements. The tiles were fixed onto the floor of the test-section using double sided tape. A 4 mm cylindrical rod at the leading edge smoothly faired the roughness panel to the incoming flow to prevent any leading-edge separation and associated separation bubbles.

It must be noted that the effects of refraction depend not only on the refractive index mismatch, but also on the incident angle of the light. Thus, close to the base of the hemispheres, the high curvatures and angles relative to the light sheet and FOV can still greatly distort and reflect the light sheet. However, this is

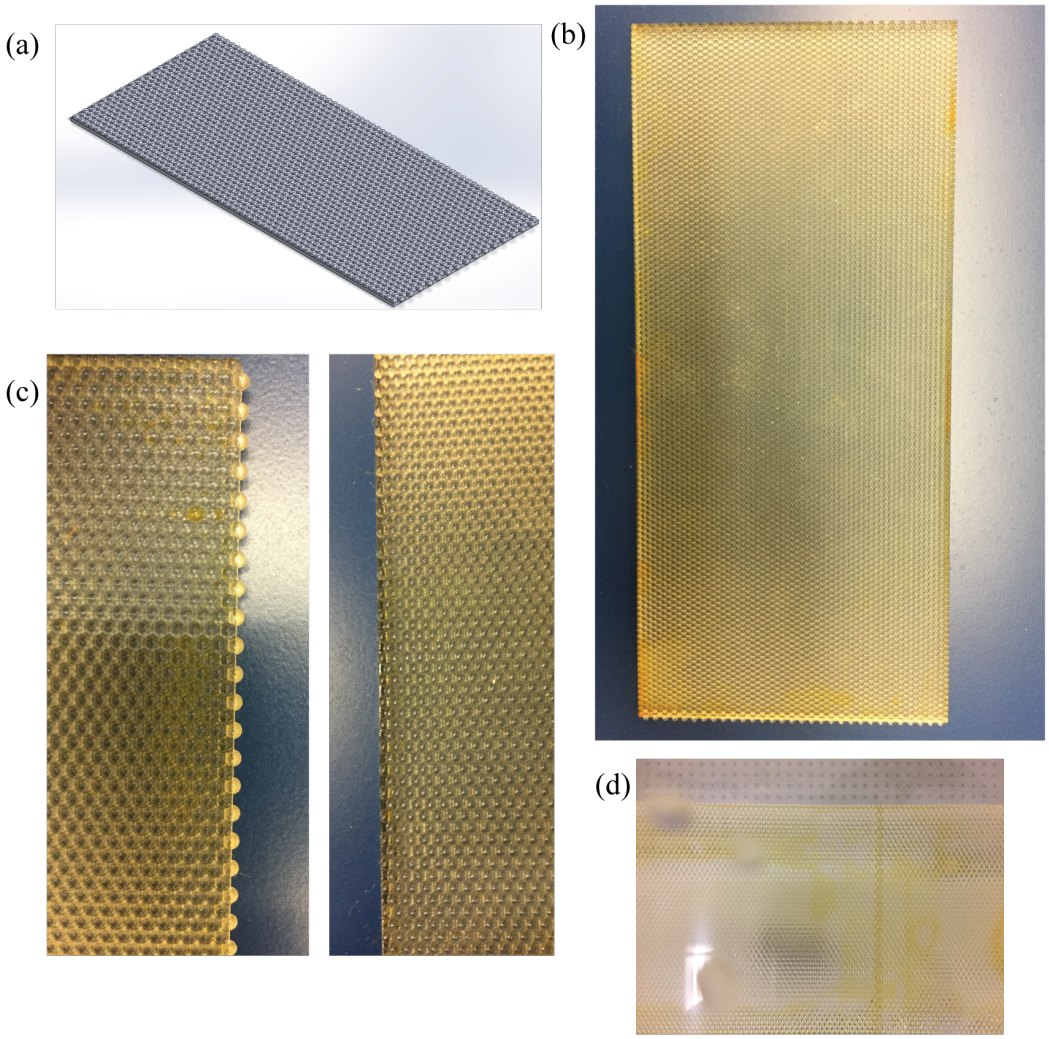

Figure 4.5: (a) Design and (b-d) images of a single tile of hemispherical roughness used for the current study. (c) shows the male and female edges of the roughness that form a seamless match when laid on the test section floor, as shown in (d).

not an issue for the current study for two reasons. First, these regions of high curvature and angle reside away from the hemispherical tip surface (i.e., they happen interior to the tile) as the surface angle of the crest is still approximately normal to the incident light sheet. Second, as we are interested in the vicinity of, but above the hemispherical roughness (not within the roughness interstitial spaces), and as these distortions dissipate quickly with distance from the wall, accurate measurements close to the wall can still be obtained satisfactorily.

4.5 Current experiments

Both smooth- and rough-wall experiments were performed using the above-mentioned experimental approach to investigate inner–outer interactions. A more elaborate analysis was performed on the smooth-wall experiments to first establish the physics, and various statistical metrics representing the modulation effects in a spatio–temporal sense. These approaches were then extended to the rough-wall cases to investigate and verify the same. The current study predominantly investigates the methods, conclusions and utility in smooth-wall flow which can easily translate to studies over roughness. Section 5.4 also demonstrates these methods on the rough-wall flow.

All smooth-wall experiments were performed along the bottom wall of the test section at its spanwise center to minimize any side-wall effects. A $4\,mm$ cylindrical trip attached at the entry section trips the incoming flow after the converging section. The boundary layer spatially develops $\approx 2\,m(\sim 50\delta)$ from the trip, before reaching the measurement section. All smooth-wall experiments were run at a pump speed of $20\,Hz$, which gives a free stream velocity of $U_\infty = 1.07\,m/s$.

Given the bFOV and sFOV characteristics in image units listed earlier in section 4.3, the final interrogation spot-sizes ($16 \times 16\,\mathrm{px}^2$ in both) yield a physical vector spacing of about $250\,\mu$m and $90\,\mu$m, respectively, in each linear dimension. It should be noted that the resolution of the smallest scales, however, depends on the interrogation window shape and weighting functions used, as discussed in

section 4.3. Both cameras were operated synchronously to capture vector fields at the same time instants. First, low sampling-rate data set was acquired at $F_s = 20\,Hz$ (i.e., 20 vector fields per second). This data was processed to obtain the various parameters required to characterize the boundary layer. The low sampling rate ($F_s\delta/U_\infty = 0.72$) gives a larger number of uncorrelated boundary-layer snapshots, and thus is a more suitable ensemble to compute the various boundary-layer parameters and statistics compared to the time series snapshots. One-thousand vector fields were sampled at this sampling rate, and this case is henceforth referred to as `S20-20`. This ensemble was processed using methods described in section 4.3, ensemble averaged first, and then line averaged in the streamwise direction to improve the ensemble (assuming streamwise homogeneity, and non-correlation of different snapshots).

The boundary-layer parameters were extracted using the best non-linear regression fit to a theoretical form (Chauhan *et al.*, 2007), with the fitted parameters giving the 'true' boundary-layer thickness ($\tilde{\delta}$), wake parameter (Π), skin friction velocity (u_τ), and a wall correction (y_c). Kármán number (κ) and intercept (C) of logarithmic profile were chosen to be 0.384 and 4.17, respectively. This is identical to the hot-wire boundary layer fit used in section 2.4. The boundary-layer thickness (δ) at this location was found based on $0.99U_\infty$ to be $38\,mm$, yielding an $Re_\tau = 1400$. The viscous length scale (y^*) is $27.1\,\mu$m and the friction velocity is $u_\tau = 0.045\,$m/s. Using these values gives an interrogation spot size, in inner units, of $(6.6y^*)^2$ and $(18.8y^*)^2$ for the sFOV and bFOV respectively, and a laser sheet thickness of $\sim 37y^*$.

After characterizing the smooth-wall boundary layer, high-frame-rate measurements were performed to resolve the dynamics in a temporal sense. For these experiments, 2734 ($\equiv$ one camera memory) time-correlated PIV snapshots per dataset were acquired at $700\,Hz$ (700 vector fields per second) for a duration of $\approx 3.9\,s$. In flow units, this gave a time-series with a temporal resolution of $2.35\,y^*/u_\tau$, and a duration of $109\,\delta/U_\infty$. This time-series is sufficient to resolve the small-scale activity, and for correlations over multiple LSM and VLSM struc-

tures (typically $O(10\,\delta)$). Twenty such datasets were collected to have an ensemble time series $\equiv 2,200\,\delta/U_\infty$, with 54,680 vector fields per FOV. These data sets are collectively referred to henceforth as `S20-700`. In comparison, the hot-wire time series had a temporal resolution of $0.3\,y^*/u_\tau$ and a duration of $\approx 21,000\,\delta/U_\infty$. Table 4.2 summarizes the boundary-layer parameters for the smooth-wall flow.

4.5.1 Rough-wall flow

Datasets collected for the rough-wall boundary layer was similar, with a few small differences. The pump speed for all rough-wall experiments was set at $19\,Hz$ (instead of $20\,Hz$ for the smooth-wall case). Doing so maintained a consistent free-stream velocity between the smooth and rough-wall flows by accounting for the blockage of the test-section by the presence of the roughness panels. The free stream velocity (U_∞) was kept at $1.07\,m/s$, with identical physical development length. One low frame-rate dataset (at $20\,Hz$) to characterize the the rough-wall boundary-layer parameters (referred to as `R19-20`), and nine high-frame-rate datasets (at $700\,Hz$, *vs* 20 datasets for the smooth-wall case) were taken (referred to as `R19-700`). A similar non-linear regression fit to a theoretical form compared to the smooth-wall profile (Chauhan *et al.*, 2007) was made to extract boundary-layer parameters, with some differences. The near-wall region can no longer be assumed to obey the Musker profile (Musker, 1979), and an additional parameter of the roughness function (ΔU) must be considered to account for the increased momentum loss due to the roughness. Thus, only the outer wake formulation in Chauhan *et al.* (2007) was used to fit the velocity profile to extract the parameters. The various mean parameters of this rough-wall boundary layer are also listed in Table 4.2. It is important to note that the five-parameter regression fit to theoretical form is mathematically redundant— as in, this procedure can yield multiple non-unique parameters with equal goodness of fit. Care must therefore be exercised before admitting the parameter values obtained. For the current study, the parameters were also compared to the Clauser method (Perry & Li,

Table 4.2: Measurement and flow parameters of RIM experiments.

Parameter	Smooth-wall		Rough-wall	
Label	`S20-20`	`S20-700`	`R19-20`	`R19-700`
Pump Speed	$20\,Hz$	$20\,Hz$	$19\,Hz$	$19\,Hz$
Vector fields per second	$20\,Hz$	$700\,Hz$	$20\,Hz$	$700\,Hz$
No. datasets	1	20	1	9
vector fields per dataset	1000	2734	1000	2734
Free-stream velocity (U_∞)	$1.07\,m/s$		$1.07\,m/s$	
Boundary layer thickness (δ)	$38\,mm$		$34.2\,mm$	
Kármán number (Re_τ)	1410		1350	
Skin-friction velocity (u_τ)	$0.045\,m/s$		$0.048\,m/s$	
viscous length scale (y^*)	$27\,\mu m$		$25.4\,\mu m$	
viscous time scale (t^*)	$610\,\mu s$		$530\,\mu s$	
Roughness function (ΔU^+)	–		2.98	
Equivalent sand grain roughness (k_s^+)	–		16.5	
Virtual origin (y_c)	–		$0.1\,mm$ below peak	

1990), without significant differences. The equivalent sand-grain roughness height, k_s^+, was found to be 16.5, which placed this rough-wall boundary layer in the transitionally rough regime.

Finally, the boundary-layer growth and wake were found to differ somewhat for the two flows, possibly owing to different tripping and growth mechanisms. While the smooth-wall flow was tripped with a $4\,mm$ cylindrical rod, the boundary layer over the roughness was not externally tripped (i.e., the wall roughness was used to trip the boundary layer). Doing so may have led to an underdevelopment of the boundary layer, relative to the smooth-wall flow considered here, as reflected in the boundary-layer thickness and wake profile (section 4.6.3). We, however, suspect this distinction to affect only via Re effects, and not significantly in modulation physics. This must be kept in mind when making direct comparisons between the smooth- and rough-wall cases in the current study.

4.6 Boundary layer characteristics

4.6.1 Smooth-wall flow: Mean velocity statistics

Figures 4.6 and 4.7 shows the ensemble-averaged fields of streamwise velocity and in-plane Reynolds stresses from `S20-20`, bFOV. The ensemble averages have not converged fully and streamwise line averaging (assuming streamwise homogeneity across the field of view) is performed to improve the statistics. The streamwise homogeneity itself can be observed from these ensemble averaged plots.

Figure 4.8 presents mean velocity profiles (generated by line averaging the above ensemble averages) in inner units for the smooth-wall case from both bFOV and sFOV. The excellent agreement between the mean streamwise velocity from the two cameras speaks to the quality of calibration for the smooth-wall measurements. Further, the utility of the sFOV measurements, particularly in obtaining measurements very close to the wall ($y^+ < 20$), is evident. Also shown for comparison is an example of a canonical zero-pressure-gradient turbulent boundary layer measured from an experiment (Örlü & Schlatter, 2013) and from DNS simulations (Schlatter & Örlü, 2010*a*), both at similar Re_τ. The mean streamwise velocity profiles reflect a weaker wake in the current flow (smaller wake parameter, Π) from that of a true zero-pressure-gradient boundary layer shown here. Particularly, this weaker wake is reflective of the slight favorable pressure gradient in the small RIM flow facility given the constant cross-sectional dimensions of the test section. This effect should, however, be limited to the wake region of the boundary layer, and we expect the near-wall physics and the modulation interactions to be unaffected by the same. Indeed, Harun *et al.* (2013) studied the impact of non-zero streamwise pressure gradient on modulation effects and found that favorable pressure gradients slightly suppress such influences. Thus, any modulation identified in the current flow cases will represents a *lower* measure of such effects compared to a true zero-pressure-gradient boundary layer.

Figure 4.9 shows the in-plane Reynolds stresses, $\langle u^2 \rangle$, $\langle v^2 \rangle$, $\langle uv \rangle$, computed from

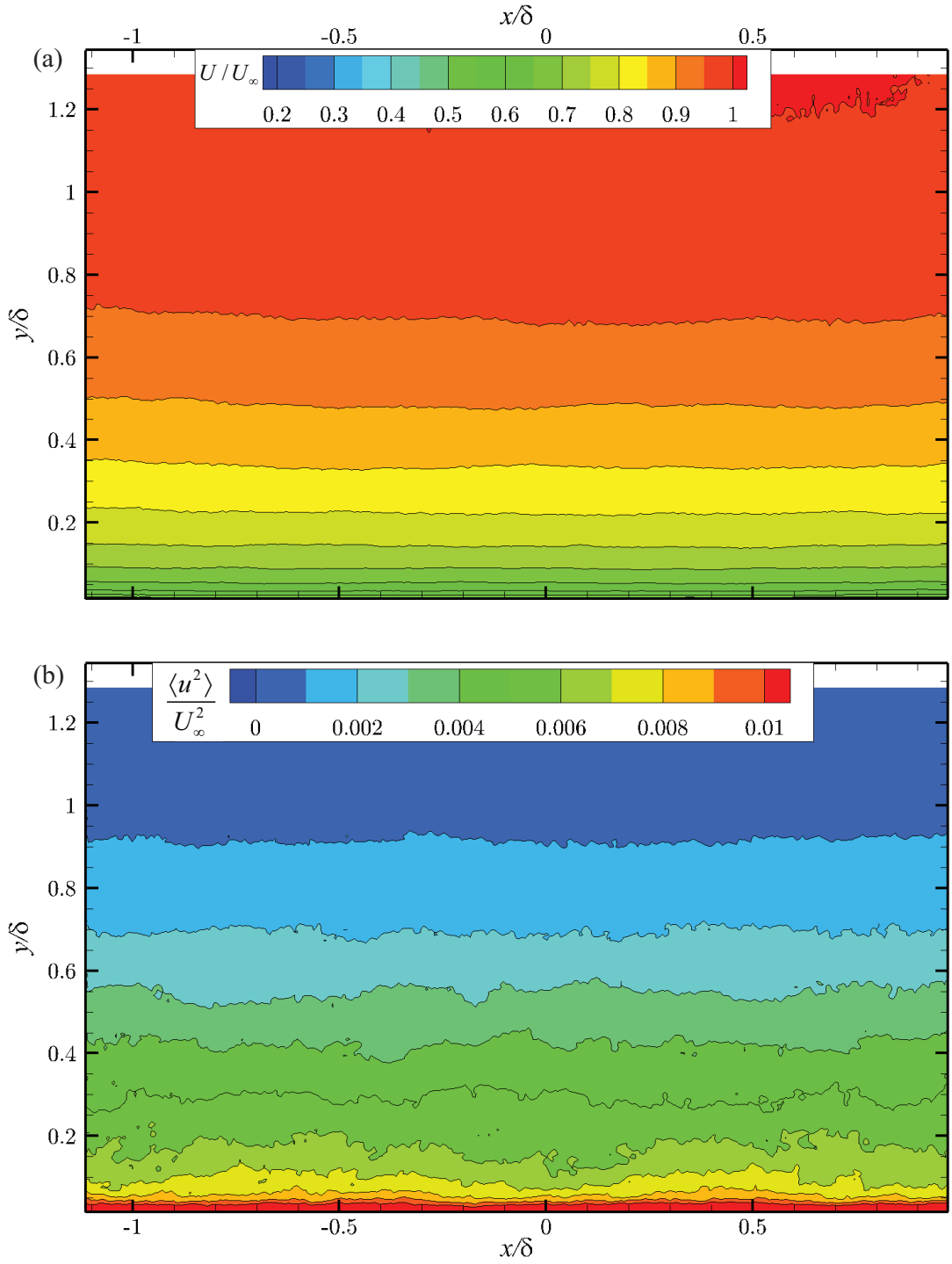

Figure 4.6: Contours of ensemble averaged (a) streamwise velocity (U/U_∞) and (b) streamwise turbulent kinetic energy ($\langle u^2 \rangle / U_\infty^2$).

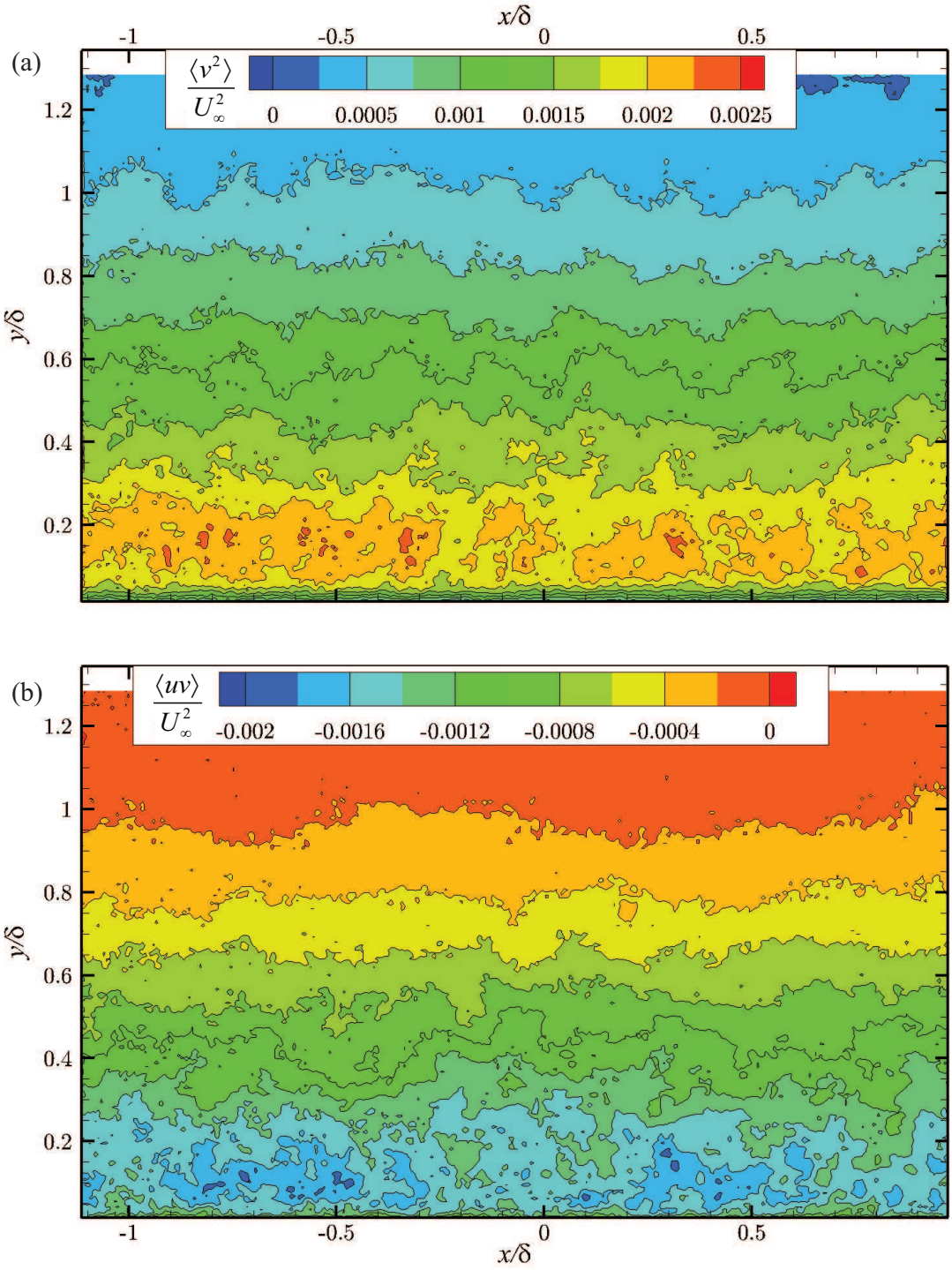

Figure 4.7: Contours of ensemble averaged (a) wall-normal turbulent kinetic energy ($\langle v^2 \rangle / U_\infty^2$) and (b) in plane Reynolds shear stress ($\langle uv \rangle / U_\infty^2$).

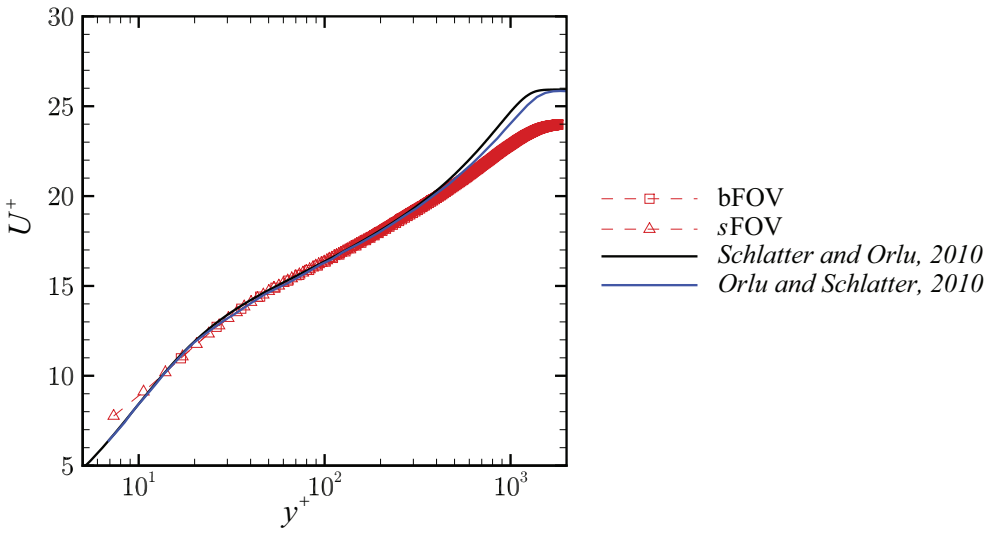

Figure 4.8: Average streamwise velocity variation with distance from the wall in inner units. Also shown are DNS and hot-wire measurements at comparable Re_τ from Schlatter & Örlü (2010*a*) and Örlü & Schlatter (2013).

the `S20-20` ensemble in the two FOVs. These line averages show good agreement with the signatures of the canonical near-wall production cycle, particularly the near-wall peak in $\langle u^2 \rangle$. Again, the utility of the near-wall sFOV is particularly evident in capturing the bulk of the small-scale energy very close to the wall– something that the bFOV has not effectively captured. There appears, however, to be a small shift in the location of the near-wall peak. This small shift ($\approx 5y^*$) is likely due to an error in wall location and/or a bias in the PIV technique in accurately resolving the location of a velocity vector within the planar interrogation spot. This near-wall offset seems to be a consistent feature in all observations herein when compared to the canonical features, as will be seen in skewness and spectra. A second inconsistency in the streamwise turbulence intensity plots is that the near-wall turbulence is measured to be higher than the DNS value (≈ 8), though we expect measurements to usually capture smaller fraction of total TKE due to spatial averaging of the small scales (Hutchins *et al.*, 2009). This slightly higher value is likely due to an underestimation of the friction velocity, u_τ, which exacerbates any normalizations of higher-order statistics. For example, a 5% error in friction velocity estimation that is typical of all indirect mean velocity-based

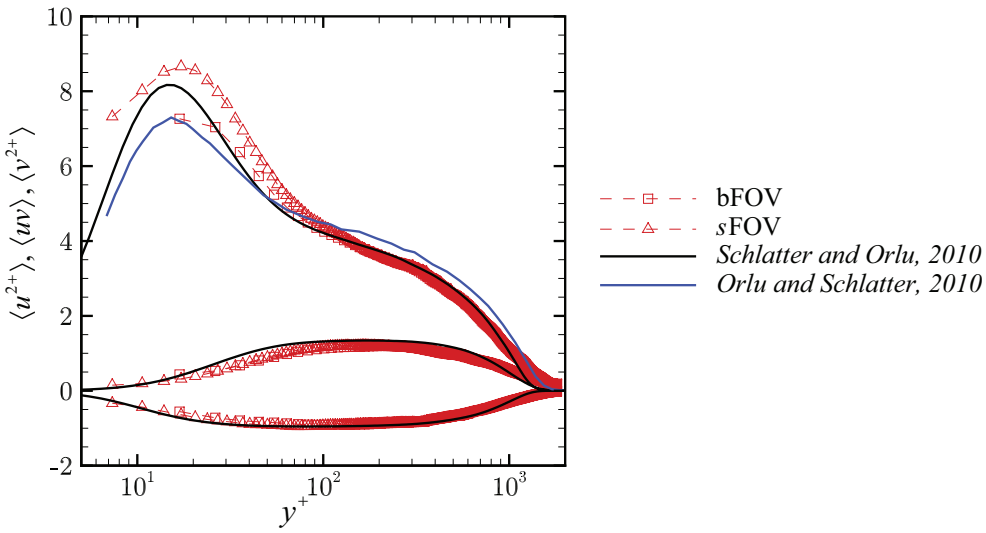

Figure 4.9: As in figure 4.8, but for in plane Reynolds stresses, $\langle u^2 \rangle$, $\langle uv \rangle$, $\langle v^2 \rangle$.

methods (as utilized herein) translates into a 10% error in turbulent statistics (normalized by u_τ^2). The agreement of skewness profiles with the canonical experiments and DNS discussed below reiterates these normalization issues, as the skewness profiles are normalized by local variance, $\langle u^2 \rangle$, rather than the friction velocity.

It should also be noted that the PIV technique is more prone to errors in wall-normal velocity measurements than the streamwise velocities. The sub-pixel resolution for displacement measurement in the PIV technique (~ 0.1 px) is similar in both streamwise and wall-normal components; however, the mean pixel displacement of the seeding particles is much higher in the streamwise direction than in the wall-normal direction (particularly close to wall due the imposed no-penetration condition). This limited dynamic range of the wall-normal velocity component therefore results in higher relative errors in this velocity component.

Finally, it is important that one accurately resolves third-order moments, at least in the streamwise velocity, before conclusions on inner–outer interactions, particularly amplitude modulation, can be drawn. In fact, amplitude modulation can also be measured via a component of skewness, $\langle u_L u_s^2 \rangle$, when time series are decomposed into large and small scales (i.e., $u = u_L + u_s$). Figure 4.10 shows the

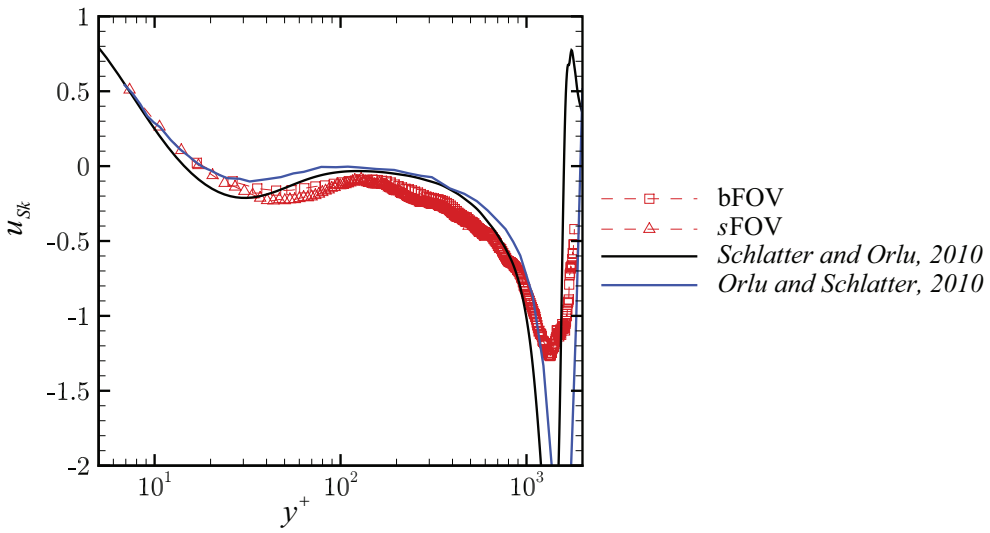

Figure 4.10: As in figure 4.8, but for streamwise turbulent skewness, $\langle u^3 \rangle / \langle u^2 \rangle^{3/2}$.

mean skewness profiles from the two FOVs of the streamwise velocity fluctuations. Comparing with the DNS and hot-wire measurements, good agreement is observed in the trends of the same. It must be noted that the volume-averaging of the PIV technique greatly affects the higher order moments of fluctuating quantities, an effect that can also be seen in the hotwire measurements by Örlü & Schlatter (2013).

4.6.2 Smooth-wall flow: Spatial and temporal spectral characteristics

The low-frame-rate data from sFOV and bFOV can be used to compute the spatial spectral characteristics. Figure 4.11 shows the pre-multiplied spatial power spectra from the two FOVs for the streamwise and wall-normal velocity fluctuations. These results are similar to the spectra from hotwire measurements in figure 2.9 in section 2.5, but without the need for Taylor's hypothesis. The near-wall turbulent intensity peak in the streamwise velocity fluctuations, corresponding to the turbulence production cycle, is evident at wavelengths $\lambda^+ \approx 1000\, y^*$ as expected in canonical wall-bounded turbulent flows (Hutchins & Marusic, 2007*b*, for example).

The high-frame-rate data can also be used to compute the temporal spectra, and converting the temporal scales to its spatial equivalent by assuming Taylor's frozen field hypothesis. Hotwire-like time series were extracted at an array of fixed wall-normal positions at the streamwise center of the sFOV, as will be described in section 5.1. Pre-multiplied temporal spectra were computed using these time series, to estimate the quality of temporal evolution of the velocity fields at a spatially fixed location. This yields spectra at much larger wavelengths than the spatial spectra can capture. Figure 4.11 also shows these pseudo-spatial spectra, with time series extracted from sFOV camera and with the temporal frequencies from the time series converted into spatial scales using Taylor's hypothesis. The results complement the spatial spectra well and speak to the validity of Taylor's hypothesis in the present context.

4.6.3 Rough-wall flow: Mean and spectral characteristics

Shown in figure 4.12 are the mean profiles of the rough-wall flow obtained from the low-frame-rate, rough-wall data (`R19-20`), similar to figures 4.8–4.10. The wake region of the mean velocity profile indicates the difference between the smooth- and rough-wall boundary layers. As discussed in section 4.4, this difference is possibly due to the difference in tripping methods used for the two flows, and the subsequent growth of the boundary layer. This results in an associated $Re_\tau \approx 1350$ for the rough-wall flow, which is smaller than the smooth-wall case.

Additionally, the Reynolds stress components and skewness of the rough-wall boundary layer are also shown in figure 4.12. Compared to the smooth-wall flow, the inner region flow is markedly different compared between the two flows. Away from the wall, the rough-wall also seems to have higher turbulence intensities than the smooth-wall in wall-normal and streamwise turbulence. Similar effects in the skewness can clearly be seen. The skewness minima in smooth-wall flows above the buffer layer ($y^+ = 30$) is absent in the current rough-wall, with mostly positive skewness. These indicate the differences between the smooth- and rough-wall flow

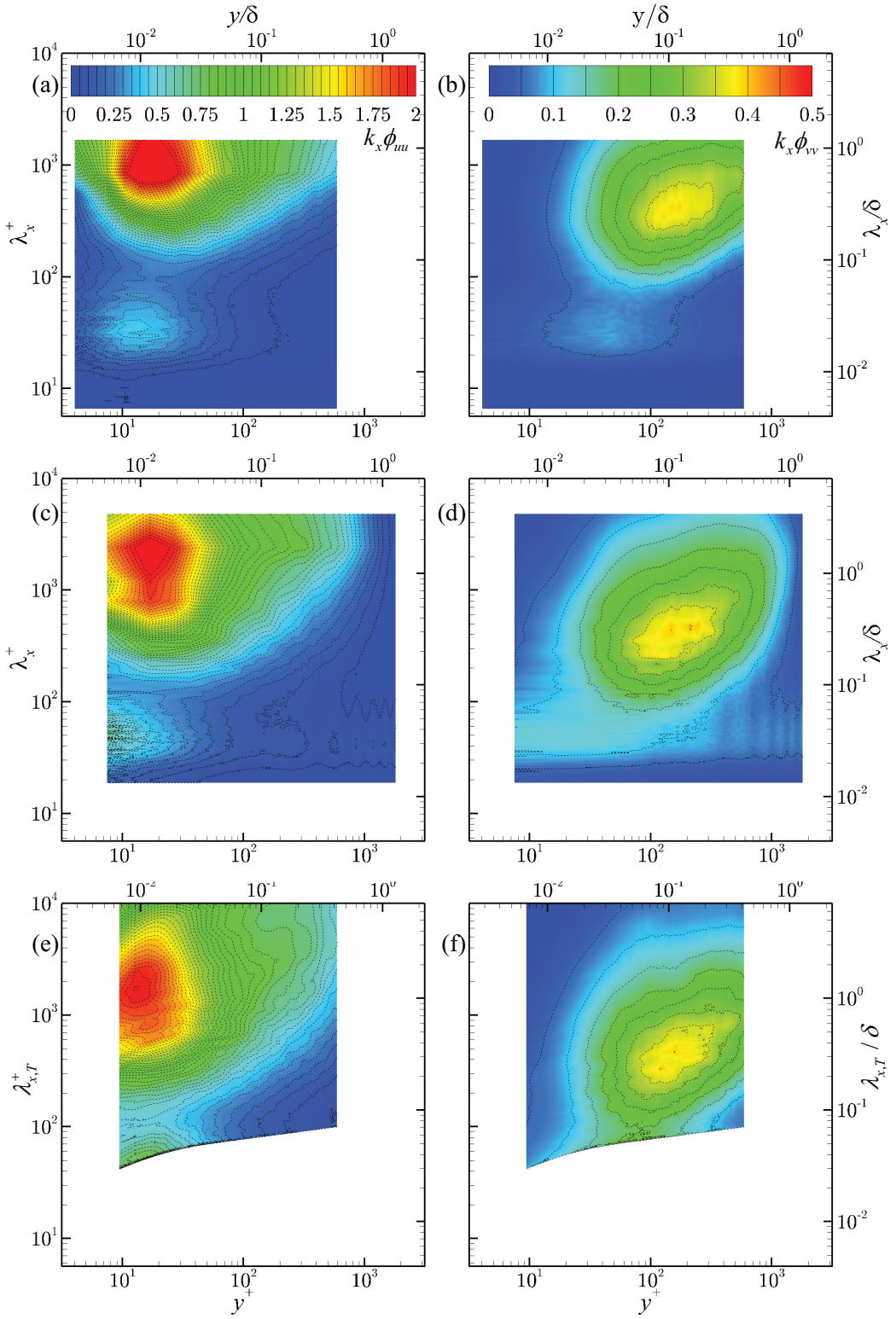

Figure 4.11: Spatial premultiplied energy spectra indicating energy distribution at various inner- and outer-scaled wavelengths for (a,c,e) streamwise turbulence and (b,d,f) wall normal turbulence. (a,b) Spatial spectra - sFOV, (c,d) Spatial spectra - bFOV, (e,f) Temporal spectra - sFOV.

inner regions.

The spatial and temporal spectra shown in figure 4.13 indicate the energy differences at the small scales in the rough-wall flow compared to the smooth-wall case (in figure 4.11). The transitionally-rough nature of this rough-wall turbulent boundary layer is evident from the spectral maps as well, implying both the structures shed by the roughness elements and the viscous dynamics due to mean shear play an important role in the near-wall dynamics. The near-wall peak in the spectral maps of streamwise turbulent kinetic energy ($\langle u^2 \rangle$) indicate similarities to the smooth-wall counter parts. However, this peak is weaker in the current case, owing to the decreased mean shear above the roughness elements. Further, the scales at which this maximum energy occurs is smaller in the rough-wall case than the smooth-wall counterpart. The pre-multiplied spectra in the wall-normal turbulent kinetic energy in figure 4.13 also shows similarities and differences between the smooth- and rough-wall boundary layers. No spectral signatures of the periodicity in roughness element arrangement on the flow can be seen in the current results, even at the location closest to the wall.

It can thus be said that the current experimental setup and instrumentation can capture all the boundary layer characteristics required to investigate the inner-outer interactions. The sFOV captures the scales close to the wall including the near-wall turbulent production peak with high resolution. With this understanding of energy distribution at various scales in the boundary layer, we can further investigate the inner-outer interactions in smooth- and rough-wall flows. This can be done as a point analysis as before (in chapter 3) or by developing newer metrics using the richer spatial information in the PIV data. This which will be undertaken in the following chapter.

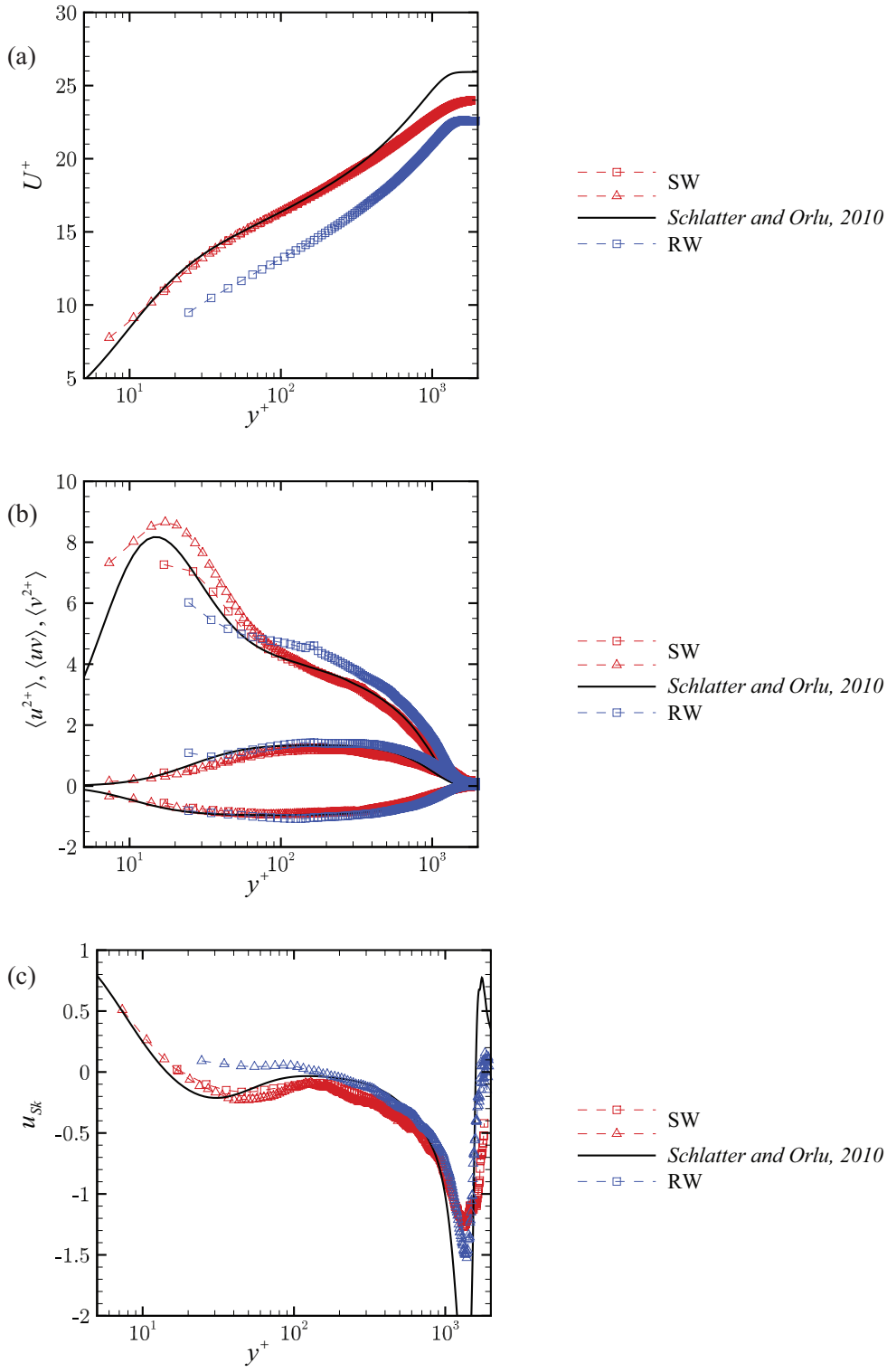

Figure 4.12: (a) Mean velocity, (b) in-plane Reynolds Stresses and (c) Streamwise turbulence skewness of the rough-wall boundary layer along side DNS (Schlatter & Örlü, 2010*a*) and smooth-wall experiments.

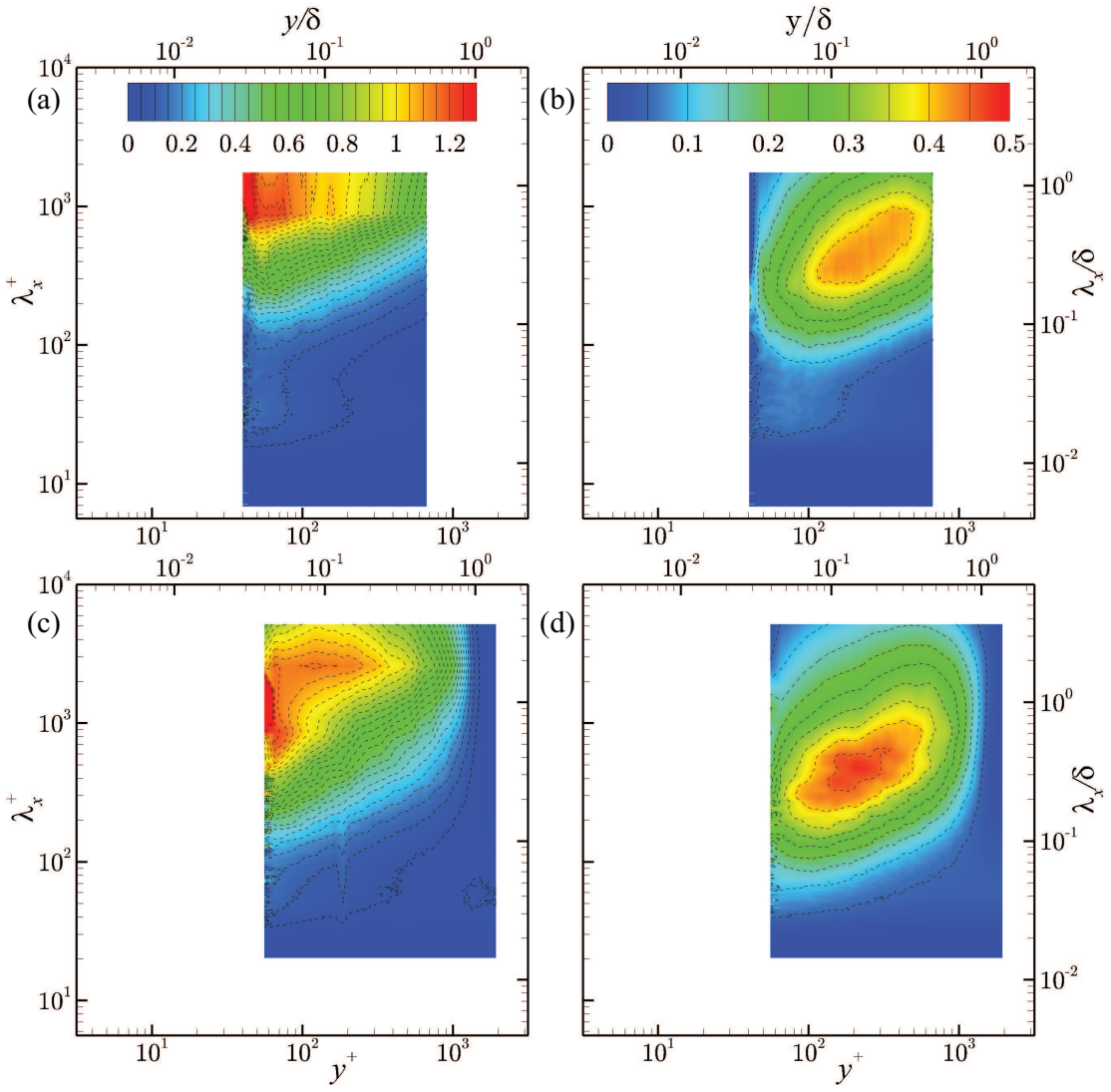

Figure 4.13: Spatial pre-multiplied spectra over rough-wall of (a,c) streamwise turbulence and (b,d) wall-normal fluctuations from (a,b) sFOV and (c,d) bFOV.

CHAPTER 5

PART-II: INNER–OUTER INTERACTIONS VIA HIGH-FRAME-RATE PIV IN RIM FACILITY

The rich spatio-temporal velocity information acquired in these experiments, including at two different spatial resolutions, can be used to quantify inner–outer interactions using a range of tools. By first examining the flow and the data in a temporal-only approach at a point, the modulation interactions can be related to many past experimental and computational studies on canonical boundary layers and channel flows. Doing so provides a reference and metric of comparison, given that this is the first study to quantify modulation effects using PIV, as well as add fidelity to the spatio-temporal metrics developed in the current work. The spatial information available in these PIV datasets is then exploited to compute conditional averages that are used to isolate the evolution of the large scales, and their subsequent correlated effects on the smaller-scale, near-wall turbulence. Finally, streamwise scale modulation is also briefly investigated via spectra conditional averaging.

5.1 Time-series extraction

The high-frame-rate PIV data acquired is analogous to acquiring two-component velocity data from an array of hot-wire probes over the entire FOV of the PIV data. Thus, a hot-wire-like time series can be taken from the PIV measurements by extracting a time evolution of velocity at a prescribed grid point in the PIV FOV, (x_p, y_p). In addition to the u-velocity time series that is often the focus of modulation studies (like the hot-wire measurements in Chapter 2), the PIV datasets allow v-velocity time series to also be extracted. Doing so enables the

investigation of these interactions on the wall-normal velocity component as well. Such interactions for all three velocity components were earlier investigated in a smooth-wall turbulent boundary layer by Talluru *et al.* (2014) using multi-component hot-wire anemometry.

A small wall-position correction [$\sim O(50\,\mu m)$] for each dataset was applied individually to account for changes in physical wall position between the data sets. While the PIV processing parameters are identical, this implies that the vector fields do not share a perfectly common grid. Thus, for a chosen probe position (x_p, y_p), a linear interpolation of the neighboring (valid) vectors was performed. Further, particularly close to the wall, clusters of missing vectors result in missing velocities at a given instant, generating a non-uniformly spaced time series (of available/measured values). To enable the use of various analysis tools, such as Fourier transforms, the missing vectors were linearly interpolated in time. Figure 5.1 shows the percentage of missing (and interpolated) vectors for each wall-normal location. Also shown in figure 5.1 is an example u-time series extracted at $y^+ = 17$ in the smooth-wall flow, with interpolated values identified.

Time series were extracted in this manner at an array of wall-normal positions at a given $x = 0$, which corresponds approximately with streamwise center of sFOV (as shown in figure 4.4). Such a time-series is used for the analysis presented here in section 5.2 and to compute the temporal spectrum shown earlier in figure 4.11.

5.2 Point–time-series modulation

Using only the temporal evolution of velocity extracted as described in the previous section, both amplitude and frequency modulation can be explored using the same methods described in chapter 3. Doing so provides a metric of comparison regarding the use of PIV-measured velocity time series for quantifying modulation effects. In addition, it provides the first evidence of correlations between the large and small scales, particularly the correlation between former and the amplitude and frequency changes of latter. Further, using the same metrics and the two-

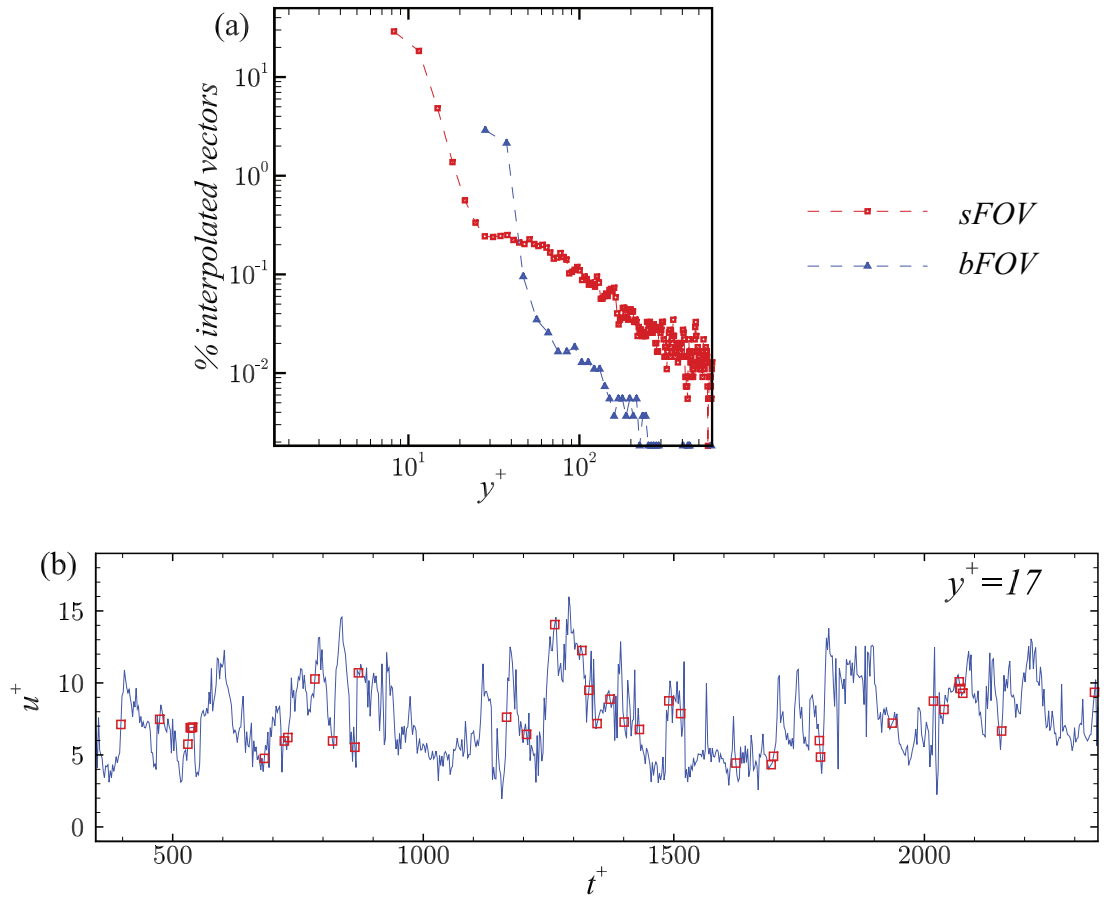

Figure 5.1: (a) Percentage interpolated vectors in the time series for various wall normal positions for the sFOV and bFOV results. (b) Sample time series with interpolated values marked.

velocity-component time series, modulation effects present within the wall-normal velocity component is also investigated. The current section demonstrates the fidelity of quantifying inner–outer interactions using PIV data through the use of these metrics. To accomplish this goal, only the temporal evolution of velocity is considered (meaning all spatial information is ignored). Thus, 'large' and 'small' in the current section implies fast and slow evolution of the velocity time series in question (as with hot-wire analysis), and not their spatial variations as captured by PIV. This latter analysis will be considered in section 5.3.

As the high-frame-rate PIV data was acquired in distinct blocks, the time series extracted from this data are thus in multiple, uncorrelated segments. Thus all analysis on each time series is performed in the same way as the hot-wire analysis described in chapter 3, but for one small distinction. While all averages from the hot-wire time series were computed via time average (i.e., $\langle E_L[u_{is}]\rangle$, $\langle \tilde{f}_L[u]\rangle$, etc.), the computation of the same for the PIV data was performed via time and ensemble averaging. Doing so improved convergence of the averages.

5.2.1 Amplitude modulation

As was discussed earlier in section 3.2, amplitude modulation can be investigated using various methods. To quickly recall, by using Hilbert transforms, the large-scale envelope of the small scales can be extracted, and be correlated to the large-scale velocity fluctuations. Alternatively, the small-scale energy in the wavelet power spectrum of the time series can be filtered to extract the large-scale variations in the same. This result can also be correlated, in lieu of envelope using the Hilbert transform, to the large scales in the logarithmic region to quantify amplitude modulation effects (detailed procedures were elaborated upon in section 3.2). With the point–time-series using PIV, one can investigate the '1-probe' and '2-probe' equivalent of the hot-wire time series amplitude modulation metrics, henceforth referred to as '1-point' and '2-point' analysis to distinguish the PIV versions from the hot-wire ones. For the 2-point analyses, the 'outer' point

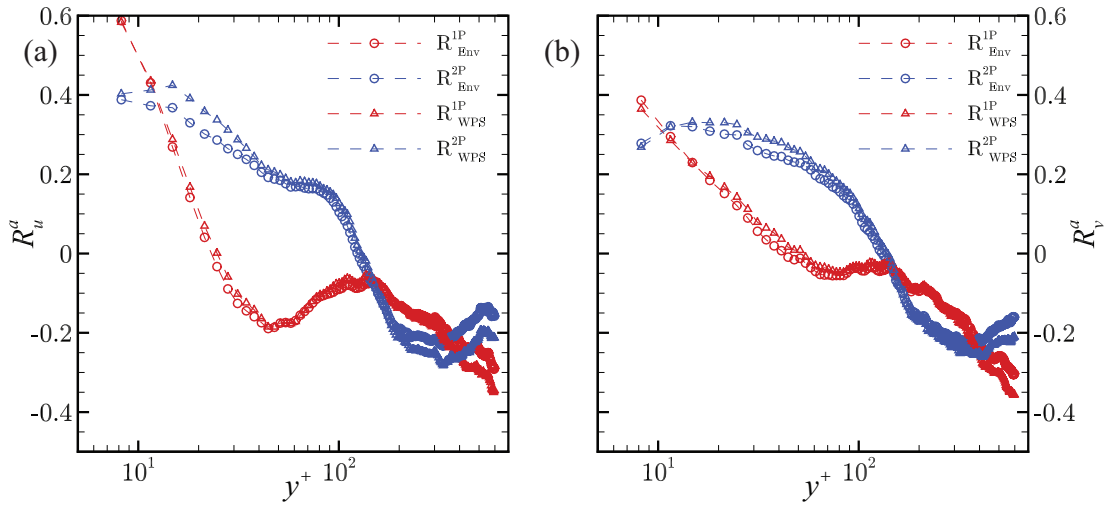

Figure 5.2: 1-point and 2-point amplitude modulation in (a) streamwise and (b) wall-normal velocities using envelope-based and wavelet-energy based methods from sFOV.

is considered to be at the center point of the logarithmic region, given by $\sqrt{15Re_\tau}$ (Ng *et al.*, 2011).

Figure 5.2 shows the amplitude modulation correlation coefficient from 1-point and 2-point analyses, using $R_{u_L,E[u_{is}]}$ (Hilbert transform envelope based approach) and $R_{u_L,\sigma_{u,is}}$ (wavelet energy based approach). The high magnitude of the correlation close to the wall for u reveals robust correlation between the large- and small-scale amplitude variations of the small scales. The two metrics– envelope based and wavelet energy based analyses – show identical results despite being rather different approaches for representing the smaller scales. This consistency confirms the equivalency of the two metrics in measuring the small-scale amplitude variations in u, and reiterates the existence of amplitude modulation in this smooth-wall flow. Further, the two-point analysis, which is a more direct measure of the amplitude modulation of the outer large scales (independently sampled) on the near-wall small scales, show even larger correlation coefficients for the u velocity component. This observation is consistent with that noted from analysis of hotwire measurements in chapter 3 (figure 3.3). Not available in the hot-wire measurements were time series of v. Here, analysis of v time series (figure 5.2)

also reveals strong amplitude modulation. These levels of modulation of the v velocity component agrees well with the observations of Talluru *et al.* (2014) who investigated and demonstrated the modulation of all three velocity components using multi-component hot-wire anemometry.

When simultaneous time-series data is available at multiple wall-normal positions, as is the case with DNS data and the current PIV data, it is helpful to visualize the amplitude modulation correlation coefficients as multi-point contours, instead of one- or two-point profiles as done above as a means to relate to hot-wire observations that are not amenable to such an approach. Bernardini & Pirozzoli (2011); Eitel-Amor *et al.* (2014), etc. used this approach to identify the outer location in the logarithmic region to which the modulation correlates best. Figure 5.3 shows the same for both the streamwise and wall-normal velocities, where y_i^+ refers to the wall-normal location where the small scales are sampled, and y_o^+ refers to the location where the large scales are sampled. Extracting the values on $y_i^+ = y_o^+$ line recovers the one-point correlation coefficients in figure 5.2, and the values along the line at $y_o^+ = \sqrt{15Re_\tau}$ recover the two-point correlation coefficients in this same figure. The presence of a secondary peak close to the wall at $y_o^+ \approx 150$ for both the u- and v- correlations provides a direct measure of amplitude modulation of the near-wall scales, and that the near-wall correlation is not simply a manifestation of the small-scale skewness (Schlatter & Örlü, 2010*b*; Bernardini & Pirozzoli, 2011; Mathis *et al.*, 2011*b*). It was shown by Bernardini & Pirozzoli (2011) that this secondary peak is absent in a synthetic signal with identical skewness characteristics of the measured signal.

Though consistency with previous hot-wire analyses are found, a few important distinctions can also be observed in the current PIV results when compared to hot-wire analysis. Firstly, the zero-crossing of the correlation coefficient in the 1-point metric occurs much closer to the wall, with remainder of the correlation being negative through the rest of the boundary layer. A plateau that is reported at higher Re in the buffer region is also not present in the current correlation coefficients (Mathis *et al.*, 2009*a*). This, we speculate, is due to the much smaller

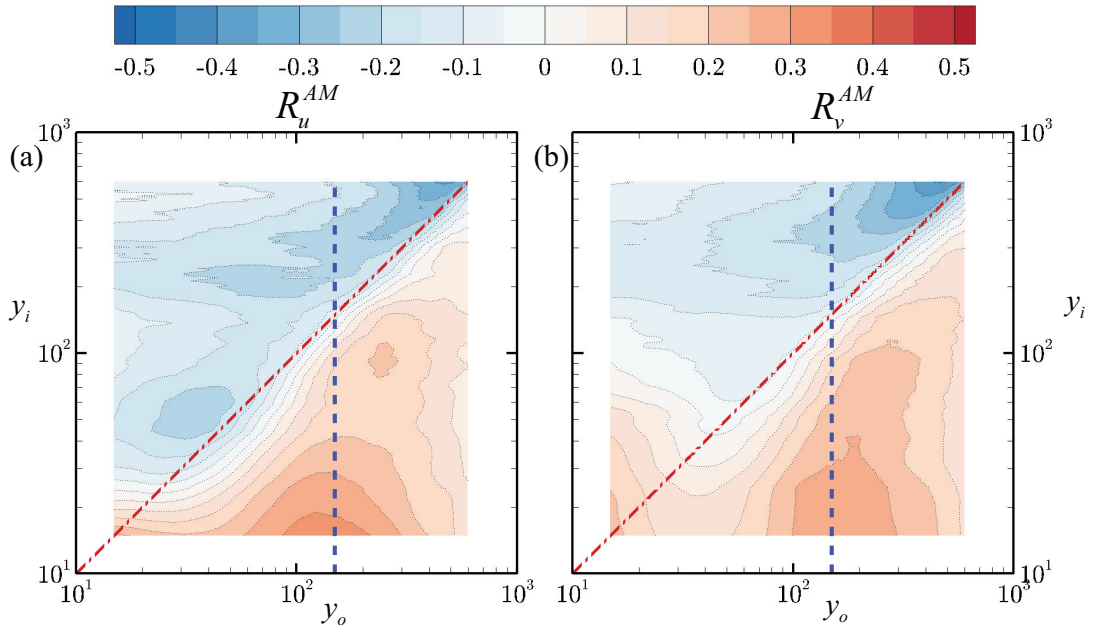

Figure 5.3: Multi-point AM correlation coefficient for (a) streamwise velocity and (b) wall-normal velocity. *Blue* dashed line indicates 2-point correlation coefficient values, and *red* line indicates the 1-point correlation coefficient values reported in figure 5.2.

Re_τ in the current RIM experiments, compared to these previousl wind-tunnel experiments. The same can be observed in the amplitude modulation correlation coefficients found via DNS simulations at smaller Re_τ, where the near-wall correlation peak in 1-point analysis is confined much closer to the wall (Bernardini & Pirozzoli, 2011; Eitel-Amor *et al.*, 2014). This peak grows in wall-normal extent with increasing Re_τ (Mathis *et al.*, 2009*a*), and the plateau becomes evident with corresponding increase in scale separation between the logarithmic and near-wall regions of the flow. Finally two metrics of amplitude modulation analysis (Hilbert transform and wavelet transform) show consistent results, similar to observations made in section 3.2 and 3.3 for hot-wire analysis.

5.2.2 Frequency modulation

Similar to section 3.3, the velocity time series extracted from the PIV data can be used to perform frequency modulation analysis. Figure 5.4 shows a sample

wavelet power spectrum (WPS) computed from the smooth-wall PIV time series. The time average of this wavelet power spectrum fully recovers the mean energy distribution among various scales in the pre-multiplied energy spectrum. A procedure similar to the one outlined in section 3.3 was used to compute the instantaneous frequency evolution of the signal, where the first moment of the energy distribution at all scales for any given instant was defined to be the corresponding 'instantaneous frequency ($\tilde{f}$)'. The current section discusses the single-, two- and multi-point correlation analysis between the larg- scale streamwise velocity fluctuations and the large-scale variations of the instantaneous frequency ($\tilde{f}_L$) of the u and v components of velocity, similar to the amplitude modulation analysis discussed above.

Figure 5.5 shows the 1-point and 2-point frequency modulation correlation coefficients in u and v. The frequency modulation coefficients for u show similar behavior to that identified in the amplitude modulation coefficients. In particular, the 1-point correlation coefficient for u shows a strong peak close to the wall before becoming negative away from the wall, and the 2-point correlation coefficient for u indicates positive frequency modulation coefficients. The multi-point correlation contours, shown in figure 5.6, indicate a structure similar to the amplitude modulation counterparts (figure 5.3), thus confirming the presence of inner–outer interactions. The frequency modulation of the wall-normal velocity v is markedly different from its streamwise counterpart as well as the amplitude modulation coefficient trends for v. Both the single- and multi-point correlation coefficients in v reach maxima in the logarithmic region and show a diminishing correlation of instantaneous frequency close to the wall. This trend can be understood by noting that the v velocity component is dampened very close to the wall due to the no-penetration boundary condition. The current study is the first, and only study so far, to investigate frequency modulation of the wall-normal velocity component, and it would be interesting to compare these conclusions with observations from DNS or hot-wire approaches that would be better optimized for this purpose.

Important distinctions are also evident in the trends of the current frequency

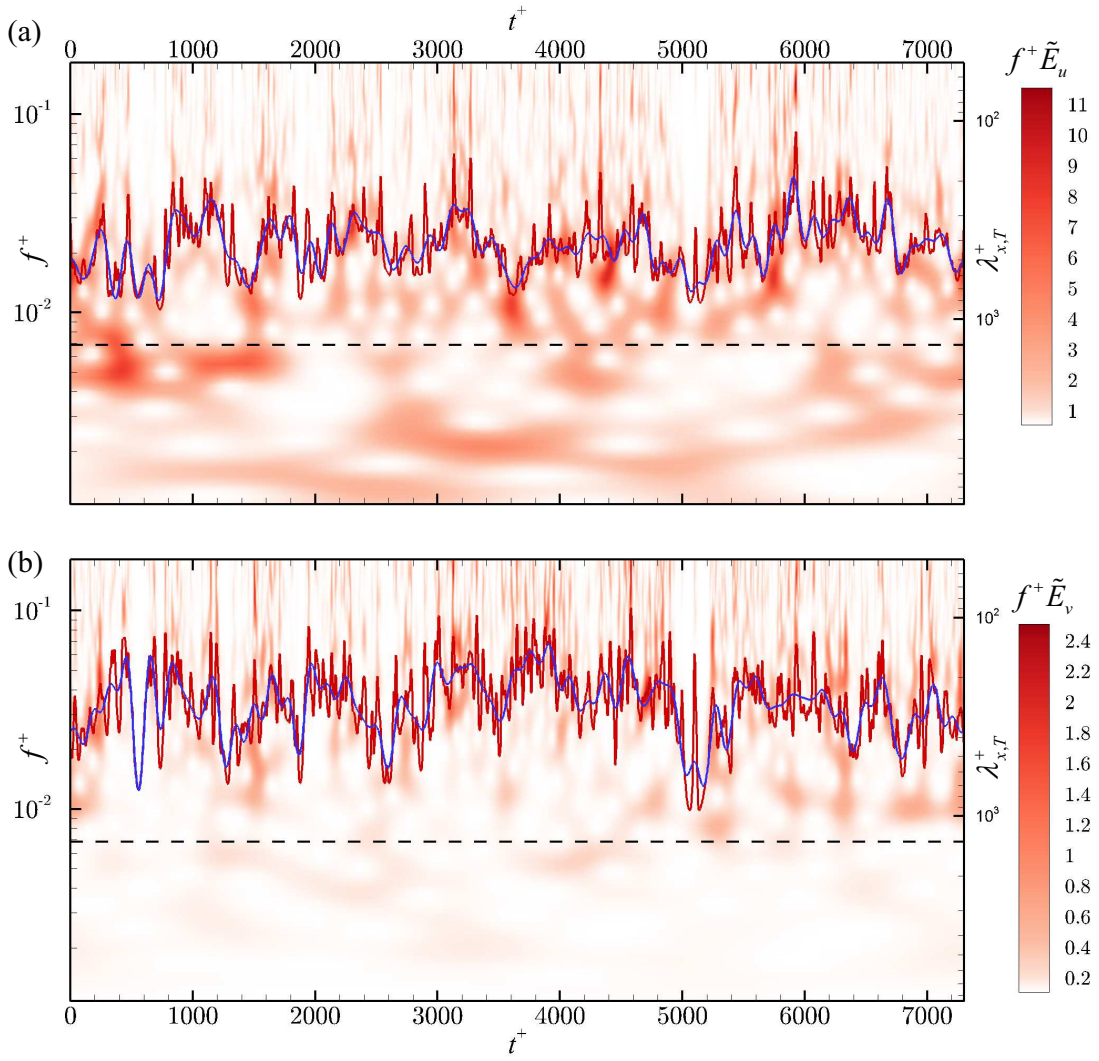

Figure 5.4: An example premultiplied wavelet power spectrum of (a) u and (b) v velocities at $y^+ = 24$. Also shown are the cut-off wavelength ($= \delta^+$, *dashed*), instantaneous frequency ($\tilde{f}$, *red*) and large scale instantaneous frequency changes with time ($\tilde{f}_L$, *blue*).

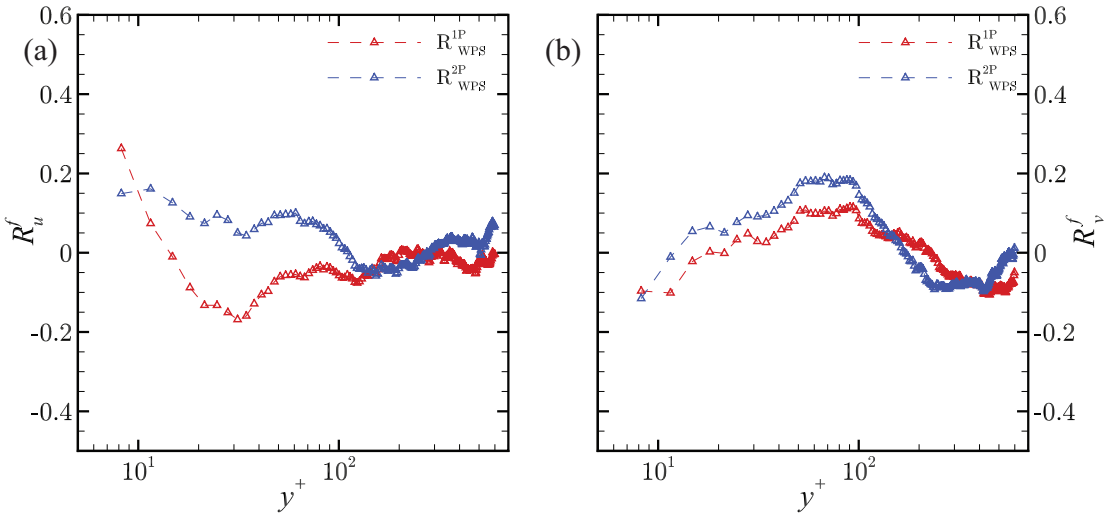

Figure 5.5: 1-point and 2-point frequency modulation in (a) streamwise and (b) wall-normal velocities using wavelet-energy based method from sFOV.

modulation coefficients compared to their hot-wire counter parts in section 3.3. First, the frequency modulation of u appears weaker in the current flow as reflected by the lower correlation coefficient (~ 0.2 vs 0.4 from hotwire analysis). Interestingly, the current frequency modulation correlation becomes negative away from the wall in one-point analysis, which is contrary to the observations in section 3.3 and Baars *et al.* (2015) where the coefficient decreased to nearly zero. The wall-normal velocity coefficient has a diminishing coefficient close to the wall, though, as reflected in the multi-point correlation maps. This diminishing correlation could be a combination of low-Re effects, no-penetration wall effects and perhaps limitations of PIV for this specific analysis (see section 5.2.3). The data, however, clearly indicate the presence of frequency modulation in the flow using the current analysis techniques.

5.2.3 Effect of noise on modulation coefficients

There are a few important distinctions between the hot-wire and high-frame-rate PIV measurements made here, relative to the respective boundary layers. In inner units, the time resolution of the hot-wire measurements was an order of magni-

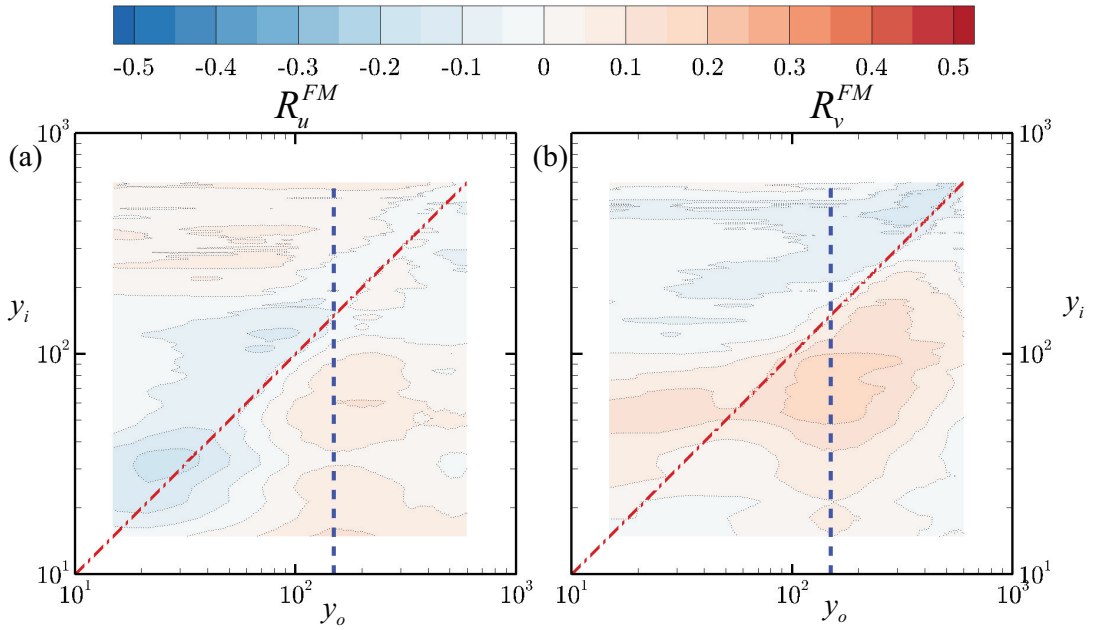

Figure 5.6: Multi-point FM correlation coefficient for (a) streamwise velocity and (b) wall-normal velocity. *Blue* dashed line indicates 2-point correlation coefficient values, and *red* line indicates the 1-point correlation coefficient values reported in figure 5.5.

tude higher than the PIV experiments ($\approx 0.3t^*$ in hot-wire versus $\approx 3t^*$ in PIV). Further, the interrogation windows in the current PIV measurements were much larger than the size of the hot-wire probes used ($0.2y^*$ linear dimension in hotwire vs $6.6y^*$ in current PIV). This results in a higher degree of spatial averaging in the PIV measurements and thus diminishes the ability of PIV to measure the small scales compared to the hot-wire probes. Furthermore, the linear interpolation that was necessary to correct intermittent PIV data, especially close to the wall (section 5.1), adds noise to the higher frequency portion of the wavelet power spectrum. Likewise, in addition to spatial averaging, there are additional sources of noise in PIV that are exacerbated close to the wall. Despite the relatively small physical scales of the PIV interrogation windows, significant shear can exist across each window which result in a bias of the measured velocity. Relatively lower seeding density and sub-pixel estimation used in PIV also compounds near-wall PIV measurements by adding random and bias errors to the measurements (Adrian &

Westerweel, 2011). Particularly, the wall-normal particle displacements close to the wall used to measure wall-normal velocity fluctuations are much smaller compared to the streamwise displacements. Thus, the fixed sub-pixel estimation error (typically 0.1 px throughout) reduces the signal-to-noise ratio of the wall-normal velocity measurements. This effect is stronger in the bFOV measurements than sFOV ones due to smaller mean particle size and displacements in the former.

The effect of noise and decreased resolution on the metrics of modulation, i.e., correlation coefficients R^a and R^f, can be analyzed by simulating the errors of the PIV measurements with the hot-wire time series. Doing so was done by subsampling the hot-wire time series data to reflect the more limited time resolution of the PIV measurements, and/or by adding a white Gaussian noise to the same with a prescribed signal-to-noise ratio (Σ). By progressively increasing the Σ, one can investigate the effect of noise on the various modulation coefficients discussed in the previous sections.

Figure 5.7 shows the effect of Σ-only, on the amplitude and frequency modulation coefficients in u. The frequency modulation correlation is much more sensitive to the presence of noise compared to the amplitude modulation correlation. This, in a sense, is evident as FM uses the first moment of the energy distribution at various frequencies, while AM only uses the energy at larger scales. Thus, relatively small changes in the energy distribution are more likely to effect the first frequency moment of the same, while the integrated small-scale energy *fluctuations* are 'preserved' (though the integral energy magnitude is going to increase due to added noise). This analysis partly explains the weaker frequency modulation coefficients in the current experiments in both streamwise and wall-normal velocities compared to previous studies, yet a better agreement of the amplitude modulation counterparts.

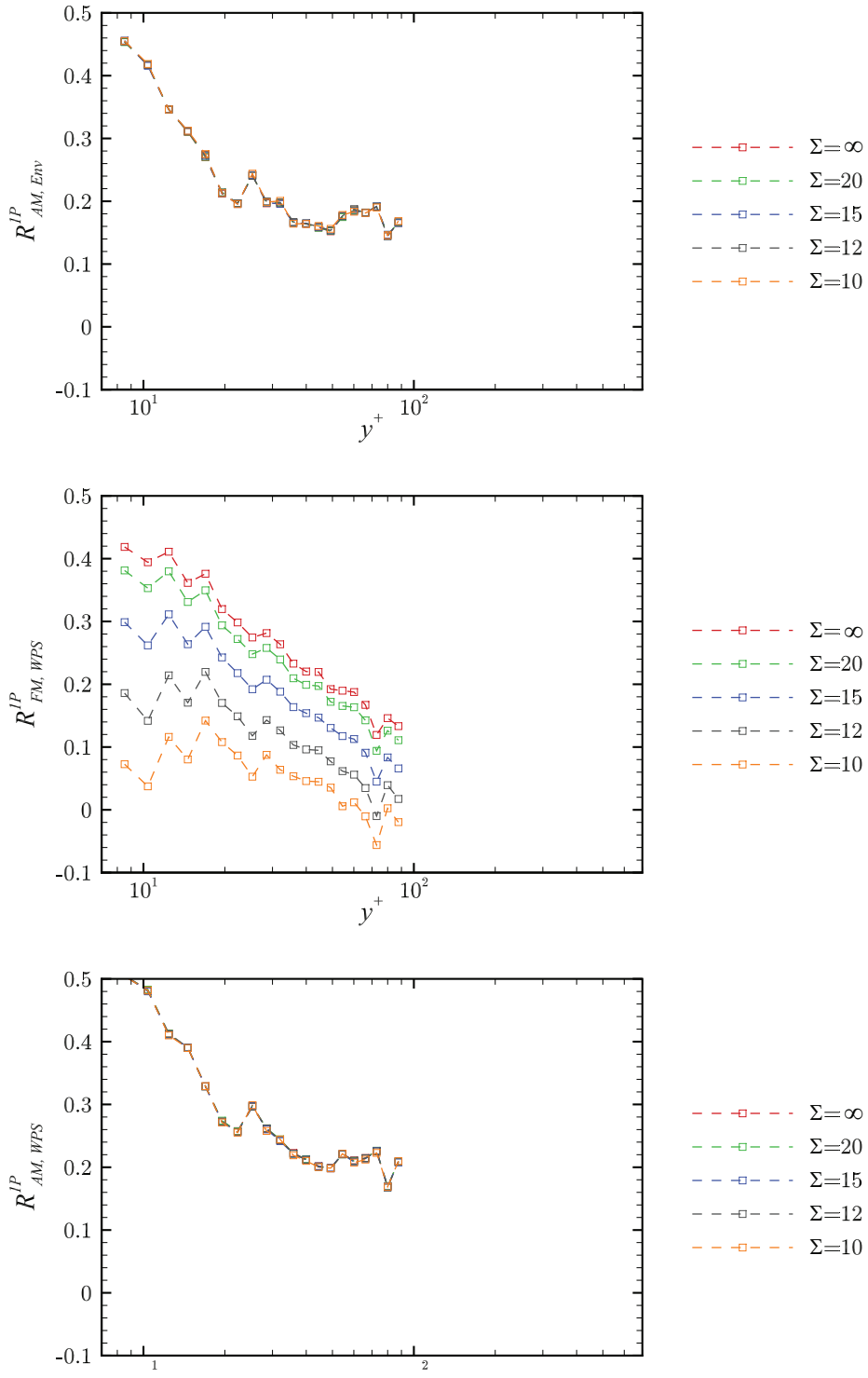

Figure 5.7: Sensitivity of signal-to-noise ratio (Σ) of added Gaussian noise on amplitude and frequency modulation correlation coefficients by envelope and wavelet energy methods. Data is from hotwire measurements (section 3). Only near-wall coefficients are shown here.

5.3 Spatio-teporal conditional averages

With the amplitude and frequency correlation examined in the previous section, further investigations of the inner-outer interactions can be done using the PIV data. Besides correlations, by conditioning the large-scale events and averaging, the spatial signatures of the inner–outer interactions can also be captured using the high-frame-rate PIV data, along with their temporal evolution. Doing so leverages the *spatial* information captured within the PIV FOV, and thus provides even richer information on the spatial characteristics of these interactions than previously reported hot-wire measurements. The current section aims to develop these ideas, and establish spatio-temporal tools that provide a more complete picture of these interactions using the high-frame-rate PIV data acquired.

To statistically investigate the effect of the large scales in the flow on the small scales close to the wall, the current study investigates the methods of simple conditional averaging. Conditional averaging requires definition of a 'conditional *event*' criterion, and an ensemble of realizations that satisfy the event criterion. Single- or multiple criteria can be defined based on flow or experiment quantities, such as velocity, pressure, temperature, inlet conditions etc. However, in experiments such as the current experiment, where the data acquisition is exclusive of the conditional events, more complex criteria occur more rarely, and it usually requires an exponentially large ensemble of raw data to extract sufficient number of conditional events for statistical analyses. While methods such as stochastic estimations (Adrian, 1977) are available to offset impractically large raw-data requirements to a limited extent, the current analysis does not require the same. The following section describes the statistical criteria and the ensemble of data thus acquired.

5.3.1 Zero-crossing conditional event

The conditional event in current context is used to identify and pin the large scale events in a time-space definition. Throughout the current study so far (and much of literature on inner-outer interactions), the streamwise velocity is used as a representative measure of the outer layer structures, and correlations have been performed on the same. In other words, the changes in the near-wall cycle have been observed in conjunction with the fluctuations in streamwise velocity in the logarithmic region. This was performed via the correlations of various quantities pertaining to the near-wall dynamics (such as near-wall velocity envelope, frequency, skin friction, etc.). The same can also be performed using conditional averages, as was also explored in Baars *et al.* (2015). For this purpose, the conditional event considered herein is defined as the occurrence of *positive zero-crossing of the large scale at the center of logarithmic region*. The following steps elucidate the conditional averaging procedure:

1. The large-scale temporal evolution of the streamwise velocity, u_{oL}, is extracted at a reference point, $\mathbf{x_o} = (x_o, y_o)$: the geometric center of the logarithmic region given by $y_o = \sqrt{15Re_\tau}$ (Ng *et al.*, 2011) and at $x_o = 0$. The time-series (extracted in section 5.1) at the reference point is filtered for large scales using a cut-off filter $\lambda_c^T = 2\delta$, similar to that for temporal-only analysis discussed in sections 3.2 and 5.2. Here, superscript T is added to the filter length definition to distinguish a temporal-filter applied in a Taylor's hypothesis sense from actual spatial filter.

2. **The instances $\tau_{\mathbf{o}^+}^{\mathbf{i}}(\mathbf{i} = \mathbf{1}, \mathbf{2}..\mathbf{n})$ where the large scale crosses from negative to positive (with time, t) are identified. These instances are referred to as the "positive zero-crossings ($\tau_{\mathbf{o}^+}$)" of the large-scale structure, and form the conditional events for the current**

analysis. In other words, the conditional event can be defined as

$$u_{oL}(\tau_{o^+}) \equiv u_L(x_o, y_o, \tau_{o^+}) = 0$$

and

$$\frac{\mathrm{d}u_L}{\mathrm{d}t}(x_o, y_o, \tau_{o^+}) > 0$$

3. The zero-conditioned ensembles of the velocity fields in bFOV and sFOV are formed by collecting the velocity vector fields as

$$[\mathbf{u}|_{o^+}(x, y, \tau)]_i = [\mathbf{u}(x, y, \tau_{o^+} + \tau)]_{\tau^i_{0^+}} . \tag{5.1}$$

   The $\mathbf{u}|_{o^+}$ ensembles around an interval (τ) from $-100t^*$ to $+100t^*$ relative to τ_{o^+} are formed. For the data collected in the current experiments, 316 positive zero-crossing events were found and formed the ensemble for each τ.

Figure 5.8 shows an example outer large-scale extracted at the above mentioned reference point (x_o, y_o). The positive zero-crossings of the large scale signal are identified, along with example temporal neighborhoods around them of width $[-100\,t^*, 100\,t^*]$ considered for the current study. For a few positive zero-crossings that occur close to each other (within $200\,t^*$ in current case), the neighborhoods overlap, and conditional instances occur repeatedly as part of multiple ensembles. But these were few and in-between, and occur at most in two neighboring ensembles. For this reason, and to stay true to the condition imposed, we do not impose any exceptions for such occurrences. Shown in figure 5.8 is the ensemble average of all zero-crossing temporal neighborhoods of large scale signals, $\langle u_{oL}(\tau)\rangle|_{\tau_{o^+}}$. The temporal neighborhood, τ, considered herein embodies an averaged crest and trough of the large scale structures in the flow at time delays $\tau_\uparrow \approx 50$ and $\tau_\downarrow \approx -50$ respectively.

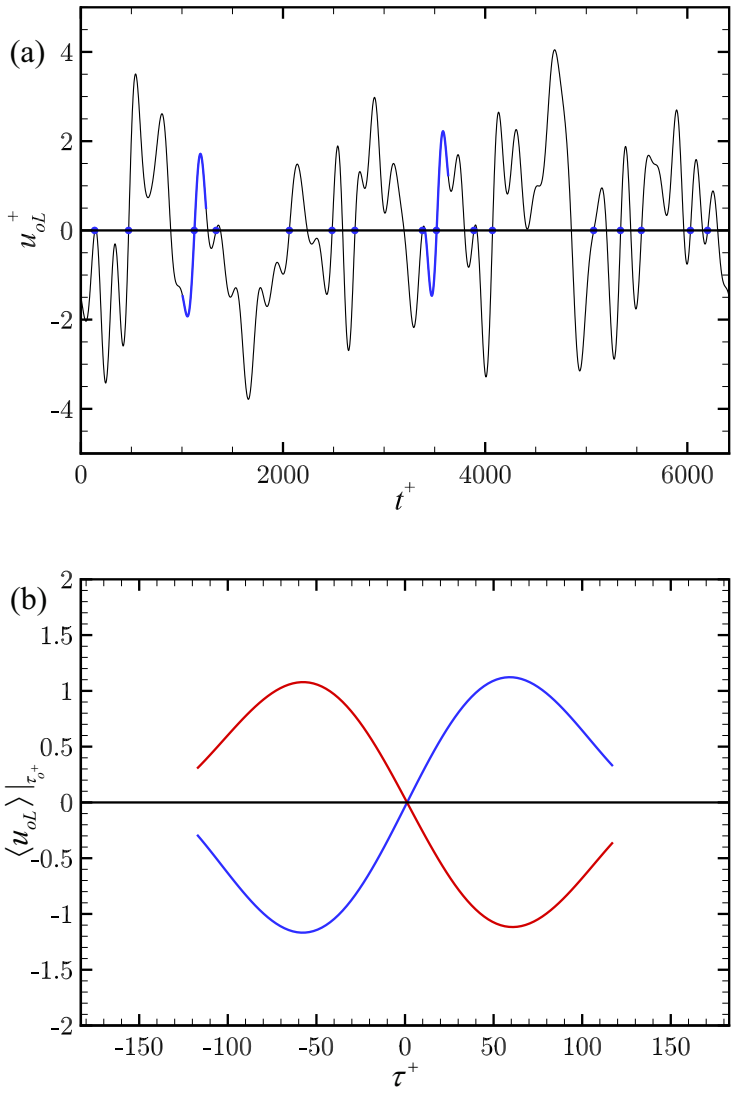

Figure 5.8: (a) An example outer large scale time series ($u_{oL}(t^+)$), with all positive zero-crossing points (τ_{o^+}) and two example neighborhoods of width $200t^*$ marked in *blue*. (b) The ensemble average of all these positive zero-crossing neighborhoods (*blue*, $\langle u_{oL}(\tau)\rangle|_{\tau_{o^+}}$) and negative zero-crossing neighborhoods (*red*, $\langle u_{oL}(\tau)\rangle|_{\tau_{o^-}}$, not marked in (a)).

The entire analysis can also be performed with a conditional event defined on negative zero-crossings of the large scale signature. The figure 5.8 shows such an averaged negative zero-crossing event of large scales, along side the positive counterpart. As expected, the structure is symmetric, with the temporal point of reference merely translated in time. All observations reported here were found to be nearly identical, and thus only the positive zero-crossing events are reported here. It is also possible to reverse the temporal direction for negative zero-crossing averages for all quantities, and obtain a larger ensemble of events from same raw data by assuming symmetry of modulating physics for $+ve$ and $-ve$ fluctuations of large scales. But this assumption was not considered for the current study, and only positive zero-crossings are considered.

5.3.2 Spatio-temporal footprint of the large scale

From the velocity fields of zero-crossing conditional ensemble, the streamwise spatial footprint and the temporal evolution of the conditional event can be calculated by ensemble averaging as $\langle \mathbf{u}|_{o^+}(x, y_o, \tau)\rangle_i$. Figure 5.9 compares the spatial footprint of the conditional averaged large scale with the temporal average of the same that was considered earlier in figure 5.8, except that the the time axis in the latter is transposed into spatial axis using Taylor's hypothesis (i.e., $x \equiv -U_o\tau$). This comparison reemphasizes the applicability of the Taylor's hypothesis for the large convecting scales, as the two measures of the structures are practically identical. Figure 5.10 further shows the conditional averaged streamwise footprint of u- and v- velocities from the bFOV camera that extend longer in the streamwise direction at three different sample times, τ. The opposite signs of the u- and v- averaged quantities at all times and positions is expected, since the average Reynolds shear stress ($\langle uv \rangle$) throughout the boundary layer is negative, as was also shown in figure 4.9. The temporal evolution of the large scale at the reference point can be seen as convection of the large scale through the reference point, as shown by the temporal snapshots in figure 5.10.

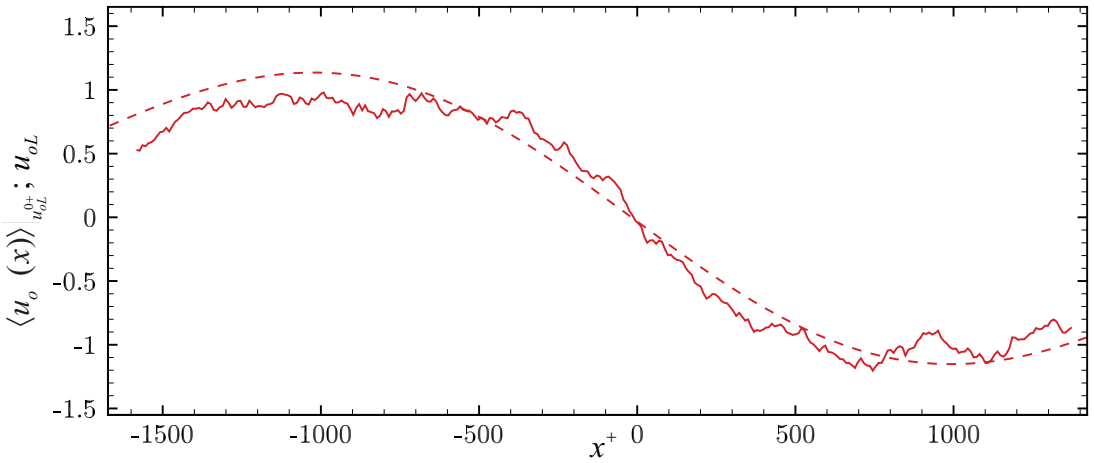

Figure 5.9: The x-spatial signature of the large scale ($\langle u_o(x)\rangle_i$, *solid*) compared with temporal large scale at $(0, y_o)$ ($\langle u_{oL}\rangle|_{\tau_{o^+}}(-U_o\tau)$, *dashed*).

With this understanding, figure 5.11 shows the full spatial conditional average of the velocity fields at the zero-crossing time instant, τ_o. The inclined large scale structure of the averaged velocity field is evident, as was measured earlier using point hotwire measurements (section 3.4 and figures 3.16 and 3.13).

For further analyses on the modulation effects, we consider this spatio-temporal picture of the conditional average for each time τ to be the corresponding measure of the large scale. In other words, the filtered 'slow' fluctuations at a reference point (x_o, y_o) were used to define the conditional ensemble. The conditional average of these fields for each time, τ, is henceforth defined to be the spatial signature of the large scale for the time instant relative to the conditional structure. Thus, the spatial filter is equivalent to a top-hat spatial filter of filter length equal to the dimensions of FOV (sFOV for small scales), which in the current case is equivalent to $1000\,y^*$.

5.3.3 Conditionally averaged large-scale–small-scale organization

Given the definition of the large scale in the previous section, the small scales in each instance can be extracted as follows.

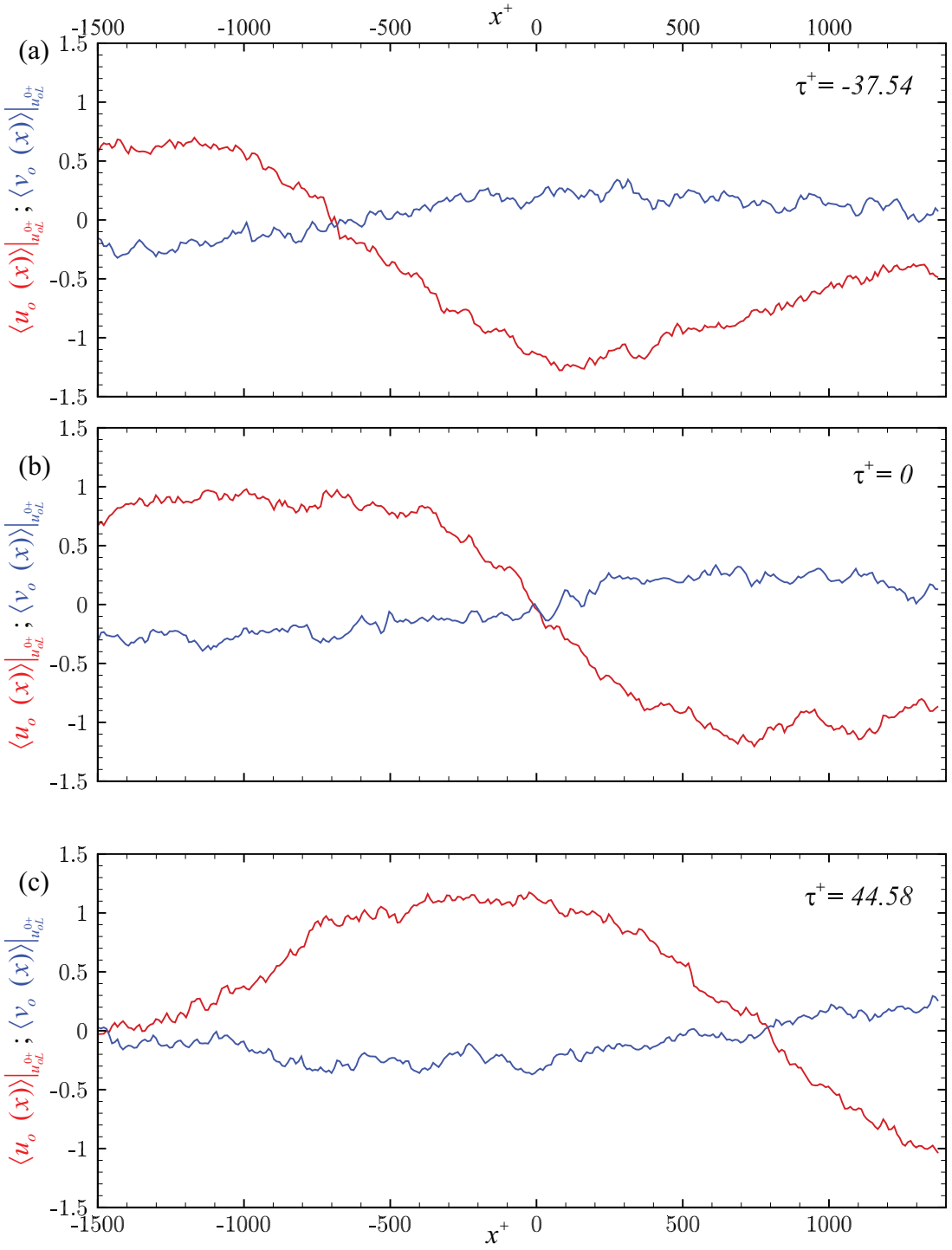

Figure 5.10: The x-spatial signature of the large scale shown in figure 5.8 at three different instances relative to zero-crossing time τ_{o^+}.

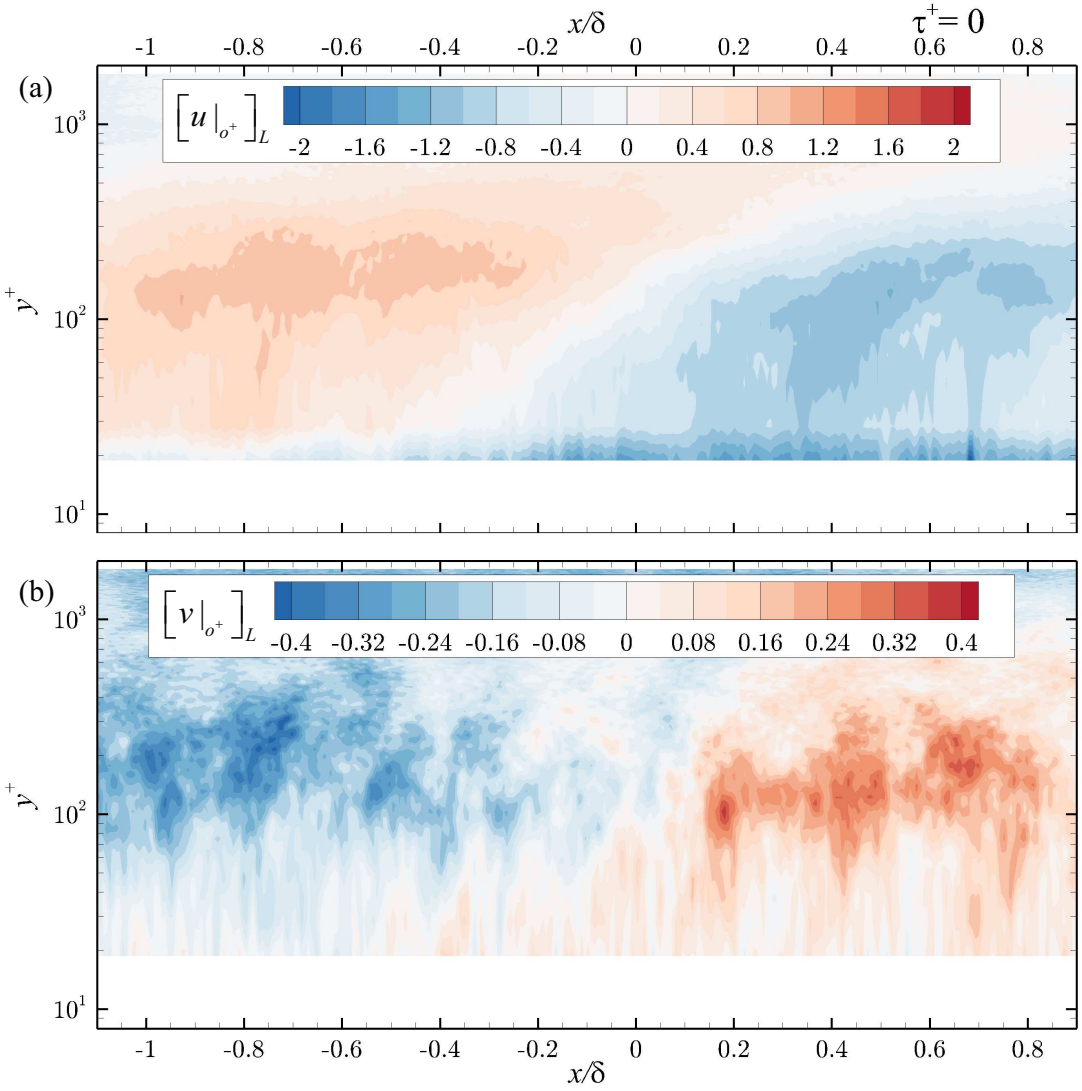

Figure 5.11: (a) $\langle u|_{o^+}\rangle_i$ and (b) $\langle v|_{o^+}\rangle_i$ – the spatial signature of the large scale corresponding to τ_o, and given by Eqn. (5.2) (see also Appendix B).

$$[\mathbf{u}|_{o^+}]_L = \langle \mathbf{u}|_{o^+} \rangle_i, \tag{5.2}$$

$$[\mathbf{u}|_{o^+}]_s^i = \mathbf{u}|_{o^+}^i - [\mathbf{u}|_{o^+}]_L \,, \tag{5.3}$$

where $\langle \cdot \rangle_i$ denotes ensemble averaging over all individual occurrences. The variance of the small scales will then indicate the energy in the small scale turbulence for each instant, and the ensemble average ($\langle [u|_{o^+}]_s^2 \rangle_i = fn(x, y, \tau)$) will quantify the mean turbulence intensity distribution and evolution for the corresponding large scale structure. The structure of the large scales, and the corresponding small scale energy distribution can be seen in figures 5.12–5.14 for the various example instances discussed before. For all the instances, the presence of high small scale turbulence associated with a large scale positive fluctuation, and low small scale turbulence relative to the large scale negative fluctuation is evident.

Further, to better highlight the differences in the small scale turbulence intensity ($\langle [u|_{o^+}]_s^2 \rangle_i$) in the conditionally averaged profiles, the small scale energy discrepancy can be computed by subtracting the unconditional intensity distribution, and only considering the perturbation from this mean. This can be shown, by assuming $\langle [u]_s^2 \rangle \equiv \langle [u|_{o^+}]_s^2 \rangle_{\tau,x}$, as

$$\Delta \langle [u|_{o^+}]_s^2 \rangle = \langle [u|_{o^+}]_s^2 \rangle - \langle [u]_s^2 \rangle, \tag{5.4}$$

where $\langle \cdot \rangle_{\tau,x}$ denotes time-averaging and streamwise averaging to compute the unconditional quantities on the entire ensemble of occurrences.

Figures 5.12 - 5.14 show three time instances of conditionally averaged large scale, $[u|_{o^+}]_L$, conditionally averaged small scale variance, $\langle [u|_{o^+}]_s^2 \rangle_i$, the discrepancy of the latter from the unconditioned mean, $\Delta \langle [u|_{o^+}]_s^2 \rangle$. The instances are chosen that best capture the large scales and the structure of small scale variance together, and around $\tau = \tau_\downarrow, 0$ and $\tau_\uparrow$ respectively. A few observations can clearly be made from the structural organization. Most importantly, a strong correlation

of the large scales and the small scale turbulence is evident. With increasing τ, as the large scale convects from a low-momentum event to the zero crossing event and towards high-momentum event, the the associated small scale influence also trails the large scales via a decrease in small scale turbulence towards an increase in turbulence respectively. The discrepancy plots identify the location of maximum modulation effect of the small scales close to the wall, which appears to be trailing the large scale occurrence when viewed in an Eulerian sense. More importantly, these observations directly support the conclusions drawn in the current study using two-probe hotwire measurements (section 3.4) and in the literature (Jacobi & McKeon, 2013; Baars *et al.*, 2015, etc.), where the amplitude and frequency modulation effects trail the large scale effects in time when the latter are measured away from the wall.

Figures 5.15 - 5.17 further shows the small scale variance in wall-normal velocity component. A similarly strong correlation, as indicated by point-temporal analysis (section 5.2), is reiterated in these spatial plots at the three temporal instances shown here. The small scale wall-normal turbulence also trails in the modulation effects with the large scales. These observations are clear quantitative depictions of the spatio-temporal structure of the amplitude modulation interaction.

5.3.4 Scale modulation

The presence of amplitude, frequency and scale modulations can be explained by the QSQH hypothesis (Zhang & Chernyshenko, 2016). We expect that high-momentum event of the large scales enhances the smaller scales of near-wall turbulence, while the low-momentum event of the same enhances the larger scales of the near-wall turbulence. While amplitude modulation and frequency modulation were clearly shown in past and the current study so far, the availability of these spatially rich conditional ensembles enables investigation of scale modulations. In the current section, we try to investigate the presence of any scale modulation

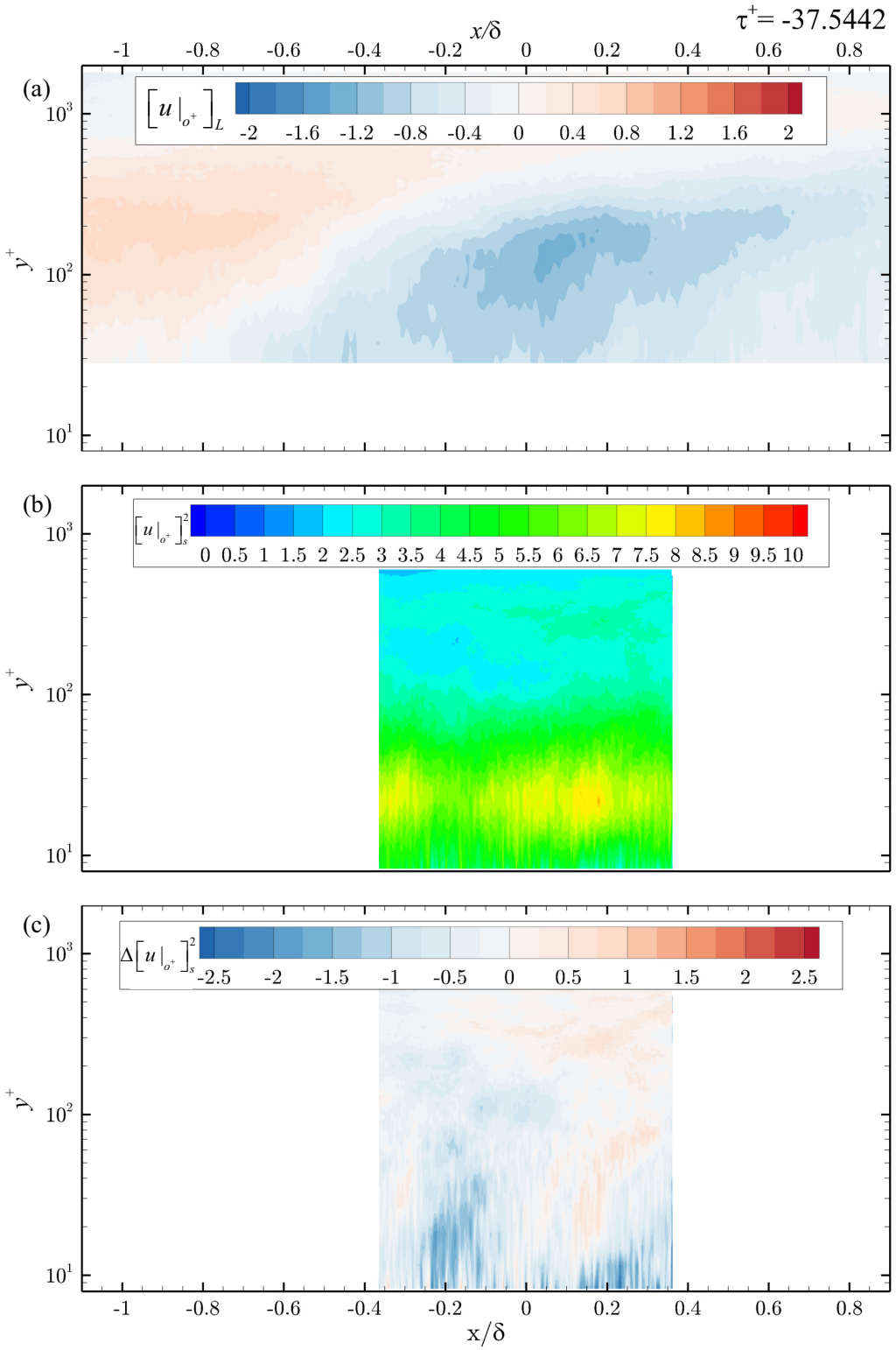

Figure 5.12: Contours of (a) large scale event ($[u|_{o^+}]_L$) (b) small scale variance ($\langle[u|_{o^+}]_s^2\rangle_i$) (c) discrepancy of small scale variance ($\Delta\langle[u|_{o^+}]_s^2\rangle_i$) at $\tau^+ = -37.5$ (see also Appendices C and D).

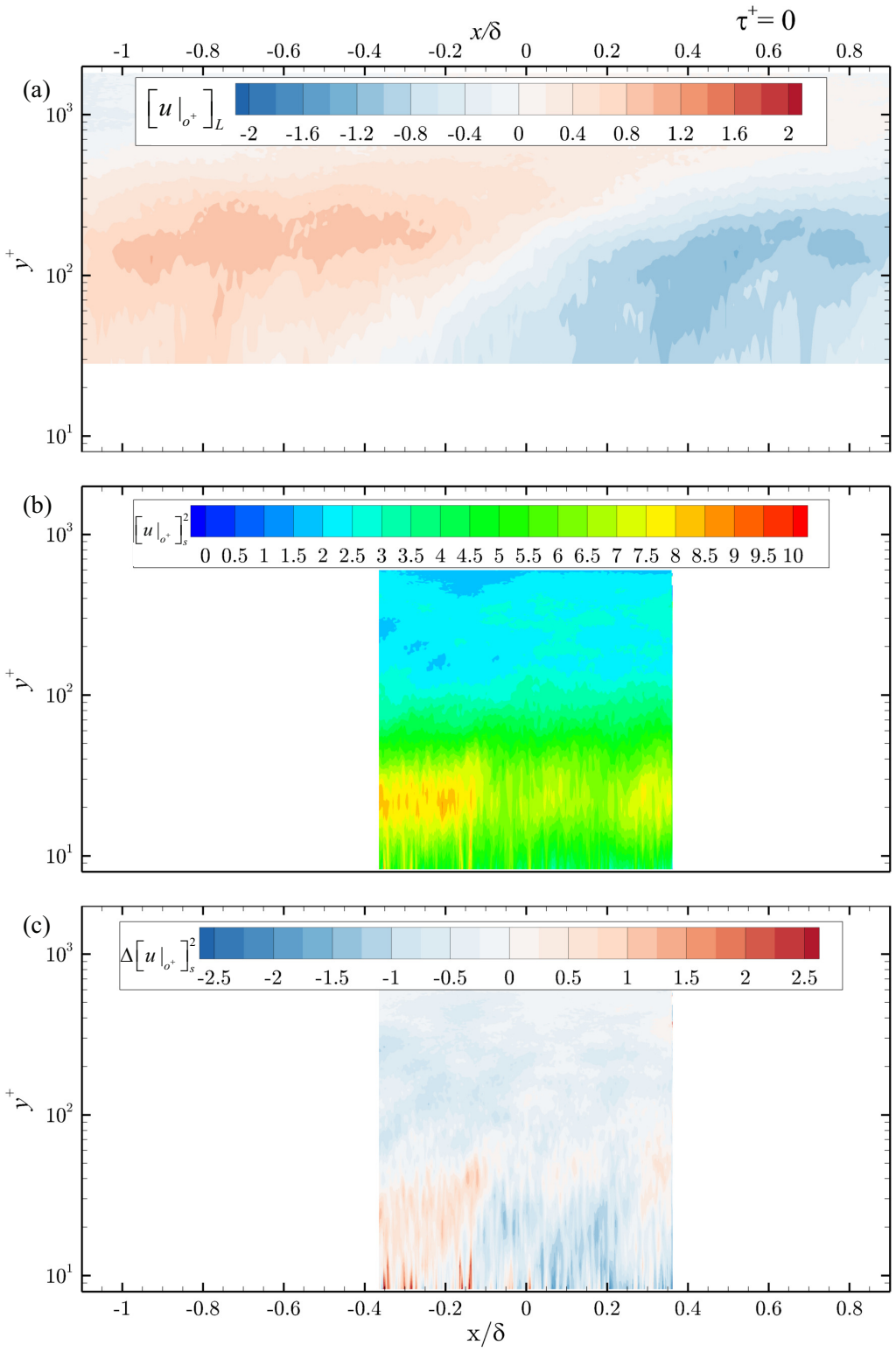

Figure 5.13: As figure 5.12, but at $\tau^+ = 0$ (see also Appendices C and D).

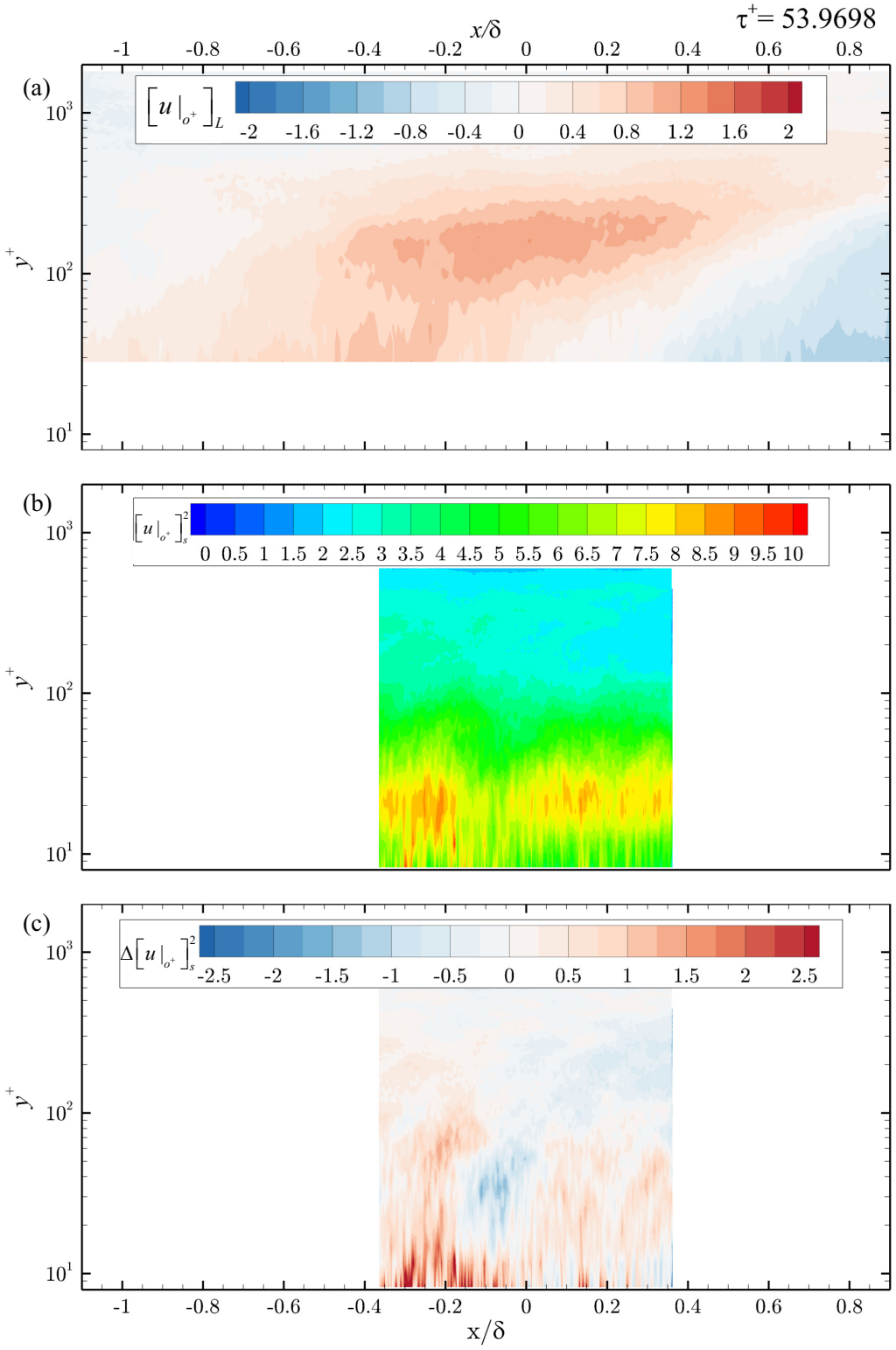

Figure 5.14: As figure 5.12, but at $\tau^+ = 54$ (see also Appendices C and D).

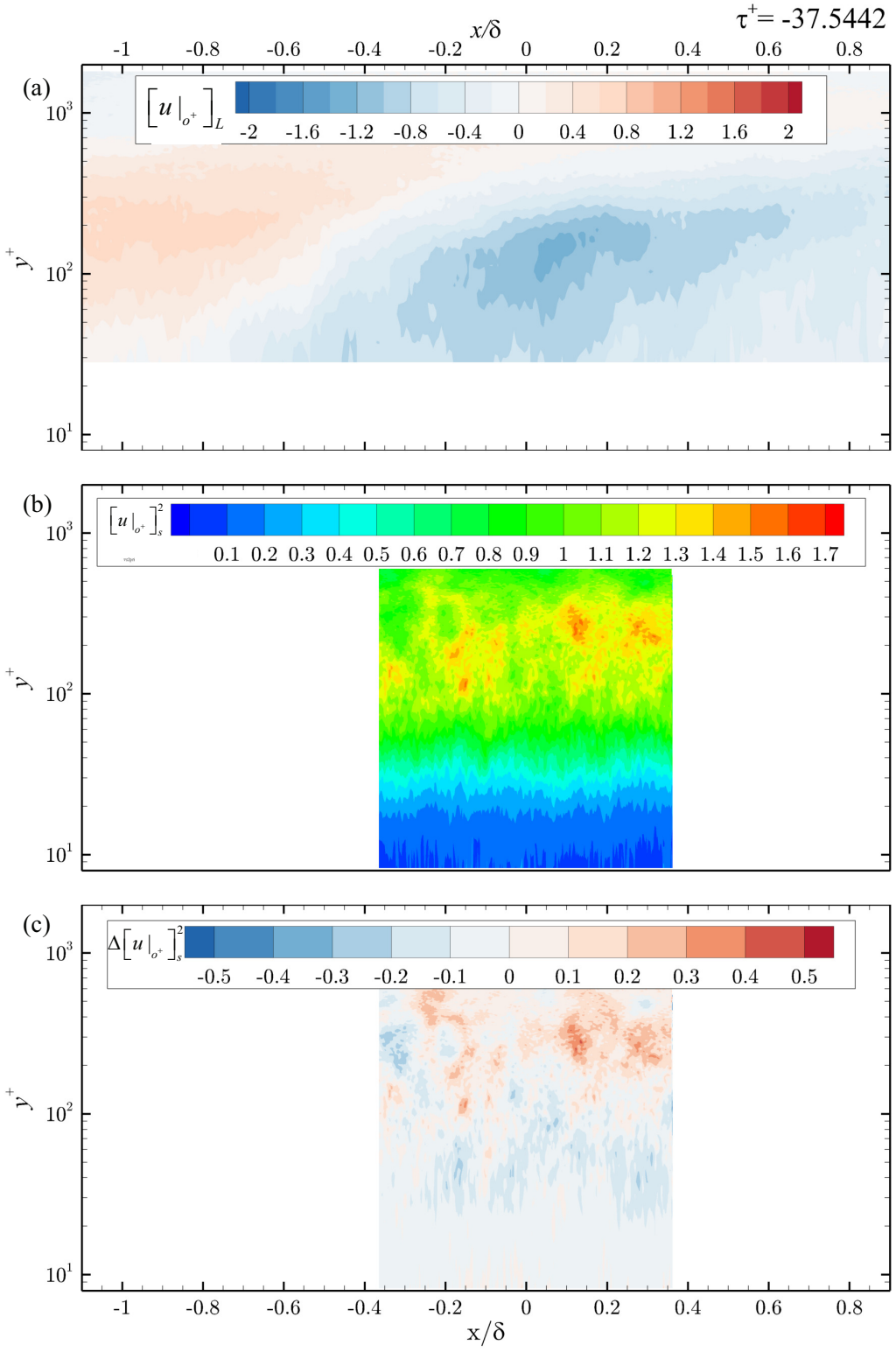

Figure 5.15: As figure 5.12, but for wall-normal small-scales ($[v|_{o^+}]_s^2$) at $\tau^+ = -37.5$ (see also Appendix E).

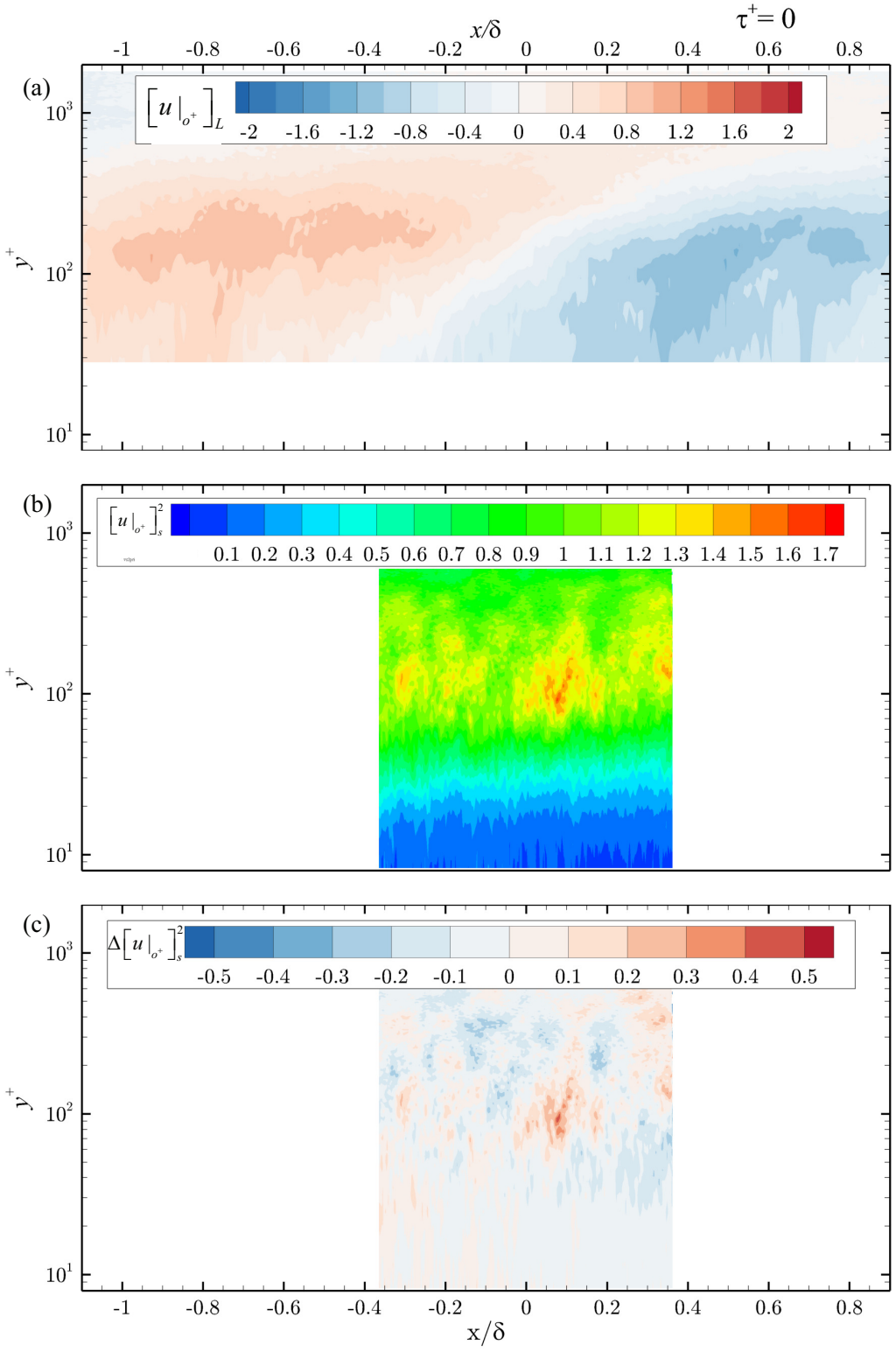

Figure 5.16: As figure 5.12, but for wall-normal small-scales ($[v|_{o^+}]_s^2$) at $\tau^+ = 0$ (see also Appendix E).

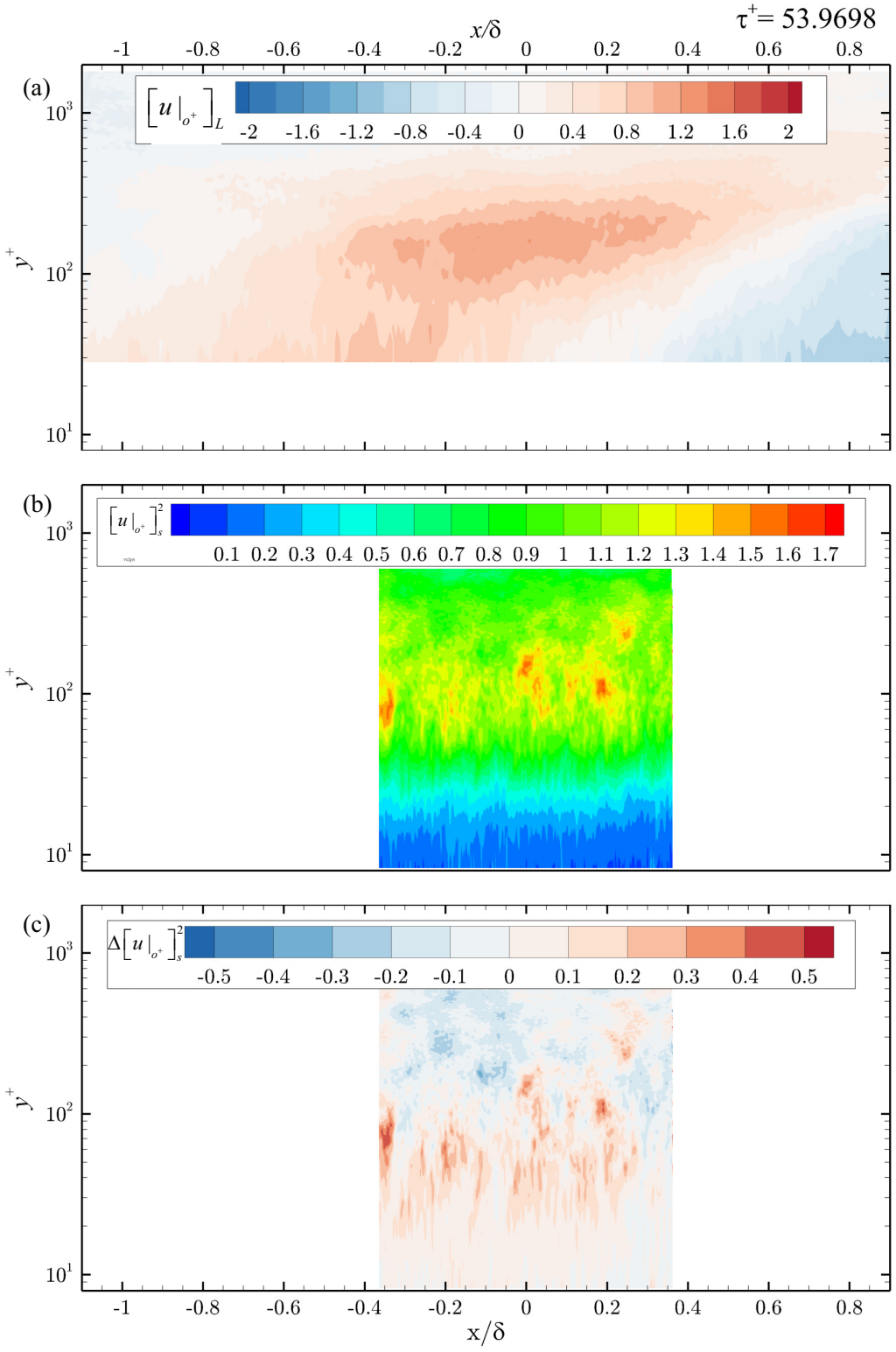

Figure 5.17: As figure 5.12, but for wall-normal small-scales ($[v|_{o^+}]_s^2$) at $\tau^+ = 54$ (see also Appendix E).

in the streamwise turbulent small scales. The methodology, as desicribed below, also provides an alternative measure of amplitude modulation.

1. A reference wall-normal position close to the wall in buffer region is chosen at $y^+_{ref} = 20$. This location, as seen in figures 5.12 - 5.14, undergoes strong modulation influences and is appropriate to observe scale modulations if any.

2. The streamwise velocity signature of small scales $[\mathbf{u}(x, y_{ref}, \tau)|_{o^+}]^i_s$ is extracted at the reference location.

3. The spatial premultiplied spectrum, $\left[k_x\phi_{uu|_{o^+}}(\lambda_x, y_{ref}, \tau)\right]^i_s$ of the above small scale ensemble can be computed, similar to those in section 4.6, and ensemble averaged to obtain $\langle k_x\phi_{uu|_{o^+},s}\rangle_i$, the average energy distribution among various spatial scales of small scale turbulence at the reference location.

Figure 5.18 shows the same, along with the conditionally averaged large scale, $[u|_{o^+}]_L$ for streamwise velocity fluctuations. Also shown is the discrepancy of the spectrum from the time-averaged distribution obtained as

$$\Delta\left[\langle k_x\phi_{uu|_{o^+},s}\rangle\right] = \langle k_x\phi_{uu|_{o^+},s}\rangle_i - \langle k_x\phi_{uu|_{o^+},s}\rangle_{i,\tau}, \tag{5.5}$$

where $\langle\cdot\rangle_{i,\tau}$ indicates both ensemble and time averaging. The discrepancy spectrum shown enhances the differences in the spectra compared to the mean small scale energy distribution. The amplitude modulation is evident with the enhancement and mitigation of the small scale energy in line with the changes in large scale fluctuations, as shown in the discrepancy plots. Any presence of scale modulation should be evident by comparing the average spectrum of energy distribution alongside the conditionally averaged large scale, $[u|_{o^+}]_L$. This should appear as a correlated shift in the near-wall energy peak with the magnitude of the conditionally averaged large scale. The figures, however, do not indicate any obvious

change energy containing scales, besides the magnitude. This could be due to a lack of convergence or insufficient scale separation for any significant scale modulation to be evident. The delay of about $40\,t^*$ between the large scales and the associated small scale energy changes is evident, with the latter trailing the former. This, again, is consistent with the overall picture of these modulations. No energy fluctuations outside of the statistical error were observed in the conditional spectra of the wall-normal velocity fluctuations. This could be because of already weak nature of the wall normal fluctuations near the wall (as can also be seen in figure 4.11), and that the spectral convergence usually requires larger ensembles for convergence.

5.4 Inner-outer interactions in rough-wall boundary layer – a preliminary analysis

The `R19-700` data sets can be used to investigate the preliminary inner-outer interactions over the rough wall. From the boundary layer parameters (section 2.5) and the mean profiles (figure 4.13), we expect a perturbed inner region with dominant viscous effects. The near-wall turbulence peak is not as significant in the rough-wall due to smaller mean shear compared to the smooth-wall (note the difference is contour levels in figures 4.11 and 4.13). However, the wall normal turbulence is relatively strong close to the wall than the smooth-wall due to the presence of roughness. Thus, compared to a smooth-wall, we expect turbulence that is less energetic in streamwise turbulence, and relatively more energetic in wall-normal turbulence. The dynamics are still dominated by viscous effects due to the small roughness effects ($k_s^+ \approx 16$), though the inner-region will be thicker than the smooth-wall boundary layer considered.

Figure 5.19(a,b) shows amplitude modulation correlation coefficient from rough-wall measurements using one- and two-point analysis from the envelope-based analysis. The wavelet based analysis for amplitude modulation gives identical conclusions, and are not shown here. The high correlation coefficient is evident

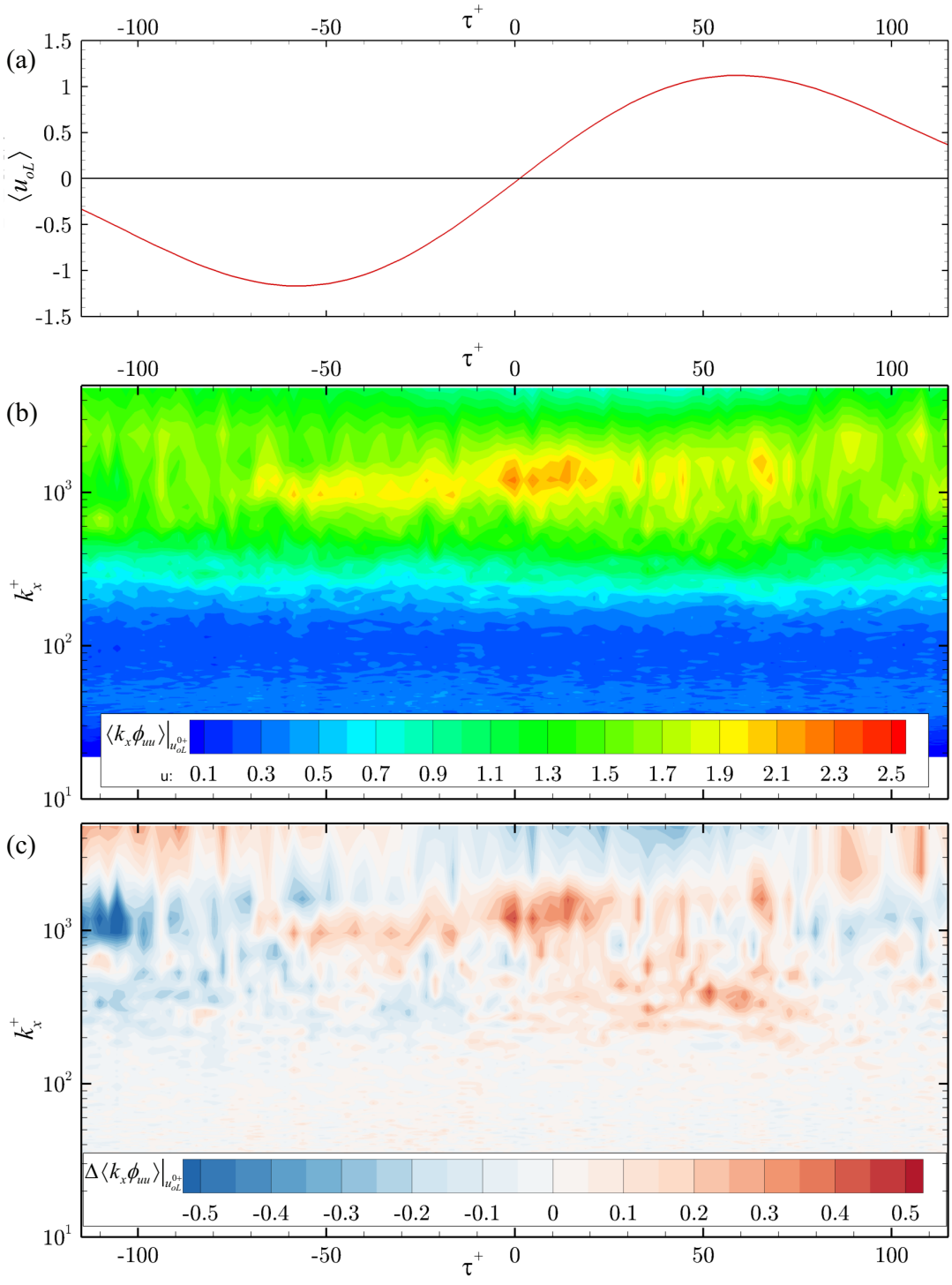

Figure 5.18: (b) Conditional u- spectrum and (a) discrepancy from unconditional spectrum at various times τ^+ from the bFOV at $y^+ \approx 37$. Also shown in (a) is the corresponding conditional outer large scale at the reference point $(0, y_o)$.

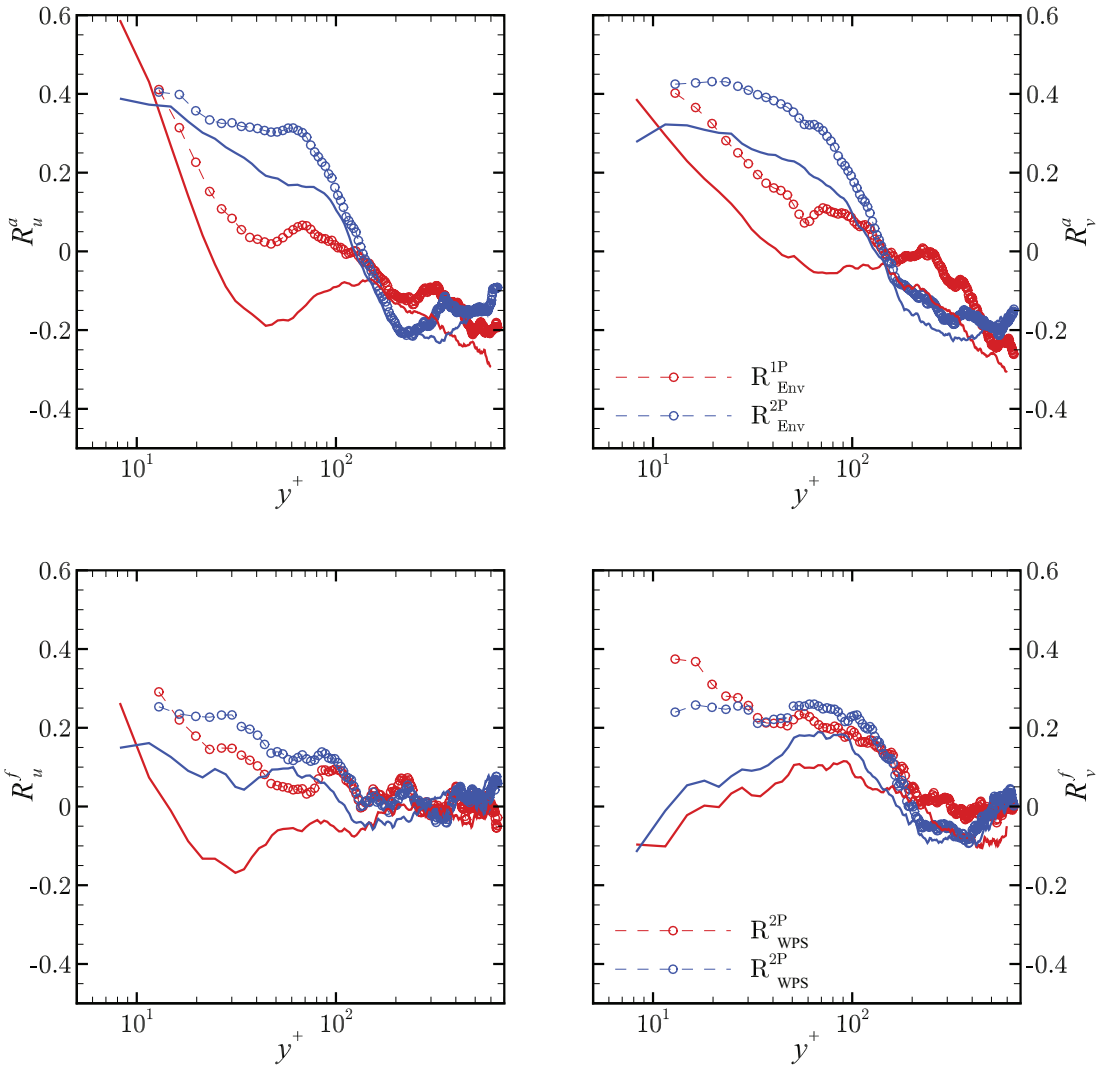

Figure 5.19: (a,b) Amplitude modulation and (c,d) frequency modulation correlation coefficient of the (a,c) streamwise and (b,d) wall-normal turbulence from one- and two-point analysis. Amplitude modulation shown is from envelop-based methods, and frequency modulation shown is from wavelet based. Also shown are corresponding smooth-wall measurements as *solid* lines.

close to the wall, which decays in the logarithmic region. Also shown are the smooth-wall counterparts for comparison. These trends indicate a higher correlation in the rough-walls relative to the smooth-walls. This observation is similar to what was observed on the complex roughness using hotwire measurements in section 3.2. Also shown in figure 5.19(c,d) is the frequency modulation counterparts of streamwise and wall-normal turbulence, indicating enhanced frequency modulation correlation too. More interestingly, the frequency modulation correlation in the wall normal correlation does not decrease close to wall as was seen in smooth-wall (figure 5.5). This could be related to the presence of stronger wall-normal turbulence, which enables the measurement of the same and subsequent interactions relatively easier.

Finally, the above modulation interactions in multi-point analysis can be seen in the 2D correlation maps, as shown in figure 5.20, similar to the smooth-wall counterparts in figures 5.3 and 5.6. First, with the amplitude modulation correlation maps, while the smooth-wall counterparts showed a dual-peak nature corresponding to 1-point and 2-point analysis (indicating the small scale correlations with local large scales AND with inertial region large scales), the same for the rough-wall measurements shows a single elongated peak, around $y_o \sim 50 - 100$. This indicates that the amplitude of small scales close to the wall does not correlate well with large scales locally ($y^+ = 10$). Further, the outer location of maximum correlation appears to be definitely closer to the wall than the outer-point chosen according to the smooth-wall metric ($y^+ = \sqrt{15Re_\tau}$). This is indicated in the amplitude modulation of both the velocity components. This is in contrast with the observation in the smooth-walls, where the outer peak appeared very close to the location of the center of the logarithmic region. Frequency modulation correlation maps from mulit-point analysis also show similar observations in the streamwise turbulence intensity. The wall normal turbulence indicates the second significant difference between the smooth and rough-wall turbulent boundary layers investigated here. The smooth-wall boundary layer had correlations dropping to 0 very close to the wall (figure 5.6). The same for the rough-wall shows a com-

pletely different picture, where the correlation indicates a definitive peak close to the wall. Similar to the smooth-wall flow, the frequency correlation structure in the wall-normal component is different compared to the streamwise turbulence, and do the amplitude modulation correlations in either components.

The current study was aimed at preliminary investigation of these interactions using the wall roughness, and a larger ensemble is required to look at the zero crossing conditional averages as in the previous sections. All the metrics developed as a part of the current work can be extended to investigate the rough-wall flows too. The presence of strong correlations close to the wall is encouraging with this 'weak' roughness. More importantly, rough-walls with such roughness (small sand-grain equivalent roughness) might be an easier way to investigate the modulation interactions experimentally, than fully smooth-wall boundary layers. The inner region is thicker than a smooth-wall boundary layer, and can thus be used to overcome some difficulties in measuring near-wall scales. The wall-normal turbulence is also enhanced in the region close to the wall where it is otherwise very weak, but modulation effects are dominant– thus using roughness to artificially impart wall-normal fluctuations. This, obviously, assumes apriori that the near-wall scales in rough-wall flows undergo inner-outer interactions the same way as the smooth-wall flow. Though this needs to be validated before undertaking such an approach to draw broader conclusions, there is preliminary evidence in the current study to indicate the same.

It can thus be seen from the findings of Part-II of current research that by using efractive index-matching and high-frame-rate dual camera PIV setup, inner-outer interaction structure can be established in a spatio-temporal sense. Besides point-measurement based correlation coefficients discussed in Part-I, the conditional averaging developed here can also be used in time-resolved PIV data to investigate the same. These metrics can also easily be extended to rough-wall flows and internal flows to investigate the same. Much work is possible in applying these observations to establish physical models that describe the inner-outer interactions in smooth- and rough-wall boundary layers.

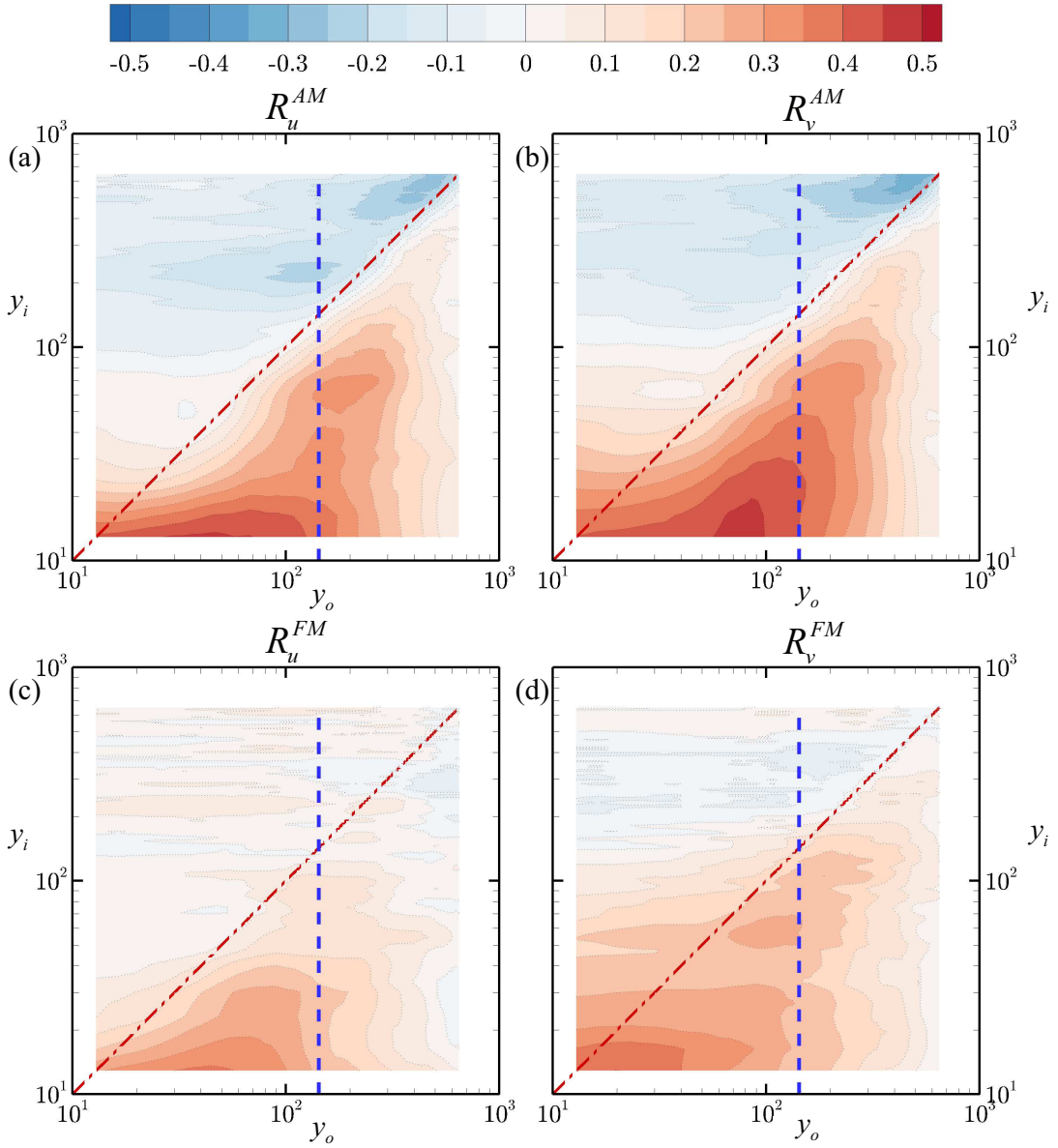

Figure 5.20: Multi-point correlation map of (a,b) Amplitude and (c,d) frequency modulation in the rough-wall turbulent boundary layer of (a,c) streamwise and (b,d) wall-normal turbulence. The *red* line indicates one-point measurements and blue line indicates the two-point measurements shown in figure 5.19.

CHAPTER 6

CONCLUSIONS AND FUTURE WORK

Studies on turbulent wall bounded flows and effects of wall-roughness on the same have been of significant engineering relevance for over a century. While much understanding has been gained using various computational, experimental and theoretical works, wall-bounded turbulence still forms important bottlenecks in many engineering applications. From the very nature of the turbulence, as was discussed in chapter 1, it is evident that breakthroughs in future rough-wall turbulent boundary layer research is going to be through a predominantly collaborative effort between the experimental, computational and theoretical community. To this end, the current work aimed to provide an experimental perspective for future models on inner–outer interactions in high Re boundary layers over wall roughness.

Recent quantification of inner–outer interactions in wall turbulence via amplitude and frequency modulation suggests that their importance increases with increasing Re, meaning such effects are important to a range of practical flow scenarios. Given that such applications occur at high Re, they also often suffer from roughness effects wherein even small surface imperfections can lead to modifications of the near-wall flow behavior (particularly drag and heat-transfer characteristics) as the viscous length scale becomes smaller than the size of these surface imperfections (i.e., the latter begin to protrude from the viscous sublayer). Thus, there exists a need to explore the characteristics of inner–outer interactions via AM and FM in rough-wall flow so that the applicability of such phenomena can be faithfully extended to practical flow scenarios. The experiments reported herein served this specific purpose as the occurrence of AM and FM is explored

in a high-Re turbulent flow over smooth- and rough-wall boundary layers

6.1 Flow over complex roughness

The first set of experiments reported herein explored the occurrence of AM and FM in a high-Re turbulent flow overlying a complex roughness topography replicated from a turbine blade damaged by deposition of foreign materials. This surface serves as a proxy for that encountered in practical flow scenarios wherein surface roughness is often multi-scale and irregular in nature. Previous studies have shown roughness-induced secondary flows to exist in the mean flow over this topography, reflected in the occurrence of low- and high-momentum pathways (LMP and HMP, respectively) alternating in the spanwise direction (Barros & Christensen, 2014; Willingham *et al.*, 2014; Anderson *et al.*, 2015). Thus, the current rough-wall measurements were made coincident with each of these mean-flow features to explore similarities and differences in the inner–outer interactions along these pathways. 1-probe and 2-probe hotwire measurements that fully resolve the temporal scales in the boundary layers were performed to investigate the modulation effects in the roughness.

The primary observation in the current work is that modulation influences are present in the rough-wall flow at both LMP and HMP locations. In particular, there existed strong similarities in the AM correlation maps for smooth- and rough-wall flow, including strong near-wall correlation indicative of modulation, inertial-region small-scale arrangement around large scales, and wake intermittency– all of which further support previous observations of outer-layer similarity in the current rough-wall flow (Wu & Christensen, 2007, 2010; Mejia-Alvarez & Christensen, 2010). However, unlike smooth-wall flow where there existed a clear separation between the near-wall modulation signature and the inertial-region scale arrangement, the rough-wall results showed ambiguity in this regard.

The FM correlation maps also showed strong similarities between the smooth-

and rough-wall cases, further supporting the occurrence of strong modulation of the near-wall small scales by the large scales in the outer region. However, as previously reported by Baars *et al.* (2015), FM analysis captured near-wall modulation influences while avoiding ambiguity from inertial-layer scale arrangement (in contrast to AM analysis) which assisted in confirming the occurrence of near-wall modulation in the two rough-wall cases. The results presented herein indicate that FM is a less ambiguous diagnostic of inner–outer interactions compared to AM, especially for the current rough-wall flow wherein near-wall modulation and inertial-region scale arrangement could not be separated in AM analysis.

The 2-probe measurements presented herein provided a direct measure of the large scales in the outer region which allowed unambiguous diagnosis of inner–outer interactions, as assumptions related to similarities and imprints of the outer large scales within the roughness sublayer were not required (as is typically assumed and previously confirmed in smooth-wall flow). Further, the validity of the superposition assumption was also tested with the velocity signatures measured simultaneously by the two probes. A strong coherence between the large scales measured from the two probes indicated that 1-probe measurements are sufficient to make conclusions on correlation structure of inner-outer interactions even on current rough-wall flows. The coherence in rough-wall flows, however, was weaker very close to the wall and at smaller scales, compared to the smooth-wall flow where a larger range of scales superpose.

The availability of the two-probe measurements enabled the investigation of inner–outer interaction predictive models assuming simple superposition and by stochastic estimation. Both models yielded similar conclusions, and suggested a possibly stronger amplitude modulation in the rough-wall than the smooth-walls as measured by the respective calibration metrics. These conclusions agree well with Squire *et al.* (2016), who also observed similarly stronger modulation constants. Additionally, the strengths of these modulations appeared different within the two regions of the turbulent flow in our complex roughness. This further signifies the need for incorporating these physics into the sub-grid scale

models of LES simulations on high Re rough-wall flows.

The quasi-steady quasi-homogenous (QSQH) formulation of these inner-outer interactions were also tested. Given that most of the assumptions in the formulation of QSQH theroy (Chernyshenko *et al.*, 2012) are valid in the rough-wall flows as well, the ability of the same to predict the calibration constants from interaction models (IOIM and mIOIM) shed further light on the similarity of the mechanisms in the two flows. While simply the agreement with the QSQH constants does not directly imply the presence of the exact mechanisms (Zhang & Chernyshenko, 2016), it adds strength to the speculative mechanisms on the effect of large scale superposition on the skin-friction coefficient, and the subsequent dynamics of the near-wall turbulence in rough-wall flows.

The similarity of these inner–outer interactions between the smooth- and rough-wall flows from these point measurements was striking. The near-wall small scales seemed to respond to outer-layer large scales, irrespective of how the former are generated, i.e., from the viscous turbulence production cycle of smooth-wall flow or from vortex shedding by roughness elements that creates a roughness sublayer that entirely replaces the viscous sublayer. Further, as was shown in section 3.2, the modulation of small scales as measured by the correlation coefficient was invariant of where the large scales are sampled. While this observation is trivial in smooth-wall flow, the fact that this was even valid in rough-wall flow re-emphasizes the similarity of inner–outer interactions between the two flows that have very different near-wall flow characteristics. This observation meant that, at least for the current rough-wall flow, 1-probe measurements, with subsequent assumptions about how the outer large scales superimpose upon the near-wall region, are sufficient to observe the basic modulation phenomena. These observations were further reinforced by the stochastic estimation of the superposition phenomenon.

Finally, the current observations tend to agree with the mechanisms proposed by Hutchins (2014) and Baars *et al.* (2015), where the small scales, irrespective of their generation mechanism, respond in a quasi-steady way to changes in the

outer-layer structure. The conclusions overall agree well with the schematic of modulations first developed by Baars *et al.* (2015), and shown here for the current experiments in figure 3.13.

6.2 Inner–outer interactions using high-frame-rate PIV and RIM

The first part of the current work established the inner-outer interactions in a boundary layer over complex roughness, albeit for point measurements. High-frame-rate PIV, using two independent PIV systems for a high resolution, was performed on the streamwise–wall-normal plane in a refractive index-matched facility. The current work was aimed at studying the modulation interactions in a spatio–temporal sense, and developing possible metrics for the same over smooth-wall flow. These can then be extended successfully to the rough-wall flows, with preliminary experiments and results discussed here.

After establishing the boundary layer and turbulence characteristics, the temporal-only, point-analytics that were employed in the demonstration of modulations using hotwire measurements, were successfully applied with the PIV measurements as well. Amplitude modulation in streamwise and wall-normal turbulence were shown using single-, two- and multi-point correlation coefficients, and agreed well with the observations in Part-I and literature. However, very weak signatures of frequency modulation were found, with a distinctive behavior in the wall-normal turbulence.

After characterizing the boundary layers, conditional averages were developed to extract the spatial structure of the inertial region large scales, and its evolution. The small scale footprint of these large scales was investigated through the conditionally averaged small scale variance. A correlated modulation in small scale energy with a time/spatial delay was clearly evident relative to the convecting large scales, lending support to similar observations made in hotwire amplitude modulation analysis. Similar observations were also found with wall-normal tur-

bulence, reiterating the observations from temporal-only analysis, and providing a structural signature of the same.

The QSQH hypothesis predicts not only amplitude and frequency modulation, but also scale modulation – where a positive large scale fluctuation energizes smaller scales near the wall and vice versa. From the conditionally averaged streamwise power-spectra of streamwise scales λ_x, such a preferential energy distribution among scales that is correlated with the large scales was not immediately observed. The amplitude modulation was, however, observed with the energy in the spectrum showing fluctuations correlated with the large scale behavior.

Temporal-only analysis was performed using a limited dataset on the rough-wall flows. The correlation coefficients indicated a stronger correlation in both streamwise and wall-normal turbulence, and for both amplitude and frequency modulations. These observations were similar to those on the complex roughness observed using hotwire measurements. While the various conditional averages applied on smooth-wall data can be applied on a more exhaustive rough-wall dataset, the presence of amplitude and frequency modulation on the hexagonal roughness shows again that these inner-outer interactions are important even on rough-wall flows.

The observations of the PIV measurements, and the conditionally averaged structures of large-scale–small-scale interactions complement very well with the point measurements using hotwire. The inclined nature of the outer large scale structure and the small scale amplitude variations trailing the same were speculated earlier in section 3.4. The observations from PIV measurements directly complement these speculations. The conclusions also lend additional support the amplitude modulation of wall-normal velocity fluctuations, as was observed using hotwire measurements in Talluru *et al.* (2014).

6.3 Future work

While the current work demonstrates the presence of amplitude and frequency modulations in rough-wall flows, much understanding should still be gained to extend these conclusions for theoretical and computational models.

Of immediate relevance to the current work is investigating the efficacy of the predictive models (such as the ones presented in Mathis *et al.* (2011*a*) and Baars *et al.* (2016)) in predicting velocity statistics of rough-wall flows. Recently, Squire *et al.* (2016) have attempted the same and expressed the inability of the mIOIM model in the current state in predicting the turbulent statistics at a Re different to that of the calibration experiment. This warrants further investigation, and ideas based on wall roughness scaling could be explored to describe the inner region. The ability of QSQH theory to reasonably predict the calibration constants tends to support the mechanisms hypothesized. Further, using the spectral stochastic tools, the receptivity of the small scales to the large scale modulations can be examined as a scale-dependent model. This will be particularly useful in more effectively extending the current conclusions to predominantly spectral-based LES models. The current theories assume that all small scales correlate with large scales uniformly (with a constant correlation R^a). While this might be more accurate with a very large Re_τ where there is an asymptotic separation between the large and small scales, intermediate scales might play a more important role at lesser Re_τ commonly investigated using experiments and DNS.

Two-dimensional, two-component models can be developed with current and future high-frame-rate PIV measurements on smooth- and rough-wall boundary layers. This will be more useful in drawing conclusions and relations between the spatial structure of the large scales, and the modulation effects. For example, spatio-temporal analytical tools such as POD, Dynamic Mode Decomposition (DMD, Schmid (2010)), resolvent mode analysis (McKeon, 2017), etc. can be extended to the conditionally sampled velocity fields to extract spatial mechanisms. More relevant conditional estimates and stochastic estimation tools

(Adrian, 1977) can be used to theoretically combine the correlation-based and conditional average-based metrics of the modulation phenomenon. Particularly, correlations based on swirling strength might prove useful in investigating the presence of any direct link between the coherent structures and the modulating interactions. Though the scale modulation phenomena could not be clearly identified in the current results, a higher statistical ensemble might reduce the uncertainty in the spectral variations and make these conclusions with higher confidence.

As mentioned before, a collaborative framework with DNS and LES simulations on similar flows will greatly extend the understanding of the physics demonstrated in the current work to enhance the fidelity of future computations on high Re rough, wall-bounded flows.

APPENDIX A

SUPPLEMENTAL FILE: EXAMPLE VECTOR FIELD

The supplemental file `ExampleVectorField.mov` shows a brief temporal evolution of flow field as seen by the two fields of views (sFOV and bFOV). sFOV is overlaid on top of bFOV, and is indicated by a solid boundary. The seamless movement of structures between the two FOVs indicate the high quality and consistency of the data. The increased resolution in the sFOV can also be observed as the structures enter and leave the view. The contours are of streamwise velocity, and all quantities are shown in real units.

APPENDIX B

SUPPLEMENTAL FILE: CONDITIONAL STRUCTURE, $\langle U|_{O^+}\rangle_I$ AND $\langle V|_{O^+}\rangle_I$

The supplemental file `LargeScaleEvolution.mp4` shows the temporal evolution with τ of the conditionally averaged large scale structure $\langle u|_{o^+}\rangle_i$ and $\langle v|_{o^+}\rangle_i$ [Eqn. (5.2)] in the temporal neighborhood of the zero-crossing event. Note that the large scale $\langle u|_{o^+}\rangle_i$ and $\langle v|_{o^+}\rangle_i$ are of opposite signs throughout the boundary layer and at all instances, reiterating the fact that the average Reynolds shear stress is negative in the boundary layer. See also figure 5.11.

APPENDIX C

SUPPLEMENTAL FILE: CONDITIONAL STRUCTURE, $\langle [U|_{O^+}]^2_S \rangle_I$

The supplemental file `SmallScale-u.mp4` shows the temporal evolution with τ of the conditionally averaged small scale streamwise variance (*bottom*) along with the large scale u-structure ($\langle u|_{o^+} \rangle_i$, Eqn. (5.2), *top*) in the temporal neighborhood of the zero-crossing event. See also figure 5.12.

APPENDIX D

SUPPLEMENTAL FILE: CONDITIONAL STRUCTURE, $\Delta\langle[U|_{O^+}]^2_S\rangle$

The supplemental file `SmallScaleDiscrepancy-Du.mp4` shows the temporal evolution with τ of the conditionally averaged small scale streamwise discrepancy (Eqn. (5.4), *bottom*) along with the large scale u-structure ($\langle u|_{o^+}\rangle_i$, Eqn. (5.2), *top*) in the temporal neighborhood of the zero-crossing event. The structure of the large scale and the amplitude modulation relative to the same tends direct support to the the interaction structure proposed by Baars *et al.* (2015) and discussed earlier in section 3.4. See also figure 5.12.

APPENDIX E

SUPPLEMENTAL FILE: CONDITIONAL STRUCTURE, $\langle [V|_{O^+}]^2_S \rangle_I$ AND $\Delta\langle [V|_{O^+}]^2_S \rangle$

The supplemental file `SmallScaleAndDiscrepancy-v.mov` shows the temporal evolution with τ of the conditionally averaged small scale wall normal variance (*middle*) and discrepancy (*bottom*) along with the large scale u-structure ($\langle u|_{o^+} \rangle_i$, Eqn. (5.2), *top*) in the temporal neighborhood of the zero-crossing event. See also figure 5.15.

REFERENCES

Adrian, R. J 1977 On the role of conditional averages in turbulence theory. *Turbulence in Liquids* **1**, 323–332.

Adrian, R. J. 2007 Hairpin vortex organization in wall turbulence a. *Physics of Fluids* **19** (4), 041301.

Adrian, R. J & Westerweel, J. 2011 *Particle image velocimetry*. Cambridge University Press.

Agostini, L. & Leschziner, M. 2016 On the validity of the quasi-steady-turbulence hypothesis in representing the effects of large scales on small scales in boundary layers. *Physics of Fluids* **28** (4), 045102.

Alfred, M. 1999 *Signal Analysis Wavelets, Filter Banks, Time-Frequency Transforms and Applications*. John Wiley and Sons, New York.

Alfredsson, H. P. & Örlü, R. 2010 The diagnostic plot–a litmus test for wall bounded turbulence data. *Euro. J. Mechanics-B/Fluids* **29** (6), 403–406.

Anderson, W. 2016 Amplitude modulation of streamwise velocity fluctuations in the roughness sublayer: evidence from large-eddy simulations. *J. Fluid Mech.* **789**, 567–588.

Anderson, W., Barros, J. M. & Christensen, K. T. 2015 Numerical and experimental study of mechanisms responsible for turbulent secondary flows in boundary layer flows over spanwise heterogeneous roughness. *J. Fluid Mech.* **748**, 316–347.

Baars, W. J., Hutchins, N. & Marusic, I. 2016 Spectral stochastic estimation of high-reynolds-number wall-bounded turbulence for a refined inner-outer interaction model. *Physical Review Fluids* **1** (5), 054406.

Baars, W. J., Hutchins, N. & Marusic, I. 2017 Reynolds number trend of hierarchies and scale interactions in turbulent boundary layers. *Phil. Trans. R. Soc. A* **375** (2089), 20160077.

Baars, W. J., Talluru, K. M., Hutchins, N. & Marusic, I. 2015 Wavelet analysis of wall turbulence to study large-scale modulation of small scales. *Exp. Fluids* **56** (10), 1–15.

Bai, K. & Katz, J. 2014 On the refractive index of sodium iodide solutions for index matching in piv. *Experiments in fluids* **55** (4), 1704.

Bailey, S. CC., Kunkel, G. J., Hultmark, M., Vallikivi, M., Hill, J. P., Meyer, K. A., Tsay, C., Arnold, C. B. & Smits, A. J. 2010 Turbulence measurements using a nanoscale thermal anemometry probe. *Journal of Fluid Mechanics* **663**, 160.

Balakumar, J. B. & Adrian, R. J. 2007 Large-and very-large-scale motions in channel and boundary-layer flows. *Phil. T. Roy. Soc. A* **365** (1852), 665–681.

Balasubramaniam, B. J. 2005 *Nature of turbulence in wall-bounded flows*.

Bandyopadhyay, P. R. & Hussain, A. K. M. F. 1984 The coupling between scales in shear flows. *Phys. Fluids* **27** (9), 2221–2228.

Barros, J. M. 2014 Cross-plane stereo-piv measurements of a turbulent boundary layer over highly irregular roughness. PhD thesis, University of Illinois at Urbana-Champaign.

Barros, J. M. & Christensen, K. T. 2014 Observations of turbulent secondary flows in a rough-wall boundary layer. *J. Fluid Mech.* **748**, R1.

Bendat, J. S. & Piersol, A. G. 2011 *Random data: analysis and measurement procedures*, , vol. 729. John Wiley & Sons.

Bernardini, M. & Pirozzoli, S. 2011 Inner/outer layer interactions in turbulent boundary layers: a refined measure for the large-scale amplitude modulation mechanism. *Phys. Fluids* **23** (6), 061701.

Blackman, K. & Perret, L. 2016 Non-linear interactions in a boundary layer developing over an array of cubes using stochastic estimation. *Physics of Fluids* **28** (9).

Bons, J. P 2010 A review of surface roughness effects in gas turbines. *Journal of turbomachinery* **132** (2), 021004.

Bons, J. P., Taylor, R. P., McClain, S. T. & Rivir, R. B. 2001 The many faces of turbine surface roughness. In *ASME Turbo Expo 2001: Power for Land, Sea, and Air*, pp. V003T01A042–V003T01A042. American Society of Mechanical Engineers.

Bruun, H. H. 1995 Hot-wire anemometry-principles and signal analysis .

Budwig, R. 1994 Refractive index matching methods for liquid flow investigations. *Experiments in fluids* **17** (5), 350–355.

Chauhan, K., Nagib, H. M. & Monkewitz, P. A. 2007 On the composite logarithmic profile in zero pressure gradient turbulent boundary layers. In *Proc. 45th AIAA Aerospace Sciences Meeting, Paper No. AIAA*, , vol. 532, pp. 1–18.

Chauhan, K. A., Monkewitz, P. A. & Nagib, H. M. 2009 Criteria for assessing experiments in zero pressure gradient boundary layers. *Fluid Dynamics Research* **41** (2), 021404.

Chen, R-C. 1991 Experimental and numerical studies of solid-liquid multiphase flow in pipes. PhD thesis, Case Western Reserve University.

Chernyshenko, S. I., Marusic, I. & Mathis, R. 2012 Quasi-steady description of modulation effects in wall turbulence. *arXiv preprint arXiv:1203.3714* .

Christensen, K. T. 2004 The influence of peak-locking errors on turbulence statistics computed from piv ensembles. *Experiments in Fluids* **36** (3), 484–497.

Christensen, K. T. & Adrian, R. J. 2001 Statistical evidence of hairpin vortex packets in wall turbulence. *J. Fluid Mech.* **431**, 433–443.

Chung, D. & McKeon, B. J. 2010 Large-eddy simulation of large-scale structures in long channel flow. *J. Fluid Mech.* **661**, 341–364.

Clauser, F. H. 1956 The turbulent boundary layer. *Adv. Appl. Mech.* **4**, 1–51.

Davidson, P. 2004 *Turbulence: an introduction for scientists and engineers*. Oxford University Press.

Dennis, D. J. C. & Nickels, T. B. 2008 On the limitations of taylor's hypothesis in constructing long structures in a turbulent boundary layer. *Journal of Fluid Mechanics* **614**, 197–206.

Dennis, D. J. C. & Nickels, T. B 2011 Experimental measurement of large-scale three-dimensional structures in a turbulent boundary layer. part 2. long structures. *Journal of Fluid Mechanics* **673**, 218–244.

Dróżdż, A., Elsner, W. & Drobniak, S. 2015 Scaling of streamwise reynolds stress for turbulent boundary layers with pressure gradient. *European Journal of Mechanics-B/Fluids* **49**, 137–145.

Duvvuri, S. & McKeon, B. J. 2015 Triadic scale interactions in a turbulent boundary layer. *J. Fluid Mech.* **767**, R4.

Duvvuri, S. & McKeon, B. J. 2016 Nonlinear interactions isolated through scale synthesis in experimental wall turbulence. *Phys. Rev. Fluids* **1** (3), 032401.

Eitel-Amor, G., Örlü, R. & Schlatter, P. 2014 Simulation and validation of a spatially evolving turbulent boundary layer up to reθ= 8300. *International Journal of Heat and Fluid Flow* **47**, 57–69.

Fiscaletti, D., Ganapathisubramani, B. & Elsinga, G. E. 2015 Amplitude and frequency modulation of the small scales in a jet. *J. Fluid Mech.* **772**, 756–783.

Flack, K. A., Schultz, M. P. & Shapiro, T. A 2005 Experimental support for townsend's reynolds number similarity hypothesis on rough walls. *Physics of Fluids* **17** (3), 035102.

Ganapathisubramani, B., Hutchins, N., Monty, J. P., Chung, D. & Marusic, I. 2012 Amplitude and frequency modulation in wall turbulence. *J. Fluid Mech.* **712**, 61–91.

Ganapathisubramani, B., Longmire, E. K. & Marusic, I. 2003 Characteristics of vortex packets in turbulent boundary layers. *J. Fluid Mech.* **478**, 35–46.

Guala, M., Metzger, M. M. & McKeon, B. J. 2011 Interactions within the turbulent boundary layer at high reynolds number. *J. Fluid Mech.* **666**, 573–604.

Gad-el Hak, M. & Bandyopadhyay, P. R. 1994 Reynolds number effects in wall-bounded turbulent flows. *Appl. Mech. Rev* **47** (8), 307–365.

Harun, Z., Monty, J. P., Mathis, R. & Marusic, I. 2013 Pressure gradient effects on the large-scale structure of turbulent boundary layers. *Journal of Fluid Mechanics* **715**, 477–498.

Head, M. R. & Bandyopadhyay, P. R. 1981 New aspects of turbulent boundary-layer structure. *Journal of Fluid Mechanics* **107**, 297–338.

Holmes, P., Lumley, J. L. & Berkooz, G. 1998 *Turbulence, coherent structures, dynamical systems and symmetry*. Cambridge university press.

Hommema, S. E. & Adrian, R. J. 2003 Packet structure of surface eddies in the atmospheric boundary layer. *Boundary-layer meteorology* **106** (1), 147–170.

Hong, J., Katz, J. & Schultz, M. P. 2011 Near-wall turbulence statistics and flow structures over three-dimensional roughness in a turbulent channel flow. *Journal of Fluid Mechanics* **667**, 1–37.

Hutchins, N. 2014 Large-scale structures in high reynolds number wall-bounded turbulence. In *Progress in Turbulence V*, pp. 75–83. Springer.

Hutchins, N. & Marusic, I. 2007*a* Evidence of very long meandering features in the logarithmic region of turbulent boundary layers. *J. Fluid Mech.* **579**, 1–28.

Hutchins, N. & Marusic, I. 2007*b* Large-scale influences in near-wall turbulence. *Phil. T. Roy. Soc. A* **365** (1852), 647–664.

Hutchins, N., Monty, J. P., Ganapathisubramani, B., Ng, H. C. & Marusic, I. 2011 Three-dimensional conditional structure of a high-reynolds-number turbulent boundary layer. *J. Fluid Mech.* **673**, 255–285.

Hutchins, N., Nickels, T. B., Marusic, I. & Chong, M. 2009 Hot-wire spatial resolution issues in wall-bounded turbulence. *J. Fluid Mech.* **635**, 103–136.

Inoue, M., Mathis, R., Marusic, I. & Pullin, D. I. 2012 Inner-layer intensities for the flat-plate turbulent boundary layer combining a predictive wall-model with large-eddy simulations. *Physics of Fluids* **24** (7), 075102.

Jacobi, I. & McKeon, B. J. 2013 Phase relationships between large and small scales in the turbulent boundary layer. *Exp. Fluids* **54** (3), 1–13.

Jiménez, J. 2004 Turbulent flows over rough walls. *Annu. Rev. Fluid Mech.* **36**, 173–196.

Jiménez, J. & Pinelli, A. 1999 The autonomous cycle of near-wall turbulence. *J. Fluid Mech.* **389**, 335–359.

Kevin, Monty, J. P, Bai, H. L., Pathikonda, G., Nugroho, B., Barros, J. M., Christensen, K. T & Hutchins, N. 2017 Cross-stream stereoscopic particle image velocimetry of a modified turbulent boundary layer over directional surface pattern. *Journal of Fluid Mechanics* **813**, 412–435.

Keylock, C. J., Ganapathasubramani, B., Monty, J. P., Hutchins, N. & Marusic, I. 2016 The coupling between inner and outer scales in a zero pressure boundary layer evaluated using a hölder exponent framework. *Fluid Dynamics Research* **48** (2), 021405.

Kim, K. C. & Adrian, R. J. 1999 Very large-scale motion in the outer layer. *Phys. Fluids* **11** (2), 417–422.

Kline, S. J., Reynolds, W. C., Schraub, F. A. & Runstadler, P. W. 1967 The structure of turbulent boundary layers. *J. Fluid Mech.* **30** (04), 741–773.

Krogstad, P-Å., Antonia, R. A. & Browne, L. W. B. 1992 Comparison between rough-and smooth-wall turbulent boundary layers. *Journal of Fluid Mechanics* **245**, 599–617.

L., Keirsbulck, Labraga, L., Mazouz, A. & Tournier, C. 2002 Surface roughness effects on turbulent boundary layer structures. *Journal of Fluids Engineering* **124**, 127–135.

Lee, M. & Moser, R. D. 2015 Direct numerical simulation of turbulent channel flow up to. *Journal of Fluid Mechanics* **774**, 395–415.

Liu, Z-C., Landreth, CC, Adrian, R. J. & Hanratty, T. J. 1991 High resolution measurement of turbulent structure in a channel with particle image velocimetry. *Experiments in fluids* **10** (6), 301–312.

Marusic, I., Mathis, R. & Hutchins, N. 2010 Predictive model for wall-bounded turbulent flow. *Science* **329** (5988), 193–196.

Mathis, R., Hutchins, N. & Marusic, I. 2009*a* Large-scale amplitude modulation of the small-scale structures in turbulent boundary layers. *J. Fluid Mech.* **628**, 311–337.

Mathis, R., Hutchins, N. & Marusic, I. 2011*a* A predictive inner–outer model for streamwise turbulence statistics in wall-bounded flows. *J. Fluid Mech.* **681**, 537–566.

Mathis, R., Marusic, I., Chernyshenko, S. I. & Hutchins, N. 2013*a* Estimating wall-shear-stress fluctuations given an outer region input. *J. Fluid Mech.* **715**, 163–180.

Mathis, R., Marusic, I., Chernyshenko, S. I. & Hutchins, N. 2013*b* Estimating wall-shear-stress fluctuations given an outer region input. *Journal of Fluid Mechanics* **715**, 163.

Mathis, R., Marusic, I., Hutchins, N. & Sreenivasan, K. R. 2011*b* The relationship between the velocity skewness and the amplitude modulation of the small scale by the large scale in turbulent boundary layers. *Phys. Fluids* **23** (12), 121702.

Mathis, R., Monty, J. P., Hutchins, N. & Marusic, I. 2009*b* Comparison of large-scale amplitude modulation in turbulent boundary layers, pipes, and channel flows. *Phys. Fluids* **21** (11), 111703.

McKeon, B. J. 2017 The engine behind (wall) turbulence: perspectives on scale interactions. *Journal of Fluid Mechanics* **817**.

Meinhart, C. D. 1994 Investigation of turbulent boundary layer structure using particle-image velocimetry. .

Meinhart, C. D. & Adrian, R. J. 1995 On the existence of uniform momentum zones in a turbulent boundary layer. *Physics of Fluids* **7** (4), 694–696.

Mejia Alvarez, R. 2011 Experimental study of low-order models of highly-irregular roughness and their impact on turbulent boundary layers. PhD thesis, University of Illinois at Urbana-Champaign.

Mejia-Alvarez, R. & Christensen, K. T. 2010 Low-order representations of irregular surface roughness and their impact on a turbulent boundary layer. *Phys. Fluids* **22** (1), 015106.

Mejia-Alvarez, R. & Christensen, K. T. 2013 Wall-parallel stereo particle-image velocimetry measurements in the roughness sublayer of turbulent flow overlying highly irregular roughness. *Phys. Fluids* **25** (11), 115109.

Mejia-Alvarez, R., Wu, Y. & Christensen, K. T. 2014 Observations of meandering superstructures in the roughness sublayer of a turbulent boundary layer. *Int. J. Heat Fluid Fl.* **48**, 43–51.

Metzger, M. M. 2002 Scalar dispersion in high reynolds number turbulent boundary layers. PhD thesis, Ph. D. thesis, University of Utah, Salt Lake City, UT.

Metzger, M. M. & Klewicki, J. C. 2001 A comparative study of near-wall turbulence in high and low reynolds number boundary layers. *Phys. Fluids* **13** (3), 692–701.

Morrison, J. F. 2007 The interaction between inner and outer regions of turbulent wall-bounded flow. *Philosophical Transactions of the Royal Society of London A: Mathematical, Physical and Engineering Sciences* **365** (1852), 683–698.

Musker, A. J. 1979 Explicit expression for the smooth wall velocity distribution in a turbulent boundary layer. *AIAA Journal* **17** (6), 655–657.

Nadeem, M., Lee, J. H., Lee, J. & Sung, H. J. 2015 Turbulent boundary layers over sparsely-spaced rod-roughened walls. *Int. J. Heat Fluid Flow* **56**, 16–27.

Natrajan, V. K. & Christensen, K. T. 2006 The role of coherent structures in subgrid-scale energy transfer within the log layer of wall turbulence. *Phys. Fluids* **18**, 065104.

Ng, H. C., Monty, J. P., Hutchins, N., Chong, M. & Marusic, I. 2011 Comparison of turbulent channel and pipe flows with varying Reynolds number. *Exp. Fluids* **51** (5), 1261–1281.

Nickels, T. B., Marusic, I., Hafez, S., Hutchins, N. & Chong, M. 2007 Some predictions of the attached eddy model for a high reynolds number boundary layer. *Philosophical Transactions of the Royal Society of London A: Mathematical, Physical and Engineering Sciences* **365** (1852), 807–822.

Nikuradse, J. 1950 *Laws of flow in rough pipes*. National Advisory Committee for Aeronautics Washington.

Nugroho, B., Hutchins, N. & Monty, J. P. 2013 Large-scale spanwise periodicity in a turbulent boundary layer induced by highly ordered and directional surface roughness. *International Journal of Heat and Fluid Flow* **41**, 90–102.

Örlü, R., Fiorini, T., Segalini, A., Bellani, G., Talamelli, A. & Alfredsson, H. P. 2017 Reynolds stress scaling in pipe flow turbulence– first results from ciclope. *Phil. Trans. R. Soc. A* **375** (2089), 20160187.

Örlü, R. & Schlatter, P. 2013 Comparison of experiments and simulations for zero pressure gradient turbulent boundary layers at moderate reynolds numbers. *Experiments in fluids* **54** (6), 1547.

Panton, R. L. 2001 Overview of the self-sustaining mechanisms of wall turbulence. *Progress in Aerospace Sciences* **37** (4), 341–383.

Pathikonda, Gokul & Christensen, K. T. 2017 Inner–outer interactions in a turbulent boundary layer overlying complex roughness. *Phys. Rev. Fluids* **2** (4), 044603.

Perry, A. E. & Li, D. J. 1990 Experimental support for the attached-eddy hypothesis in zero-pressure-gradient turbulent boundary layers. *Journal of Fluid Mechanics* **218**, 405–438.

Perry, A. E., Schofield, W. H & Joubert, P. N. 1969 Rough wall turbulent boundary layers. *Journal of Fluid Mechanics* **37** (02), 383–413.

Pope, S. B. 2001 *Turbulent flows*. IOP Publishing.

Rao, K. N., Narasimha, R. & Narayanan, B. M. A. 1971 The bursting phenomenon in a turbulent boundary layer. *J. Fluid Mech.* **48** (02), 339–352.

Raupach, M. R., Antonia, R. A. & Rajagopalan, S. 1991 Rough-wall turbulent boundary layers. *Appl. Mech. Rev.* **44** (1), 1–25.

Reynolds, O. 1883 An experimental investigation of the circumstances which determine whether the motion of water shall be direct or sinuous, and of the law of resistance in parallel channels. *Proceedings of the royal society of London* **35** (224-226), 84–99.

Robinson, S. K. 1991 Coherent motions in the turbulent boundary layer. *Annual Review of Fluid Mechanics* **23** (1), 601–639.

Schlatter, P. & Örlü, R. 2010*a* Assessment of direct numerical simulation data of turbulent boundary layers. *Journal of Fluid Mechanics* **659**, 116.

Schlatter, P. & Örlü, R. 2010*b* Quantifying the interaction between large and small scales in wall-bounded turbulent flows: A note of caution. *Phys. Fluids* **22** (5), 051704.

Schmid, P. J. 2010 Dynamic mode decomposition of numerical and experimental data. *Journal of fluid mechanics* **656**, 5–28.

Schultz, M. P. & Flack, K. A. 2005 Outer layer similarity in fully rough turbulent boundary layers. *Experiments in Fluids* **38** (3), 328–340.

Shida, S., Kosukegawa, H. & Ohta, M. 2011 Development of a methodology for adaptation of refractive index under controlling kinematic viscosity for piv. In *ASME 2011 International Mechanical Engineering Congress and Exposition*, pp. 313–321. American Society of Mechanical Engineers.

Sidebottom, W., Cabrit, O., Marusic, I., Meneveau, C., Ooi, A. & Jones, D. 2014 Modelling of wall shear-stress fluctuations for large-eddy simulation. In *Proc. 19th Australasian Fluid Mechanics Conf., Melbourne, Australia*.

Smits, A. J., McKeon, B. J & Marusic, I. 2011 High–reynolds number wall turbulence. *Annual Review of Fluid Mechanics* **43**, 353–375.

Squire, D. T., Baars, W. J., Hutchins, N. & Marusic, I. 2016 Inner–outer interactions in rough-wall turbulence. *Journal of Turbulence* **17** (12), 1159–1178.

Stoots, C., Becker, S., Condie, K., Durst, F. & McEligot, D. 2001 A large-scale matched index of refraction flow facility for lda studies around complex geometries. *Experiments in fluids* **30** (4), 391–398.

Talluru, K. M., Baidya, R., Hutchins, N. & Marusic, I. 2014 Amplitude modulation of all three velocity components in turbulent boundary layers. *J. Fluid Mech.* **746**, R1.

Torrence, C. & Compo, G. P. 1998 A practical guide to wavelet analysis. *Bulletin of the American Meteorological society* **79** (1), 61–78.

Townsend, A. A. 1976 *The structure of turbulent shear flow*. Cambridge University Press.

Uzol, O., Chow, Y-C., Katz, J. & Meneveau, C. 2002 Unobstructed particle image velocimetry measurements within an axial turbo-pump using liquid and blades with matched refractive indices. *Experiments in Fluids* **33** (6), 909–919.

Vincenti, P., Klewicki, J., Morrill-Winter, C., White, C. M. & Wosnik, M. 2013 Streamwise velocity statistics in turbulent boundary layers that spatially develop to high reynolds number. *Experiments in fluids* **54** (12), 1629.

Willingham, D., Anderson, W., Christensen, K. T. & Barros, J. M. 2014 Turbulent boundary layer flow over transverse aerodynamic roughness transitions: Induced mixing and flow characterization. *Phys. Fluids* **26** (2), 025111.

Wu, Y. & Christensen, K. T. 2007 Outer-layer similarity in the presence of a practical rough-wall topography. *Phys. Fluids* **19** (8), 85108–85108.

Wu, Y. & Christensen, K. T. 2010 Spatial structure of a turbulent boundary layer with irregular surface roughness. *J. Fluid Mech.* **655**, 380–418.

Zagarola, M. V. & Smits, A. J. 1998 Mean-flow scaling of turbulent pipe flow. *Journal of Fluid Mechanics* **373**, 33–79.

Zhang, C. & Chernyshenko, S. I. 2016 Quasisteady quasihomogeneous description of the scale interactions in near-wall turbulence. *Phys. Rev. Fluids* **1** (1), 014401.

Zhou, J., Adrian, R. J., Balachandar, S. & Kendall, T. M. 1999 Mechanisms for generating coherent packets of hairpin vortices in channel flow. *Journal of Fluid Mechanics* **387**, 353–396.